TRANSIENT PHENOMENA IN HYDROELECTIC POWER PLANTS

NOTES DE COURS

LABORATOIRE DE MACHINES HYDRAULIQUES

Institut des sciences de l'énergie

SECTION DE GÉNIE MÉCANIQUE

Christophe NICOLET
François AVELLAN

Lausanne, EPFL
2007

Contents

Notations

Nomenclature

Latin characters

a	Wave speed $a = \sqrt{E/\rho}$ (for infinite fluid)	[m/s]
dx	Spatial discretization step	[m]
dt	Temporal discretization step	[s]
f	Frequency $f = 1/T$	[Hz]
g	Terrestrial acceleration $g \simeq 9.81$ m/s^2	[m/s^2]
h	Piezometric head $h = z + p/(\rho g)$	[m/s^2]
l_c	Characteristic length	[m]
n	Polytropic coefficient	[-]
n	Rotational frequency	[Hz]
p	Static pressure	[Pa]
$\tilde{p}$	Fluctuating pressure	[Pa]
t	Time	[s]
x	Abscissa	[m]
y	Guide vane opening (GVO)	[-]
z	Elevation	[m]
A	Pipe area	[m^2]
C	Absolute flow velocity	[m/s]
D	Diameter	[m]
E	Massic energy $E = gH = p/\rho + gz + C^2/2$	[J/Kg]
E	Bulk modulus	[Pa]
E_c	Young modulus	[Pa]
E_r	Massic energy loss	[J/kg]
H	Head	[m]
K	Local loss coefficient	[-]
N	Rotational speed	[rpm]
R	Radius $R = D/2$	[m]
T	Torque	[Nm]

T	Period	[s]
U	Peripheral velocity	[m/s]
V	Volume	[m^3]
$\underline{Z}$	Complex acoustic impedance $\underline{Z} = \underline{h}/\underline{Q}$	[m/s^2]
Z	Acoustic impedance	[m/s^2]

Greek symbols

α	Flow angle	[rad]
β	Blade angle	[rad]
γ	Wave number $\gamma = 2\pi/\lambda = \omega/a$	[1/m]
$\underline{\gamma}$	Complex wave number	[1/m]
θ	Polar abscissa of turbine characteristic $\theta = (Q/Q_{BEP})/(N/N_{BEP})$	[-]
κ	Adiabatic coefficient	[-]
λ	Wave length $\lambda = a/f$	[m]
λ	Local loss coefficient	[-]
μ	Fluid dynamic viscosity	[Pa s]
ν	Fluid kinematic viscosity $\nu = \mu/\rho$	[m^2/s]
ρ	Density	[kg/m^3]
σ	Stress	[Pa]
τ	Shear stress	[Pa]
ϕ	Phase	[rad]
χ	Mass flow gain factor $\chi = -\partial V/\partial Q$	[s]
ω	Pulsation $\omega = 2\pi f$	[rad/s]

Non-dimensional values in turbomachinery

Fr	Froude number $Fr = C_\infty/\sqrt{gl_c}$	[-]
Re	Reynolds number $Re = C_\infty l_c/\nu$	[-]
St	Strouhal number $St = C_\infty/fl_c$	[-]
η	Efficiency $\eta = T\omega/(\rho QE)$	[-]
ν	Specific speed $\nu = \varphi^{1/2}/\psi^{3/4}$	[-]
σ	Thoma number $\sigma = (p_\infty - p_v)/(\frac{1}{2}\rho C_\infty^2)$	[-]
φ	Flow coefficient $\varphi = Q/(\pi\omega R^3)$	[-]
ψ	Energy coefficient $\psi = 2E/(\omega^2 R^2)$	[-]
$NPSE$	Net Positive Suction Energy $NPSE = \sigma E$	[J/Kg]

Hydroacoustic equivalent scheme

R	Hydraulic resistance $R = \lambda dx\|\overline{Q}\|/(2gDA^2)$	[s/m^2]
R_d	Diaphragm hydraulic resistance $R = K\|\overline{Q}\|/(2gA^2)$	[s/m^2]
R_{ve}	Viscoelastic resistance $R_{ve} = \mu/(\rho g A dx)$	[s/m^2]
L	Hydraulic inductance $L = dx/(gA)$	[s^2/m^2]
L	General hydraulic inductance $L = \int dx/(gA(x))$	[s^2/m^2]
C	Hydraulic capacitance $C = dxgA/a^2$	[m^2]
C	Cavitation capacitance $C = -\partial V/\partial h = V/(nh)$	[m^2]

Turbine location and section definition

I	Reference section high pressure side; inlet spiral casing
3	Stay vanes
2	Guide vanes
1	Runner blade high pressure side edge
i	Runner blade interior streamline (shroud)
e	Runner blade exterior streamline (hub)
$\overline{1}$	Runner blade low pressure side edge
$\overline{2}$	Draft tube inlet
$\overline{I}$	Reference section low pressure side; outlet draft tube

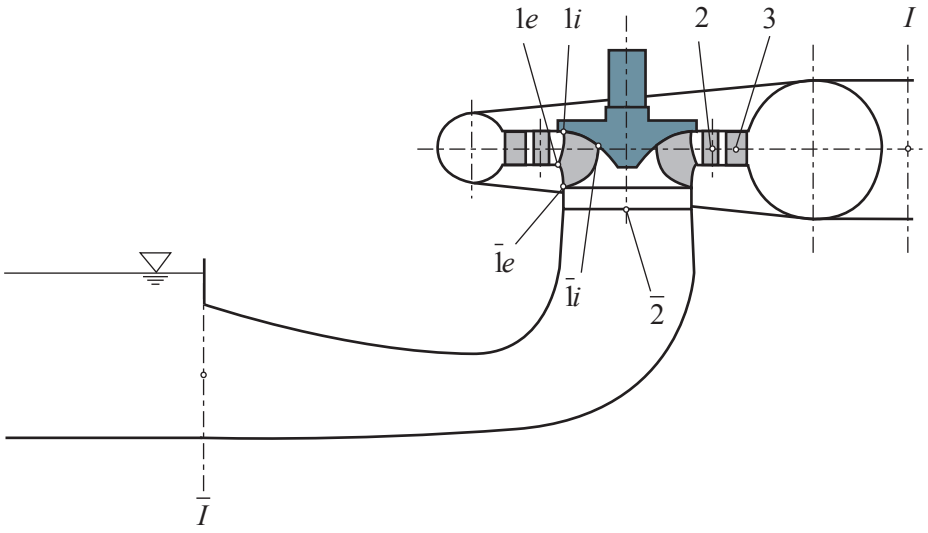

Subscript

BEP	Best efficiency point
n	Nominal operating point
i	Incident
r	Reflected
t	Transmitted

Chapter 1

Introduction

1.1 Hydropower: Facts and Issues

The demand for electricity is constantly increasing because of the demographic growth and social level increase of developing countries. Worldwide projections for the period 2003 2030 predict that the electricity consumption will more than double from 14'781 TWh/year to 30'116 TWh/year [30]. Figure 1.1 shows the evolution of the sources of electricity generation from 2003 until 2030. To cope with this need, a gain in efficiency in all domains, *i.e.* production, transport, consumption, but also an increase of renewable energies capacity are required in order to refrain the development of solutions generating greenhouse gases. The development of the related infrastructure and technologies minimizing social and environmental impacts represents a huge challenge for mankind.

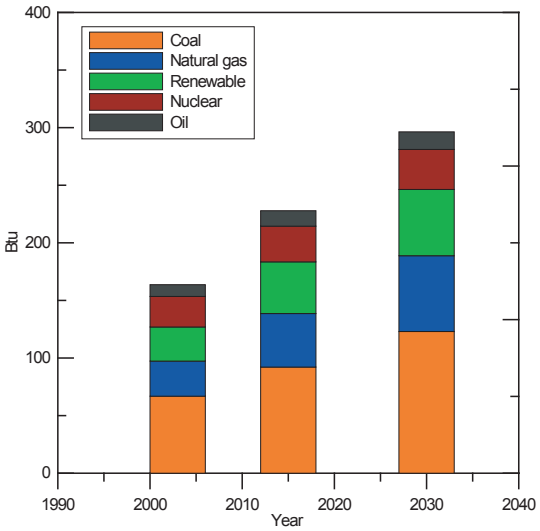

Figure 1.1: Projection of the electricity generation by fuel type for 2003, 2015 and 2030 in Btu (British thermal units) [30].

The contribution of renewable energy in the future is expected to grow mainly due to the increase of large hydropower capability. In 1999, the hydropower production covered

19% of the world electricity needs with a total installed capacity estimated around 692 GW [22], [73], [49]. The geographical distribution of the total production capacity is illustrated in figure 1.2 with about 31% of the installed capacity in Europe, 25% in Asia, 23% in North America, 15% in South America and the remaining 6% are shared between Africa, Oceania and the Middle East. However, the 2'633 TWh of hydroelectricity produced in 1999 represents only 33.2% of the economically exploitable resources and 18.3% of the technically exploitable capability. Therefore, hydropower has still a high potential for growth in the 21^{st} century. As illustrated in figure 1.3, the regions with the highest potential are Asia, Africa, South America but also in Europe. In addition, hydropower presents the advantage of avoiding emissions of gases in spite of others environmental impacts on the fauna, flora and sediments. The social impact are on the one hand detrimental because of the population displacements and land transformation but on the other hand positive as hydropower offers the possibility to mitigate flood, enabling better fluvial navigation and irrigation and providing employment. Moreover, the drawbacks related to hydropower production can be mitigated by taking appropriate counter measures at the early stages of the projects.

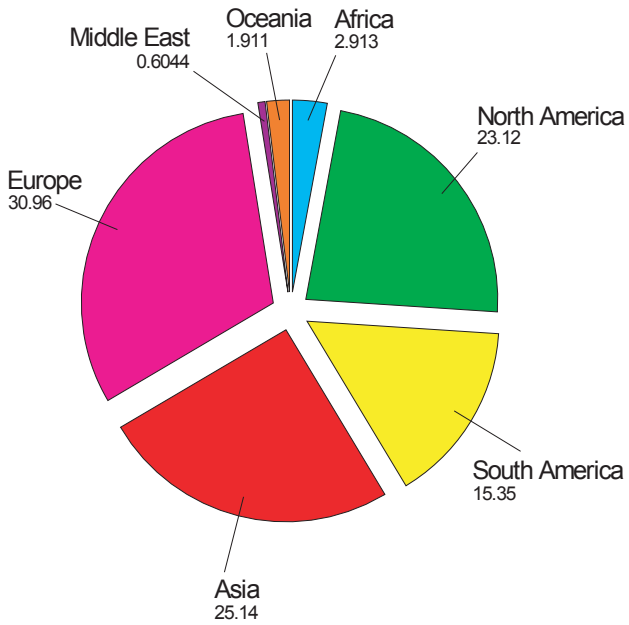

Figure 1.2: Distribution of hydropower capacity (for the year 1999); 100% being 692 GW [73].

1.2 The Increase of Hydropower Production

1.2.1 Increase of the Capacity

As illustrated in figure 1.1, the contribution of hydropower is expected to grow considerably in the next 30 years, and 553 GW of renewable production capability increase are predicted, corresponding to an annual rate of 1.9% [22]. Regarding the development of the hydroelectric production, it can be decomposed in 4 main areas:

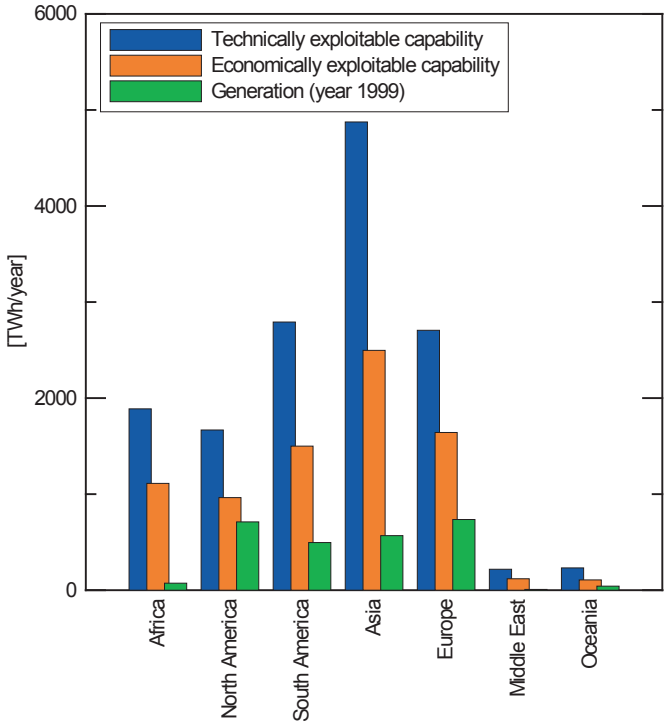

Figure 1.3: Distribution of the hydropower technically and economically exploitable capability and generation (for the year 1999) [73].

- **exploitation of new hydropower resources:** the main contribution is expected to come from the completion of hydro facilities in Asia and particularly in China;
- **refurbishment of existing power plants:** a gain of efficiency on old electromechanical equipment can represent a significant increase of the production capacity. It is mainly the case in Europe and North America for 50 years old facilities;
- **rehabilitation of old power plants:** older facilities in Europe and North America are subject to full re-equipments considering also new civil work in order to increase drastically the capacity of a power plant;
- **small hydro:** is related to developing countries where electrification of rural area can be achieved through small-hydro with reduced environmental impacts.

1.2.2 Over-Equipment for Improving Network Stability

Another aspect of development of the hydroelectric market is the increasing need for power plants able to stabilize the global power network by allowing quick set point changes in terms of both active and reactive power in generating and in motor mode. Indeed, the increase of renewable energy source contribution such as wind power, whose availability cannot be ensured, will represent a source of disturbances for power networks that are nowadays considered to be stable. For example in Europe, where thermal power plants still represent the major contribution, the impact of sudden changes of wind production

cannot be counter-balanced by thermal power plants but goes to hydropower. Therefore, there is a need for the development of pump-storage capability in order to be able not only to change the set point, but also to store exceeding produced energy. Actually, pump-storage power plants are the only high capacity solution for storing energy and balancing with nuclear broad band production at various time scales, *i.e.* daily as well as seasonally. Another side effect of deregulated energy market is the gain of interest for peak production requiring availability of high production capability.

New technologies like variable speed solutions also provide an additional degree of freedom for reducing time response of power plants and offering flexibility to the power management. Variable speed solutions enable taking advantage of flywheel effects of hydrogenerators for fast loading or unloading of units and spinning reserve [60].

1.2.3 The Hydropower Challenge

Modern hydropower has to face new challenges related to completely different exploitation strategies leading to an increase of the solicitation of the entire machine. Thus, hydraulic machines are increasingly subject to off-design operation, startup and shutdown sequences, quick set point changes, etc. To be competitive on the energy market, the specific power and efficiency of hydro units, which are already high, are constantly increased in order to meet economical issues but lead to higher loading of the structure of the turbines.

Consequently, manufacturers, consultants and utilities of hydro power plants need integrating new technologies and methodologies for improving dynamic performances, ensuring the safety and increasing the competitiveness of hydroelectric power plants. This requires developing appropriate experimental and numerical tools and methods for a better understanding and thus a wiser prediction of the micro and macro-scale behavior of hydroelectric power plants.

1.3 Francis Turbine in the Context of Hydropower

The hydraulic power P_h results from the product of the mass flow $\dot{M} = \rho \cdot Q$ and of the specific energy $E = g \cdot H$ and is therefore given by:

$$P_h = \rho \cdot Q \cdot E \tag{1.1}$$

The role of a hydraulic turbine is to convert the hydraulic power into mechanical power $P_m = T \cdot \omega$ with the highest hydraulic efficiency η_h which is given for a turbine by:

$$\eta_h = \frac{P_m}{P_h} = \frac{T \cdot \omega}{\rho \cdot Q \cdot E} \tag{1.2}$$

According to the hydrology and the exploitation strategy of a given hydraulic project, a goal discharge Q_{plant} and a goal specific energy E_{plant} are determined for the site. Then, depending on the number of machines and the selection of the synchronous rotational speed $N = (f_{network} \cdot 60)/(pairepoles)$, the type of turbine can be chosen between the "standard" hydraulic turbines which are: (i) Pelton turbines, (ii) Francis turbines, (iii) Kaplan turbines, (iv) bulbe turbine, (v) or propellers.

Figure 1.4 shows the domain of application of the different types of turbines as function of the nominal net head H_n and the nominal discharge Q of the machine. Typically,

for high head, medium head and low head, Pelton, Francis and Kaplan turbines are respectively chosen. However, for the intermediate range of head, 2 types of turbines are in competitions. Then, the final selection of a type of turbine results from an iteration process aiming the maximization of the produced energy on a standard year of exploitation taking into account maintenance, civil work and flexibility of operation issues. Because of its high application range, the Francis turbine is often selected. Table 1.1 summarizes the worldwide percentage sales of turbines of each type for the period 1997 2001. It appears that 56% of the turbines are of the Francis type with an additional 5% of pump-turbines.

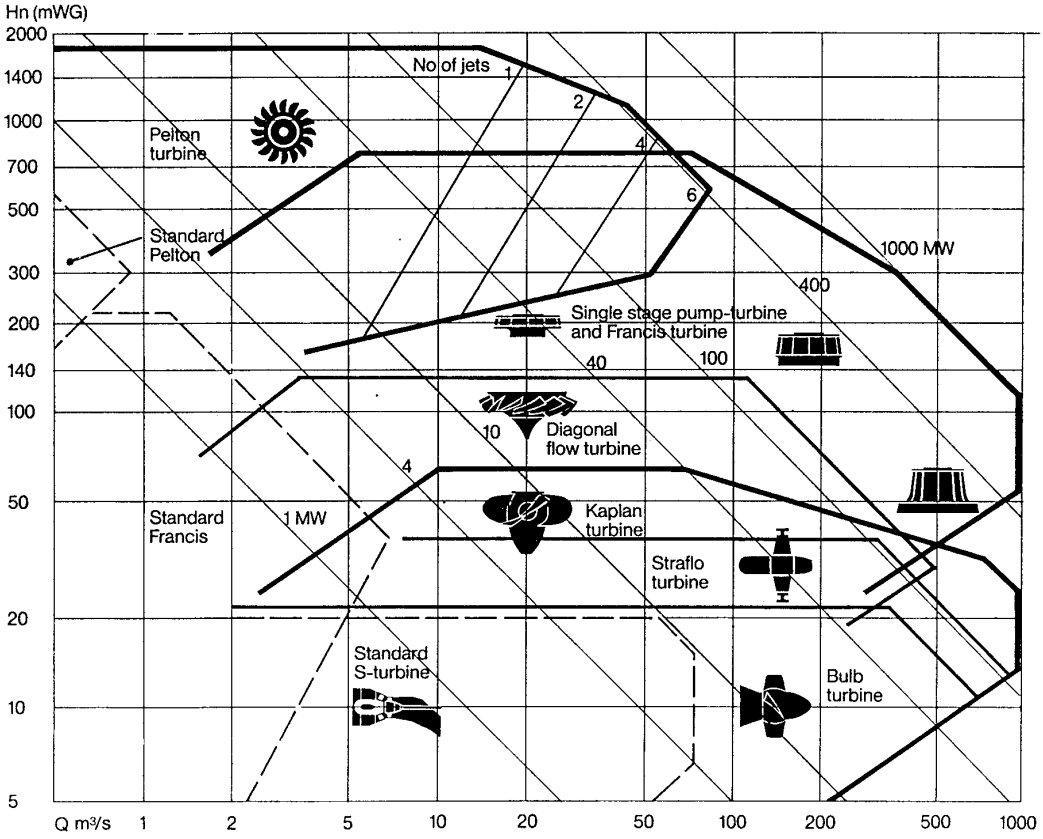

Figure 1.4: Turbine application range [33].

Table 1.1: Distribution of sales of the different types of turbines during the period 1997 to 2001 [79].

Francis %	Pelton %	Kaplan %	Bulbes %	Pump-turbines %
56	15	15	9	5

Once the nominal discharge Q_n, specific energy E_n and rotational pulsation ω_n are

known, the specific speed of the machine can be determined as follow:

$$\nu = \omega \cdot \frac{(Q_n/\pi)^{1/2}}{(2 \cdot E_n)^{3/4}} \tag{1.3}$$

All turbines having the same specific speed are geometrically similar.

1.3.1 The Francis Turbine

General

The francis turbine is made of 5 main components as illustrated by figure 1.5:

- **the spiral case:** converts axial momentum into angular momentum and distributes uniformly the flow into the stay vanes;
- **the stay vanes:** are fixed blades having the structural role to close the force loop of the pressurized spiral case ;
- **the guide vanes:** are mobile blades allowing controlling the flow through the turbine;
- **the runner:** converts the angular momentum of the flow into mechanical momentum by deviating the flow from the inlet to the outlet so that the flow has no more angular momentum at the outlet, the reaction force acting on the blade inducing the mechanical torque;
- **the diffuser or draft tube:** has the role to convert the kinetic energy of the flow into potential energy and therefore enables increasing the efficiency of the turbine by reducing the pressure level at the runner outlet.

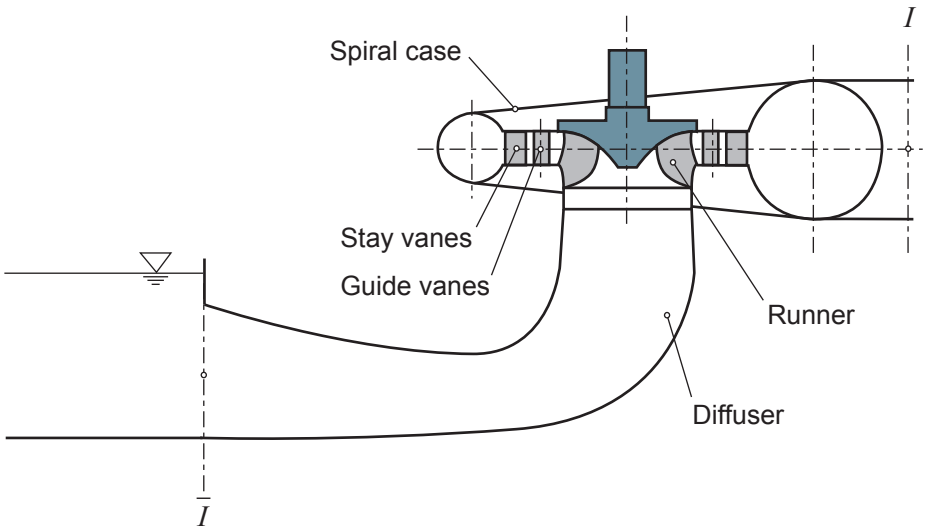

Figure 1.5: Components of a Francis turbine.

Figure 1.6 shows an example of turbine prototype and figure 1.7 shows typical geometries of Francis turbine runner for different specific speed ν.

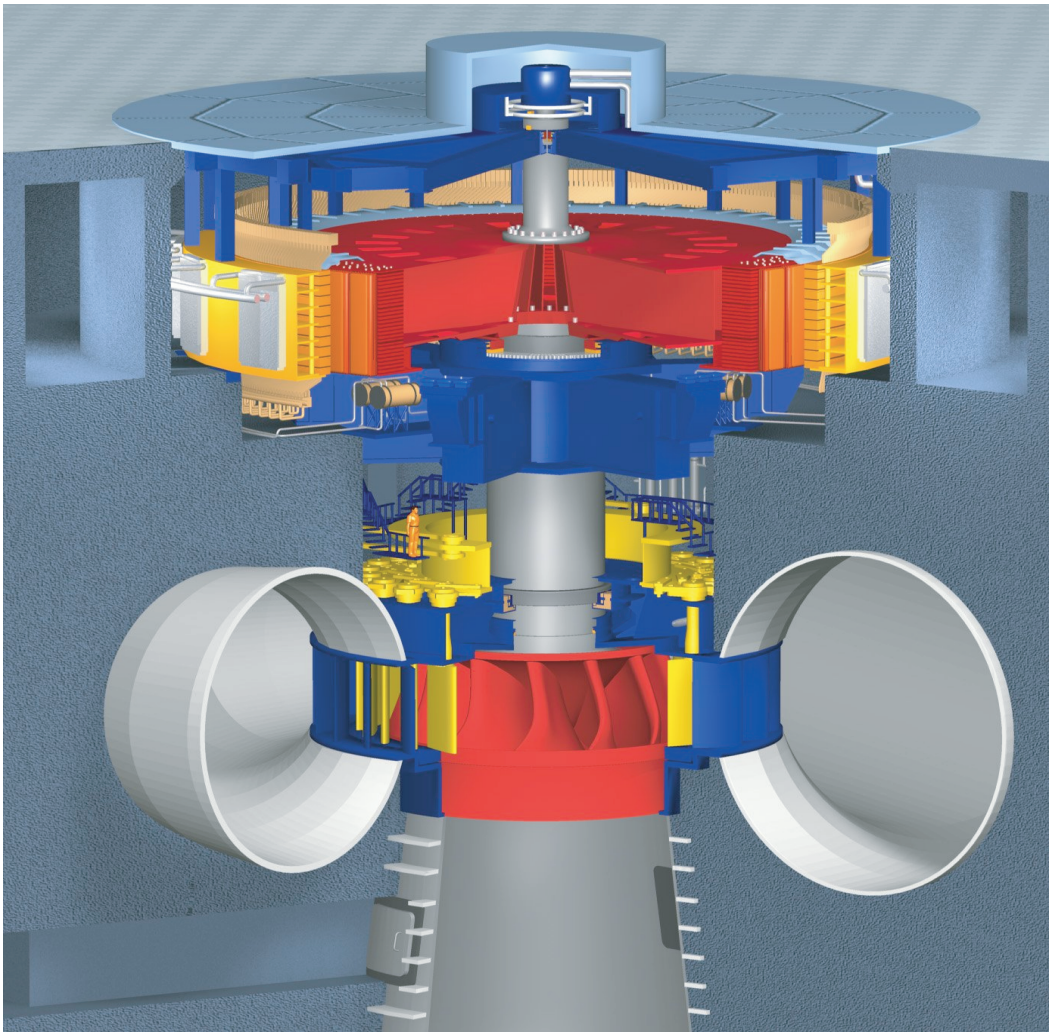

Figure 1.6: Example of prototype turbine; Three Gorges (Sanxia) 26×700 MW (Courtesy of Voith-Siemens Hydro).

Velocity Triangles

The absolute velocity $\overrightarrow{C}$ at any point of the turbine can be decomposed as the sum of the peripheral velocity of the turbine $\overrightarrow{U}$ and of the relative velocity $\overrightarrow{W}$ and is therefore given by:

$$\overrightarrow{C} = \overrightarrow{U} + \overrightarrow{W} \tag{1.4}$$

The velocity triangle at the inlet and outlet of a Francis turbine runner for the optimum operating conditions is illustrated in figure 1.8. The relative velocity $\overrightarrow{W}$ is perfectly adapted at both leading edge and trailing edge of the blade profile while the absolute velocity at the outlet $\overrightarrow{C}_{\bar{1}}$, is usually almost axial. The influence of the discharge on the velocity triangle at the runner outlet is illustrated in figure 1.9. It can be seen that for discharge below the optimum discharge, the flow at the runner outlet is animated with

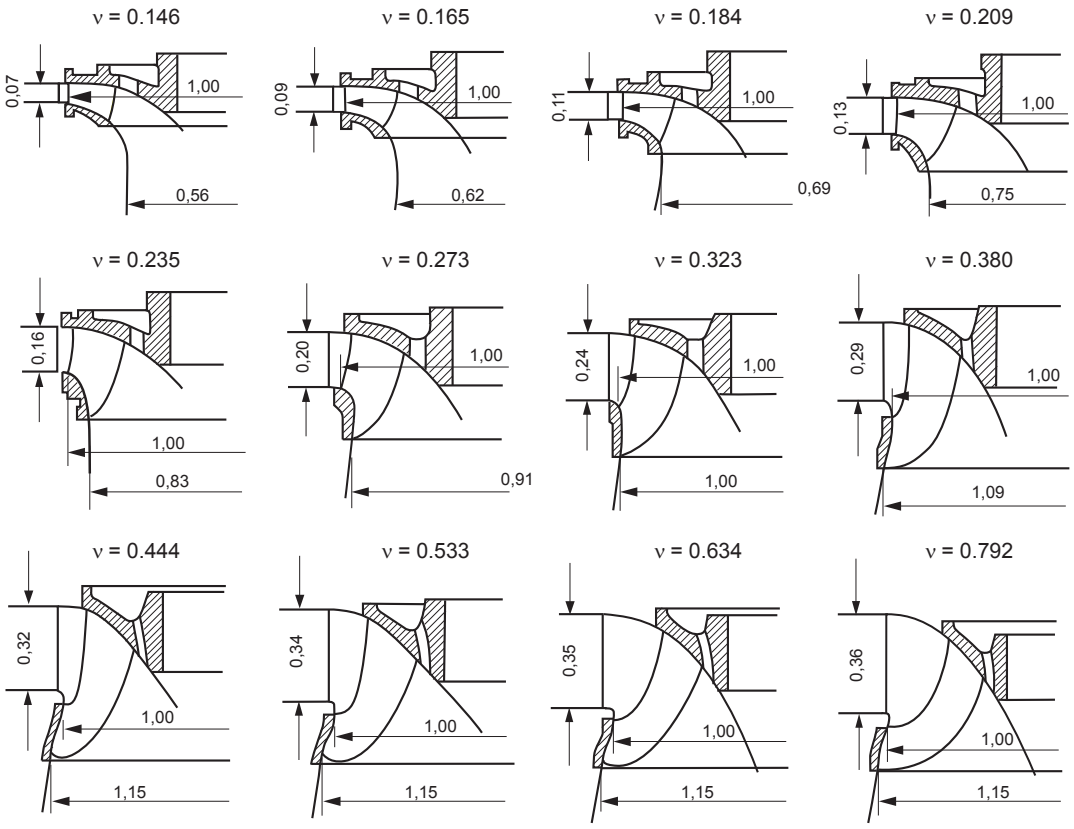

Figure 1.7: Francis turbine runner geometry as function of the specific speed ν [6].

a positive absolute circumferential velocity $\overrightarrow{C}_{u\bar{1}}$, while it is negative for discharge above optimum discharge.

The energy of the flow is converted into mechanical torque along the runner blade. This transformation can be expressed by the momentum of angular momentum conservation equation:

$$\frac{d}{dt}(\overrightarrow{r} \times m \cdot \overrightarrow{C}) = \overrightarrow{T} \tag{1.5}$$

Where m is the mass of the fluid particle, $\overrightarrow{r}$ is the radius and $\overrightarrow{T}$ is the mechanical torque. The balance of the momentum of angular momentum between runner inlet (1) and the runner outlet ($\bar{1}$) leads to the well known Euler's equation. The transformed energy, E_t, is given by:

$$\overrightarrow{E}_t = \overrightarrow{U}_1 \cdot \overrightarrow{C}_1 - \overrightarrow{U}_{\bar{1}} \cdot \overrightarrow{C}_{\bar{1}} \tag{1.6}$$

The scalar value of the transformed energy is given by:

$$E_t = U_1 \cdot C_{u1} - U_{\bar{1}} \cdot C_{u\bar{1}} \tag{1.7}$$

The transformed energy, is by definition given by:

$$E_t = \frac{T \cdot \omega}{\rho \cdot Q} \tag{1.8}$$

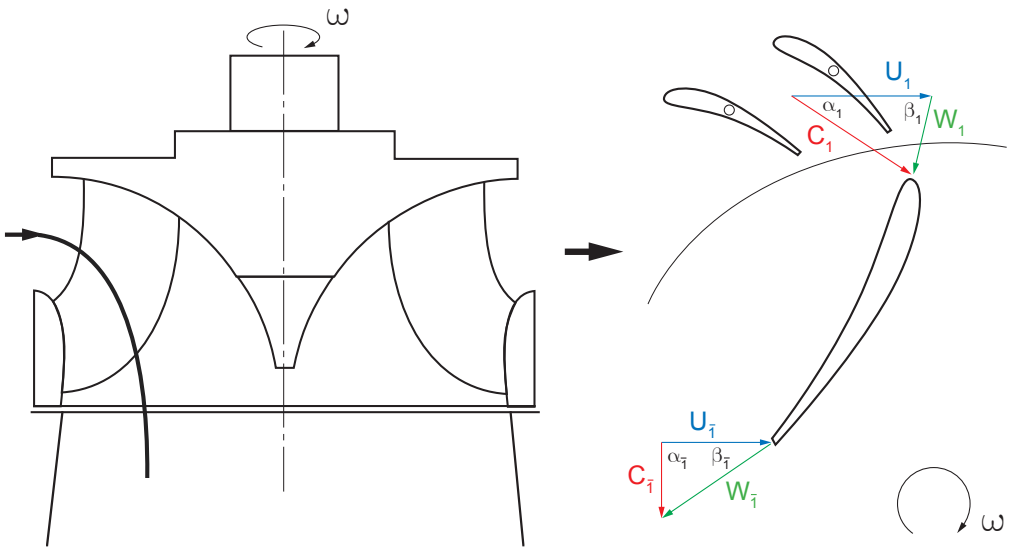

Figure 1.8: Velocity triangles at inlet and outlet of the runner blade.

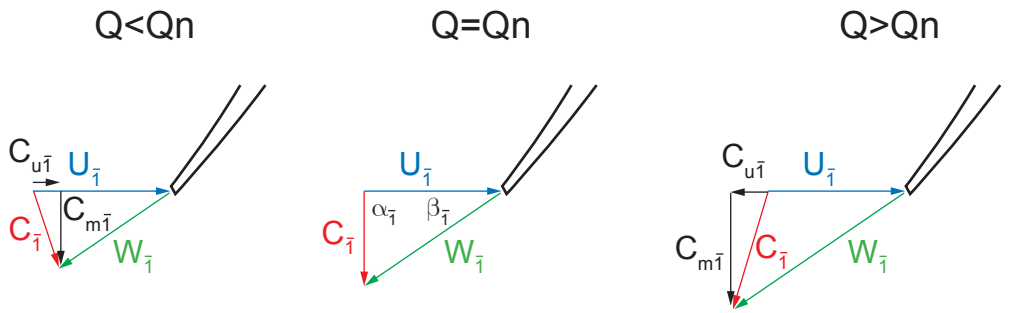

Figure 1.9: Influence of the discharge on the circumferential component of the absolute velocity.

And consequently it yields to:

$$\eta_h = \frac{E_t}{E} \tag{1.9}$$

The analysis of equation 1.7 shows that the energy transferred from the fluid to the runner depends on the change of circumferential velocity C_u through the runner, *i.e.* the deviation of the flow induced by the blades. It points out that it is interesting to minimize the outlet C_u in order to reduces losses by residual kinetic energy.

Turbine Performances

The evaluation of the performances of a turbine on its whole operating range requires, according to equation 1.2, measuring the discharge Q, the specific energy E, the rotational

speed N and the mechanical torque T for different guide vanes openings. The representation of the efficiency as function of the operating conditions $[Q, E, N, T]$ requires to suppress one operating parameter to enable a 3 dimensional representation. For performances purposes, it is convenient to use dimensionless coefficient where the rotational speed N is eliminated, leading to the expression of 2 coefficients:

- the discharge coefficient: $\varphi = \frac{Q}{\pi \cdot \omega \cdot R_{1e}^3}$;
- the energy coefficient: $\psi = \frac{2 \cdot E}{\omega^2 \cdot R_{1e}^2}$

According to these definitions, the specific speed becomes:

$$\nu = \frac{\varphi^{1/2}}{\psi^{3/4}} \tag{1.10}$$

Then, for a given turbine, the hydraulic efficiency η_h can be evaluated on the complete operating range of the turbine and represented as a function of the discharge and energy coefficients: $\eta_h = \eta_h(\varphi, \psi)$, providing the efficiency hill chart of the machine. However, it is convenient to rate the 2 coefficients by their values at the Best Efficiency Point of the machine (BEP), *i.e.* $\eta_h = \eta_h(\varphi/\varphi_{BEP}, \psi/\psi_{BEP})$ as illustrated in figure 1.10.

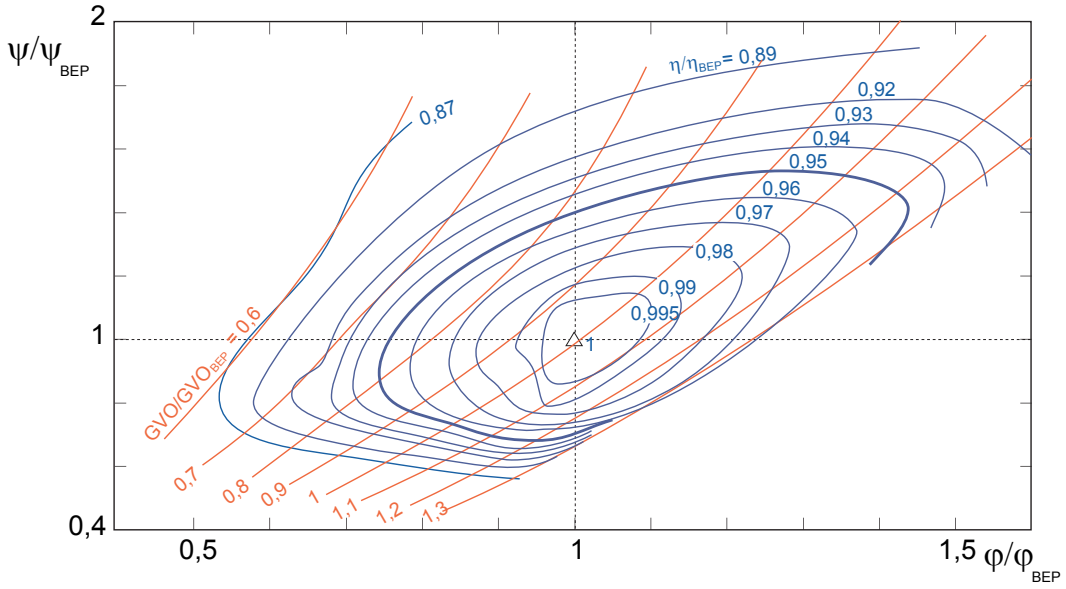

Figure 1.10: Efficiency hill diagram of a Francis turbine [33].

Cavitation

The velocity magnitude in a turbine are very high and can easily reach 40 m/s. According to Bernoulli's law, low pressure arise in areas of high velocities. Then, depending on the local mean static pressure, the water can vaporize if the pressure drops below the vaporization pressure p_v. This phenomenon, referred as cavitation, corresponds to vaporization

at constant temperature due to pressure decrease. Consequently, the cavitation is most likely to appear in the low pressure sides of a hydraulic machine. To qualify the pressure level inside the turbine, the Net Positive Suction Energy (NPSE) is introduced and refers to the downstream conditions of the turbine ($\overline{I}$) as follows:

$$NPSE = \frac{p_{\overline{I}}}{\rho} + g \cdot (Z_{\overline{I}} - Z_{ref}) + \frac{1}{2} \cdot C_{\overline{I}}^2 - \frac{p_v}{\rho} \tag{1.11}$$

Where p_v is the vaporization pressure and Z_{ref} is a reference elevation, for example the center line of the guide vanes.

The dimensionless cavitation number also known as the Thoma number is then introduced:

$$\sigma = \frac{NPSE}{E} \tag{1.12}$$

Low cavitation numbers indicate high risks of cavitation. The undesirable effects of the cavitation are the risk of erosion, noise and mechanical vibrations but also flow distortions and efficiency drop [33].

At off design operating conditions, the outlet velocity triangles features circumferential velocity component. At part load operation, the swirl flow induced in the draft tube may lead to flow instabilities resulting in the apparition of a helicoidal vortex precessing in the draft tube with a frequency of about 0.2 to 0.4 times the rotational frequency n [69], [50]. This vortex, called the "vortex rope", is visible if the tailrace water level is sufficiently low, *i.e.* for low cavitation number. Depending on the cavitation number and the rotational speed, a pressure surge may occurs, resulting into unacceptable pressure amplitudes due to resonance between pressure excitation induced by the vortex rope and the natural frequency of the hydraulic circuit [70].

1.3.2 Operating Stability of Francis Turbine Units

Scale Model Testing

Scale model testing offers the opportunity to evaluate the performances of a hydraulic turbine in the phase of the design of a project. Homologous reduced-scale model of the hydraulic turbine comprising the spiral case, distributor, runner and draft tube are tested on test rig [14]. The flow similitude is ensured by having the model geometry similar to that of the prototype. The similitude of the velocity triangles at the runner inlet and outlet is ensured by the identical φ and ψ conditions [46]. From the scale model tests, the following investigations can be undertaken: (i) efficiency hill chart measurement, (ii) cavitation inception/influence, (iii) pressure fluctuations measurement, (iv) axial thrust measurements, (v) test of mitigating counter-measures, and so on.

Typical observations of cavitation on a reduced-scale model are presented in figure 1.11 for the whole operating range of a Francis turbine. The following types of cavitation and related influences are identified:

- (1) and (2) inlet edge cavitation types that occurs at low and large energy coefficient ψ: may present a risk of erosion [57];
- (3) interblade cavitation vortices: can induce high cycle fatigue breaks [28], [64];

- (5) part load vortex rope: can be associated with pressure source excitation that may lead to resonance with the hydraulic system [25];
- (6) full load vortex rope: can lead to self-excited pressure fluctuations [53], [62];
- (7) outlet edge bubble cavitation: can lead to erosion of cavitation [47].

Regarding the operating stability of Francis turbine prototype, the pressure fluctuations measurements are of major concerns. The pressure fluctuations measured at different draft tube wall locations during the model tests can be presented in a waterfall diagram as a function of the rated frequency and of the rated discharge as illustrated in figure 1.12. This diagram evidences high pressure amplitudes of 3 different types:

- (2) part load pressure fluctuations;
- (3) upper part pressure fluctuations;
- (5) full load pressure fluctuations.

While no pressure pulsation are measured close to the best efficiency operating point (4) in figure 1.11 where the velocity triangle at the outlet leads to almost purely axial flow.

Part Load Draft Tube Vortex Rope

Francis turbine power plants operating at part load may present instabilities in terms of pressure, discharge, rotational speed and torque. These phenomena are strongly linked to the swirl flow structure at the runner outlet inducing a vortex core precession in the draft tube [69]. This leads to hydrodynamic instabilities [50]. The decrease of the tailrace pressure level makes the vortex core visible as a gaseous vortex rope. The volume of the gaseous vortex rope is dependent on the cavitation number σ and affects the parameters characterizing the hydroacoustic behavior of the entire power plant. As a result, eigen frequencies of the hydraulic system decrease with the cavitation number. Interaction between excitation sources like vortex rope precession and eigen frequencies may result in resonance effect and induce a so called draft tube surge and electrical power swing [35]. Consequences on pressure fluctuations and power oscillations were observed in the framework of many prototypes projects [80], [16], [31], [90], [35], [52] and [61].

Full Load Draft Tube Vortex Rope

Full load operation of Francis turbine creates a circumferential component of the outflow velocity inducing a swirl flow rotating in the opposite direction of the runner. For some operating points, the resulting axisymmetric vortex rope developing in the draft tube is known to start breathing [51]. These specific operating conditions may lead on prototype to severe self excited pressure fluctuations [53], [62], [61].

Rotor-Stator Interactions

Interactions between rotating parts and stationary parts of Francis turbine result in pressure fluctuations that propagate in the entire machine [21]. The combination of these pressure waves may result in resonance effects and induces unacceptable pressure fluctuations jeopardizing the safety of the whole power plant [45], [72], [34] and [26].

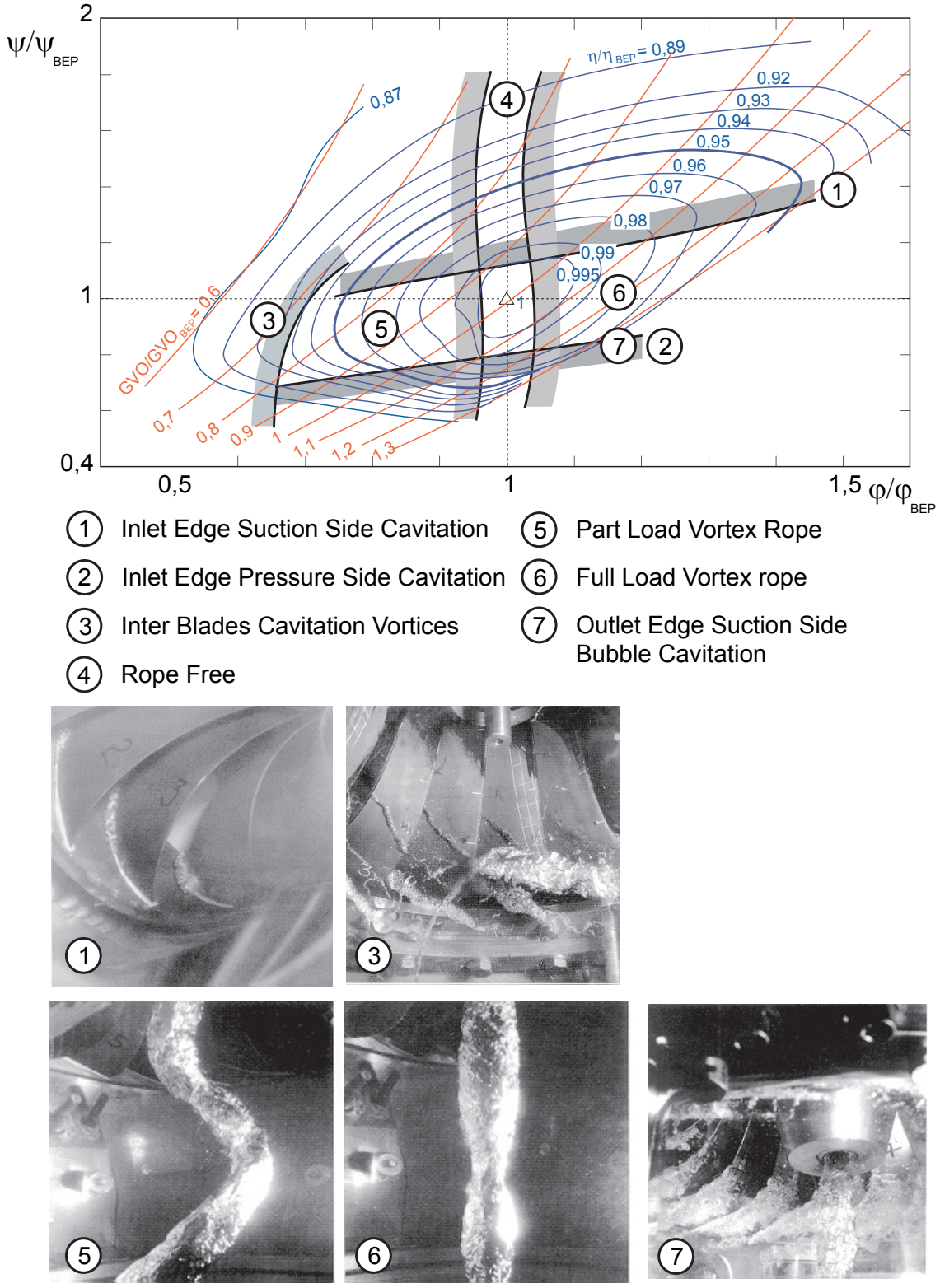

Figure 1.11: Typical cavitation regimes in the Francis turbine [33].

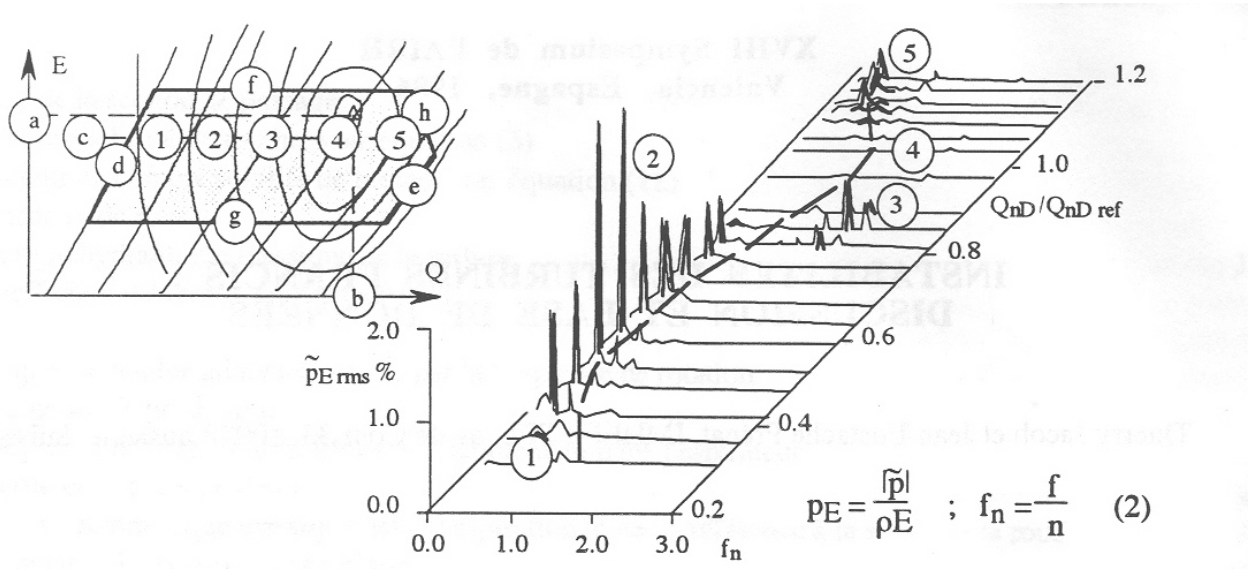

Figure 1.12: Waterfall diagram of pressure pulsations at the turbine draft tube cone at constant ψ [51].

Mitigation Measures

The mitigation of resonance problems requires acting either on the excitation source or on the system parameters in order to detune the excitation from the system eigen frequencies. The main solutions to achieve the mitigation are:

- **draft tube fins**, used in order to induce swirl flow distortions and then modify pressure source frequencies or amplitudes [39], [8];
- **cylinder in the draft tube** or **extensions of the runner cone**, also used to induce swirl flow distortions and then modify the pressure source frequencies or amplitudes [39];
- the **air injection**, to modify the hydroacoustic parameters of the turbine in order to detune the system eigen frequencies from the excitation sources[39], [77], [76];
- **mechanical dampers** act like Frahm dampers in order to absorb energy of resonance [4], [75];
- **active control of the pressure fluctuations**, using complex control strategy based on rotating valve or mechanical piston in order to inject pressure fluctuations in the draft tube with the same amplitude as the source but opposition of the phase [12], [10];
- **water jet control** located in the center of the runner cone to modify the swirl momentum ratio and eliminate pressure source [87].

However, the success of the use of one of the above mitigating solutions is never ensured and often has detrimental effect on the turbine efficiency. In addition, some of them are technically complex solutions and difficult to setup.

Regarding the full load surge, injection of air appeared to be successful in some cases [62], [5]. Use of fins is also sometimes beneficial.

The resonances resulting from rotor-stator problems can usually be solved by modifying the rotor-stator arrangement, *i.e.* the number of guide vanes or runner blades. It is also possible to mitigate pressure excitations by changing the rotor-stator interface geometry by increasing the guide vane-runner blade gap, or using blades with skew angle. If resonance occurs with specific mechanical parts of the turbine, their structural characteristics can be modified in order to change their eigen frequencies, and again detune the resonance.

1.3.3 Transient Behavior of Francis Turbine Units

General

In the deregulated electricity market, hydropower plants are more and more solicited in order to adapt the production to the demand in energy. Consequently, the power plants are victim of their availability and are then subject to an increasing number of startup and shutdown sequences. During operation, short-circuits resulting from the failure of power lines may trigger emergency shutdown of the power plant. In addition, hydropower plant are constantly modernized to increase their flexibility by taking advantage of new control strategies or installing new technologies such as variable speed solutions. Such events are parts of the today's normal operation of hydropower plants whose solicitations changes according to technologies and energy market issues.

Transients: the Safety Issues

Transient phenomena result from a change in the operating conditions of a system. In the case of hydroelectric power plants, transient phenomena can be caused by: (i) unit shutdown or startup, (ii) change in operating set point, (iii) load rejection or acceptance, (iv) emergency shutdown and (v) electrical faults such as earth fault, short-circuit, out of phase synchronization, and so on.

All the above listed events induce changes of discharge, pressure, rotational speed, voltage, current and so on in the entire power plant. The impacts of these changes on the safety of the power plants should be assessed at the early stage of any hydroelectric project in order to be able to select the critical dimensions of the system with appropriate margins. Therefore transient analysis should be performed accounting for the entire system; *i.e.* the whole adduction system, the hydraulic machines, the mechanical inertias, the electrical machines, the controllers, the emergency systems, etc, as illustrated in figure 1.13. The transient analysis aims to determine: the pipe wall thickness, the surge tank diameters, the coupling shaft diameters, appropriate emergency procedure, control parameters, conductors diameters, etc.

Improving the Stability of Power Network

Due to their flexibility of exploitation, hydroelectric power plant have an important role to play in stabilizing electrical power networks. This is the case not only in Europe, because of the decentralization of the production and the use of renewable energies whose availability cannot be influenced, but also in emerging countries where the network are

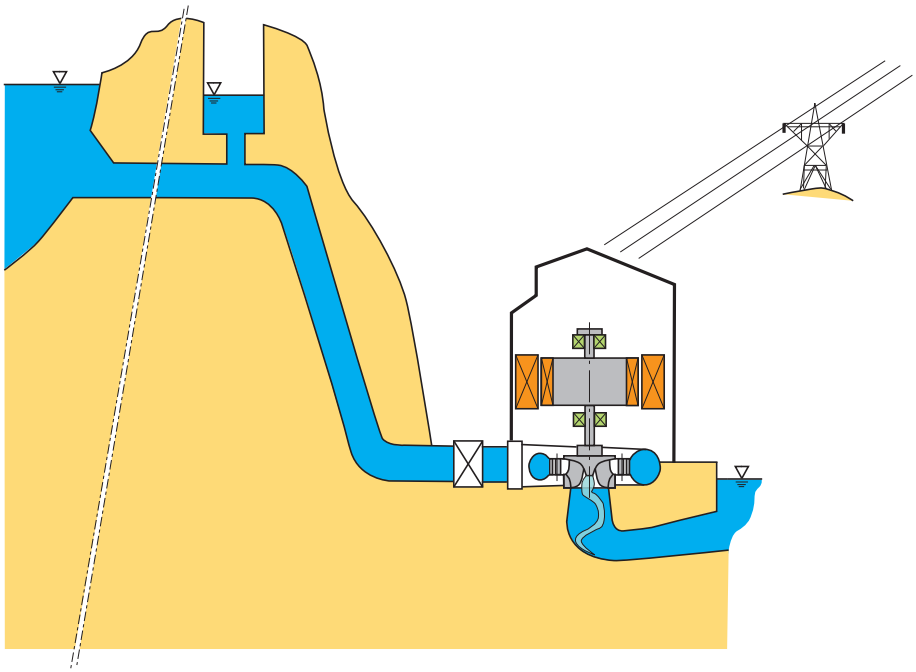

Figure 1.13: Layout of Francis power plant.

poorly interconnected and distances between electricity producers and consumers are large.

Thus, the controllers and governors parameters should be optimized according to operating conditions that the power plants will face. Typically, 3 production modes are distinguished:

- interconnected production: the power plant is connected to very large power grid;
- islanded production: the power plant is connected to weak power grid typically smaller than 10 GW;
- isolated production: the power plant is producing energy only for the subsidiaries and local loads.

The regulation of a hydropower plant is achieved using at least 2 and sometimes 3 regulators:

- the turbine speed governor: has usually both speed and power set points and acts on the guide vane opening of the Francis turbine;
- the generator voltage regulator has a line voltage set point and acts on the excitation voltage of the rotor;
- the Power System Stabilizer (PSS) acts also on the excitation voltage but has the rotational speed and power as set points.

In addition, for variable speed solutions, a supervisor governor is necessary to select appropriate rotational speed set points and enabling rotational speed changes. The determination of the parameters sets of these regulators represents a challenging task that should account for the system layout and exploitation conditions.

In the control strategy of power networks, 3 different levels are distinguished: the primary, secondary and tertiary levels. The related regulation times and devices are summarized in table 1.2.

Table 1.2: Regulation levels [29].

Level	Governors	Regulation time
Primary	- turbine speed governor - generator voltage regulator	10 - 20 sec.
Secondary	- frequency/power regulation - energy transfer regulation	20 - 120 sec.
Tertiary	- power production dispatching	1 - 15 min.

1.4 The Role of Numerical Simulation in Improving Hydropower Operation

As illustrated in the previous sections, the design, operation and regulation of hydroelectric power plant require the ability to predict the dynamic behavior of the power plant taking into account various aspects of the exploitation of the installation. Therefore, mathematical models able to represent the dynamic behavior of hydropower plants with high fidelity are necessary. The complexity of the model used for the simulation should be adapted according to the issues.

Since most of the issues aforementioned regard optimization or parametrization, small computation times are required. In addition, many of the investigations require a **multi-physics** model of the power plant, comprising: (i) the entire hydraulic circuit, (ii) the mechanical inertias, (iii) the electrical installation, and (iv) the regulation systems.

For these applications, one-dimensional models offer the best compromise in terms of computational feasibility and accuracy. As propagation phenomena globally dominate in the dynamic behavior of the entire hydraulic circuit, hydroacoustic models are the most appropriate.

Chapter 2

Fundamental Equations

2.1 General

Mathematical model based on mass and momentum conservation can describe properly the dynamic behavior of a pipe filled with water. Hydraulic installations feature longitudinal dimensions greater than transversal dimensions, thus justifying a one-dimensional approach based on the following assumption:

- the flow is normal to the cross-sections A;
- the pressure p, the flow velocity C and the density ρ are uniform in a cross-section A.

2.2 Momentum Equation

The momentum equation is applied the volume of control, dashed line, of the pipe of length dx, figure 2.1. The momentum equation expresses the balance of the forces acting on this fluid volume, the momentum flux through the surfaces and the rate of change of the momentum in the volume itself. The integral form of the momentum equation applied to a volume of fluid is given by:

$$\int_V \frac{\partial}{\partial t}\left(\rho \cdot \overrightarrow{C} \cdot \overrightarrow{n}\right) dV + \int_{\partial V} \rho \overrightarrow{C} \cdot \left(\overrightarrow{C} - \overrightarrow{u}\right) \cdot \overrightarrow{n}\, dA = \Sigma \overrightarrow{F} \tag{2.1}$$

The momentum equation along the x-axis neglecting axial displacement of the pipe u, and considering gravity, pressure and friction forces is expressed as:

$$\rho A dx \frac{DC}{Dt} = pA - [pA + \frac{\partial (pA)}{\partial x} dx] + (p + \frac{\partial p}{\partial x}\frac{dx}{2})\frac{\partial A}{\partial x} dx - \tau_o \pi D dx - \rho g A dx \sin(\alpha) \tag{2.2}$$

With:
A : pipe cross-section $[m^2]$;
ρ : density $[Kg/m^3]$;
C : flow velocity $[m/s]$;
τ : shear stress $[N/m^2]$;

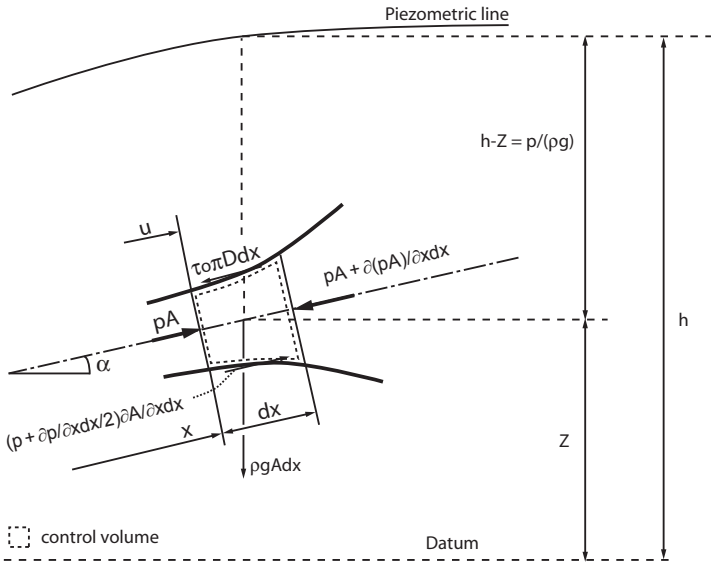

Figure 2.1: Momentum equation applied to the volume of control of length dx.

D : pipe diameter $[m]$.

Rearranging equation 2.2 and neglecting the second order terms dx^2, yields to :

$$A\frac{\partial p}{\partial x} + \tau_o \pi D + \rho g A \sin(\alpha) + \rho A \frac{DC}{Dt} = 0 \tag{2.3}$$

Let introduce the friction coefficient according to Darcy-Weisbach [86]:

$$\tau_o = \frac{\rho \lambda C^2}{8} \tag{2.4}$$

The particular derivative is given by:

$$\frac{DC}{Dt} = \frac{\partial C}{\partial t} + C\frac{\partial C}{\partial x} \tag{2.5}$$

Combining equations 2.3, 2.4 and 2.5, gives:

$$\frac{1}{\rho}\frac{\partial p}{\partial x} + \frac{\partial C}{\partial t} + C\frac{\partial C}{\partial x} + g\sin(\alpha) + \frac{\lambda C|C|}{2D} = 0 \tag{2.6}$$

The absolute value of the velocity ensure always dissipative term.

2.3 Continuity Equation

The mass balance in volume of control of length dx figure 2.2 can be expressed as follow:

$$\frac{dM}{dt} = \frac{\partial}{\partial t}\int\limits_{V} \rho dV + \int\limits_{\partial V} \rho \cdot \left(\overrightarrow{C} - \overrightarrow{u}\right) \cdot \overrightarrow{n} \cdot dA = 0 \tag{2.7}$$

Developing all the terms and neglecting the axial displacement of the pipe u, yields to:

$$\frac{\partial(\rho A dx)}{\partial t} = \rho AC - \left[\rho AC + \frac{\partial(\rho AC)}{\partial x}dx\right] \tag{2.8}$$

Then:

$$\frac{\partial(\rho A)}{\partial t} = -\frac{\partial(\rho AC)}{\partial x} \tag{2.9}$$

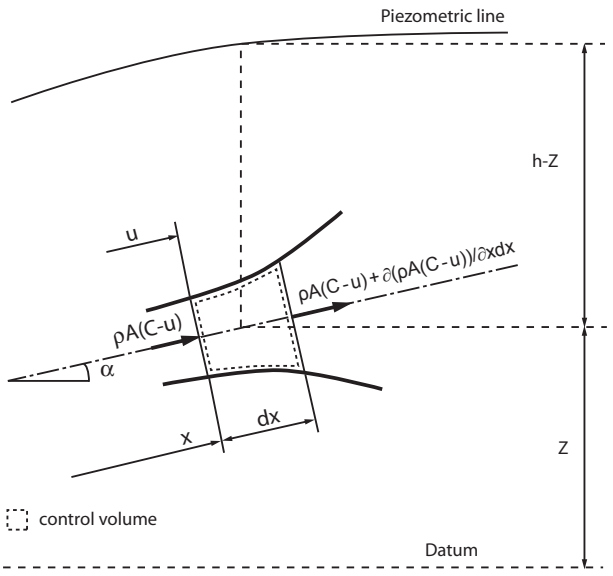

Figure 2.2: Continuity equation applied to pipe control volume of length dx.

Expressing the partial derivative gives:

$$\frac{1}{\rho}\frac{\partial \rho}{\partial x} + \frac{1}{A}\frac{\partial A}{\partial x} + \frac{1}{C}\frac{\partial C}{\partial x} + \frac{1}{\rho C}\frac{\partial \rho}{\partial t} + \frac{1}{AC}\frac{\partial A}{\partial t} = 0 \tag{2.10}$$

Introducing:

$$\frac{D\rho}{Dt} = \frac{\partial \rho}{\partial t} + C\frac{\partial \rho}{\partial x} \quad and \quad \frac{DA}{Dt} = \frac{\partial A}{\partial t} + C\frac{\partial A}{\partial x} \tag{2.11}$$

Equation 2.10 becomes:

$$\frac{1}{\rho}\frac{D\rho}{Dt} + \frac{1}{A}\frac{DA}{Dt} + \frac{\partial C}{\partial x} = 0 \tag{2.12}$$

Assuming barotropic behavior of the fluid, *i.e.* $\rho = \rho(p)$, and introducing the fluid bulk modulus E_{water} yields to:

$$dp = E_{water}\frac{d\rho}{\rho} \tag{2.13}$$

Then:

$$\frac{1}{\rho}\frac{d\rho}{dt} = \frac{1}{E_{water}}\frac{dp}{dt} \tag{2.14}$$

The traction strain of the pipe wall can be expressed as follows:

$$\sigma = E_c\frac{dR}{R} \tag{2.15}$$

With the change of pipe cross section:

$$\frac{dA}{dt} = 2\pi R\frac{dR}{dt} = \frac{2\pi R^2}{E_c}\frac{d\sigma}{dt} \tag{2.16}$$

The strain in the pipe wall is deduced from figure 2.3:

$$\sigma = \frac{pD}{2e} \quad \text{gives} \quad \frac{d\sigma}{dt} = \frac{D}{2e}\frac{dp}{dt} \tag{2.17}$$

With:

e = pipe wall thickness [m]

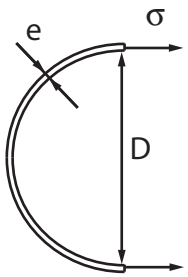

Figure 2.3: Traction stress in pipe wall due to pressure.

Finally :

$$\frac{1}{A}\frac{dA}{dt} = \frac{D}{eE_c}\frac{dp}{dt} \tag{2.18}$$

Combining equations 2.13 and 2.18 with equation 2.11 yields to :

$$\rho a^2\frac{\partial C}{\partial x} + \frac{dp}{dt} = 0 \tag{2.19}$$

Where the wave speed is given by :

$$a^2 = \frac{1}{\rho\left(\frac{1}{E_{water}} + \frac{D}{eE_c}\right)} \tag{2.20}$$

Knowing $p = p(x,t)$ gives:

$$\rho a^2\frac{\partial C}{\partial x} + \frac{\partial p}{\partial t} + C\frac{\partial p}{\partial x} = 0 \tag{2.21}$$

2.4 Simplified Equations

The mathematical model of the dynamic behavior of an elementary pipe of length dx consists of 2 equations: the conservation of both mass and momentum.

$$\begin{cases} \frac{1}{\rho}\frac{\partial p}{\partial x} + \frac{\partial C}{\partial t} + C\frac{\partial C}{\partial x} + g\sin(\alpha) + \frac{\lambda C\,|C|}{2D} = 0 \\ \rho a^2 \frac{\partial C}{\partial x} + \frac{\partial p}{\partial t} + C\frac{\partial p}{\partial x} = 0 \end{cases} \tag{2.22}$$

In hydraulics, it is useful to use the discharge Q and the piezometric head h as state variables in stead of the flow velocity C and pressure p. The discharge and the piezometric head are defined as:

$$h = Z + \frac{p}{\rho g} \tag{2.23}$$

$$Q = C \cdot A \tag{2.24}$$

With Z the elevation $[m]$. The piezometric head is the pressure given in meters of water column, mWC, above a given datum. Injecting equations 2.23 and 2.24 in equation 2.22, assuming no vertical displacements of the pipe $\partial z/\partial t \cong 0$ and noticing that $\partial z/\partial x = sin(\alpha)$, gives:

$$\begin{cases} \frac{\partial h}{\partial x} + \frac{1}{gA}\left[\frac{\partial Q}{\partial t} + C\frac{\partial Q}{\partial x}\right] + \frac{\lambda Q\,|Q|}{2gDA^2} = 0 \\ \left[\frac{\partial h}{\partial t} + C\frac{\partial h}{\partial x}\right] + \frac{a^2}{gA}\frac{\partial Q}{\partial x} = 0 \end{cases} \tag{2.25}$$

Hydroacoustic phenomena are characterized by a high wave speed $a(a = 1430m/s$ at $20^{\circ}C)$ and low flow velocities $(C = 10m/s)$, thus the convective terms $C\partial/\partial x$ related to the transport phenomena can be neglected with respect to the propagative terms $\partial/\partial t$. This simplification leads to the following set of of partial derivative equations:

$$\begin{cases} \frac{\partial h}{\partial x} + \frac{1}{gA}\frac{\partial Q}{\partial t} + \frac{\lambda Q\,|Q|}{2gDA^2} = 0 \\ \frac{\partial h}{\partial t} + \frac{a^2}{gA}\frac{\partial Q}{\partial x} = 0 \end{cases} \tag{2.26}$$

2.5 Resolution Methods

The system of equations 2.26 can be rewritten in matrix form:

$$\begin{bmatrix} \frac{\partial Q}{\partial t} \\ \frac{\partial h}{\partial t} \end{bmatrix} + \underbrace{\begin{bmatrix} 0 & gA \\ \frac{a^2}{gA} & 0 \end{bmatrix}}_{[A]} \cdot \begin{bmatrix} \frac{\partial Q}{\partial x} \\ \frac{\partial h}{\partial x} \end{bmatrix} = \begin{bmatrix} -\frac{\lambda Q|Q|}{2DA} \\ 0 \end{bmatrix} \tag{2.27}$$

The eigen values of this set of equations are the roots of the following characteristic equation:

$$\det\left([A] - \delta[I]\right) = 0 \tag{2.28}$$

The equation system 2.27 has the 2 following distinct roots:

$$\delta = \pm a \tag{2.29}$$

Since the eigen values of the equation system 2.27 are real, it corresponds to a system of hyperbolic partial differential equations. This type of equation is related to propagative problems that can be solved with various methods:

- arithmetic method of Allievi (1925) [2];
- graphical method of Schnyder-Bergeron (1950) [7];
- method of characteristics (MOC) [86], [88], [20];
- transfer matrix method [86], [32];
- impedance method [86].

All these methods enable analyzing of the dynamic behavior of hydraulic system.

Chapter 3

Resolution Method of Partial Differential Equations

3.1 Electrical Analogy

The solution of a system of hyperbolic partial differential equations such as the set of equation 2.26, was at first inspired by the methods developed in the field of telecommunication [74], [55]. The resolution of the propagation of electrical waves in conductors is based on equivalent scheme representation providing a high level of abstraction and having a rigorous formalism. The study of electrical wave propagation in conductors leads to the establishment of the set of equations expressed as follow, referred as the telegraphist's equation:

$$\begin{cases} \dfrac{\partial U}{\partial x} + L'_e \dfrac{\partial i}{\partial t} + R'_e i \ = 0 \\ \dfrac{\partial U}{\partial t} + \dfrac{1}{C'_e} \dfrac{\partial i}{\partial x} = 0 \end{cases} \tag{3.1}$$

Where:
i: electrical current $[A]$
U : electrical potential $[V]$
Re' : lineic electrical resistance $[\Omega/m]$
Le' : lineic electrical inductance $[H/m]$
Ce' : lineic electrical capacitance $[F/m]$

The analogy between equation set 2.26 modelling the propagation of pressure waves in hydraulic systems and the equation set 3.1 modelling the propagation of voltage waves in conductors allows identifying a lineic hydraulic resistance R', a lineic hydraulic inductance L' and a lineic hydraulic inductance C'. Thus, equation set 2.26 can be rewritten as:

$$\begin{cases} \dfrac{\partial h}{\partial x} + L' \dfrac{\partial Q}{\partial t} + R'(Q)Q = 0 \\ \dfrac{\partial h}{\partial t} + \dfrac{1}{C'} \dfrac{\partial Q}{\partial x} = 0 \end{cases} \tag{3.2}$$

Where the lineic hydroacoustic parameters are defined as:

- lineic hydroacoustic capacitance $C' = \frac{g \cdot A}{a^2}[m]$;
- lineic hydroacoustic inductance $L' = \frac{1}{g \cdot A}[s^2/m^3]$;
- lineic hydroacoustic resistance $R' = \frac{\lambda \cdot |\bar{Q}|}{2 \cdot g \cdot D \cdot A^2}[s/m^3]$.

Hydraulic and electrical systems are both characterized by an extensive state variable, *i.e.* discharge Q and current i, and by a potential state variable, *i.e.* piezometric head h and voltage U. The electrical analogy permits to apply the mathematical formalism developed initially for electrical purposes to hydroacoustic problems and to use powerful concepts such as equivalent scheme, impedance or transfer matrix. Two types of system are distinguished:

- systems with distributed parameters, or continuous systems;
- systems with lumped parameters, or discrete systems.

Continuous systems can be easily studied with analytical methods while discrete system requires numerical methods. Analytical solutions require linearizing the dynamic behavior of the studied system, restricting the analysis to small perturbations. However, continuous systems can be modelled as a series of lumped elements with infinitesimal length. Such approach allows taking into account system non-linearities by using numerical methods for the analysis of its dynamic behavior. Nevertheless, this modelling approach introduces approximation errors that have to be quantified.

3.2 Set of Hyperbolic Partial Differential Equation: Continuous System

Pressure wave propagation in hydraulic systems can be modelled using continuity and momentum equations. The resulting set of hyperbolic partial differential equations can be written as:

$$\begin{cases} \dfrac{\partial h}{\partial x} + L' \cdot \dfrac{\partial Q}{\partial t} + R' \cdot Q = 0 \\ \dfrac{\partial h}{\partial t} + \dfrac{1}{C'} \cdot \dfrac{\partial Q}{\partial x} = 0 \end{cases} \tag{3.3}$$

The set of equations 3.3 can be rewritten using the separation of variables method assuming a sinusoidal variation of the piezometric head $h(x,t)$ and of the discharge $Q(x,t)$ defined as complex function:

$$\begin{cases} \underline{h}(x,t) = \underline{h}(x) \cdot e^{\underline{s}t} \\ \underline{Q}(x,t) = \underline{Q}(x) \cdot e^{\underline{s}t} \end{cases} \tag{3.4}$$

Where the constant $\underline{s}$ is the complex frequency also referred as Laplace variable. The complex frequency is composed of an imaginary part and of a real part:

$$\underline{s} = \sigma + j \cdot \omega \tag{3.5}$$

The complex frequency $\underline{s}$ is written as s in the next section of this document. The set of equations 3.3 is rewritten as follows:

$$\begin{cases} \dfrac{\partial^2 \underline{h}}{\partial x^2} = \underline{\gamma}^2 \cdot \underline{h}(x) \\ \dfrac{\partial^2 \underline{Q}}{\partial x^2} = \underline{\gamma}^2 \cdot \underline{Q}(x) \end{cases} \tag{3.6}$$

Where $\underline{\gamma}$ is the complex wave number:

$$\underline{\gamma}^2 = C' \cdot s \cdot (L' \cdot s + R') \tag{3.7}$$

3.2.1 Resolution of the Wave Equation: Exact Solution

Equation 3.3 admits as a particular solution for the piezometric head:

$$\underline{h}(x,t) = e^{st} \cdot (C_1 \cdot e^{-\underline{\gamma} \cdot x} + C_2 \cdot e^{\underline{\gamma} \cdot x}) \tag{3.8}$$

The constants C_1 and C_2 are to be determined from the boundary conditions. Thus equation 3.6 for the piezometric head admits as solution both a progressive wave $\underline{h}_p(x)$ and a retrograde wave $\underline{h}_r(x)$, defined from the boundary condition at $x = 0$:

$$\underline{h}_p(x) = \underline{h}_p(0) \cdot e^{-\underline{\gamma} \cdot x} \tag{3.9}$$

$$\underline{h}_r(x) = \underline{h}_r(0) \cdot e^{\underline{\gamma} \cdot x} \tag{3.10}$$

Rewriting the equations set 3.3 assuming a sinusoidal evolution of the piezometric head and of the discharge yields to:

$$-\frac{\partial \underline{h}}{\partial x} = (L' \cdot s + R') \cdot \underline{Q} \tag{3.11}$$

$$-\frac{\partial \underline{Q}}{\partial x} = C' \cdot s \cdot \underline{h} \tag{3.12}$$

Equations 3.11 and 3.12 provide the solution of the discharge equation of equation 3.3 admitting as solution a progressive discharge wave $\underline{Q}_p(x)$ and a retrograde discharge wave $\underline{Q}_r(x)$ expressed as:

$$\underline{Q}_p(x) = -\frac{1}{(L' \cdot s + R')} \cdot \frac{\partial \underline{h}_p(x)}{\partial x} = -\frac{(-\underline{\gamma})}{(L' \cdot s + R')} \cdot \underline{h}_p(x) = \frac{\underline{h}_p(x)}{\underline{Z}_c} \tag{3.13}$$

$$\underline{Q}_r(x) = -\frac{1}{(L' \cdot s + R')} \cdot \frac{\partial \underline{h}_r(x)}{\partial x} = -\frac{\underline{\gamma}}{(L' \cdot s + R')} \cdot \underline{h}_r(x) = -\frac{\underline{h}_r(x)}{\underline{Z}_c} \tag{3.14}$$

The ratio between the piezometric head and the discharge variations is the characteristic impedance of the pipe $\underline{Z}_c$ defined as:

$$\underline{Z}_c = \sqrt{\frac{(L' \cdot s + R')}{C' \cdot s}} \tag{3.15}$$

The solution to the equation system 3.6 is the sum of the progressive and the retrograde waves yielding to:

$$\underline{h}(x) = \underline{h}_p(x) + \underline{h}_r(x) \tag{3.16}$$

$$\underline{h}(x) = \frac{\underline{h}_p(x) + \underline{h}_r(x)}{\underline{Z}_c} \tag{3.17}$$

Combining equations 3.9 and 3.10 with the equations 3.16 and 3.17 established for $x = 0$, gives:

$$\underline{h}_p(x) = \frac{\underline{h}(0) + \underline{Z}_c \cdot \underline{Q}(0)}{2} \cdot e^{-\underline{\gamma} \cdot x} \tag{3.18}$$

$$\underline{h}_r(x) = \frac{\underline{h}(0) - \underline{Z}_c \cdot \underline{Q}(0)}{2} \cdot e^{-\underline{\gamma} \cdot x} \tag{3.19}$$

The constants $\underline{C}_1$ and $\underline{C}_2$ are derived from equation 3.8:

$$\underline{C}_1 = \frac{\underline{h}(0) + \underline{Z}_c \cdot \underline{Q}(0)}{2} \tag{3.20}$$

$$\underline{C}_2 = \frac{\underline{h}(0) - \underline{Z}_c \cdot \underline{Q}(0)}{2} \tag{3.21}$$

Reformulating the equations 3.16 and 3.17 with equations 3.18 and 3.19, gives:

$$\begin{cases} \underline{h}(x) = \underline{h}(0) \cdot \cosh(\underline{\gamma} \cdot x) - \underline{Z}_c \cdot \underline{Q}(0) \cdot \sinh(\underline{\gamma} \cdot x) \\ \underline{Q}(x) = -\dfrac{\underline{h}(0)}{\underline{Z}_c} \cdot \sinh(\underline{\gamma} \cdot x) + \underline{Q}(0) \cdot \cosh(\underline{\gamma} \cdot x) \end{cases} \tag{3.22}$$

For a pipe of length l in matrix notation:

$$\begin{bmatrix} \underline{h}(l) \\ \underline{Q}(l) \end{bmatrix} = \begin{bmatrix} \cosh(\underline{\gamma} \cdot l) & -\underline{Z}_c \cdot \sinh(\underline{\gamma} \cdot l) \\ -\frac{1}{\underline{Z}_c} \cdot \sinh(\underline{\gamma} \cdot l) & \cosh(\underline{\gamma} \cdot l) \end{bmatrix} \cdot \begin{bmatrix} \underline{h}(0) \\ \underline{Q}(0) \end{bmatrix} \tag{3.23}$$

The transfer matrix offers the possibility to determine the fluctuations of piezometric head and discharge at the end of a pipe resulting from the excitation at the other end. For a system made of pipes in series, it is possible to compute the global transfer matrix of the system by performing the matricial product of the transfer matrices of all the pipes in series:

$$[\underline{M}_{tot}] = \prod_{1 \leq k \leq n} [\underline{M}_i] \tag{3.24}$$

3.2.2 Resolution of the Wave Equation: Conservative Form

Neglecting dissipation, ($R' = 0$) the complex number of waves of equation 3.7 becomes:

$$\gamma = s \cdot \sqrt{C' \cdot L'} = s \cdot \sqrt{\frac{g \cdot A}{a^2} \cdot \frac{1}{g \cdot A}} = \frac{\omega}{a} \tag{3.25}$$

Similarly, the characteristic complex impedance $\underline{Z_c}$ of equation 3.15 becomes a scalar value:

$$Z_c = \sqrt{\frac{L'}{C'}} = \frac{a}{g \cdot A} \tag{3.26}$$

Without damping, the complex frequency s is simplified as $s = j\omega$. In addition, noticing that $\cosh(\alpha) = \cos(j \cdot \alpha)$ and $\sinh(\alpha) = -j \cdot \sin(j \cdot \alpha)$, the transfer matrix of equation 3.23 for a frictionless pipe becomes:

$$\begin{bmatrix} \underline{h}(l) \\ \underline{Q}(l) \end{bmatrix} = \begin{bmatrix} \cos(\frac{\omega \cdot l}{a}) & -j \cdot Z_c \cdot \sinh(\frac{\omega \cdot l}{a}) \\ -j \cdot \frac{1}{Z_c} \cdot \sinh(\frac{\omega \cdot l}{a}) & \cosh(\frac{\omega \cdot l}{a}) \end{bmatrix} \cdot \begin{bmatrix} \underline{h}(0) \\ \underline{Q}(0) \end{bmatrix} \tag{3.27}$$

3.2.3 Solution of d'Alembert of the Wave Equation

The spatial partial derivative of the piezometric head combined with the equation of discharge of the equation system 3.3 gives:

$$\frac{\partial^2 Q}{\partial x^2} = C' \cdot L' \cdot \frac{\partial^2 Q}{\partial t^2} + C' \cdot R' \cdot \frac{\partial Q}{\partial t} \tag{3.28}$$

The time partial derivative of the piezometric head combined with the equation of discharge of the equation system 3.3 gives:

$$\frac{\partial^2 h}{\partial x^2} = C' \cdot L' \cdot \frac{\partial^2 h}{\partial t^2} + C' \cdot R' \cdot \frac{\partial h}{\partial t} \tag{3.29}$$

The above system expressed for a frictionless system, *i.e.* $R' = 0$, yields to the wave equation:

$$\begin{cases} \dfrac{\partial^2 h}{\partial x^2} = a^2 \cdot \dfrac{\partial^2 h}{\partial t^2} \\ \dfrac{\partial^2 h}{\partial x^2} = a^2 \cdot \dfrac{\partial^2 h}{\partial t^2} \end{cases} \tag{3.30}$$

D'Alembert has derived the general solution of this set of equations for the piezometric head back in 1747:

$$h(x,t) = F_p(a \cdot t - x) + G_r(a \cdot t + x) = F_p(t - x/a) + G_r(t + x/a) \tag{3.31}$$

The function $F_p(t - x/a)$ is a progressive wave whose shape is fixed, and is propagating at the wave speed a towards positive x values and $G_r(t + x/a)$ is a retrograde wave propagating at the same wave speed towards negative x values.

Wave Reflection at an Open End

The open end of a pipe located at $x = 0$ implies no piezometric head fluctuations, thus:

$$\begin{aligned} h(x,t) &= F_p(a \cdot t - x) + G_r(a \cdot t + x) \\ 0 &= F_p(a \cdot t - 0) + G_r(a \cdot t + 0) \\ &\Rightarrow F_p(a \cdot t) = -G_r(a \cdot t) \end{aligned} \tag{3.32}$$

A progressive wave reflected at a pipe open end becomes a retrograde wave with the same shape but opposite sign as presented in figure 3.1.

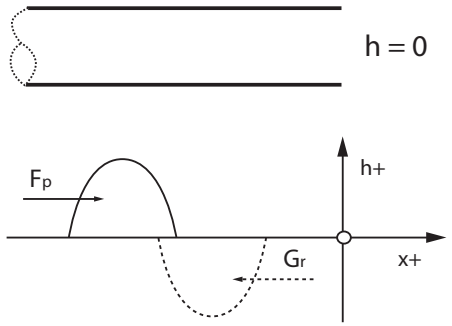

Figure 3.1: Reflection of a progressive wave at an open end of a pipe.

Wave Reflection at a Dead End

The dead end of a pipe located at $x = 0$ implies no discharge fluctuations. Thus, expressing the piezometric head fluctuation for the same location using the equation 3.11, yield to:

$$-\frac{\partial h}{\partial x} = (L' \cdot s + R') \cdot Q = (L' \cdot s + 0) \cdot 0 \tag{3.33}$$

Considering purely real piezometric head gives:

$$\begin{aligned} h(x,t) &= F_p(a \cdot t - x) + G_r(a \cdot t + x) \\ -\frac{\partial h}{\partial x} &= -F_p(a \cdot t) + G_r(a \cdot t) \\ &\Rightarrow F_p(a \cdot t) = G_r(a \cdot t) \end{aligned} \tag{3.34}$$

A progressive wave reflected at a pipe dead end becomes a retrograde wave with same shape and same sign as presented in figure 3.2.

Wave Reflection at a Junction

A progressive wave propagating in a pipe with change of hydroacoustic parameters in the longitudinal axis is subject to wave reflection. A change of hydroacoustic nature can

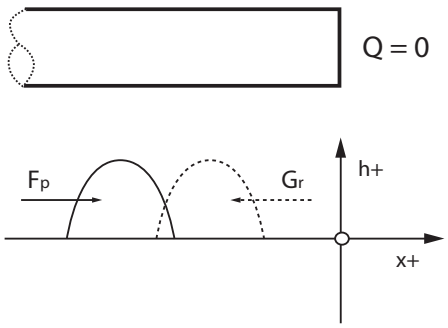

Figure 3.2: Reflection of a progressive wave at a dead end of a pipe.

be understood as a change of the complex characteristic impedance of the pipe $\underline{Z}_c$, see equation 3.15. The characteristic impedance $\underline{Z}_c$ depends mainly on 2 parameters: the pipe diameter D and the pipe wave speed a. One considers a junction located at $x = 0$ between 2 pipes characterized by the complex characteristic impedances $\underline{Z}_{c1}$ and $\underline{Z}_{c2}$ as illustrated by figure 3.3. The impedance at a location x defines the ratio between the complex piezometric head $\underline{h}$ and the complex discharge $\underline{Q}$ and is therefore given by:

$$\underline{Z}(x) = \frac{\underline{h}(x)}{\underline{Q}(x)} \tag{3.35}$$

Expressing the impedance of the second pipe using the sum of incident and reflected waves of pipe 1, and introducing equations 3.13 and 3.14 gives:

$$\underline{Z}_{c2} = \frac{\underline{h}_t}{\underline{Q}_t} = \frac{\underline{h}_i + \underline{h}_r}{\underline{Q}_i + \underline{Q}_r} = \frac{\underline{h}_i + \underline{h}_r}{\frac{1}{\underline{Z}_{c1}} \cdot (\underline{h}_i - \underline{h}_r)} \tag{3.36}$$

As the reflected wave is retrograde, its sign os negative, after rearranging it becomes:

$$\underline{Z}_{c2} = \underline{Z}_{c1} \cdot \frac{\underline{h}_i + \underline{h}_r}{\underline{h}_i - \underline{h}_r} \tag{3.37}$$

From equation 3.37, one can express the ratio between the incident and the reflected waves as:

$$\frac{\underline{h}_r}{\underline{h}_i} = \frac{\underline{Z}_{c2} - \underline{Z}_{c1}}{\underline{Z}_{c2} + \underline{Z}_{c1}} \tag{3.38}$$

In addition, the piezometric head at the junction is identical for both pipes, thus:

$$\underline{h}_i + \underline{h}_r = \underline{h}_t \tag{3.39}$$

The ratio between the incident and transmitted waves for the piezometric head is therefore given by:

$$\frac{\underline{h}_t}{\underline{h}_i} = \frac{2 \cdot \underline{Z}_{c2}}{\underline{Z}_{c2} + \underline{Z}_{c1}} \tag{3.40}$$

For the cases of open and dead end pipes, one get:

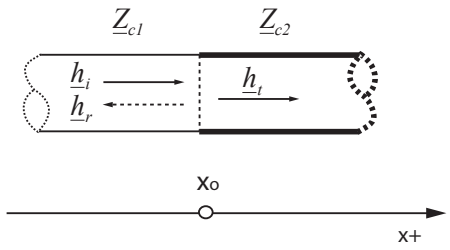

Figure 3.3: Wave reflection of incident wave i at a junction of 2 pipes having different characteristic impedance $\underline{Z}_{c1}$ amd $\underline{Z}_{c2}$.

- open end: $\underline{h}(x_o) = 0 : \underline{Z}_{c2} = 0 \Rightarrow \frac{\underline{h}_r}{\underline{h}_i} = \frac{0-\underline{Z}_{c1}}{0+\underline{Z}_{c1}} = -1$
- dead end: $\underline{Q}(x_o) = 0 : \underline{Z}_{c2} \approx \infty \Rightarrow \frac{\underline{h}_r}{\underline{h}_i} = \frac{\infty-\underline{Z}_{c1}}{\infty+\underline{Z}_{c1}} \approx 1$

Rearranging equation 3.36 with respect to the discharge gives:

$$\frac{\underline{Q}_r}{\underline{Q}_i} = \frac{\underline{Z}_{c1} - \underline{Z}_{c2}}{\underline{Z}_{c1} + \underline{Z}_{c2}} \tag{3.41}$$

In addition the discharge at the junction is identical for both pipes, thus:

$$\underline{Q}_i + \underline{Q}_r = \underline{Q}_t \tag{3.42}$$

Then the ratio between the incident and the transmitted wave is given by:

$$\frac{\underline{Q}_t}{\underline{Q}_i} = \frac{2 \cdot \underline{Z}_{c1}}{\underline{Z}_{c1} + \underline{Z}_{c2}} \tag{3.43}$$

Thus, for a dead or open end pipe, one obtains:

- open end: $\underline{h}(x_o) = 0 : \underline{Z}_{c2} = 0 \Rightarrow \frac{\underline{Q}_r}{\underline{Q}_i} = \frac{\underline{Z}_{c1}-0}{\underline{Z}_{c1}+0} = 1$
- dead end: $\underline{Q}(x_o) = 0 : \underline{Z}_{c2} \approx \infty \Rightarrow \frac{\underline{Q}_r}{\underline{Q}_i} = \frac{\underline{Z}_{c1}-\infty}{\underline{Z}_{c1}+\infty} \approx -1$

These results are in good accordance with the previous results obtained from d'Alembert equation.

Paradox of the Wave Reflection Consecutive to a Waterhammer

The case of a pressure wave induced by the sudden closure of a valve downstream of a pipe, as presented in figure 3.4, inducing a waterhammer in the pipe can be first analyzed using the d'Alembert solution. It is important to notice that the solution of the pressure wave given by equation 3.31 for a given time t and a given location x, is the sum of **all** the incident, transmitted and reflected waves.

The pressure wave of amplitude Δh generated by the downstream valve closure is reflected by the upstream tank with a negative sign because of the open end boundary condition. In turn the piezometric head in the pipe is the sum of the incident and the

reflected waves as the amplitude of both waves is identical and therefore, their sum is zero. As a result, when the reflected wave reaches the downstream valve, the piezometric head in the pipe recovers its initial value, *i.e.* h_o. At this moment, the reflected wave is reflected again with the same sign, as the closed valve represents a dead end boundary condition. The sum of the 3 waves propagating in the pipe, 1 incident wave with positive amplitude Δh and 2 reflected waves with negative amplitudes $-\Delta h$ gives a piezometric head below h_o equal to $h = h_o - \Delta h$.

The paradox lies to the fact that observing the time evolution of the piezometric head in the pipe gives the impression that the incident wave is reflected at the upstream valve with the same sign, which is not the case. If the piezometric head recovers the value h_o, this is because the sum of incident and reflected wave is zero. Similarly, the reflection at the downstream valve gives the impression that the wave is reflected with opposite sign which is again not the case. If the piezometric head reaches values below h_o, this is because the sum of the 3 waves is smaller than h_o.

This example demonstrates that even for a simple case, made of one pipe, it is not easy to predict the time evolution of the piezometric head h because it results from the summation of all the wave propagating in the pipe. Therefore, it becomes very difficult to predict accurately the piezometric head time evolution with d'Alembert solution in complex cases made of several pipes, connections and junctions. Only numerical solution of momentum and mass conservation equation can describe the phenomenon with sufficient accuracy.

3.2.4 Hydroacoustic Impedance Method

The complex characteristic impedance of equation 3.15,characterizes the hydroacoustic system in which the pressure/discharge waves are propagating. It is function of the local parameters of the pipe such as (D, a and λ) which are constant along the x abscissa [86].

The complex characteristic impedance defines the ratio between the piezometric head phasor and the discharge phasor at a given location of the pipe for progressive or retrograde waves only and only if this system is reflectionless. One can notice that if this system is frictionless, then the discharge and piezometric head phasors are in phase. In a system with reflections, the characteristic impedance does not define the ratio between piezometric head and discharge anymore. It is then necessary to evaluate the *specific hydroacoustic impedance* $\underline{Z}_a$ which is a function of the location x and of the boundary conditions of the system. The specific hydroacoustic impedance can be defined from equation 3.22 as follows:

$$\underline{Z}_a(x) = \frac{\underline{h}(x)}{\underline{Q}(x)} = \frac{\cosh(\underline{\gamma} \cdot x) \cdot \underline{h}(0) - \underline{Z}_c \cdot \sinh(\underline{\gamma} \cdot x) \cdot \underline{Q}(0)}{-\frac{1}{\underline{Z}_c} \sinh(\underline{\gamma} \cdot x) \cdot \underline{h}(0) + \cosh(\underline{\gamma} \cdot x) \cdot \underline{Q}(0)} \tag{3.44}$$

Expressing the specific impedance $\underline{Z}_a(l)$ for $x = l$ from the specific impedance $\underline{Z}_a(0)$ at $x = 0$ provides:

$$\underline{Z}_a(l) = \frac{\underline{Z}_a(0) - \underline{Z}_c \cdot \tanh(\underline{\gamma} \cdot l)}{1 - \frac{\underline{Z}_a(0)}{\underline{Z}_c} \cdot \tanh(\underline{\gamma} \cdot l)} \tag{3.45}$$

Using known boundary conditions such as $\underline{Z}_a(0) = 0$ (open end) or $\underline{Z}_a(0) = \infty$ (dead end) it is possible to determine the specific impedance for any location x. It is then

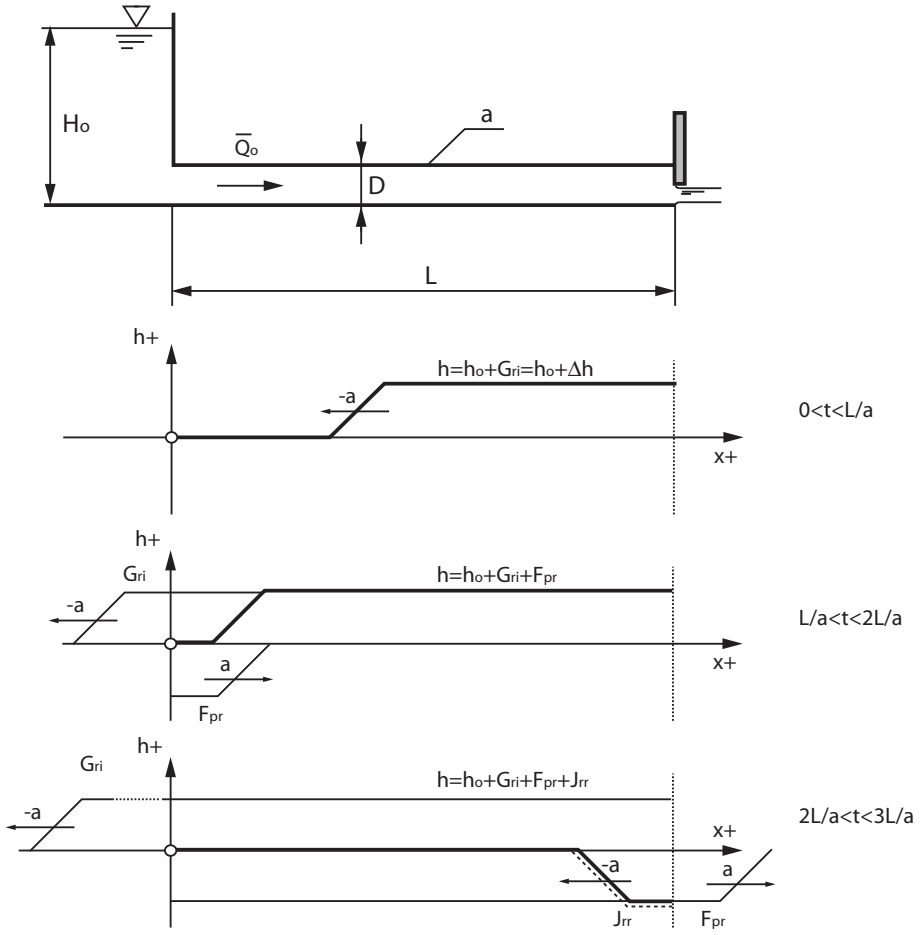

Figure 3.4: Time evolution of the piezometric head h resulting from the closure of the downstream valve inducing waterhammer.

possible to determine the specific impedance of one end of a system, by combining the impedance of all hydraulic components starting from the other end where the impedance is known. It is also possible to determine the specific impedance at $x = 0$ from the specific impedance at $x = l$ giving:

$$\underline{Z}_a(0) = \frac{\underline{Z}_a(l) + \underline{Z}_c \cdot \tanh(\underline{\gamma} \cdot l)}{1 + \frac{\underline{Z}_a(l)}{\underline{Z}_c} \cdot \tanh(\underline{\gamma} \cdot l)} \tag{3.46}$$

For infinite pipe, one get:

- $\underline{Z}_a(0) = \underline{Z}_c$
- $\underline{Z}_a(\infty) = \underline{Z}_c$

An ambiguity appears related to the fact that the specific impedance of a given system can be determined either from $x = 0$ to $x = l$, or from $x = l$ to $x = 0$, and these two impedance are usually different. It means that the problem to be solved, is to find the complex frequency s *i.e.* fulfilling both boundary conditions. This problem corresponds

to the search of the natural frequencies of the system; *i.e.* the free oscillations analysis, see the next section. For simplicity, the specific impedance will be denoted impedance in the following sections of the document.

3.2.5 Free Oscillation Analysis: Continuous System

The study of the free oscillations regime of a hydraulic facility can be treated for a continuous system through 2 methods: (i) the transfer matrix method and (ii) the impedance method. These calculation methods are described below.

Free Oscillation Analysis: Transfer Matrix Method

Using the transfer matrix of each hydraulic component, it is possible to combine them to set up the global matrix of the system including the boundary conditions leading to the following equation:

$$[\underline{G}] \cdot \overrightarrow{x} = \overrightarrow{0} \tag{3.47}$$

Where the complex matrix $[\underline{G}]$ is the global matrix of the system, and $\overrightarrow{x}$ is the state vector. Obtaining a non trivial solution of equation 3.47 requires the determinant of matrix $[\underline{G}]$ to be equal to zero:

$$\det([\underline{G}]) = 0 \tag{3.48}$$

Equation 3.48 is the characteristic equation of the system whose k complex roots $s_k = \sigma_k + j \cdot \omega_k$ are the complex eigen values and $\overrightarrow{x}_k$ the eigen vectors. The free oscillation regime of the system is then given by:

$$\overrightarrow{x}(t) = \overrightarrow{x}_1 \cdot e^{s_1 \cdot t} + \overrightarrow{x}_2 \cdot e^{s_2 \cdot t} + \overrightarrow{x}_3 \cdot e^{s_3 \cdot t} + \dots \tag{3.49}$$

Free Oscillation Analysis: Impedance Method

Combining the n impedances of each element constituting the system allows determining the global impedance of the system at one end:

$$\underline{Z}_{atot}(x_n) = \frac{\underline{Z}_a(x_{n-1}) - \underline{Z}_{cn} \cdot \tanh(\underline{\gamma}_n \cdot (x_n - x_{n-1}))}{1 - \frac{\underline{Z}_a(x_{n_1})}{\underline{Z}_{cn}} \cdot \tanh(\underline{\gamma} \cdot (x_n - x_{n-1}))} \tag{3.50}$$

If the boundary condition at this end is known, the problem to be solved boils down to find the k complex frequencies $s_k = \sigma_k + j \cdot \omega_k$ satisfying the following equation :

$$\underline{Z}_{atot}(x_{end}, s_k) = \underline{Z}_{end} \tag{3.51}$$

Once the complex frequencies, *i.e.* the eigen frequencies, are known, the corresponding eigen modes can be determined using equations 3.22.

3.3 Set of Hyperbolic Partial Differential Equation: Discrete System

The hyperbolic partial differential equation set 3.3, can be solved numerically leading to a discrete system. The state variables that are the piezometric head h and the discharge Q cannot be determined for any x or t, but are known only for given locations and given times according to the numerical scheme used to solve equation set 3.3.

3.3.1 Numerical Resolution of the Hyperbolic Partial Differential Equation set

The numerical integration in space and in time of equation set 3.3 requires appropriate discretization. Regarding the spatial discretization, the centered scheme illustrated in figure 3.5 can be used.

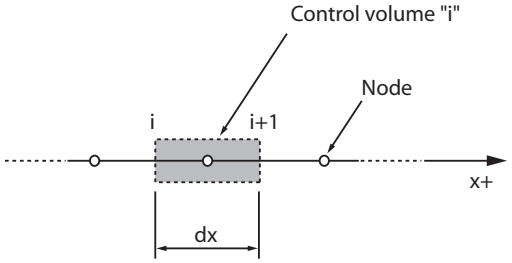

Figure 3.5: Control volume i having center node at i+1/2.

Using the scheme centered at location $i + 1/2$ of the figure 3.5, one get the following expression for the piezometric head and discharge space partial derivatives:

$$\frac{\partial h}{\partial x}|_{i+1/2} = \frac{h_{i+1} - h_i}{dx} \tag{3.52}$$

$$\frac{\partial Q}{\partial x}|_{i+1/2} = \frac{Q_{i+1} - Q_i}{dx} \tag{3.53}$$

Considering the above numerical scheme and using the total differential in equation set 3.3 expressed for a location $i + 1/2$ gives:

$$\begin{cases} \dfrac{dh_{i+1/2}}{dt} + \dfrac{1}{C'} \cdot \dfrac{Q_{i+1} - Q_i}{dx} = 0 \\ \dfrac{h_{i+1} - h_i}{dx} + L' \cdot \dfrac{dQ_{i+1/2}}{dt} + R' \cdot Q_{i+1/2} = 0 \end{cases} \tag{3.54}$$

In order to ensure stability of the computation, a numerical scheme of Lax, based on the mean value of the discharge, is used:

$$Q_{i+1/2} = \frac{Q_{i+1} + Q_i}{2} \tag{3.55}$$

Equations set 3.54 becomes:

$$\begin{cases} C' \cdot dx \dfrac{dh_{i+1/2}}{dt} = Q_i - Q_{i+1} \\ \underbrace{h_{i+1} + \dfrac{L' \cdot dx}{2} \cdot \dfrac{dQ_{i+1}}{dt} + \dfrac{R' \cdot dx}{2} \cdot Q_{i+1}}_{h_{i+1/2}} = \underbrace{h_i - \left(\dfrac{L' \cdot dx}{2} \cdot \dfrac{dQ_i}{dt} + \dfrac{R' \cdot dx}{2} \cdot Q_i \right)}_{h_{i+1/2}} \end{cases} \tag{3.56}$$

Noticing that the second part of the equation corresponds to the piezometric head for the location $i + 1/2$, the system can be expressed under implicit matrix form:

$$\begin{bmatrix} C & 0 & 0 \\ 0 & L/2 & 0 \\ 0 & 0 & L/2 \end{bmatrix} \cdot \frac{d}{dt} \cdot \begin{bmatrix} h_{i+1/2} \\ Q_i \\ Q_{i+1} \end{bmatrix} + \begin{bmatrix} 0 & 1 & -1 \\ 1 & R/2 & 0 \\ 1 & 0 & R/2 \end{bmatrix} \cdot \begin{bmatrix} h_{i+1/2} \\ Q_i \\ Q_{i+1} \end{bmatrix} = \begin{bmatrix} 0 \\ h_i \\ -h_{i+1} \end{bmatrix} \tag{3.57}$$

Set of equations 3.57 is written using the hydroacoustic parameters obtained for a length dx given by:

$$\begin{cases} R = R' \cdot dx \\ L = L' \cdot dx \\ C = C' \cdot dx \end{cases} \tag{3.58}$$

The compact expression of equation set 3.57 is given by:

$$[A] \cdot \frac{d\overrightarrow{x}}{dt} + [B] \cdot \overrightarrow{x} = \overrightarrow{C} \tag{3.59}$$

Set of equations 3.57 can be integrated numerically using classical methods such as Euler, Runge-Kutta, etc. Courant-Friederichs-Lewy have demonstrated that it exists a numerical stability criteria known as the "CFL" criteria linking the space and time discretization, respectively dx and dt through the wave speed a [23]. This criteria ensures the causality of the system because the information cannot transit faster than the wave speed. The CLF criteria is given by:

$$dt < \frac{dx}{a} \tag{3.60}$$

The equation set 3.57 features the following state variables:

- piezometric head in the middle of the element i: $h_{i+1/2}$
- discharge at the inlet of the elements i: Q_i
- discharge at the outlet of the elements i: Q_{i+1}

The system has the following boundary conditions:

- piezometric head at the inlet of the elements i: h_i
- piezometric head at the outlet of the elements i: h_{i+1}

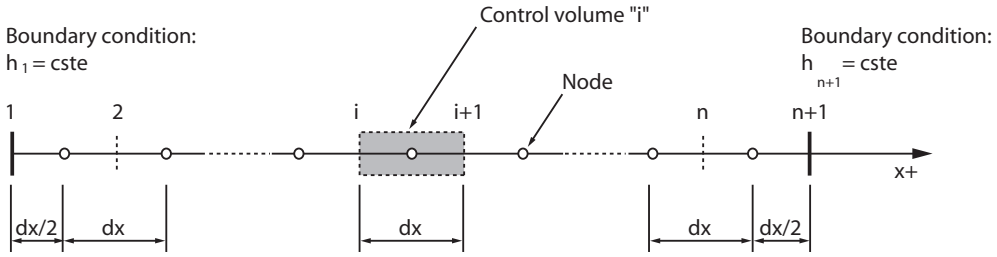

Figure 3.6: Spatial discretization of a pipe of length l.

Equation set 3.57 corresponds to the equation describing the dynamic behavior of a pipe of length dx. A pipe is modelled by n pipes of length dx and $dx = L/n$. The corresponding spatial discretization is presented in figure 3.6.

For a pipe of length l, the boundary conditions are the piezometric head at both ends of the pipe, whereas momentum equations can be merged 2 by 2, introducing the piezometric head at each node $i + 1/2$. The matrices $[A]$ and $[B]$ of equations set 3.57 becomes for a pipe of length l:

$$[A] = \begin{bmatrix} C & & & & (n) & & & & (2n+1) \\ & C & & & & & & & \\ & & \ddots & & & & 0 & & \\ & & & C & & & & & \\ (n) & & & & C & & & & \\ & & & & & L/2 & & & \\ & & & & & & L & & \\ & & 0 & & & & & \ddots & \\ & & & & & & & & L \\ (2n+1) & & & & & & & & L/2 \end{bmatrix} \tag{3.61}$$

And:

$$[B] = \begin{bmatrix} & & & & (n) & -1 & 1 & & & (2n+1) \\ & & & & & & -1 & 1 & & \\ & & 0 & & & & & \ddots & & \\ & & & & & & & -1 & 1 & \\ & & & & & & & & -1 & 1 \\ (n) & & & & & & & & & \\ 1 & & & & & R/2 & & & & \\ -1 & 1 & & & & & R & & & \\ & & \ddots & & & & & \ddots & & \\ & & & -1 & 1 & & & & R & \\ (2n+1) & & & & -1 & & & & & R/2 \end{bmatrix} \tag{3.62}$$

One can notice that the equation set has the dimension $(2n + 1) \cdot (2n + 1)$ and the state vector comprises n piezometric head along the pipe for the nodes $1 + 1/2$ to $n + 1/2$ and $n + 1$ discharges at both end of n pipes of length dx.

The state vector of dimension $(2n+1)\cdot 1$ is given by:

$$\overrightarrow{x} = \begin{bmatrix} h_{1+1/2} & h_{2+1/2} & \dots & h_{n+1/2} & Q_1 & Q_2 & \dots & Q_{n+1} \end{bmatrix}^T \tag{3.63}$$

The boundary conditions vector of dimension $(2n+1)\cdot 1$ is given by:

$$\overrightarrow{C} = \begin{bmatrix} 0 & \dots & 0 & h_1 & 0 & \dots & 0 & -h_{n+1} \end{bmatrix}^T \tag{3.64}$$

It is also important to notice that the matrix $[B(Q_i)]$ is function of the discharge and introduces a non-linear behavior. For the numerical integration of this set of equation, all the discharge Q_i in matrix $[B(Q_i)]$ are retrieved from the previous time step.

3.3.2 Equivalent Scheme Representation

Set of equation 3.57 corresponds to the equations of an equivalent scheme which is a T-shaped "quadripol" as presented in figure 3.7 [85].

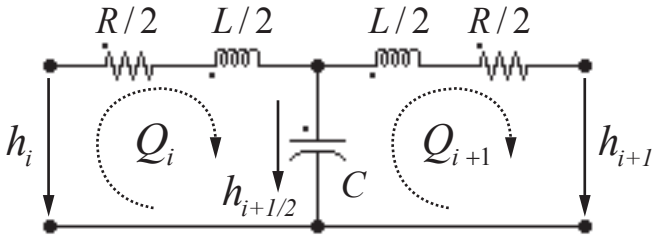

Figure 3.7: Equivalent scheme of a pipe of length dx.

This equivalent scheme is the model of a pipe with length dx where the hydroacoustic parameters are defined as follows:

- hydroacoustic capacitance $C = \frac{dx \cdot g \cdot A}{a^2}$ $[m^2]$, related to storage effect due to pressure increase and is therefore function of the wave speed ; in the wave speed equation 2.20, the term ρ/E_{water} account for water compressibility storage and the term $D/(eE_c)$ account for pipe wall deflection storage;
- hydroacoustic inductance $L = \frac{dx}{g \cdot A}$ $[s^2/m^2]$, related to inertia effect of the water;
- hydroacoustic resistance $R = \frac{\lambda \cdot dx \cdot |\bar{Q}|}{2 \cdot g \cdot D \cdot A^2}$ $[s/m^2]$, related to the head losses through the pipe.

Qualitative Analysis of the Equivalent Scheme

The equivalent scheme can be analyzed qualitatively for both steady state and transient conditions. First, for the steady state conditions the inductances and capacitances do not play any role: only the resistance causes head losses along the x coordinates according to the length of the pipe. The discharge in both loops are identical: $Q_i = Q_{i+1}$ and the head

losses correspond to the piezometric head difference between the inlet and the outlet. The steady state conditions lead to the following equation:

$$\begin{aligned} h_i - h_{i+1/2} &= \frac{R}{2} \cdot Q_i \\ h_{i+1/2} - h_{i+1} &= \frac{R}{2} \cdot Q_{i+1} \end{aligned} \tag{3.65}$$

The sum of the two above equations gives:

$$h_i - h_{i+1} = R \cdot Q_i \tag{3.66}$$

During transients, assuming a sudden increase of the downstream head h_{i+1} gives the following equation for the second loop of the equivalent scheme:

$$h_{i+1/2} - h_{i+1} - \frac{R}{2} \cdot Q_{i+1} = \frac{L}{2} \cdot \frac{dQ_{i+1}}{dt} \tag{3.67}$$

For an increase of the downstream piezometric head h_{i+1}, the inequality is obtained:

$$h_{i+1/2} - h_{i+1} - \frac{R}{2} \cdot Q_{i+1} < 0 \rightarrow \frac{dQ_{i+1}}{dt} < 0 \tag{3.68}$$

The increase of the downstream piezometric head induces the decrease of the discharge in the second loop, and as a result, the piezometric head in the middle of the pipe increases because the discharge in the first loop has not changed after an infinitesimal time interval:

$$C \cdot \frac{dh_{i+1/2}}{dt} = Q_i - Q_{i+1} \rightarrow \frac{dh_{i+1/2}}{dt} > 0 \tag{3.69}$$

This qualitative explanation describes how the equivalent scheme of a pipe represents the propagation of pressure waves in a pipe when the downstream pressure increases suddenly.

Generalized Representation of a Pipe

The implicit system of equation 3.57 can be derived directly from the equivalent scheme of the pipe of figure 3.7 using Kirchhoff's law. The same approach can be used to model a pipe of length l made of n pipes of length dx as presented in figure 3.6. Kirchhoff's law applied to this system leads to equation 3.57.

It can be noticed that the piezometric heads are determined for the node $i + 1/2$ and the discharges are determined for the loops i as indicated in figure 3.8. The corresponding equivalent scheme is presented in figure 3.9 where n equivalent schemes are concatenated together.

The 3-step modelling procedure is summarized by figure 3.10: (i) a mathematical model of the physical system is established, providing a set of hyperbolic partial differential equations; (ii) a numerical integration scheme in space provides the structure of the equivalent scheme that can be generalized, meaning that the set of total partial derivative can be obtained directly from the equivalent scheme using Kirchhoff's law; (iii) the set of total derivative equations is integrated numerically using standard algorithm such as Runge-Kutta.

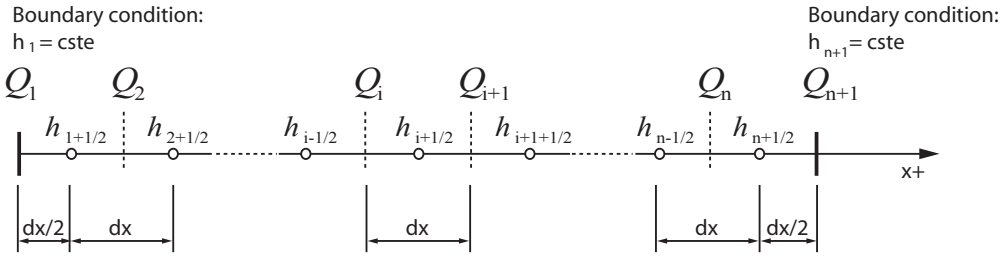

Figure 3.8: State variable location definition.

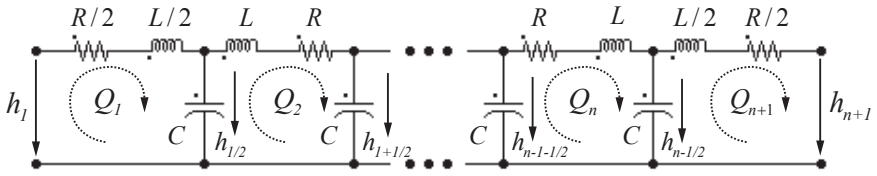

Figure 3.9: Equivalent scheme of the system of figure 3.8.

3.3.3 Free Oscillation Analysis: Discrete System

The free oscillation analysis of a hydraulic facility can be performed from its equivalent circuit with 2 different approaches: (i) solving the eigen value/vectors problem, directly from the total differential equation set 3.59; (ii) performing a numerical calculation of the system impedance, and searching for the complex frequencies satisfying all the boundary conditions.

Eigen Values/Vectors Problem

The free oscillation analysis of a discrete system modelled by n elements corresponds to the problem of the determination of the eigen values/vectors of the system of partial differential equations 3.59 using Kirchhoff's law:

$$[A] \cdot \frac{d\overrightarrow{x}}{dt} + [B] \cdot \overrightarrow{x} = \overrightarrow{0} \tag{3.70}$$

Introducing Laplace operator $s = \sigma + j \cdot \omega$ yields to:

$$[A] \cdot s \cdot \overrightarrow{x} + [B] \cdot \overrightarrow{x} = \overrightarrow{0} \tag{3.71}$$

Rearranging equation 3.71 gives a system of dimension $(2n+1) \times (2n+1)$:

$$\left([I] \cdot s + [A]^{-1}[B]\right) \cdot \overrightarrow{x} = \overrightarrow{0} \tag{3.72}$$

Where $[I]$ is the identity matrix. To ensure a non-trivial solution, the determinant of the global matrix of the system must be zero:

$$\det\left([I] \cdot s + [A]^{-1}[B]\right) = 0 \tag{3.73}$$

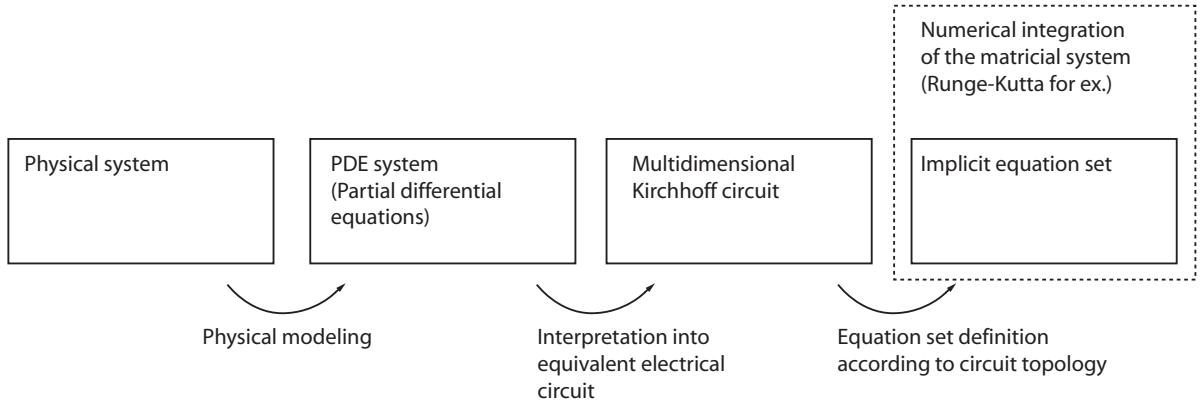

Figure 3.10: Global discrete modelling approach.

This equation is the characteristic equation of the system whose $(2n+1)$ roots comprising a null root and n double complex roots $s_n = \sigma_n \pm j \cdot \omega_n$ are the eigen values of the system with the corresponding eigen vectors $\overrightarrow{x}_n$. The free oscillation regime of this system is then given by:

$$\overrightarrow{x}(t) = \overrightarrow{x}_1 \cdot e^{s_1 \cdot t} + \overrightarrow{x}_2 \cdot e^{s_2 \cdot t} + \ldots + \overrightarrow{x}_n \cdot e^{s_n \cdot t} \tag{3.74}$$

It can be noticed that the real part of the eigen values σ_n are the damping coefficients; negative values correspond to damped modes. Stability of the system is ensured only if all the damping coefficient of the system are negative. This stability criteria is represented graphically in the complex plane where the shadow area in figure 3.11 is the stable domain.

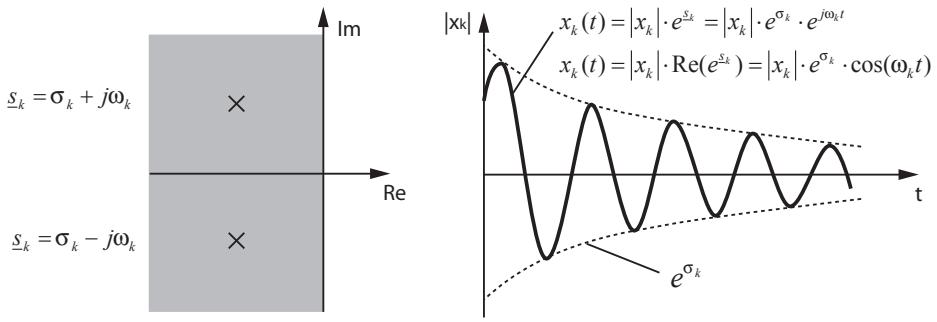

Figure 3.11: Complex eigen values with complex conjugates.

Discrete Impedance Method

This method is similar to the impedance method applied to a continuous system except the fact that the impedance is calculated from the equivalent scheme [11]. The impedance

is calculated starting from one end where the boundary condition are known, for example an open end or a dead end, and then calculated until another end. The calculation is done by successive series and parallel equivalent computation of the branches of the system. The first loop of a pipe with a load impedance $\underline{Z}_{load}$ at the end is presented in figure 3.12.

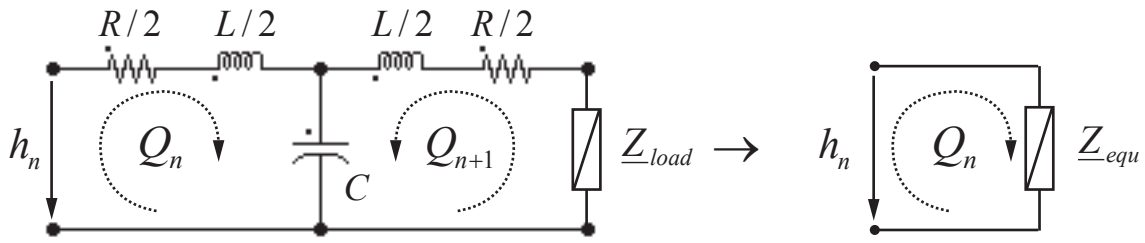

Figure 3.12: Equivalent impedance of the last loop of a pipe with load impedance Z_{load} .

The equivalent impedance of figure 3.11 can be expressed as follows:

$$\underline{Z}_{equ} = (L/2 \cdot s + R/2) + \frac{(L/2 \cdot s + R/2 + \underline{Z}_{load}) \cdot \frac{1}{C \cdot s}}{(L/2 \cdot s + R/2 + \underline{Z}_{load}) + \frac{1}{C \cdot s}} \tag{3.75}$$

If the pipe is modelled by n elements, the equivalent impedance is calculated recursively considering as load impedance $\underline{Z}_{load}$ for the loop $n-1$, the equivalent impedance $\underline{Z}_{equ}$ of the loop n, given by :

$$\underline{Z}_{equ_i} = (L/2 \cdot s + R/2) + \frac{\left(L/2 \cdot s + R/2 + \underline{Z}_{equ_{i+1}}\right) \cdot \frac{1}{C \cdot s}}{\left(L/2 \cdot s + R/2 + \underline{Z}_{equ_{i+1}}\right) + \frac{1}{C \cdot s}} \tag{3.76}$$

The computation is done for a given complex frequency. The problem to be solved is therefore to find the complex frequency satisfying all the boundary conditions. This leads to a minimization calculation based, for example, on Newton-Raphson's algorithm. It is convenient to use a first guess obtained from frictionless system whose complex roots become:

$$s = j \cdot \omega$$

This approach allows computing the impedance of the system at one end for a given range of pulsation ω and identifying which are satisfying the boundary conditions. The typical boundary conditions are:

- open end: $|\underline{Z}_x(j\omega)| = 0$
- dead end: $|\underline{Z}_x(j\omega)| = \infty$

The pulsations obtained from frictionless conditions are an excellent guess for the research of the eigen values $s_k = \sigma_k + j \cdot \omega_k$ of the dissipative system as the damping affects only slightly the eigen pulsation of a system. Once the eigen frequencies are known, the impedance can be computed along the system for the eigen value of interest indicating the location of minima and maxima of the discharge and the head.

3.4 Comparison of Continuous and Discrete Simulation Model

3.4.1 Truncation Error

The spatial discrtization of the partial derivative introduce truncation errors as the Taylor development of a value u is given for a progressive scheme by:

$$u_{i+1} \simeq u_i + \left(\frac{\partial u}{\partial x}\right)_i \cdot \Delta x + \left(\frac{\partial^2 u}{\partial x^2}\right)_i \cdot \frac{(\Delta x)^2}{2} + \left(\frac{\partial^3 u}{\partial x^3}\right)_i \cdot \frac{(\Delta x)^3}{6} + \dots \tag{3.77}$$

After rearrangement, the approximation of the partial derivative of u at the location i is given by:

$$\left(\frac{\partial u}{\partial x}\right)_i \simeq \frac{u_{i+1} - u_i}{\Delta x} + O(\Delta x) \tag{3.78}$$

A progressive or backward finite difference scheme leads to a truncation error $O(\Delta x)$ of first order (Δx). A centered scheme leads to a truncation error of second order $O(\Delta x^2)$. In order to assess this truncation error, the transfer matrix of a pipe is computed using the discrete model and compared with the exact solution obtained for a continuous system and taken as reference value. Finally, the error is quantified in the frequency domain. This quantification is done for 3 numerical finite difference scheme: (i) the "progressive" scheme, (ii) the "backward" scheme and (iii) the "centered" scheme. This comparison permits to establish a *confidence threshold*.

Centered Scheme

The finite difference scheme developed above leads to an equivalent scheme, see figure 3.13, whose set of ordinary differential equations can be derived directly from Kirchhoff's law.

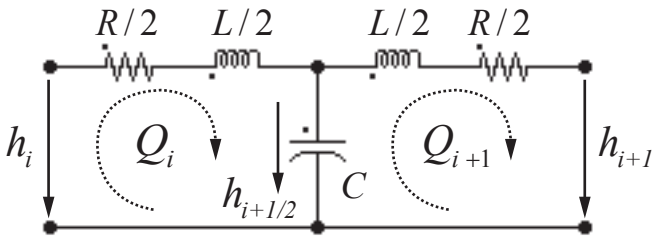

Figure 3.13: Centered equivalent scheme of a pipe of length dx.

The corresponding set of equations is given by:

$$\begin{cases} h_i = \dfrac{L}{2} \cdot \dfrac{dQ_i}{dt} + \dfrac{R}{2} \cdot Q_i + h_{i+1/2} \\ C \cdot \dfrac{dh_{i+1/2}}{dt} = Q_i - Q_{i+1} \\ h_{i+1/2} = \dfrac{L}{2} \cdot \dfrac{dQ_{i+1}}{dt} + \dfrac{R}{2} \cdot Q_{i+1} + h_{i+1} \end{cases} \tag{3.79}$$

Combining equations 3.79 yields to the transfer matrix of the equivalent circuit of figure 3.13 :

$$\begin{bmatrix} \underline{h}_i \\ \underline{Q}_i \end{bmatrix} = \begin{bmatrix} \left(\frac{\underline{\gamma}_x^2}{2} + 1\right) & \left(\frac{\underline{\gamma}_x^2}{2 \cdot C \cdot s} \cdot \left[1 + \left[\frac{\underline{\gamma}_x^2}{2} + 1\right]\right]\right) \\ C \cdot s & \left(\frac{\underline{\gamma}_x^2}{2} + 1\right) \end{bmatrix} \cdot \begin{bmatrix} \underline{h}_{i+1} \\ \underline{Q}_{i+1} \end{bmatrix} \tag{3.80}$$

Where: $\underline{\gamma}_x = \underline{\gamma} \cdot dx$.

Backward Scheme

Conserving the RL terms of the branch of the equivalent scheme of a pipe while moving the capacitance upstream leads to the equivalent scheme of figure 3.14. This equivalent scheme is based on backward numerical scheme without Lax scheme.

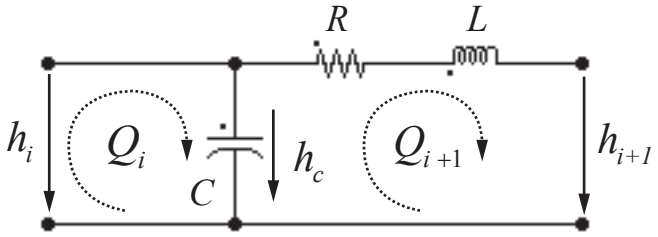

Figure 3.14: Backward equivalent scheme of a pipe of length dx.

The corresponding set of equations is given by:

$$\begin{cases} h_i = h_{i+1/2} \\ C \cdot \dfrac{dh_{i+1/2}}{dt} = Q_i - Q_{i+1} \\ h_{i+1/2} = L \cdot \dfrac{dQ_{i+1}}{dt} + R \cdot Q_{i+1} + h_{i+1} \end{cases} \tag{3.81}$$

Combining equations 3.81 yields to the transfer matrix of the equivalent circuit of figure 3.14:

$$\begin{bmatrix} \underline{h}_i \\ \underline{Q}_i \end{bmatrix} = \begin{bmatrix} 1 & \frac{\underline{\gamma}_x^2}{C \cdot s} \\ C \cdot s & \left(\underline{\gamma}_x^2 + 1\right) \end{bmatrix} \cdot \begin{bmatrix} \underline{h}_{i+1} \\ \underline{Q}_{i+1} \end{bmatrix} \tag{3.82}$$

Progressive Scheme

As it is done for the backward scheme, RL terms are conserved, but the capacitance is moved downstream. This leads to the equivalent scheme of figure 3.15, corresponding to a progressive numerical scheme without Lax scheme.

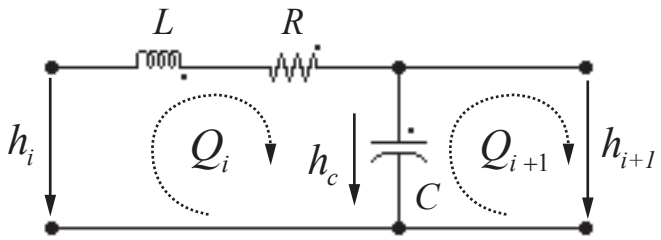

Figure 3.15: Progressive equivalent scheme of a pipe of length dx.

The corresponding set of equations is given by:

$$\begin{cases} h_i = \dfrac{L}{2} \cdot \dfrac{dQ_i}{dt} + \dfrac{R}{2} \cdot Q_i + h_{i+1/2} \\ C \cdot \dfrac{dh_{i+1/2}}{dt} = Q_i - Q_{i+1} \\ h_{i+1/2} = h_{i+1} \end{cases} \tag{3.83}$$

Combining the above equations 3.83, yields to the transfer matrix of the equivalent circuit of figure 3.15:

$$\begin{bmatrix} \underline{h}_i \\ \underline{Q}_i \end{bmatrix} = \begin{bmatrix} \left(\underline{\gamma}_x^2 + 1\right) & \frac{\underline{\gamma}_x^2}{C \cdot s} \\ C \cdot s & 1 \end{bmatrix} \cdot \begin{bmatrix} \underline{h}_{i+1} \\ \underline{Q}_{i+1} \end{bmatrix} \tag{3.84}$$

3.4.2 Comparison of Hydroacoustic Models

The transfer matrix of the following 4 models are compared: (i) the continuous hyperbolic model, (ii) the discrete centered model, (iii) the discrete backward model, and (iv) the discrete progressive model. The transfer matrix and the equivalent scheme of these models are summarized in figure 3.1.

Table 3.1: Comparison of the transfer matrix of 4 models of a pipe of length dx.

Model	Equivalent scheme	Transfer matrix
Continuous hyperbolic	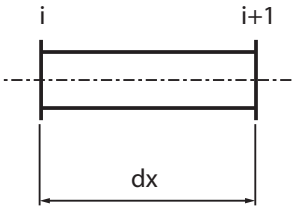	$\begin{bmatrix}\underline{h}(dx)\\ \underline{Q}(dx)\end{bmatrix} = [M]\cdot\begin{bmatrix}\underline{h}(0)\\ \underline{Q}(0)\end{bmatrix}$ $[M] = \begin{bmatrix}\cosh(\underline{\gamma}\cdot dx) & -\underline{Z}_c\cdot\sinh(\underline{\gamma}\cdot dx)\\ -\frac{1}{\underline{Z}_c}\cdot\sinh(\underline{\gamma}\cdot dx) & \cosh(\underline{\gamma}\cdot dx)\end{bmatrix}$
Discrete centered	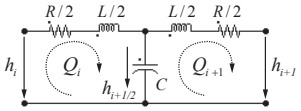	$\begin{bmatrix}\underline{h}_i\\ \underline{Q}_i\end{bmatrix} = [M]\cdot\begin{bmatrix}\underline{h}_{i+1}\\ \underline{Q}_{i+1}\end{bmatrix}$ $[M] = \begin{bmatrix}\left(\frac{\underline{\gamma}_x^2}{2}+1\right) & \left(\frac{\underline{\gamma}_x^2}{2\cdot C\cdot s}\cdot\left[1+\left[\frac{\underline{\gamma}_x^2}{2}+1\right]\right]\right)\\ C\cdot s & \left(\frac{\underline{\gamma}_x^2}{2}+1\right)\end{bmatrix}$
Discrete backward	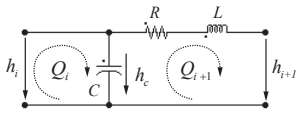	$\begin{bmatrix}\underline{h}_i\\ \underline{Q}_i\end{bmatrix} = \begin{bmatrix}1 & \frac{\underline{\gamma}_x^2}{C\cdot s}\\ C\cdot s & \left(\underline{\gamma}_x^2+1\right)\end{bmatrix}\cdot\begin{bmatrix}\underline{h}_{i+1}\\ \underline{Q}_{i+1}\end{bmatrix}$
Discrete progressive	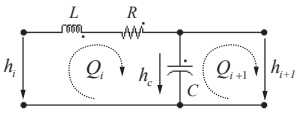	$\begin{bmatrix}\underline{h}_i\\ \underline{Q}_i\end{bmatrix} = \begin{bmatrix}\left(\underline{\gamma}_x^2+1\right) & \frac{\underline{\gamma}_x^2}{C\cdot s}\\ C\cdot s & 1\end{bmatrix}\cdot\begin{bmatrix}\underline{h}_{i+1}\\ \underline{Q}_{i+1}\end{bmatrix}$

Assuming frictionless regime, the transfer matrix of equation 3.27 becomes for a length dx:

$$\begin{bmatrix} \underline{h}(dx) \\ \underline{Q}(dx) \end{bmatrix} = \begin{bmatrix} \cos(\frac{\omega \cdot dx}{a}) & -j \cdot Z_c \cdot \sinh(\frac{\omega \cdot dx}{a}) \\ -j \cdot \frac{1}{Z_c} \cdot \sinh(\frac{\omega \cdot dx}{a}) & \cosh(\frac{\omega \cdot dx}{a}) \end{bmatrix} \cdot \begin{bmatrix} \underline{h}(0) \\ \underline{Q}(0) \end{bmatrix} \tag{3.85}$$

Introducing the wave length λ:

$$\lambda = \frac{a}{f} = \frac{2 \cdot \pi \cdot a}{\omega}, \tag{3.86}$$

the attribute of the trigonometric functions of 3.85 is given by:

$$\frac{\omega \cdot dx}{a} = 2 \cdot \pi \cdot \frac{dx}{\lambda} \tag{3.87}$$

The key parameter for a study in the frequency domain is the ratio:

$$\frac{dx}{\lambda} \tag{3.88}$$

It is necessary that the wavelength of the phenomenon of interest is at least 10 times larger than the length of the elements modelling the pipe [50]. The amplitude of the 4 terms of the matrix transfer are computed for a pipe characterized by $\lambda/dx = 10$ and presented in figure 3.16. The boundary conditions of the pipe is set as open end for $x = 0$. The 4 terms of the transfer matrix are defined as follows:

$$\begin{bmatrix} \underline{h}(dx) \\ \underline{Q}(dx) \end{bmatrix} = \begin{bmatrix} \underline{M}_{11} & \underline{M}_{12} \\ \underline{M}_{21} & \underline{M}_{22} \end{bmatrix} \cdot \begin{bmatrix} \underline{h}(0) \\ \underline{Q}(0) \end{bmatrix} \tag{3.89}$$

The impedance of the pipe of length dx is evaluated starting from the open end $x = 0$ until the end of the pipe $x = dx$ using one element for the modelling of the pipe. The resulting impedance amplitude are represented in figure 3.17. The impedance of the pipe with open end is given by:

$$\underline{Z}(dx) = \frac{\underline{M}_{12}(dx)}{\underline{M}_{22}(dx)} \tag{3.90}$$

3.4.3 Frequency Confidence Threshold of the Model

The amplitude of the impedance can be used to compare the accuracy of the 3 discrete models, the continuous hyperbolic model being taken as reference. The error of the impedance amplitude is represented for the 3 discrete models as a function of the rated wavelength λ/dx in figure 3.18. The error is provided in table 3.2 for $\lambda/dx = 10$ and $\lambda/dx = 20$.

The numerical scheme of the centered model is of the second order while the numerical scheme of both the backward and the progressive scheme are of the first order. As a result, the centered scheme features an error less than 3% for $\lambda = 10 \cdot dx$ and even less than 1% for $\lambda = 20 \cdot dx$. This means that 20 nodes are required to model properly a standing wave of one wavelength with less than 1% of error. The 4 terms of the transfer matrix

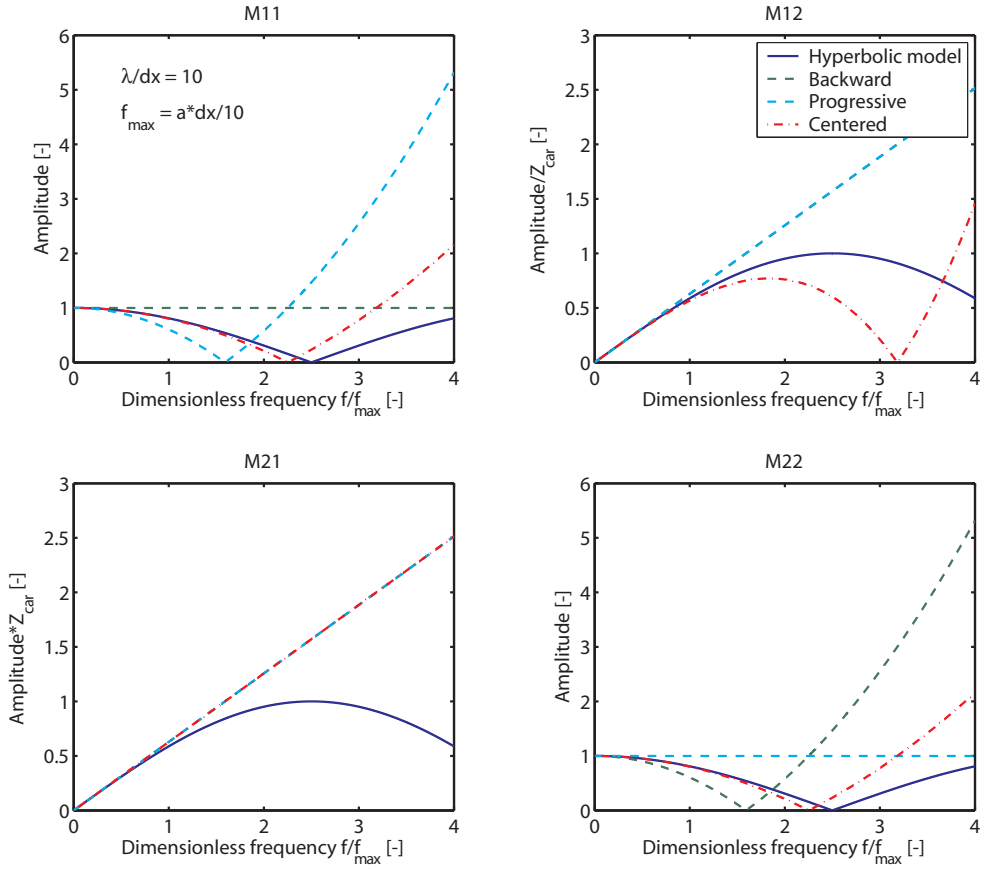

Figure 3.16: Comparison of the amplitude of the 4 terms of the transfer matrix of the 4 models.

of the centered scheme presented in figure 3.16 show good agreement with the hyperbolic solution up to $f = f_{max}$ corresponding to $\lambda = 10 \cdot dx$. Whereas for both first order scheme the accuracy is much worst due to the non symmetry of the models. Thus, the models behave differently if they are considered from one side or the other. The increase of spatial resolution presents the drawback of increasing the size of the equation system to be solved and reducing the integration time step. It is therefore very important to have criteria to define the appropriate discretization offering a good balance between accuracy and computational time.

To summarize, the spatial discretization of a hydraulic system should be defined prior

Error	Centered scheme [%] $(\|Z\| - \|Z_{ref}\|)/\|Z_{ref}\|$	Backward scheme [%] $(\|Z\| - \|Z_{ref}\|)/\|Z_{ref}\|$	Progressive scheme [%] $(\|Z\| - \|Z_{ref}\|)/\|Z_{ref}\|$
$\lambda = 10 \cdot dx$	2.9	13.5	42.9
$\lambda = 20 \cdot dx$	0.8	3.3	7.3

Table 3.2: Error on the impedance amplitude obtained for a pipe of length dx with the 3 discrete models as a function of the rated wavelength λ/dx.

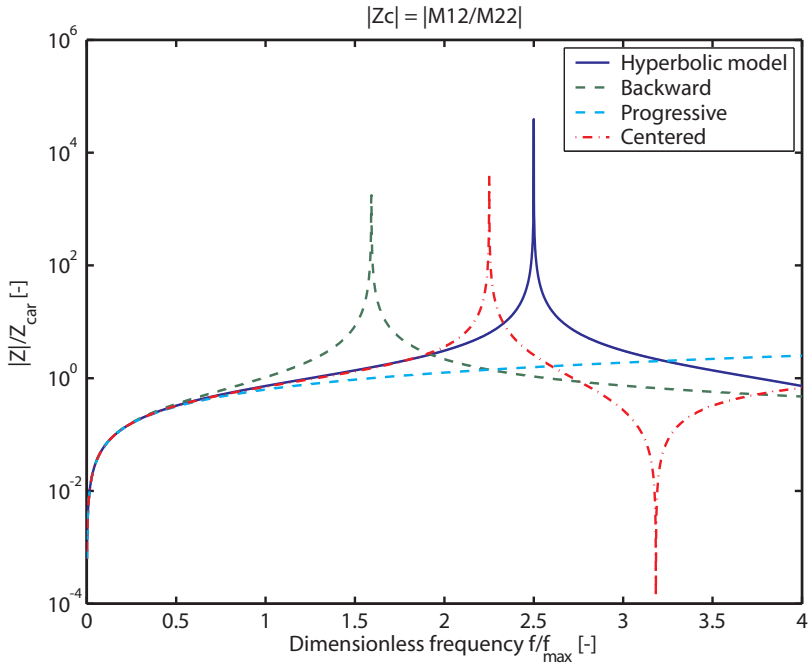

Figure 3.17: Comparison of the magnitude of the impedance $\underline{Z}_{x=dx}$ of the 4 terms of the transfer matrix obtained for the 4 models.

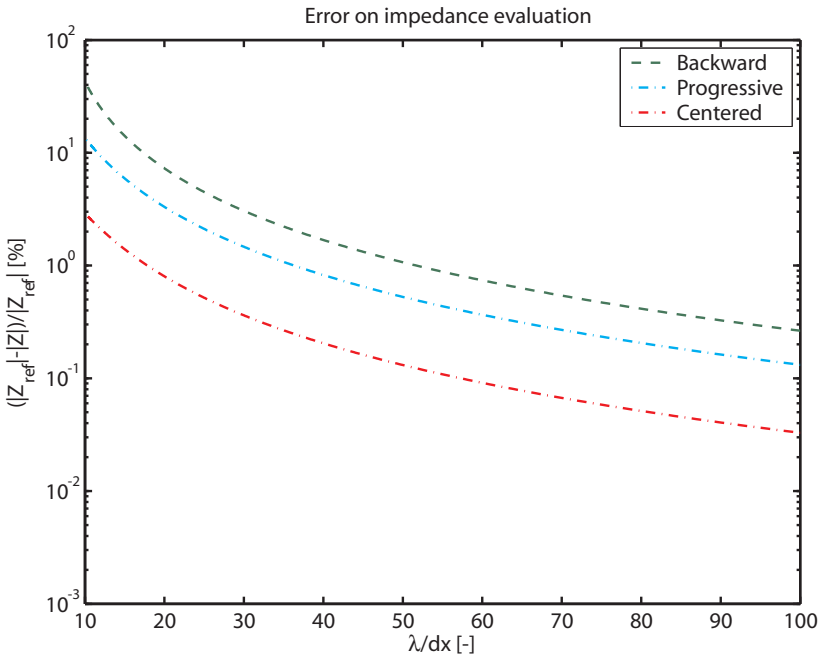

Figure 3.18: Comparison of the error on the impedance amplitude of the 3 discrete models regarding the continuous model.

to the simulation and setup according to the frequency of interest $f_{interest}$ and the wave speed a of the pipe with the following resolution:

$$\begin{aligned} dx &= \frac{a}{10 \cdot f_{interest}} \rightarrow error < 3\%; \\ dx &= \frac{a}{20 \cdot f_{interest}} \rightarrow error < 1\%. \end{aligned} \tag{3.91}$$

3.5 Summary of the Approach

Figure 3.19 is a synoptic representation of the analysis of the dynamic behavior of a hydraulic circuit by solving equation 2.26. Two general approaches are considered: (i) a continuous model with analytical resolution and (ii) a discrete model with numerical resolution.

The approach based on a continuous system has the advantage of providing the exact solution of the set of hyperbolic partial differential equations. The resolution in the frequency domain is rather convenient, however the resolution in time domain is complex because it requires to perform a Fourrier inverse transform. Moreover, the determination of the natural frequencies of the system requires an iterative algorithm.

The discrete approach presents numerical modelling errors that can be evaluated with equation 3.91 in order to use an appropriate spatial discretization ensuring reasonable accuracy at the frequency of interest while minimizing computation time.

Furthermore, the approach based on equivalent schemes is an intuitive way to represent and understand the dynamic behavior of hydraulic systems and helps for the elaboration of advanced models.

Moreover, once the ordinary equation set is established for a given topology, matrix mathematical operators can be used for the study in the frequency domain (eigen value/vector problem) and in the time domain (simulation of the dynamic behavior of the system considering all the system non-linearities).

Overall, the discrete approach offers many advantages in spite of the errors introduced by the numerical scheme. Such approach appears to be the most suitable for analyzing in detail the dynamic behavior of hydraulic circuits.

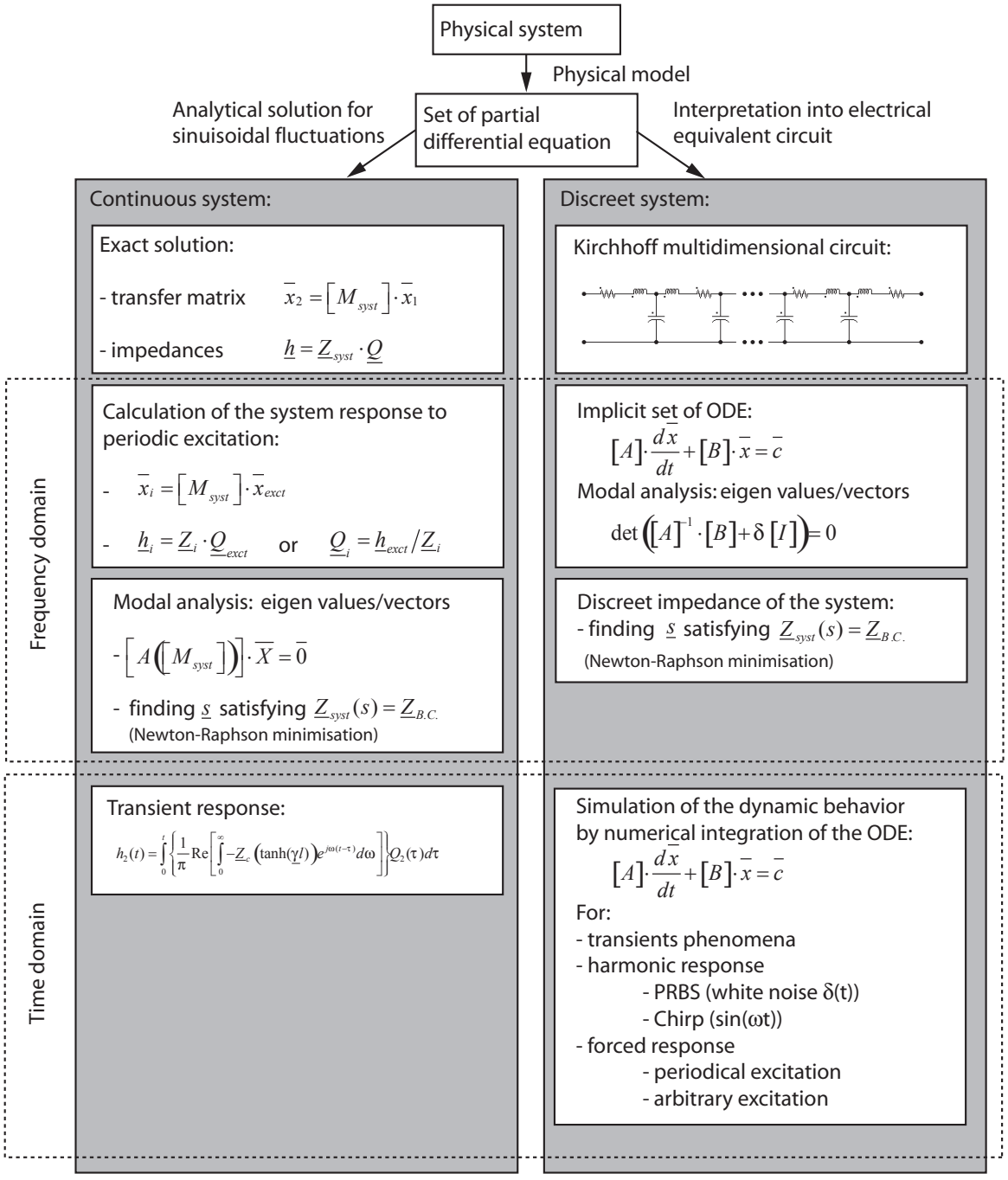

Figure 3.19: Summary of the method for analyzing dynamic behavior of a pipe.

Chapter 4

Hydroacoustic Characterization of a Pipe

4.1 Case Study Definition: Pipe with Constant Parameters

To illustrate the hydroacoustic modelling methods presented in chapter 3, the case of a single pipe of figure 4.1 is investigated. The pipe is fed by an upstream reservoir and the discharge through the pipe is controlled by a downstream valve. The main characteristics of the problem are summarized in table 4.1.

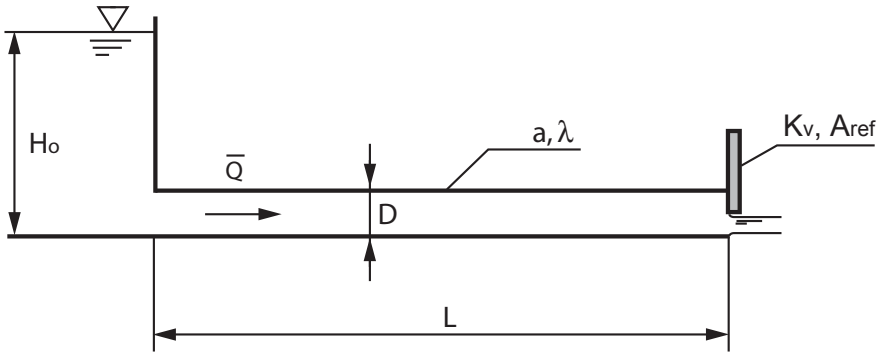

Figure 4.1: Case study of a pipe of length L.

Table 4.1: Parameters of the hydraulic system of figure 4.1.

L $[m]$	D $[m]$	a $[m/s]$	λ $[-]$	Q_o $[m^3/s]$	$f_o = a/(4L)$ $[Hz]$
600	0.5	1200	0.02	0.5	0.5

In order to characterize the hydroacoustic behavior of the above hydraulic installation, both frequency domain and time domain analysis are performed. The frequency domain

analysis consists of: (i) a free oscillation analysis, (ii) a forced response, (iii) an impedance calculation of the system. The time domain analysis consists of: (i) the determination of the maximum amplitude of the waterhammer overpressure, (ii) the graphical resolution of the waterhammer problem by the method of the characteristics, (iii) the numerical resolution of the waterhammer problem.

4.2 Frequency Domain Analysis

The hydraulic system of interest includes a valve characterized by a energetic loss coefficient K_v and a reference cross section A_{ref}. The head losses through the valve for a given discharge are given by:

$$H_r = \frac{K_v}{2 \cdot g \cdot A_{ref}^2} Q^2 = R_v \cdot Q \tag{4.1}$$

The valve resistance is given by:

$$R_v = \frac{K_v}{2 \cdot g \cdot A_{ref}^2} \left|\overline{Q}\right| [s/m2] \tag{4.2}$$

The valve impedance $\underline{Z}_v$ can be obtained by linearizing the energetic loss for a mean discharge $\overline{Q}$:

$$dH_r = \frac{K_v}{2 \cdot g \cdot A_{ref}^2} dQ^2 = \frac{K_v}{2 \cdot g \cdot A_{ref}^2} 2 \cdot \overline{Q} \cdot dQ \tag{4.3}$$

The valve impedance is given by:

$$\underline{Z}_v = \frac{\underline{H}(j\omega)}{\underline{Q}(j\omega)} = R_v \cong \frac{dH_r}{dQ} = \frac{K_v}{2 \cdot g \cdot A_{ref}^2} 2 \cdot \overline{Q} \tag{4.4}$$

For a given valve stroke position, the energetic losses can be expressed by:

$$\frac{H_{ro}}{Q_o^2} = \frac{K_v}{2 \cdot g \cdot A_{ref}^2} \tag{4.5}$$

The impedance is finally expressed as function of the nominal values:

$$\underline{Z}_v \cong \frac{K_v}{2 \cdot g \cdot A_{ref}^2} 2 \cdot \overline{Q} = \frac{2 \cdot H_{ro}}{\overline{Q}_o} \tag{4.6}$$

4.2.1 Free Oscillation Analysis

Continuous System

The analytical expression of the eigen frequencies of the system can be determined using the characteristic impedance of the system, equation 3.45. The eigen values of the system are the complex frequencies s satisfying the following boundary conditions:

- for x=0 ; $\underline{Z}_a(0) = 0$;

- for x = L ; $\underline{Z}_a(L) = \underline{Z}_v$.

Introducing the above boundary conditions in equation 3.45 yields to:

$$\underline{Z}_v \cdot \cosh(\underline{\gamma \cdot l}) + \underline{Z}_C \cdot \sinh(\underline{\gamma \cdot l}) = 0 \tag{4.7}$$

The exponential expression of the hyperbolic functions gives:

$$e^{2 \cdot \underline{\gamma} \cdot l} \left(\underline{Z}_C + \underline{Z}_v\right) + \left(\underline{Z}_v - \underline{Z}_C\right) = 0 \tag{4.8}$$

Thus:

$$2 \cdot \underline{\gamma} \cdot l = \ln\left((-1)^k \frac{\underline{Z}_C - \underline{Z}_v}{\underline{Z}_C + \underline{Z}_v}\right) + i \cdot (k \cdot \pi) \tag{4.9}$$

Assuming frictionless pipe gives $\underline{\gamma} = s/a$, $\underline{Z}_C = Z_C = a/(gA)$; and noticing that $\underline{Z}_v = Z_v$, enables the separation of the imaginary and the real part of equation 4.9:

$$\omega = \frac{k \cdot \pi \cdot a}{2 \cdot l} \quad ; k = 1, 2, 3, ... \tag{4.10}$$

And:

$$\sigma = \frac{a}{2 \cdot l} \ln\left((-1)^k \frac{Z_C - Z_v}{Z_C + Z_v}\right) \tag{4.11}$$

As the attribute of logarithm functions must be positive, 2 cases are identified for real positive values of Zc and Zv:

- $Z_v > Z_C$: $\sigma = \frac{a}{2 \cdot l} \ln\left(\frac{\underline{Z}_v - \underline{Z}_C}{\underline{Z}_C + \underline{Z}_v}\right)$ and $\omega = \frac{k \cdot \pi \cdot a}{2 \cdot l} \quad ; k = 1, 3, 5, ...$

(4.12)

- $Z_v < Z_C$: $\sigma = \frac{a}{2 \cdot l} \ln\left(\frac{\underline{Z}_C - \underline{Z}_v}{\underline{Z}_C + \underline{Z}_v}\right)$ and $\omega = \frac{k \cdot \pi \cdot a}{2 \cdot l} \quad ; k = 2, 4, 6, ...$

(4.13)

The following conclusion can be drawn:

- if $Z_v > Z_C$, the eigen mode are the odd harmonics; the valve behaves as a dead end;
- si $Z_v < Z_C$, the eigen mode are the even harmonics; the valve behaves as an open end;

Discrete System

For the hydraulic system of figure 4.1 the eigen frequencies and corresponding mode shapes are determined from equation 2.28 for the 2 following boundary conditions:

- 2 open ends ($K_v = 0$) ;
- 1 open and 1 dead end ($K_v = \infty$).

The 3 first eigen modes of the pipe are determined for both above boundary conditions with a model of the pipe made of $n = 100$ elements and are presented in figure 4.2. It can be noticed that eigen frequencies computed with the discrete model present good agreement with the eigen frequencies obtained with the continuous model given by equations 4.12 and 4.13.

Table 4.2: Three first eigen mode shape determined with the discrete model with $n = 100$ elements for open/open and open/dead boundary conditions.

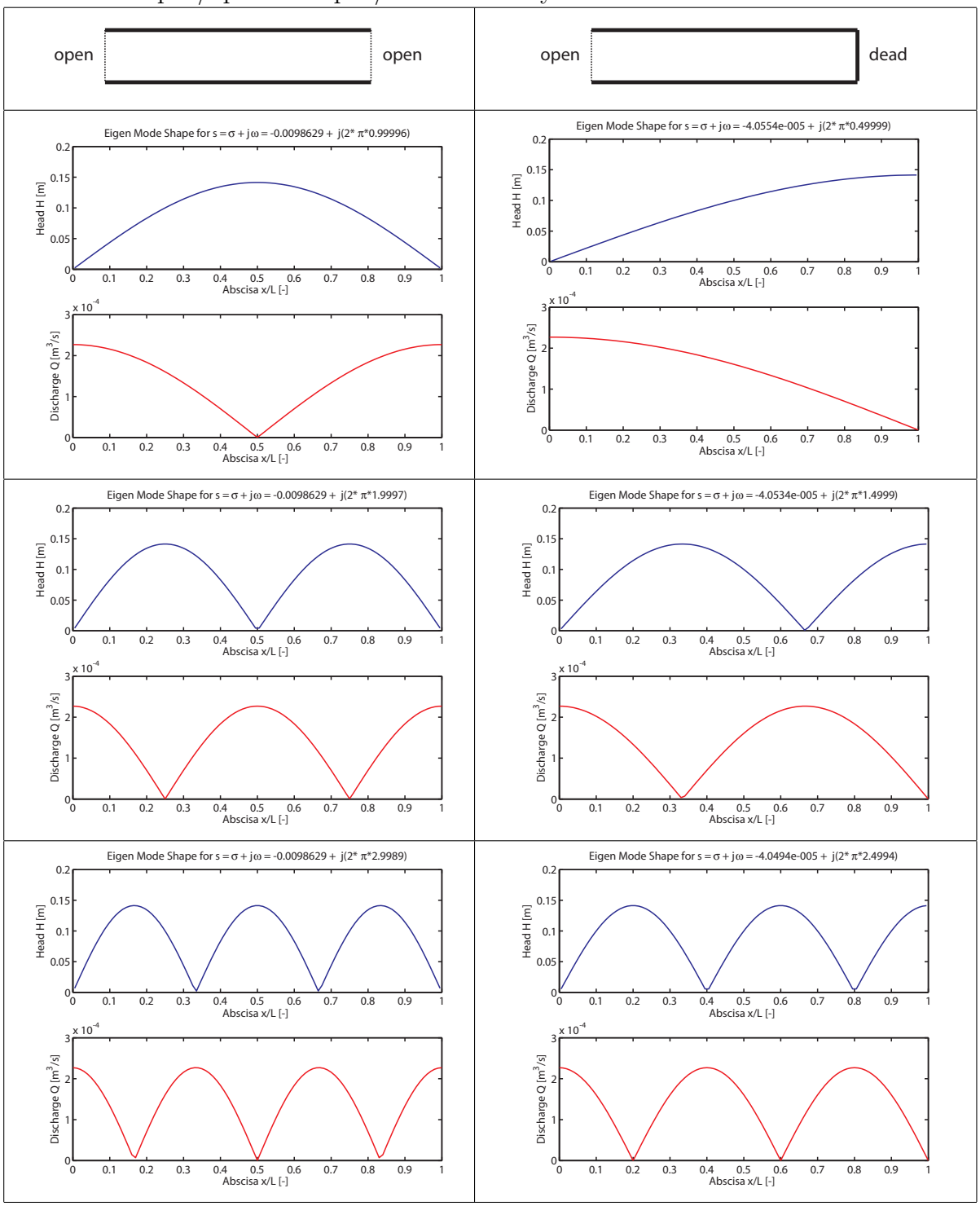

Influence of the Number of Elements Modelling the Pipe

Increasing the number of elements n modelling the pipe enables improving the accuracy of the value of the eigen frequencies of the pipe. The evolution of the first eigen frequency f_o of figure 4.1 is reported in figure 4.2 as a function of the number of elements n considering open/dead boundary conditions. It can be seen that a good accuracy on the determination of the first eigen frequency of the pipe is reached from $n = 10$ elements, with an error equal to 0.1%.

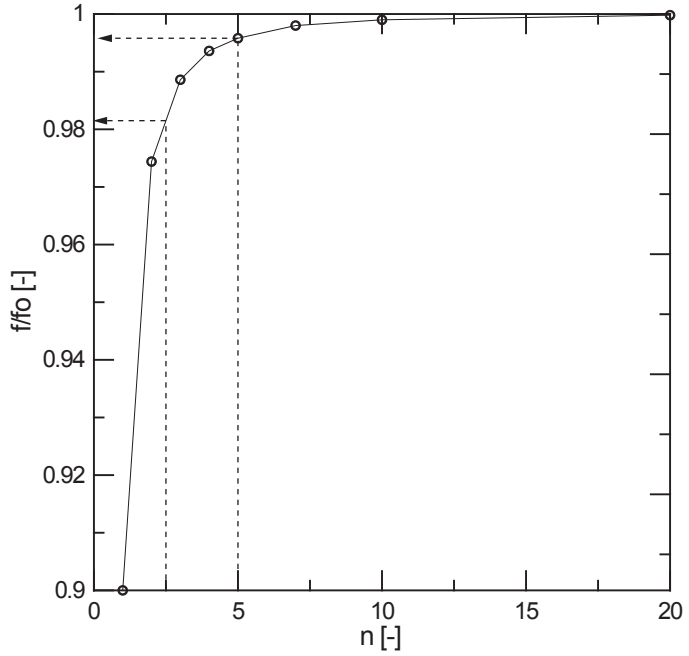

Figure 4.2: First natural frequency f_o as function of the number of elements n modelling the pipe.

The confidence threshold is connected to the number of elements as follow:

$$\frac{\lambda}{dx} = \frac{a}{f \cdot dx} = \frac{a \cdot n}{f \cdot L} \tag{4.14}$$

Therefore:

$$n = \frac{\lambda}{dx} \cdot \frac{f \cdot L}{a} \tag{4.15}$$

For the confidence threshold previously determined the following values are obtained:

- confidence threshold of 3 % : $n = \frac{\lambda}{dx} \cdot \frac{f \cdot L}{a} = 10 \cdot \frac{0.5 \cdot 600}{1200} = 2.5$; from figure 4.2 $\rightarrow 1.85\% < 3\%$ ok!;

- confidence threshold of 1 % : $n = \frac{\lambda}{dx} \cdot \frac{f \cdot L}{a} = 20 \cdot \frac{0.5 \cdot 600}{1200} = 5$; from figure 4.2 $\rightarrow 0.42\% < 1\%$ ok!.

The above results show good agreement with the confidence threshold.

4.2.2 Forced Response Analysis

The eigen frequencies of the system, see figure 4.1, can be also determined from a time domain simulation with a frequency domain analysis. Therefore, a simulation model made of the upstream reservoir, a pressure source excitation $H(t)$, the studied pipe and the downstream valve is setup. The time domain simulation is performed considering a Pseudo Random Binary Sequence, PRBS, pressure source excitation. The pressure source is in series, and therefore corresponds to a difference of pressure specified between 2 elements (and not the pressure at a given node).

A PRBS signal is a random sequence of number of value 0 or 1. Such a signal is a good approximation of white noise excitation as the energy of the signal is distributed almost uniformly in the frequency domain. The amplitude spectra of a PRBS signal with period $dT = 0.01s$ is presented in figure 4.4 and the corresponding energy spectra of the signal are presented in figure 4.5. This PRBS signal is obtained using a shift register as illustrated by figure 4.6. The energy spectra shows that the energy of the signal is distributed uniformly in the range 0 to 50 Hz.

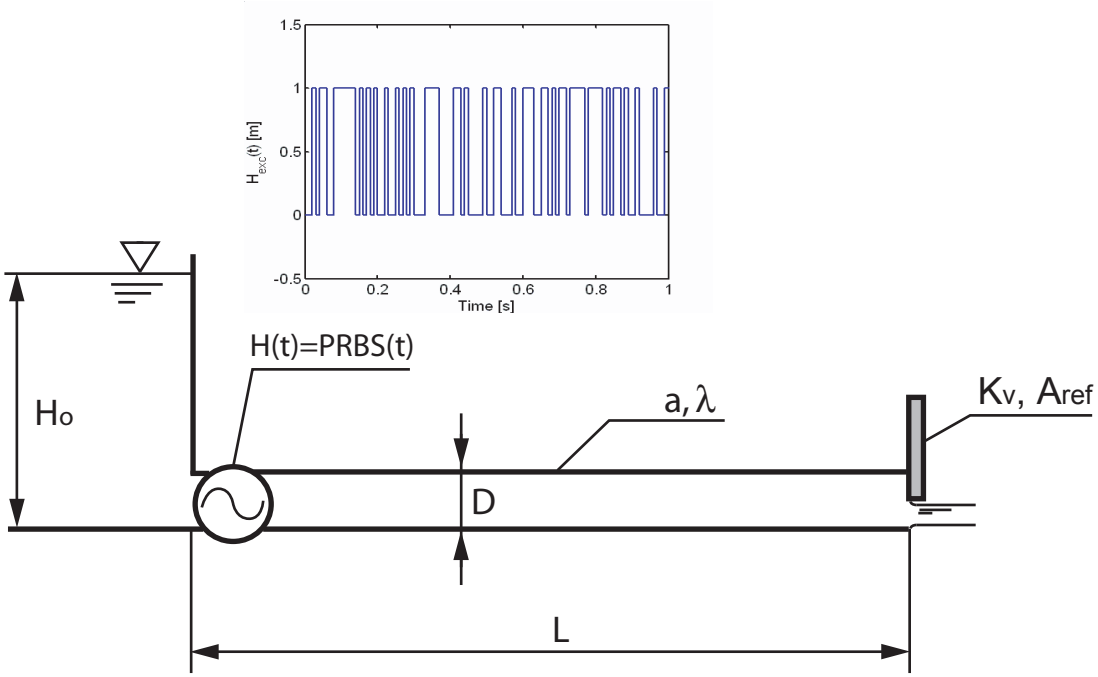

Figure 4.3: Case study including pressure source excitation for forced response analysis.

The simulation of the dynamic behavior of the case study with the pipe modelled by $n = 100$ elements under PRBS pressure source excitation provides the pressure and discharge fluctuations in the time domain. The waterfall diagram representation of the pressure fluctuations reveals the eigen mode and frequencies of the system. The downstream valve opening is selected ranging from open end until dead end conditions, and is characterized using the linearized impedance Z_v. The resulting waterfall diagrams are presented as a function of the rated valve impedance Z_v/Z_c in table 4.3; where Z_c is the

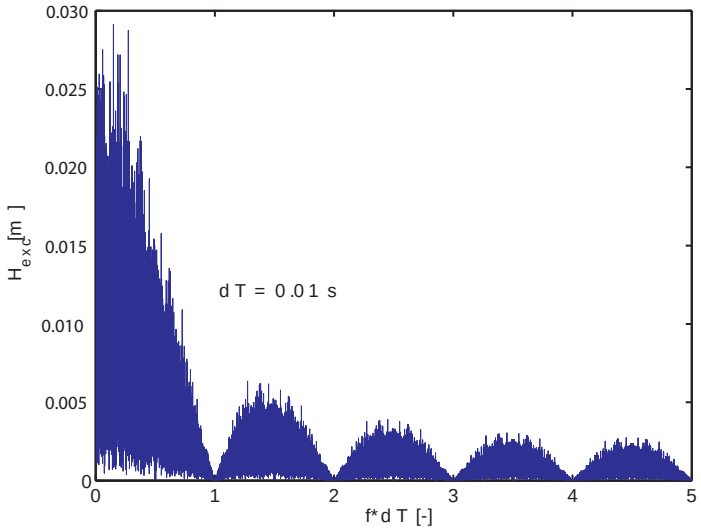

Figure 4.4: Amplitude spectra of a PRBS signal for period $dT = 0.01s$.

characteristic impedance of the pipe. As expected, the resulting eigen modes fulfil the specified boundary conditions.

When $Z_v/Z_c < 1$, according to equation 4.12 the eigen frequencies obtained are given by:

$$f_k = k\frac{a}{2 \cdot L} \quad ; \; k = 1, 2, 3, ... \tag{4.16}$$

When $Z_v/Z_C > 1$, according to equation 4.13 the eigen frequencies are given by:

$$f_k = (2 \cdot k - 1)\frac{a}{4 \cdot L} \quad ; \; k = 1, 2, 3, ... \tag{4.17}$$

When $Z_v/Z_C = 1$, the boundary condition is "anechoic", and there is no wave reflection downstream the pipe and no piping mode shape can be excited. To summarize:

- $f_k = k\frac{a}{2 \cdot L} \quad ; \; k = 1, 2, 3, ...$ for $Z_v/Z_C < 1$, it is an open end;

(4.18)

- $f_k = (2 \cdot k - 1)\frac{a}{4 \cdot L} \quad ; \; k = 1, 2, 3, ...$ for $Z_v/Z_C > 1$, it is a dead end.

(4.19)

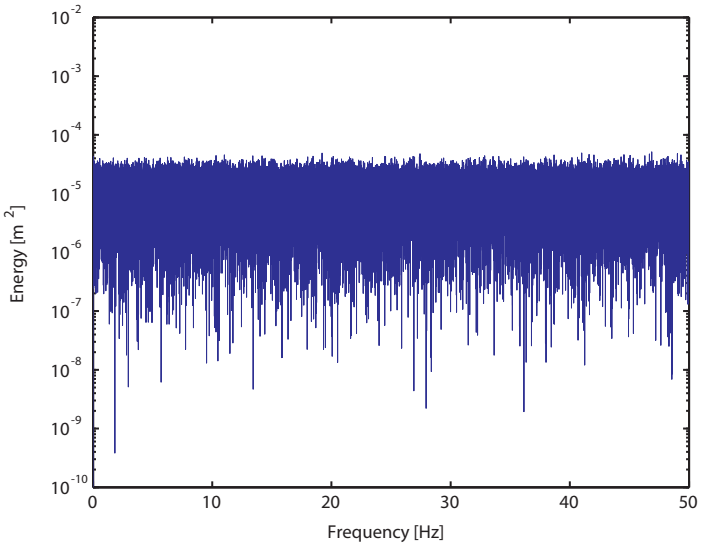

Figure 4.5: Energy spectra of a PRBS signal for period $dT = 0.01s$.

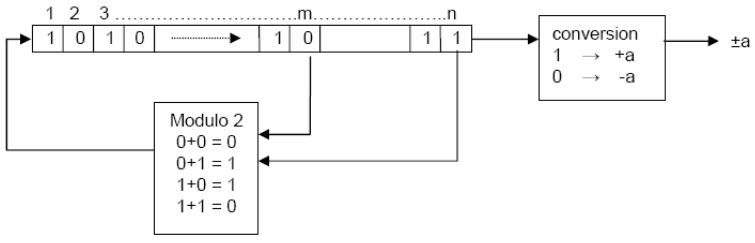

Figure 4.6: Shift register algorithm for generation of PRBS signal.

Table 4.3: Waterfall diagram obtained from PRBS excitation of the pipe with downstream valve.

$Z_v/Z_C = 0$	$Z_v/Z_C = 0.96$
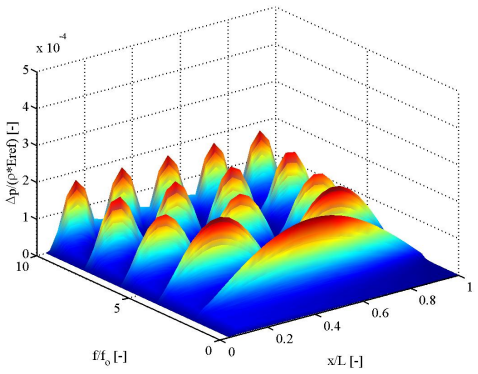	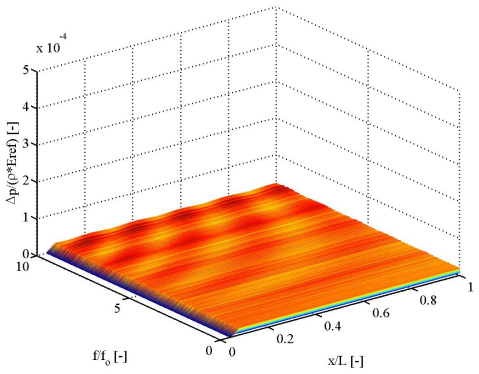
$Z_v/Z_C = 0.04$	$Z_v/Z_C = 3.13$
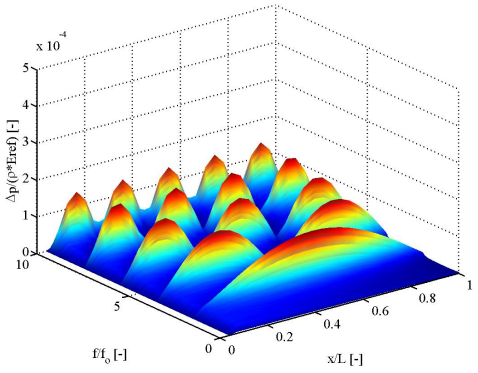	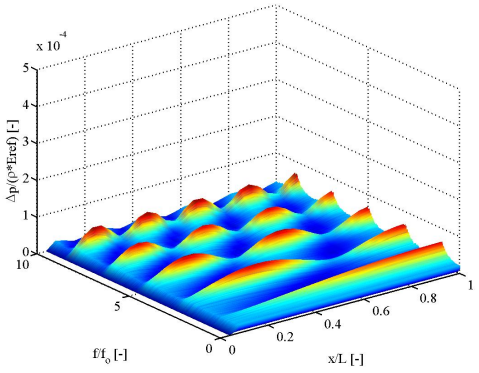
$Z_v/Z_C = 0.25$	$Z_v/Z_C = 10.1$
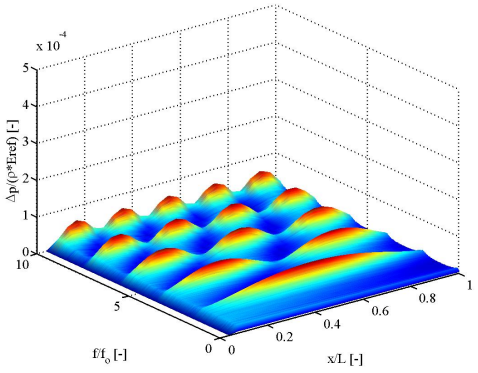	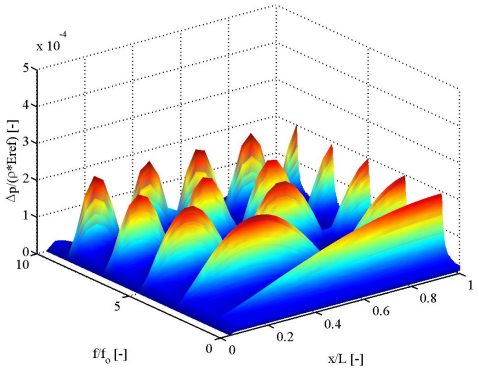

4.2.3 System Impedance

The impedance of the hydraulic system of figure 4.1 can also be calculated using equation 3.76. The impedance of this system $\underline{Z} = \underline{Z}(x, f)$, is calculated assuming an upstream tank impedance $Z = 0$. The magnitude of the impedance divided by the characteristic impedance of the pipe Z_c is represented as a 3D plot function of the rated frequency f/f_o and rated location x/L, see figure 4.7. This impedance reveals 2 information:

- the impedance downstream the pipe, $|\underline{Z}(x = L, f)|$, providing to the determination of the eigen frequencies f_k;
- the longitudinal impedance, $|\underline{Z}(x, f = f_k)|$, providing the location of pressure/discharge minima and maxima.

The downstream impedance corresponds to the front face of the 3D impedance while the longitudinal impedance is a cut at an eigen frequency $f = f_k$. The downstream impedance is extracted from figure 4.7 and presented in figure 4.8.

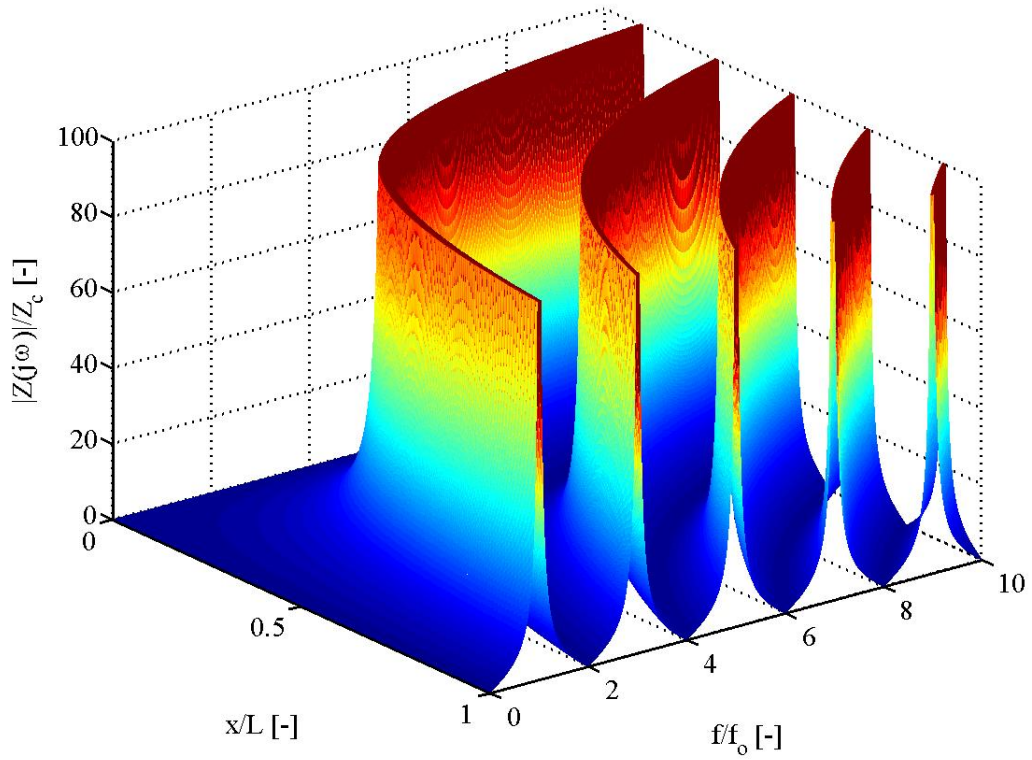

Figure 4.7: Three dimensional representation of the magnitude of the impedance of the pipe.

As the downstream conditions are supposed to be known, it is possible to identify the eigen frequencies of the whole system. The odd modes, $f/f_o = 1, 3, 5, etc$, correspond to the dead end condition $|\underline{Z}(x = L, f)| = \infty$, while the even modes $f/f_o = 2, 4, 6, etc$ correspond to the open end condition $|\underline{Z}(x = L, f)| = 0$. The longitudinal impedance

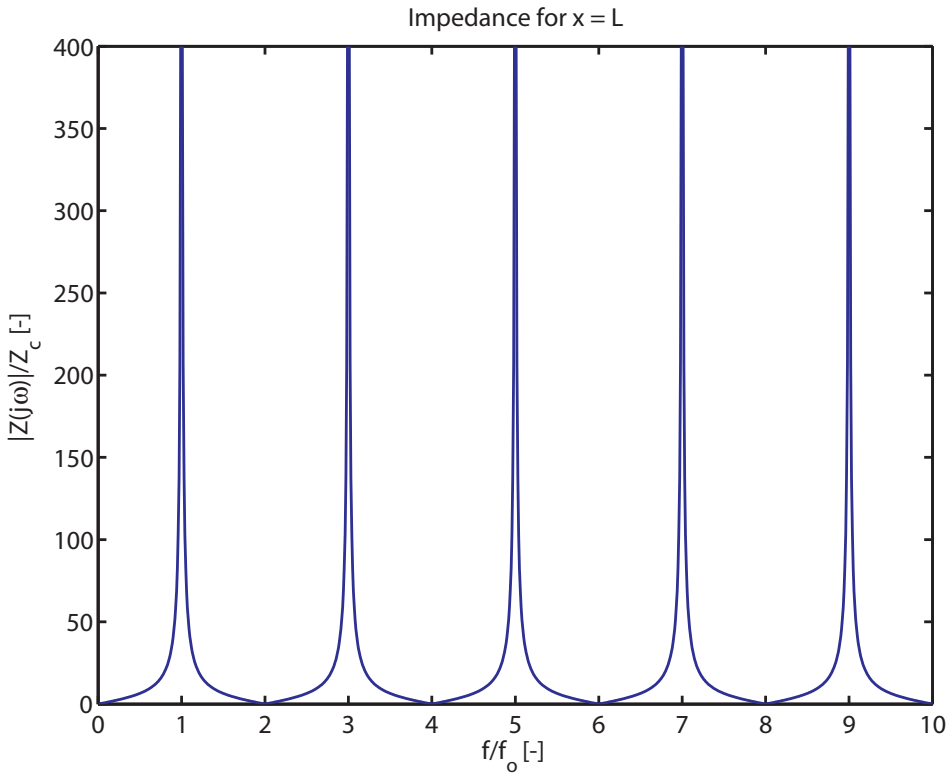

Figure 4.8: Downstream impedance of the pipe.

extracted for the first 4 eigen frequencies identified from 4.8 are presented in table 4.4. The minima and maxima of pressure and discharge locations are determined knowing that:

- for $\underline{Z}_x(f_k) = \underline{H}(j\omega)/\underline{Q}(j\omega) = 0$ are the minima of pressure and maxima of discharge;
- for $\underline{Z}_x(f_k) = \underline{H}(j\omega)/\underline{Q}(j\omega) = \infty$ are the maxima of pressure and minima of discharge.

The locations of pressure and discharge minima and maxima present good agreement with the results of table 4.2.

Table 4.4: Longitudinal impedance of the pipe for the different eigen frequencies $f/f_o = 1, 2, 3$ and 4.

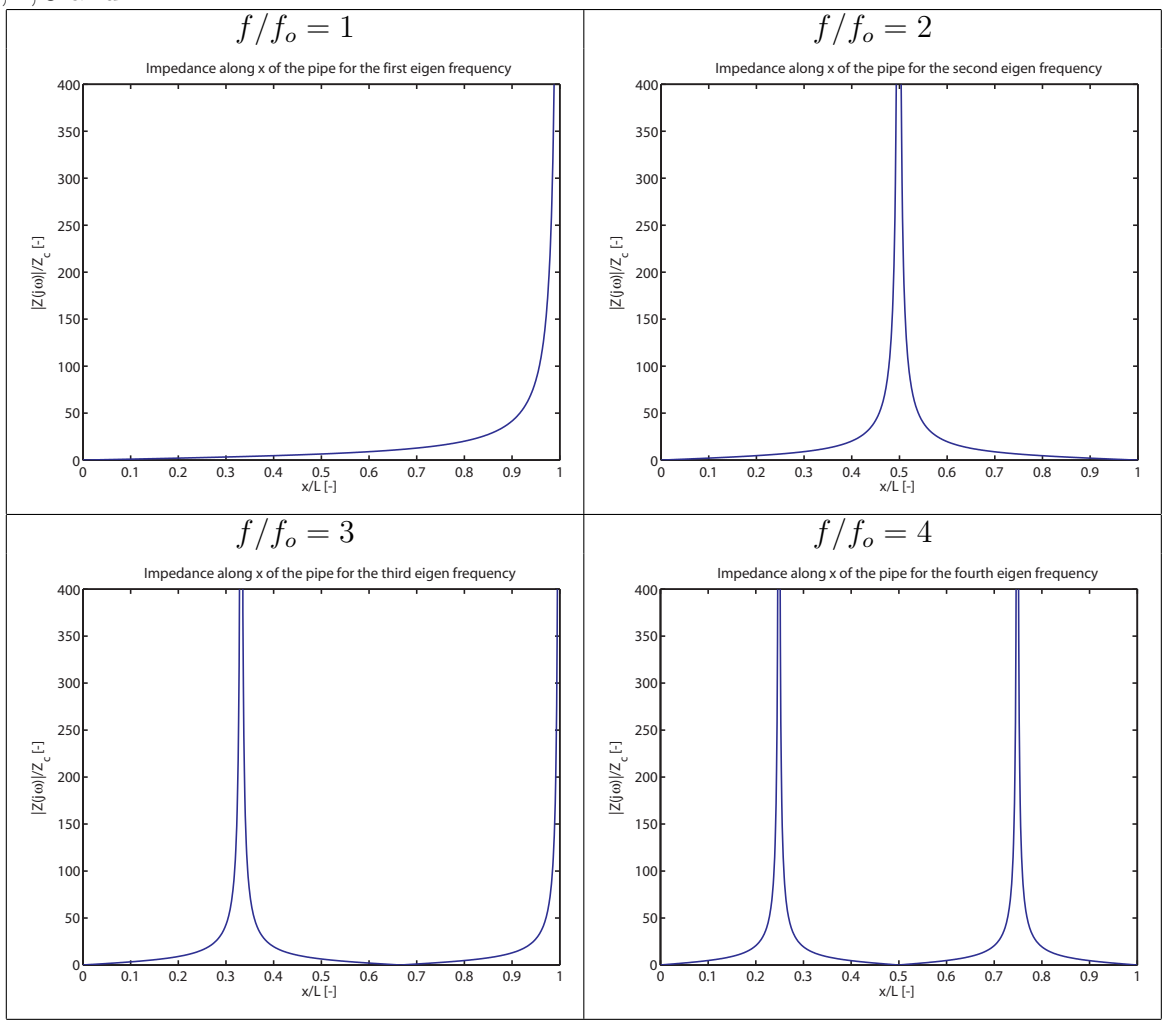

4.3 Transient Behavior Simulation

Waterhammer are produced by sudden closure of valves in piping system. In this section, the waterhammer problem is treated for the case study of figure 4.1 via 3 different time domain approaches: (i) analytical determination of the overpressure, (ii) graphical resolution, and (iii) numerical simulation.

4.3.1 Determination of the Maximum Amplitude of Waterhammer Overpressure

Applying mass and momentum conservation law to the volume of control $V3$ of figure 4.9 leads to the determination of the overpressure due to the valve closure.

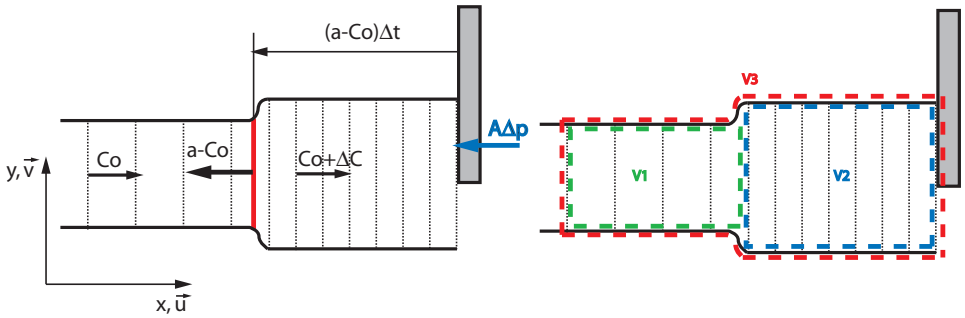

Figure 4.9: Control volume definition at the end of the pipe.

The momentum conservation equation applied to the volume of control $V3$ is expressed as:

$$\int_{V3} \frac{\partial}{\partial t}\left(\rho \cdot \overrightarrow{C} \cdot \overrightarrow{n}\right) dV + \int_{\partial V3} \rho \overrightarrow{C} \cdot \left(\overrightarrow{C} \cdot \overrightarrow{n}\right) dA = \Sigma F_x \tag{4.20}$$

The momentum change in control volume $V3$ can be decomposed in momentum change in the volumes $V1$ and $V2$:

$$\int_{V3} \frac{\partial}{\partial t}\left(\rho \cdot \overrightarrow{C} \cdot \overrightarrow{n}\right) dV = \int_{V1} \frac{\partial}{\partial t}\left(\rho \cdot \overrightarrow{C} \cdot \overrightarrow{n}\right) dV + \int_{V2} \frac{\partial}{\partial t}\left(\rho \cdot \overrightarrow{C} \cdot \overrightarrow{n}\right) dV \tag{4.21}$$

There is no momentum variation in the volume $V1$ while momentum change in volume $V2$ for a time interval Δt is given by:

$$\int_{V3} \frac{\partial}{\partial t}\left(\rho \cdot \overrightarrow{C} \cdot \overrightarrow{n}\right) dV = 0 + A(a - C_o)\Delta t \frac{[(\rho + \Delta\rho) \cdot (C_o + \Delta C) - \rho \cdot C_o]}{\Delta t} \tag{4.22}$$

The momentum balance at the inlet and the outlet surfaces of the volume $\partial V3$ gives:

$$\int_{\partial V3} \rho \overrightarrow{C} \cdot \left(\overrightarrow{C} \cdot \overrightarrow{n}\right) dA = (\rho + \Delta\rho)\,(C_o + \Delta C)^2 \cdot A - \rho \cdot A \cdot C_o^2 \tag{4.23}$$

Introducing equations 4.22 and 4.23 in equation 4.20 and expressing the force resulting from the pressure balance yields to:

$$A(a-C_o)\Delta t\frac{[(\rho+\Delta\rho)\cdot(C_o+\Delta C)-\rho\cdot C_o]}{\Delta t}+(\rho+\Delta\rho)\left(C_o+\Delta C\right)^2\cdot A-\rho\cdot A\cdot C_o^2=(p_2-p_1)A \tag{4.24}$$

The mass conservation equation for the same volume $V3$ can be written as:

$$\frac{dM}{dt}=\frac{\partial}{\partial t}\int\limits_{V3}\rho dV+\int\limits_{\partial V3}\rho\cdot\overrightarrow{C}\cdot\overrightarrow{n}\cdot dA=0 \tag{4.25}$$

For a time interval Δt, one gets:

$$A\left(a-C_o\right)\Delta t\frac{[(\rho+\Delta\rho)-\rho]}{\Delta t}-A\left[\rho C_o-(\rho+\Delta\rho)\cdot(C_o+\Delta C)\right]=0 \tag{4.26}$$

Combining equations 4.24 and 4.26 leads to an expression for the overpressure as a function of the velocity change:

$$\Delta p=-\rho A\Delta C \tag{4.27}$$

The overpressure expressed in water column:

$$\Delta H=-\frac{a\cdot\Delta C}{g} \tag{4.28}$$

For a total closure of the valve: $\Delta C=-Co$, leading to the maximum overpressure given by:

$$H_{\max}=\frac{a\cdot C_o}{g} \tag{4.29}$$

4.3.2 Graphical Method of Characteristics (MOC)

The hyperbolic partial differential equations 2.26 can be solved using the method of characteristics [7]. The set of differential equations to be solved is given by:

$$\begin{aligned}L_1&=\frac{\partial Q}{\partial t}+gA\frac{\partial h}{\partial x}+\frac{\lambda Q\left|Q\right|}{2DA^2}=0\\L_2&=gA\frac{\partial h}{\partial t}+a^2\frac{\partial Q}{\partial x}=0\end{aligned} \tag{4.30}$$

The linear combination of the 2 equations above gives:

$$L_1+\mu L_2=0 \tag{4.31}$$

Combining equations 4.30 and 4.31 yields to:

$$\left(\frac{\partial Q}{\partial t}+\mu a^2\frac{\partial Q}{\partial x}\right)+\mu gA\left(\frac{\partial h}{\partial t}+\frac{1}{\mu}\frac{\partial h}{\partial x}\right)+\frac{\lambda Q\left|Q\right|}{2DA^2}=0 \tag{4.32}$$

The piezometric head and discharge are both functions of the location x and the time t, Thus:

$$\frac{dh}{dt} = \frac{\partial h}{\partial x}\frac{dx}{dt} + \frac{\partial h}{\partial t} \quad ; \quad \frac{dQ}{dt} = \frac{\partial Q}{\partial x}\frac{dx}{dt} + \frac{\partial Q}{\partial t} \tag{4.33}$$

Introducing:

$$\frac{dx}{dt} = \frac{1}{\mu} = \mu a^2 \tag{4.34}$$

One obtains:

$$\frac{dQ}{dt} + \mu g A \frac{dh}{dt} + \frac{\lambda Q\,|Q|}{2DA^2} = 0 \tag{4.35}$$

With:

$$\mu = \pm\frac{1}{a} \tag{4.36}$$

Finally, the following set of equations is obtained:

$$\begin{cases} \dfrac{dQ}{dt} + \dfrac{gA}{a}\dfrac{dh}{dt} + \dfrac{\lambda Q\,|Q|}{2DA^2} = 0 \\ \dfrac{dx}{dt} = a \end{cases} \tag{4.37}$$

$$\begin{cases} \dfrac{dQ}{dt} - \dfrac{gA}{a}\dfrac{dh}{dt} + \dfrac{\lambda Q\,|Q|}{2DA^2} = 0 \\ \dfrac{dx}{dt} = -a \end{cases} \tag{4.38}$$

The 2 above equation sets 4.37 and 4.38 consists of a "compatibility" equation, which is only a function of the time derivative and a characteristic equation given by $dx/dt = \pm a$. The linear combination of equations 4.30 leads to the more convenient equations of compatibility, but its validity is restricted along the characteristic lines.

For graphical resolution purposes, the equation sets 4.37 and 4.38 are expressed with finite difference while head losses are assumed to be concentrated at one pipe end, yielding to:

$$\begin{cases} \dfrac{\Delta h}{\Delta Q} = -\dfrac{a}{gA} \\ \dfrac{\Delta x}{\Delta t} = a \end{cases} \tag{4.39}$$

$$\begin{cases} \dfrac{\Delta h}{\Delta Q} = +\dfrac{a}{gA} \\ \dfrac{\Delta x}{\Delta t} = -a \end{cases} \tag{4.40}$$

The equation sets 4.39 and 4.40 define straight lines in the diagram $[Q, h]$ with the slopes $\pm a/(gA)$ with respective straight lines in the diagram $[x, t]$ with slopes $\pm a$. Figures 4.10 and 4.11 presents the graphical resolution in both diagram $[x, t]$ and $[Q, h]$ of a waterhammer resulting from a valve closure with $t_{closure} = 4L/a$. The resolution is based on the survey of 2 observers leaving at same time locations A and B, respectively the reservoir and the valve. The 2 observers travel with the wave speed velocity a along the characteristic lines $dx/dt = +/-a$ in the diagram $[Q, h]$, see figure 4.11 left, going forth and back from the valve characteristic $H_v(K_v(t_i))$ and reservoir characteristic $H_o - H_r$. The combination of the journey of the 2 observers in terms of location and time in both diagrams $[x, t]$ and $[Q, h]$, provides the time evolution of the head and the discharge at the valve and reservoir. In addition, the $[Q, h]$ diagram provides the maximum amplitude of the pressure $H_{max} = a \cdot C_o/g$ from the characteristic line starting from the steady state operation $A(t1)$ to the vertical abscissa H. From this characteristic line, it can be stated that:

$$t_{closure} < 2L/a \rightarrow \Delta H = \Delta H_{\max} \tag{4.41}$$

It leads to the expression of the critical closure time of the valve given by:

$$t_{crit} = \frac{2L}{a} \tag{4.42}$$

Finally, it can be noticed that:

- valves closing faster than the critical time t_{crit}, induces the maximum overpressure H_{max};
- valves closing slower than the critical time $t_{crit} = 2(L/a)$ leads to amplitudes amplitudes below H_{max}.

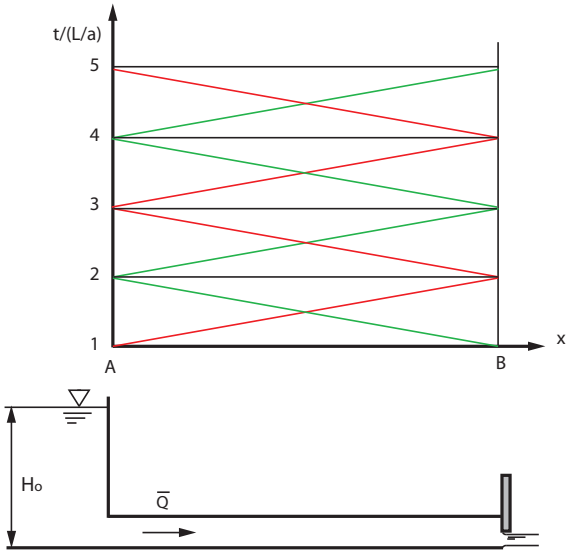

Figure 4.10: Diagram $[x, t]$ for the graphical resolution by the method of the characteristic

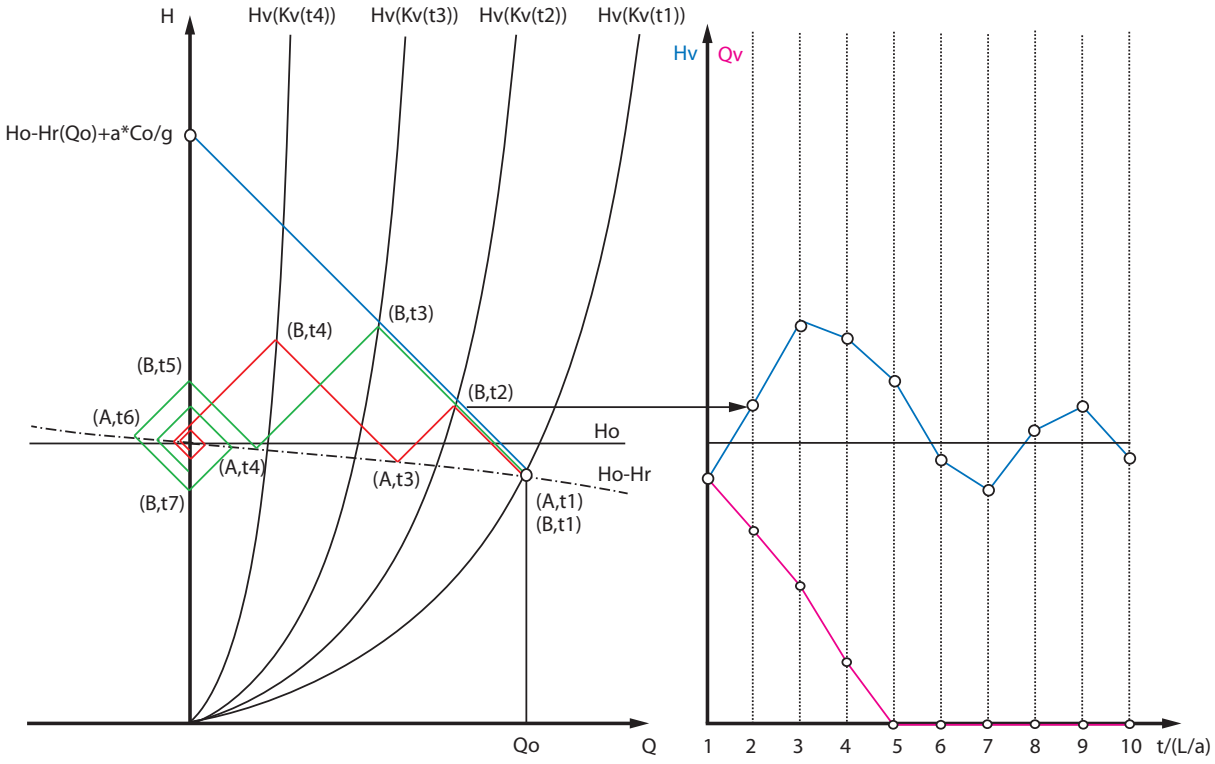

Figure 4.11: Diagram $[Q, h]$ for the graphical resolution by the method of the characteristic and resulting time evolution of the discharge and the pressure.

4.3.3 Numerical Simulation of Waterhammer

The equivalent scheme of the system presented in figure 4.1 is presented in figure 4.12. The equivalent scheme is made of a pressure source Ho, a series of n T-shaped equivalent schemes of elements of length dx and a variable resistance modelling the downstream valve.

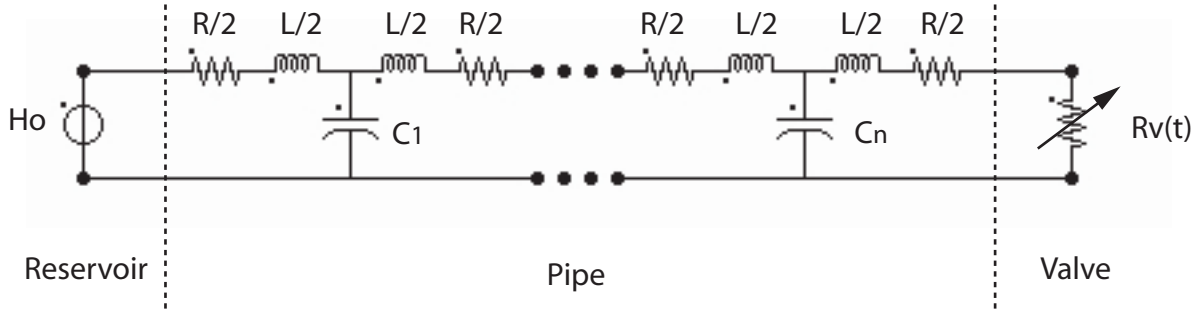

Figure 4.12: Equivalent scheme of the case study.

The downstream valve is closed according to:

$$y_1 = 1 - \left(\frac{t - T_{start}}{T_{closure}} \right)^{0.75} \tag{4.43}$$

With:
T_{start}: time at the start of the closure $[s]$
T_{close} : valve closure time $[s]$

The valve loss coefficient is defined as follows:

$$K_v(t) = \frac{K_{vo}}{y_1(t)^2} \tag{4.44}$$

Applying Kirchhoff's law to the equivalent scheme of figure 4.12 leads to a set of ordinary differential equations given by:

$$[A] \cdot \frac{d\overline{x}}{dt} + [B] \cdot \overline{x} = \overline{C} \tag{4.45}$$

This system is solved by using the 4^{th} order explicit Runge-Kutta method. The simulation parameters are summarized in table 4.5.

Table 4.5: Simulation parameters

$n[-]$	$dt[s]$	$T_{close}[s]$
50	0.005	2.1

The critical time of the valve closure is for the case study $t_{crit} = 2L/a = 1s$. As a result, the amplitude of the waterhammer overpressure with a valve closing time of 2.1s is

below the maximum overpressure H_{max}. The time evolution of the head at the valve, H_v, of the discharge at the valve, Q_v and of the discharge at the reservoir, Q_b, are represented in figure 4.13. It can be noticed that the discharge at the valve decreases until zero within the valve closure time inducing an overpressure at the valve of amplitude $0.8 \cdot Ho$. The maximum overpressure occurs at the instant $T_{start} + 2L/a$.

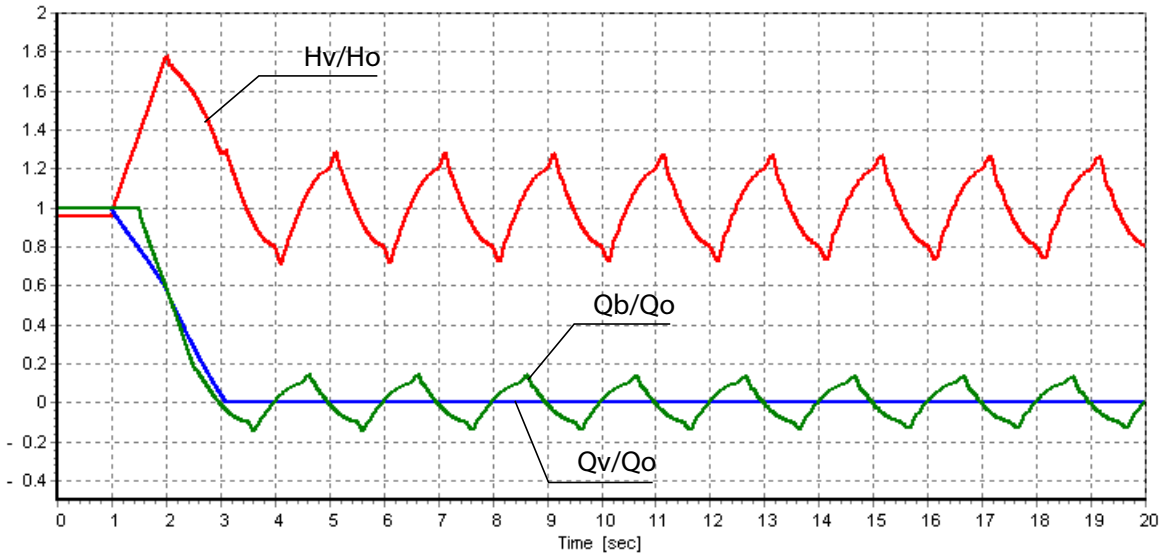

Figure 4.13: Time evolution in rated values of the head at the valve H_v/Ho, the discharge at the valve Q_v/Qo and of the discharge at the reservoir Q_b/Qo resulting from a valve closure in $2.1s$, *i.e.* $4.2L/a$.

The simulation results obtained with the equivalent scheme are compared with the simulation results obtained by MOC solved using a finite difference method. The comparison of the simulation results is presented for the head at the valve and the discharge at the reservoir in table 4.14. The results obtained with the equivalent scheme show good agreements with the ones obtained with MOC.

The results of the simulation of the valve closure in 0.2s ($0.1 \cdot t_{crit}$) are presented in figure 4.15. The maximum amplitude of $H_v/Ho = 3$ is reached after the full valve closure for $t = 0.2s$. The time evolution of the pressure exhibits square shape with period $T = 4L/a$.

The piezometric line along the pipe is represented in figure 4.16 for 8 different times extending from $t_o + T/8$ to $t_o + T$ with $T = 4L/a$. This representation evidences the pressure wave propagation and also shows the steep slope of the pressure wave propagating in the pipe for valve closure time below the critical time t_{crit}. The pipe experiences successively overpressure and underpressure phases lasting each $2L/a$. The 4 phases are summarized in figure 4.17.

Figure 4.16 depicts numerical instabilities visible on the head signal and on the discharge signal at the valve. The longer the simulation, the higher the numerical instabilities. These simulation errors are amplified at each wave reflection owing to the fact that the model of the pipe is of the second order in the middle of the pipe but only of the first order at the end. Furthermore, the quicker is the valve closure, the higher is the amplitude

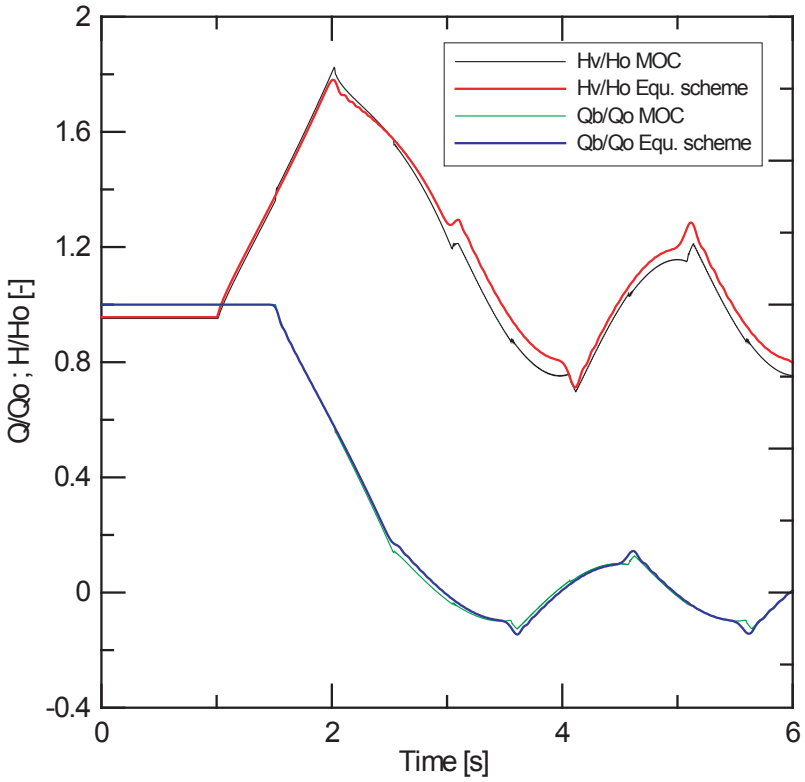

Figure 4.14: Comparison of the time evolution of the pressure at the valve (left) and discharge at the reservoir (right) obtained with equivalent scheme and method of characteristic (MOC).

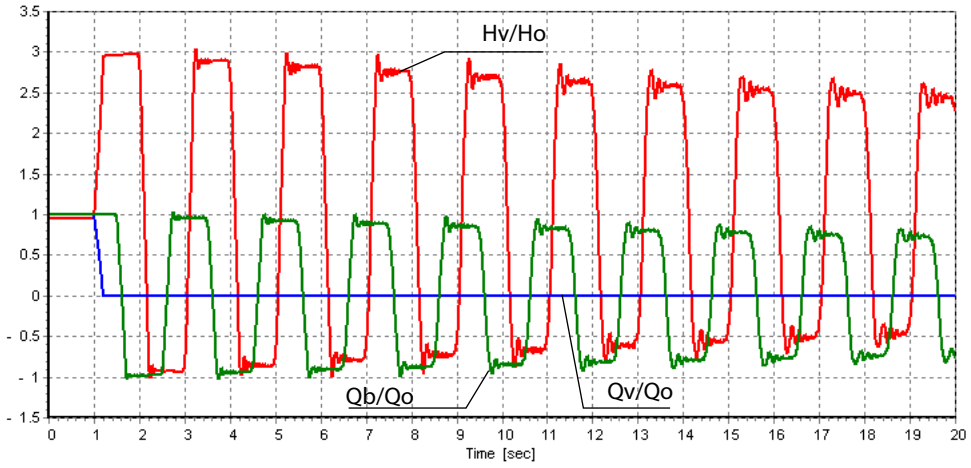

Figure 4.15: Time evolution of the rated head at the valve H_v/Ho, of the rated discharge at the valve Q_v/Qo and of the rated discharge at the reservoir Q_b/Qo resulting from valve closure in $0.2s$, $(0.4 \cdot L/a)$.

of the numerical instabilities because the frequency content of the pressure wave shape becomes higher and thus requires a higher number of elements to model properly the phenomenon. Figure 4.18 shows how numerical instabilities can be reduced by increasing the number of elements n from 10 to 100. This means that for simulating an instantaneous valve closure, an infinite number of elements would be required and therefore, infinitely small time steps. The influence of the integration method on the numerical instabilities is discussed in appendix A.

For the realistic cases encountered in the operation of hydropower plants, instantaneous valve closures are not supposed to be experienced. Indeed, designing the pipe walls with a thickness capable of supporting the maximum amplitudes of waterhammer overpressure or underpressure is not possible for economical reasons. Thus, the appropriate spatial discrtization must be a compromise between computational time and simulation accuracy.

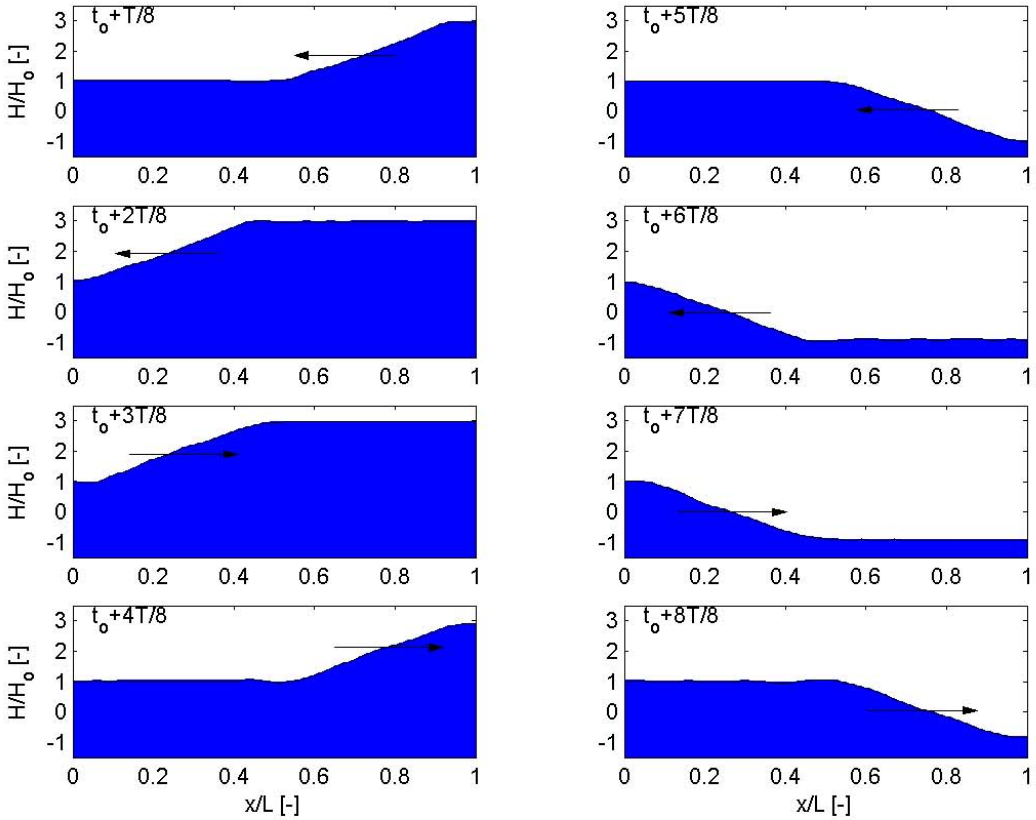

Figure 4.16: Piezometric line along the piping for different time ($T = 4L/a$).

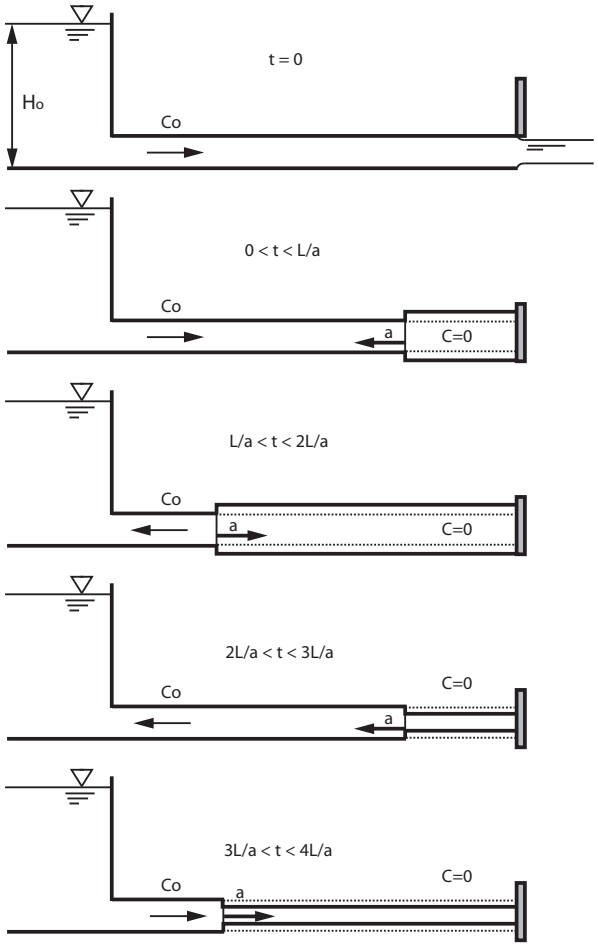

Figure 4.17: Definition of the 4 phases of the waterhammer.

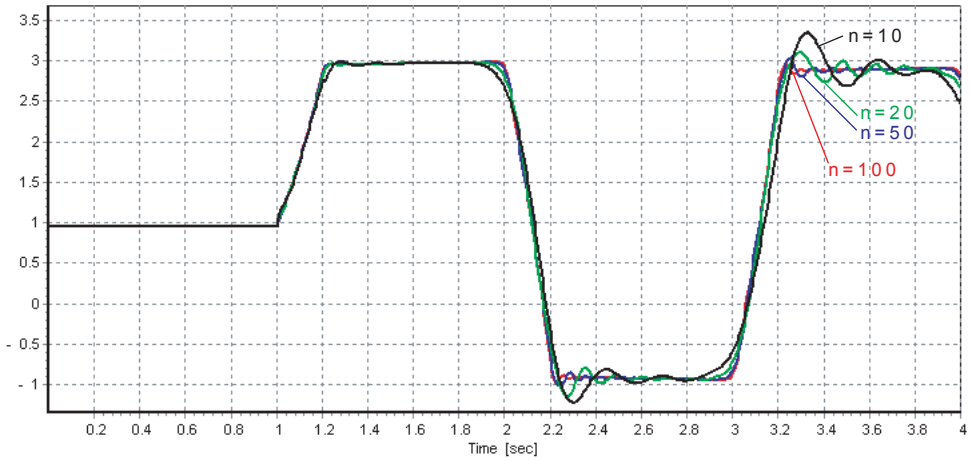

Figure 4.18: Comparison of the time evolution of the head at the valve for different spatial discretization of the pipe.

Chapter 5

Modelling of Hydraulic Components

5.1 Circuit Components Modelling

The hydraulic circuits of hydroelectric power plants are made of several components that have to be included to model its dynamic behavior. The modelling of the following components are presented: (i) elastic or viscoelastic pipe, (ii) valve, (iii) surge tank, (iv) surge shaft, (v) air vessel, (vi) cavitating flow.

5.1.1 Pipe

The pipe model is the key component of the hydroacoustic modelling. In most of industrial applications pipes are made of metallic materials with elastic behavior. However, recent developments in the domain of polymer materials has brought a wide range of new materials to hydraulic installations. PVC for industrial applications and fiber glass for prototyping are 2 examples of polymers that are commonly used in the construction of hydraulic circuits.

Many polymers materials exhibit a viscoelastic behavior that induces additional damping in the systems that has to be properly taken into account especially for stability analysis purposes. Therefore, the model of the pipe presented in chapter 3 is extended for taking into account possible viscoelastic effects of the pipe wall material. The concept of viscoelastic behavior is also extend to the fluid.

Elastic Pipe

The model of the pipe derived from the momentum and mass equations leads to the representation of pipe of length dx by an equivalent electrical circuit made of 2 resistances, 2 inductances and one capacitance as presented in figure 5.1.

This modelling approach can be extended to a full length pipe by considering n equivalents schemes in series as shown in figure 5.2.

Viscoelastic Pipe

Viscoelastic materials present dynamic behavior as stress σ in the material is not proportional to the rated deformation $\varepsilon = dl/l$ but is also function of the rate of deformation

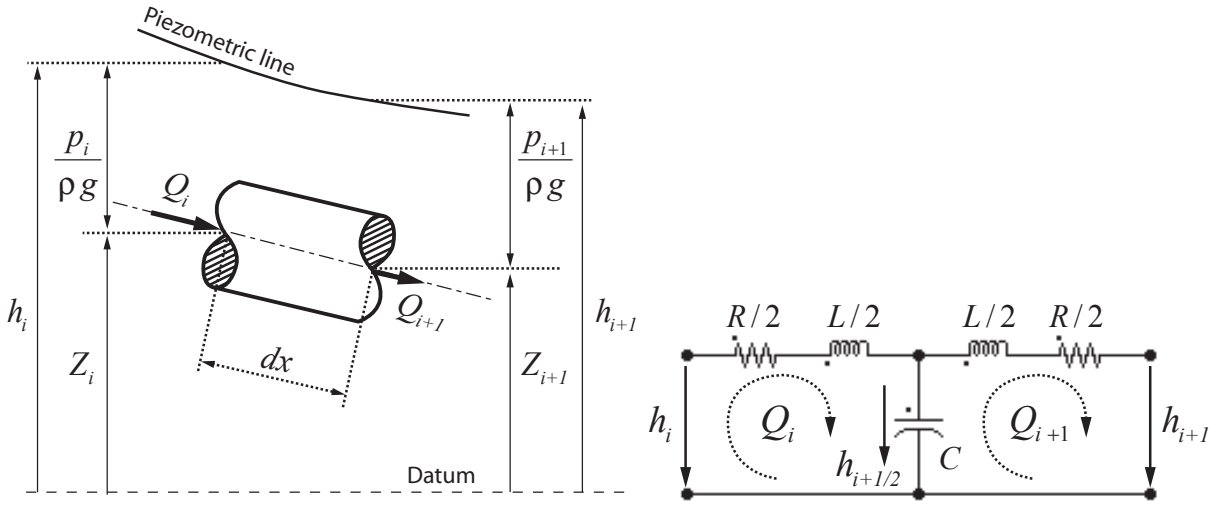

Figure 5.1: Modelling of a pipe of length dx (left), with the corresponding equivalent scheme (right).

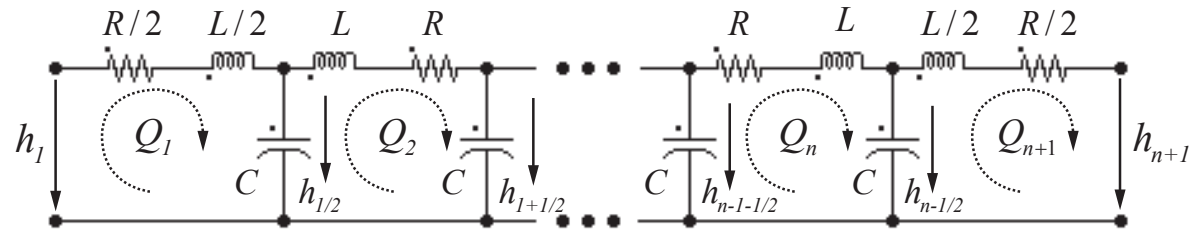

Figure 5.2: Full length pipe model made by n elements.

$d\varepsilon/dt$. Figure 5.3 shows typical time evolution of the stress as a function of the rated deformation for viscoelastic materials.

The modelling of the viscoelastic behavior can be achieved using rheologic models made of springs and dashpots. Maxwell's, Kelvin-Voigt's and Standard models are 3 common rheologic models presented in table 5.1 with their equivalent electrical schemes. Theses models are elementary models from which more advanced models can be derived.

Without loss of generality, a viscoelastic pipe accounting for both pipe material and water viscoelasticity can be modelled by 2 Kelvin-Voigt models as presented in figure 5.4. Therefore, considering first the pipe wall material viscoelastic behavior and assuming a pipe perimeter deflection $\varepsilon = dD/D$ due to pressure increase leads to:

$$\sigma = E_{pipe} \cdot \varepsilon + \mu_{pipe} \cdot \frac{d\varepsilon}{dt} = E_{pipe} \cdot \frac{dD}{D} + \mu_{pipe} \cdot \frac{1}{D} \cdot \frac{d(dD)}{dt} \tag{5.1}$$

The total derivative of the volume of the pipe V of length dx is given by:

$$dV = d(\pi D^2/4) \cdot dx = \frac{\pi \cdot D}{2} dD \tag{5.2}$$

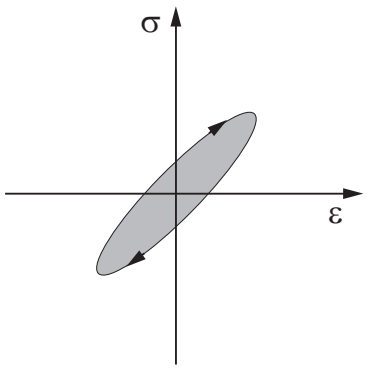

Figure 5.3: Stress as function of the deformation for a viscoelastic material.

Table 5.1: Rheologic models of viscoelastic materials and their equivalent scheme.

Model	Rheologic model	Equivalent scheme	Equations
Maxwell	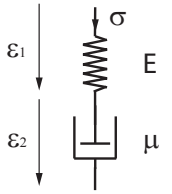	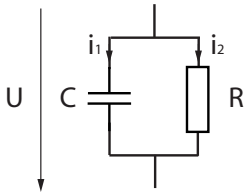	$\sigma = \varepsilon_1 \cdot E = \mu \cdot \frac{d\varepsilon_2}{dt}$ $U = \frac{1}{C} \int i_1 \cdot dt = R \cdot i_2$
Kelvin-Voigt	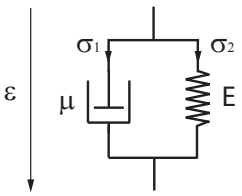	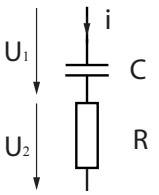	$\sigma = \sigma_1 + \sigma_2 = \varepsilon \cdot E + \mu \cdot \frac{d\varepsilon}{dt}$ $U = U_1 + U_2 = \frac{1}{C} \int i \cdot dt + R \cdot i$
Standard	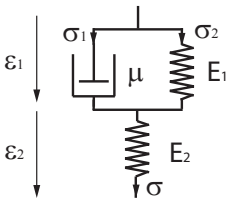	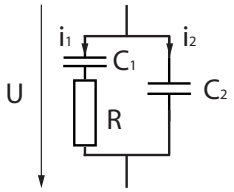	$\sigma = \varepsilon_2 \cdot E_2 = \varepsilon_1 \cdot E_1 + \mu \cdot \frac{d\varepsilon_1}{dt}$ $\varepsilon = \varepsilon_1 + \varepsilon_2$ $U = \frac{1}{C_2} \int i_2 \cdot dt$ $U = \frac{1}{C_1} \int i_1 \cdot dt + R \cdot i_1$ $i = i_1 + i_2$

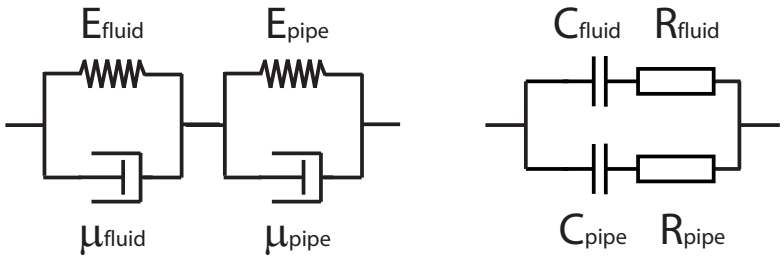

Figure 5.4: Rheologic (left) and equivalent (right) models of a viscoelastic pipe with contribution of water and and pipe material viscoelastic behavior.

Introducing the piezometric head, $h = p/(\rho g) + z$, in equation 2.18, and neglecting vertical displacement of the pipe ($dz/dt = 0$), gives:

$$\frac{d\sigma}{dt} = \frac{D\rho g}{2e} \cdot \frac{dh}{dt} \tag{5.3}$$

Combining equations 5.1, 5.2 and 5.3 and introducing the stored discharge $Q_p = dV/dt$ leads to:

$$\frac{dh}{dt} = \frac{E_{pipe}e}{AD\rho g dx} \cdot Q_p + \frac{\mu_{pipe}e}{AD\rho g dx} \cdot \frac{dQ_p}{dt} \tag{5.4}$$

By integrating equation 5.4, one get Kelvin-Voigt's equation of the pipe wall material:

$$h = \frac{1}{C_{pipe}} \int Q_p \cdot dt + R_{pipe} \cdot Q_p \tag{5.5}$$

Where the viscoelastic resistance R_{pipe} and capacitance C_{pipe} of a pipe of length dx are given by:

$$R_{pipe} = \frac{\mu_{pipe}e}{AD\rho g dx} \quad ; \quad C_{pipe} = \frac{AD\rho g dx}{E_{pipe}e} \tag{5.6}$$

Then, considering the fluid compressibility from equation 2.14 and the second viscosity μ_{fluid} leads to:

$$\frac{dp}{dt} = \frac{E_{fluid}}{\rho} \cdot \frac{d\rho}{dt} + \frac{\mu_{fluid}}{\rho} \cdot \frac{d^2\rho}{dt^2} \tag{5.7}$$

Reintroducing the piezometric head $h = p/(\rho g) + z$ and the stored discharge due to fluid compressibility $Q_f = -\frac{V}{\rho} \cdot d\rho/dt$ gives:

$$\frac{dh}{dt} = \frac{E_{fluid}}{A\rho g dx} \cdot Q_f + \frac{\mu_{fluid}}{A\rho g dx} \cdot \frac{dQ_f}{dt} \tag{5.8}$$

By integration of equation 5.8, one get Kelvin-Voigt's equation of the pipe fluid:

$$h = \frac{1}{C_{fluid}} \int Q_f \cdot dt + R_{fluid} \cdot Q_f \tag{5.9}$$

Where the viscoelastic resistance R_{fluid} and capacitance C_{fluid} of a pipe of length dx are given by:

$$R_{pipe} = \frac{\mu_{fluid}}{A\rho g dx} \quad ; \quad C_{pipe} = \frac{A\rho g dx}{E_{fluid}} \tag{5.10}$$

It can be noticed that:

- both viscoelastic resistance are proportional to the invert of the length of the pipe dx;
- the viscoelastic losses are proportional to the discharge and **not** to the square of the discharge.

It can be also noticed that, if, in the model of the pipe of figure 5.4, the 2 viscoelastic resistances of the fluid and of the wall material are neglected, the 2 capacitances in parallel are equivalent to the capacitance of the elastic pipe:

$$C_{equ} = C_{pipe} + C_{fluid} = A\rho g dx \left[\frac{D}{E_{pipe}e} + \frac{1}{E_{fluid}}\right] = \frac{gAdx}{a^2} \tag{5.11}$$

In the same way, if compressibility effects are neglected, the 2 viscoelastic resistances in parallel can be expressed as:

$$R_{equ} = \frac{1}{\frac{1}{R_{pipe}} + \frac{1}{R_{fluid}}} = \frac{1}{A\rho g dx} \cdot \frac{1}{\frac{D}{\mu_{pipe}e} + \frac{1}{\mu_{fluid}}} = \frac{\mu_{equ}}{A\rho g dx} \tag{5.12}$$

From the strict modelling point of view, a viscoelastic pipe is modelled by considering the equivalent scheme of figure 5.4 made of 2 Kelvin-Voigt models for both the pipe material and the fluid instead of the single capacitance of the elastic pipe model of table 5.1 (right). From the practical point of view, the determination of either the second viscosity of the fluid or the viscosity of the pipe material is very difficult to perform with good accuracy. However, experiments described by Haban *et al.* [41] have provided data for a pipe filled with water. In this case, the equivalent viscosity is determined rather than the fluid viscosity as in the experiment both viscosity contributions can not be dissociated. As a result, it is very convenient to use a model made only of one Kelvin-Voigt model of the whole pipe and accounting for both the fluid and the pipe material. In this model the capacitance is calculated according to equation 5.11 and the viscoelastic resistance R_{ve} is calculated according to equation 5.12. The resulting model is presented in figure 5.5.

5.1.2 Valve

A valve induces head losses in hydraulic systems which are function of the valve obturator position s. The head losses through a valve are given by:

$$H_v = \frac{K_v(s)}{2gA_{ref}^2} \cdot Q_i^2 \tag{5.13}$$

With K_v the valve head loss coefficient. Therefore the valve corresponds to a variable resistance function of the obturator position. The valve hydraulic resistance is given by:

$$R_v(s) = \frac{K_v(s)}{2gA_{ref}^2} \cdot |Q_i| \tag{5.14}$$

The valve equivalent scheme is presented in figure 5.6.

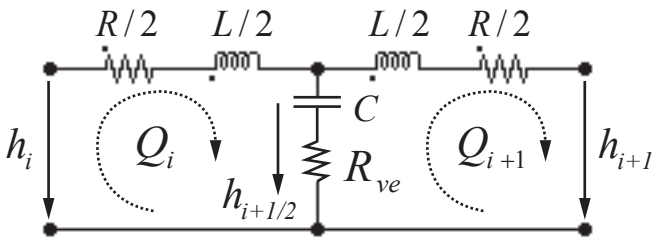

Figure 5.5: Equivalent scheme of a viscoelastic pipe of length dx.

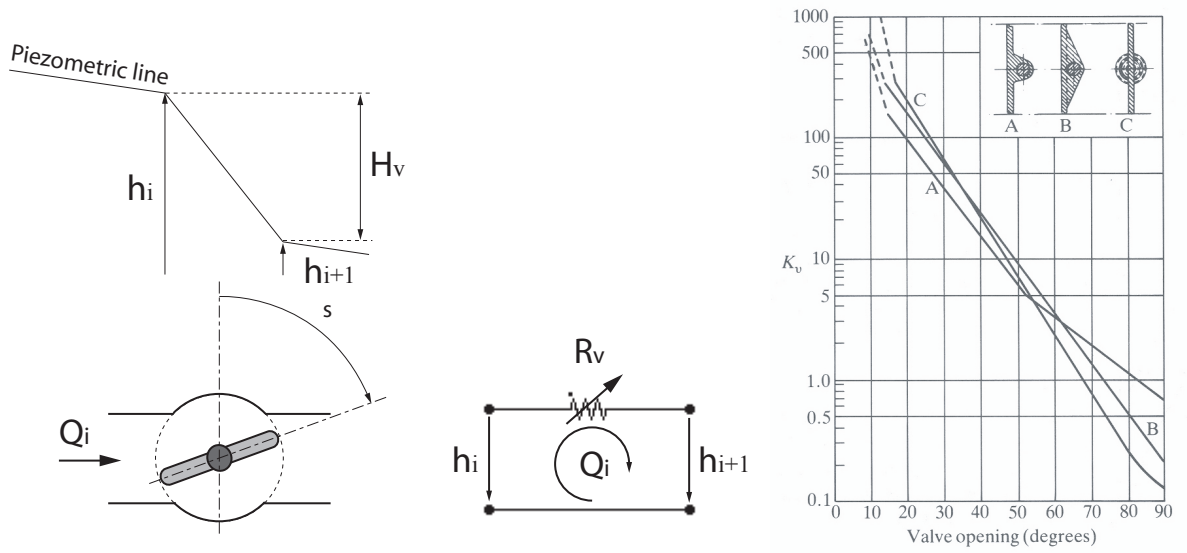

Figure 5.6: Valve modelling with the example of butterfly valve characteristic [68].

5.1.3 Surge Tank

The surge tank is a protection device against waterhammer effect behaving as a free surface for wave reflection but where the water level is function of the discharge time history. Surge tanks sometimes feature cross section being function on the elevation Z. The volume of the surge tank is therefore expressed as the integral of the cross section $A(Z)$ along the elevation Z and is given by:

$$V_{ST} = \int A(Z)dZ \tag{5.15}$$

The time derivative of the surge tank volume is:

$$\frac{dV_{ST}}{dt} = A(Z) \cdot \frac{dZ}{dt} \tag{5.16}$$

Noticing that the volume variation of the water in the surge tank is equivalent to the stored discharge $Q_c = dV_{ST}/dt$ and introducing the piezometric head h_c leads to:

$$A(Z) \cdot \frac{dh_c}{dt} = Qc \tag{5.17}$$

Equation 5.17 evidences the capacitive behavior of the surge tank whose capacitance is directly the surge tank cross section:

$$C_{ST} = A(Z) \tag{5.18}$$

The flow incoming and leaving the surge tank is subject to sudden cross section changes and therefore energetic losses. It is common to have a diaphragm at the surge tank inlet in order to increase the damping of water level oscillations. The head losses through the diaphragm or the sudden change of cross section are given by:

$$H_d = \frac{K_d}{2gA_{ref}^2} \cdot Q_c^2 \tag{5.19}$$

With K_d, the diaphragm head loss coefficient $[-]$. The corresponding hydraulic resistance is given by:

$$R_d(Q_c) = \frac{K_d(Q_c)}{2gA_{ref}^2} \cdot |Q_c| \tag{5.20}$$

The head at the T-junction H_{ST} is given by:

$$H_{ST} = h_c + R_d(Q_c) \cdot Q_c \tag{5.21}$$

It can be noticed that the diaphragm loss coefficient K_d is usually function of the discharge amplitude and direction: $K_d = K_d(Q_c)$. The equivalent scheme of the surge tank is made of a resistance and a capacitance in series as presented in figure 5.7. The discharge incoming into the surge tank Q_c is equal to the difference of the discharges at the T-junction and is given by:

$$Q_c = Q_i - Q_{i+1} \tag{5.22}$$

5.1.4 Surge Shaft

Surge shafts are surge tanks with small cross sections. If the surge tank inductance effects can be neglected as the inductance is inversely proportional to the cross section $L = l/(gA)$, it is not anymore the case for the surge shaft. The inductance related to the water inside the surge shaft is given by integrating the inductance along elevation axis Z and is given by:

$$L_{SS} = \int_{Z_{min}}^{h_c} \frac{dZ}{g \cdot A(Z)} = \frac{h_c - Z_{min}}{g \cdot \overline{A}} \tag{5.23}$$

The capacitance and resistance of the surge shaft have the same expression as that of the surge tank and are given by:

$$R_d(Q_c) = \frac{K_d(Q_c)}{2gA_{ref}^2} \cdot |Q_c| \quad \text{and} \quad C_{SS} = A(Z) \tag{5.24}$$

The head at the T-junction H_{SS} is then given by:

$$H_{SS} = h_c + R_d(Q_c) \cdot Q_c + L_{SS} \cdot \frac{dQ_c}{dt} \tag{5.25}$$

The resulting surge shaft equivalent scheme is presented in figure 5.8.

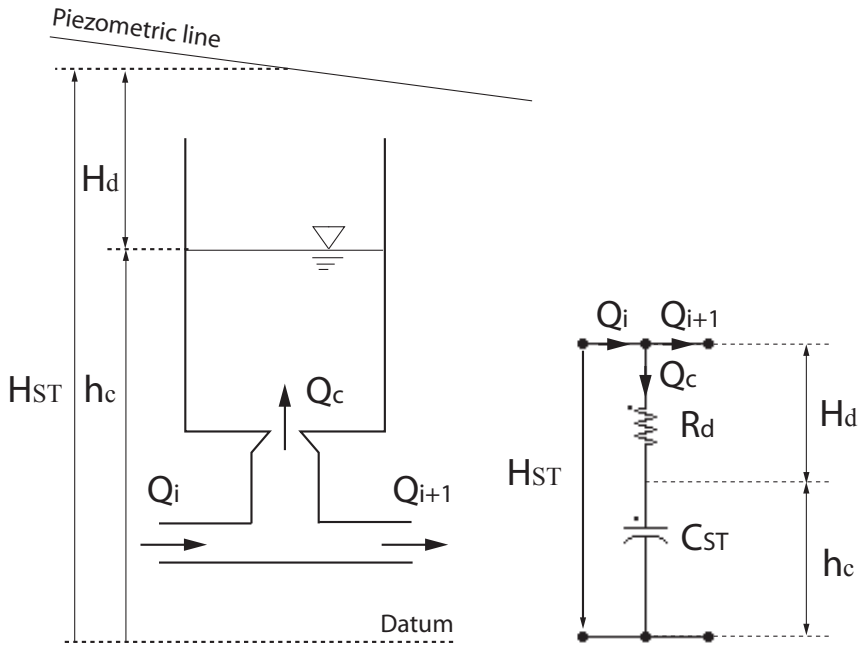

Figure 5.7: Surge tank model.

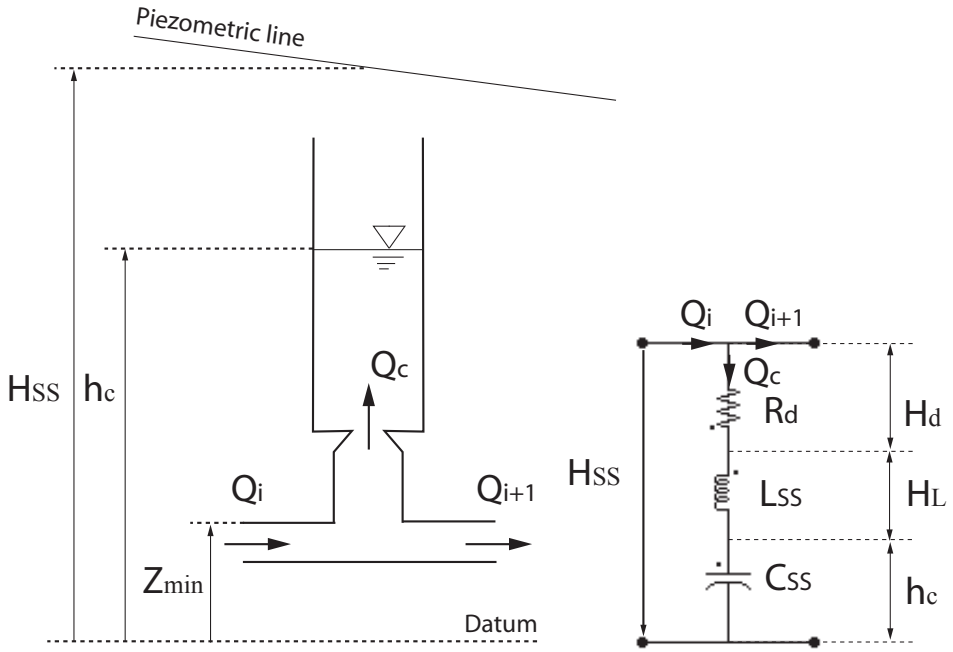

Figure 5.8: Surge shaft model.

5.1.5 Air Vessel

Air vessels are used for mitigating pressure fluctuations induced in hydraulic systems by pumps, vortex shedding, valves openning/closure, etc. The water level h_c changes in the vessel lead to capacitive behavior. The stored discharge Q_c and the cross section are linked as follows:

$$A(Z) \cdot \frac{dh_c}{dt} = Qc \tag{5.26}$$

The capacitance is given by:

$$C_g = A(Z) \tag{5.27}$$

The gas volume is varying due to water level changes. Assuming a polytropic transformation of the gas leads to:

$$h_g \cdot V_g^n = cste \tag{5.28}$$

The total derivative of equation 5.28 gives:

$$h_g \cdot n \cdot V_g^{n-1} \cdot d_g V + V_g^n \cdot dh_g = 0 \tag{5.29}$$

After rearrangement, and introducing the stored discharge Q_c yields to:

$$\frac{V_g}{h_g \cdot n} \cdot \frac{dh_g}{dt} = -\frac{dV_g}{dt} = Q_c \tag{5.30}$$

Equation 5.30 evidences the non-linear capacitive behavior of the gas volume for which the capacitance is given by:

$$C_{AV}(V_g, h_g) = \frac{V_g}{h_g \cdot n} \tag{5.31}$$

The head at the junction H_{AV} is then given by:

$$H_{AV} = h_c + h_g \tag{5.32}$$

The equivalent scheme of the air vessel is therefore made of 2 capacitances in series as presented in figure 5.8.

5.1.6 Cavitating Flow

The development of cavitation in fluid flows is known to be a source of instabilities for the whole hydraulic system. It was found that cavitation does not only represent a passive additional compliance to the flow [15] but can play a crucial role of self excitation source like of the famous POGO effect in propulsion systems of aerospace aircrafts [82]. The stability of such system was studied using an one-dimensional approach to model the cavitation development as a lumped elements. The volume of a cavitation development is function of the head and discharge, therefore the total derivative of the volume is given by:

$$V(Q,h)_{i+1} \Rightarrow dV = \frac{\partial V}{\partial h_{i+1}} \cdot dh_{i+1} + \frac{\partial V}{\partial Q_{i+1}} \cdot dQ_{i+1} \tag{5.33}$$

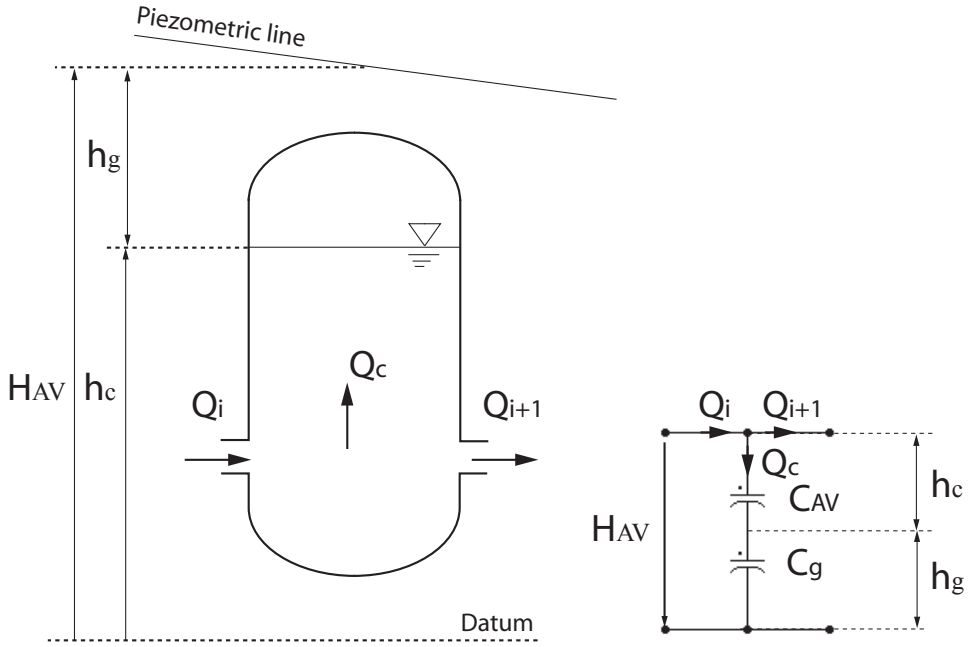

Figure 5.9: Air vessel model.

Time variation is given by:

$$\frac{dV}{dt} = \frac{\partial V}{\partial h_{i+1}} \cdot \frac{dh_{i+1}}{dt} + \frac{\partial V}{\partial Q_{i+1}} \cdot \frac{dQ_{i+1}}{dt} \tag{5.34}$$

Defining:

- the cavity compliance $C = -\frac{\partial V}{\partial h}$;
- the mass flow gain factor $\chi = -\frac{\partial V}{\partial Q_{i+1}}$.

yields to:

$$Q_i - Q_{i+1} = Q_c = C \cdot \frac{dh_{i+1}}{dt} + \chi \cdot \frac{dQ_{i+1}}{dt} \tag{5.35}$$

In addition, no losses or inertias effects are considered, and leads to:

$$h_i = h_{i+1} \tag{5.36}$$

Cavitation development can be modelled using equations 5.35 and 5.36. The resulting equivalent scheme of the cavitation development is made of 1 capacitance as presented in figure 5.10. The representation of the mass flow gain factor is difficult as it is kind of mutual inductance effect and it is represented in figure 5.10 only by the χ value referring to the discharge Q_{i+1}

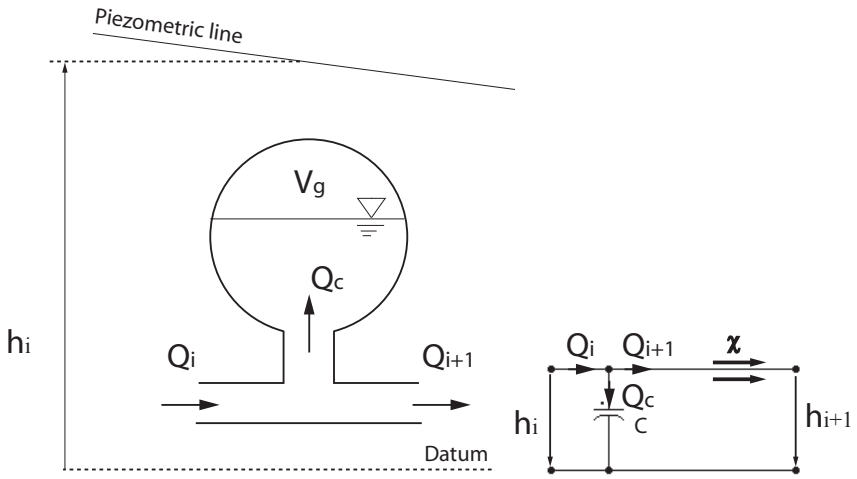

Figure 5.10: Cavitating flow model.

5.2 Quasi Static Modelling of Hydraulic Machines

5.2.1 General

There is 3 different types of hydraulic machines that are commonly used in the context of hydroelectric power production: (i) the Francis turbine, or pump-turbine, (ii) the Pelton turbine and (iii) the Kaplan turbine.

For safety purposes, the transient behavior of the entire hydraulic system comprising the turbine must be undertaken with appropriate turbine models. However, during the exploitation, these hydraulic machines are subject to off design operations where 3D complex flow structures such as flow separations, secondary flows, reverse flows, vortices, cavitation development, arise. Mathematical modelling of such flows leads to Computational Fluid Dynamic codes, which are nowadays far from being able to provide the transient turbine parameters at a reasonable computational time with sufficient accuracy for all the flow regimes experienced during transients. Therefore, experimental data are required for the modelling of the dynamic behavior of turbines and pump-turbines. It is assumed that the transient behavior of the hydraulic machines can be accurately simulated by considering that the machines are experiencing a succession of different steady state operating points and therefore, can be modelled using the static characteristic of the machine [58]. These models are called "quasi-static" models.

An operating point of a hydraulic machine is characterized by 5 quantities: the specific energy E, the discharge Q, the rotational speed N, the torque T, and the guide vane opening y. Therefore, the graphical representation of a turbine characteristic requires the elimination of one of these quantities by the use of the hydraulic machines similitude laws. For efficiency purposes, where the rotational speed can be considered to be constant, it is convenient to use the dimensionless representation with φ , ψ and τ. For transients analysis, it is more convenient to use dimensional factors where the specific energy E is eliminated. These factors are given by:

$$N_{11} = \frac{N \cdot D_{ref}}{\sqrt{(E/g)}} \quad ; \quad Q_{11} = \frac{Q}{D_{ref}^2 \cdot \sqrt{(E/g)}} \quad ; \quad T_{11} = \frac{T}{D_{ref}^3 \cdot E/g} \tag{5.37}$$

The modelling of hydraulic turbines based on the quasi-static approach is described below.

5.2.2 Francis Pump-Turbine

Francis pump-turbines are reaction turbines, *i.e.* they convert both kinetic and potential energy of the fluid into mechanical work. The Francis turbine features fixed blades and therefore the discharge through the turbine is controlled by the distributor. Figure 5.11 presents a vertical cutting plan of a Francis turbine.

Figure 5.12 presents a 4 quadrants characteristics of a Francis pump-turbine having a specific speed of $\nu = 0.217$. The discharge and torque factors are represented as a function of the speed factor with the guide vane opening y as parameter; all values are rated by the best efficiency point (BEP) value.

Some of the curves $Q_{11} = Q_{11}(N_{11})$ of the pump-turbine characteristics of figure 5.12 exhibit a typical pump-turbine "S" shape between the 1^{st} and the 4^{th} quadrants leading to numerical troubles for the interpolation of the Q_{11} values in the surface characteristics

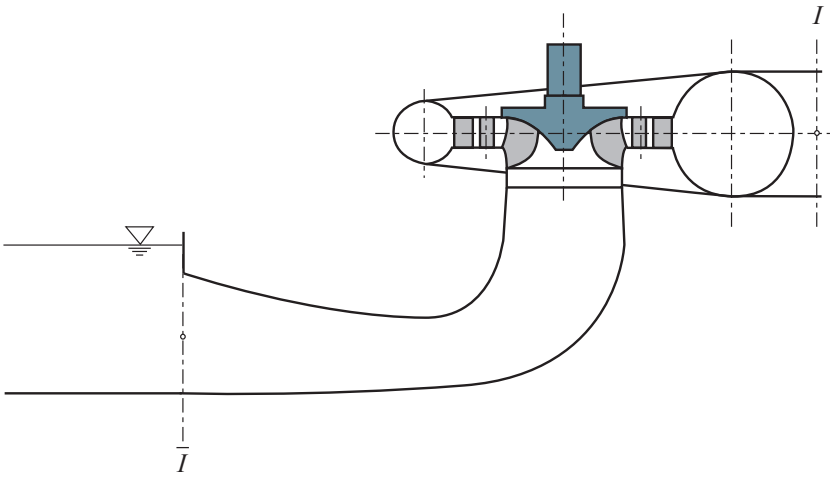

Figure 5.11: Francis turbine cutting plan.

as illustrated in figure 5.13. This problem has been successfully solved by Marchal *et al.* [65] who used a polar representation of the turbine characteristics. The polar coordinates are defined in the plane $N_{11} - Q_{11}$. Accordingly the polar angle θ is given by:

$$\theta = \text{atan}\left(\frac{Q_{11}/Q_{11BEP}}{N_{11}/N_{11BEP}}\right) \tag{5.38}$$

After simplification:

$$\theta = \text{atan}\left(\frac{Q/Q_{BEP}}{N/N_{BEP}}\right) \tag{5.39}$$

The radial coordinate of the polar representation is defined as:

$$r(\theta)^2 = \left(Q_{11}/Q_{11BEP}\right)^2 + \left(N_{11}/N_{11BEP}\right)^2 \tag{5.40}$$

Lets introduce the new parameter $W_H(\theta)$:

$$W_H(\theta) = \frac{1}{r(\theta)^2} \tag{5.41}$$

After rearranging the terms:

$$W_H(\theta) = \frac{H/H_{BEP}}{\left(Q/Q_{BEP}\right)^2 + \left(N/N_{BEP}\right)^2} \tag{5.42}$$

A new parameter $W_B(\theta)$ is introduced for the torque and is given by:

$$W_B(\theta) = W_H(\theta) \cdot \frac{T_{11}}{T_{11BEP}} = \frac{T/T_{BEP}}{\left(Q/Q_{BEP}\right)^2 + \left(N/N_{BEP}\right)} \tag{5.43}$$

The polar representation of the turbine characteristics of figure 5.12 is presented in figure 5.14. This representation has the advantage of preserving the similitude law. However, numerical troubles appears for closed guide vanes where there is no discharge and

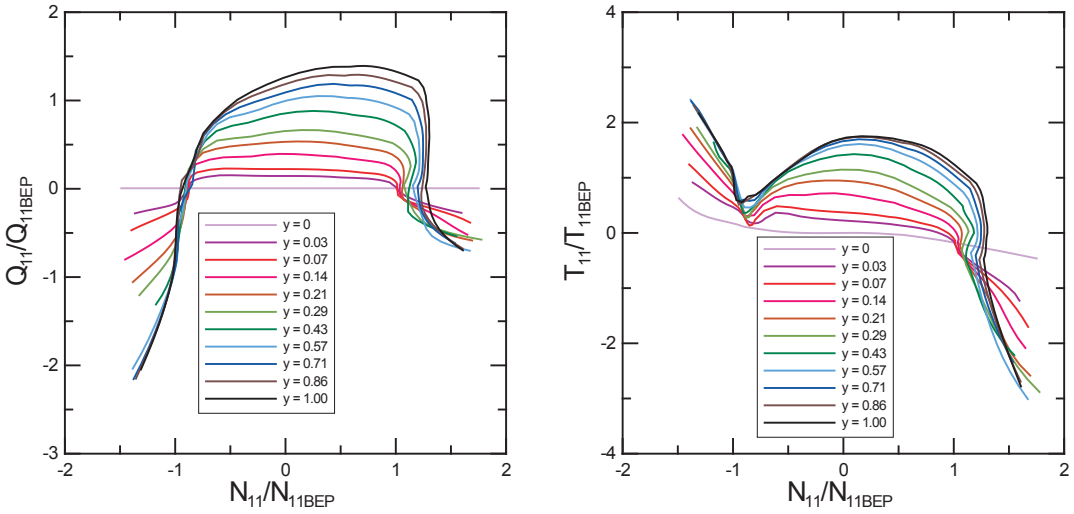

Figure 5.12: 4 quadrants characteristics of a turbine with specific speed $\nu = 0.217$.

therefore the abscissa θ is equal either to 0 or to π. This problem can be overcome by considering small leakage discharge for closed guide vanes.

From the modelling point of view, the turbine behaves essentially as a pressure source converting hydraulic energy into mechanical work. Inertia effects of the water in the turbine can be taken into account through the equivalent inductance of the turbine that can be determined by a curvilinear integration from turbine inlet I to turbine outlet $\overline{I}$ as follows:

$$L_t = \int_I^{\overline{I}} \frac{dx}{g \cdot A(x)} = \frac{l_{equ}}{g \cdot \overline{A}} \tag{5.44}$$

The full closure of the guide vanes of the turbine must ensure no discharge through the turbine. This can be only achieved, from the simulation point of view, with a resistance. This resistance is effective only for small discharge, below 5% of the nominal value. The resulting equivalent scheme of the Francis pump-turbine is made of an inductance, a resistance and a pressure source in series as presented in figure 5.15. The pressure source of the model is directly driven from the turbine characteristic $W_H(y, \theta(Q, N))$ function of the guide vane opening y, the rotational speed N and the discharge Q. The connection with the mechanical inertias in rotations is achieved through the momentum equation applied to the rotational inertias and given by:

$$J \cdot \frac{d\omega}{dt} = \sum T_{ext} = T_{turb} - T_{elect} \tag{5.45}$$

Where:

- J: total inertia of the rotating parts $[kgm^2]$
- ω: rotational pulsation $[rd/s]$
- T_{turb}: mechanical torque of the turbine $[Nm]$

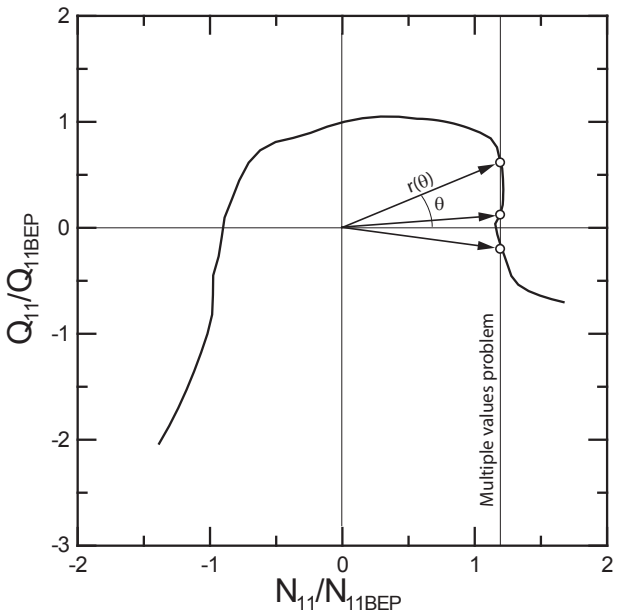

Figure 5.13: Multiple value problem due to "S" shape of the characteristics and definition of the polar representation.

- T_{elect}: electromagnetic torque of the generator $[Nm]$

The mechanical torque of the pump-turbine is obtained from the torque characteristic $W_B(y, \theta(Q, N))$ also function of the guide vane opening y, the rotational speed N and the discharge Q.

It is possible to improve the model of the turbine by considering the dynamic behavior of the spiral case and of the diffuser of the turbine that can be both modelled as straight pipes. Doing so, the compressibility and inertias effects of the spiral case and diffuser are also taken into account. Such model has been successfully validated by Bolleter in the case of a pump [13]. Such an approach is suitable for transients purposes. However, the modelling of more complex phenomena occurring in the hydraulic machine itself requires even more detailed modelling.

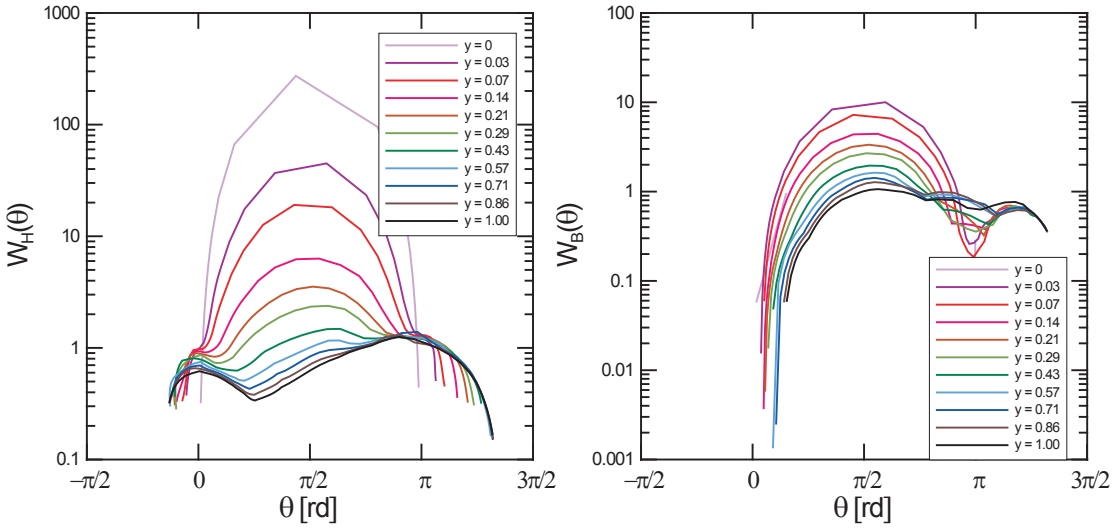

Figure 5.14: Polar representation of the pump-turbine characteristics of figure 5.12.

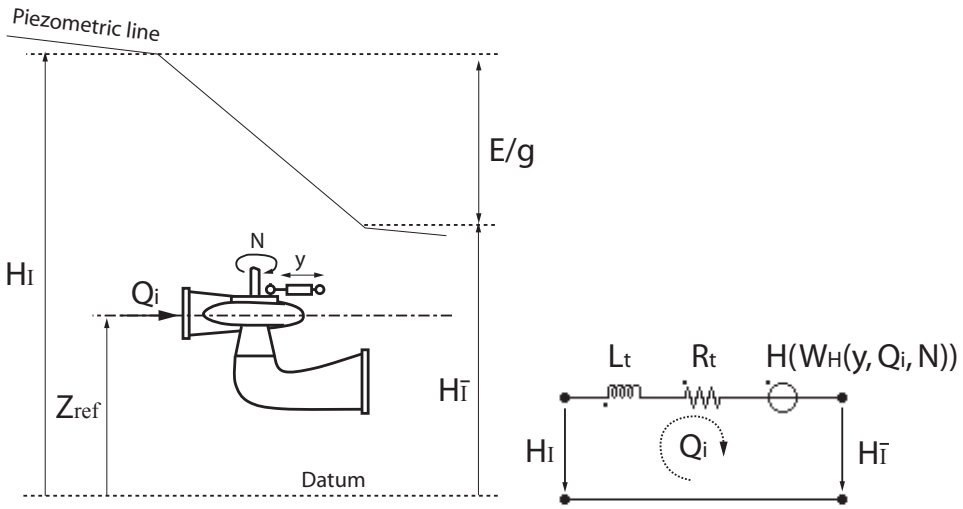

Figure 5.15: Francis turbine model.

5.2.3 Pelton Turbine

Single Injector Modelling

Pelton turbines are impulse turbines; *i.e.* the conversion of the kinetic energy of the flow into mechanical work is performed at the atmospheric pressure. The discharge of each injector is controlled by a nozzle leading to a free water jet. The jet interacts with the turbine buckets deviating the jet so that the outflow has almost no kinetic energy.

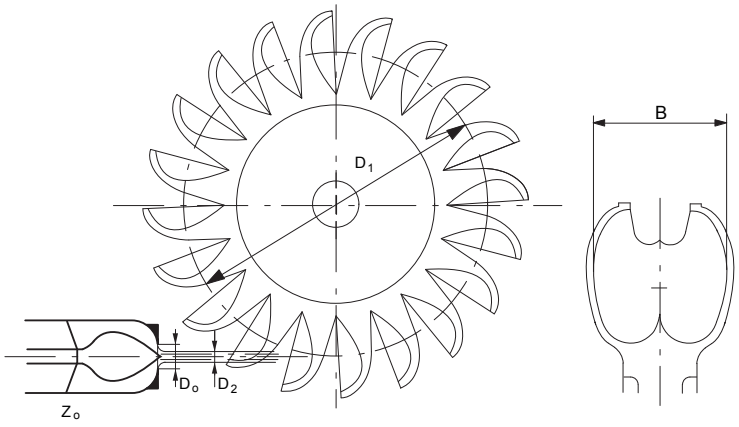

Figure 5.16: Pelton turbine.

The Pelton turbine is modelled by N_{inj} times a single injector turbine characteristic. As a result, the Pelton turbine is viewed from the hydraulic circuit only as N_{inj} valves in parallels. The equivalent circuit modelling the Pelton turbine corresponds to an equivalent resistance of all injectors single resistance, as illustrated in figure 5.17:

$$R_t = \frac{1}{\sum_{i=1}^{N_{inj}} \frac{1}{R_{inj_i}}} \tag{5.46}$$

The single injector resistance is calculated from the characteristic of the turbine $Q_{11} = Q_{11}(y_{inj})$, see figure 5.18, and is given by:

$$R_{inj} = \frac{|Q_{inj}|}{Q_{11}^2(y_{inj}) \cdot D_{ref}^4} \tag{5.47}$$

The mechanical torque of the machine is calculated as the sum of the contribution of the torque of each single injectors as follows:

$$T = K_t \cdot \sum_{i=1}^{N_{inj}} T_{11}(N_{11}, y_{inj_i}) \cdot D_{ref}^3 \cdot H \tag{5.48}$$

Where K_t is a torque coefficient that accounts for the unsteadiness of the torque during operation.

This modelling, neglects both the influence on the efficiency of the multi-injectors operation and the dynamic behavior of the piping of the flow repartitor. However, with this

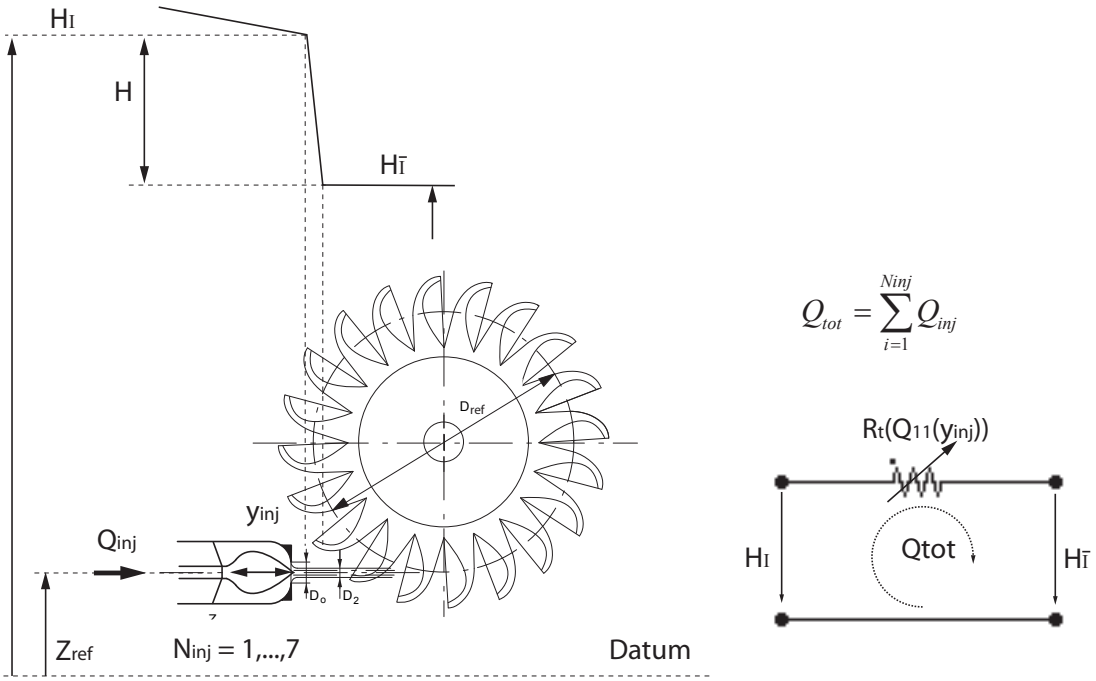

Figure 5.17: Pelton turbine model.

model, injectors can be put in operation or shut off using the same turbine characteristic. As the main purpose of such model is to perform transient simulations and not performing energy production optimization, the single injector model is the most suitable.

Deflector Modelling

Pelton installations usually feature very long penstocks. As a consequence, the piping critical valve closure time are very long and usually in contradiction with flywheel time constants of the rotating parts. Specific protection devices have been developed, consisting of deflectors cutting or deviating the jet between the injector and the turbine runner, see figure 5.19. Such system can be activated within very short time, $1-3$ seconds, and inducing a quick drop to zero of the mechanical torque, providing time for a slow closure of the injectors in order to minimize the waterhammer effects in the piping.

As it exists several different types of deflectors, it is suitable to use a general method for its modelling allowing to take into account any kind of deflectors. Therefore, a deflector coefficient is introduced and is given by the ratio between the discharge that effectively reaches the turbine and the discharge of the injector and is given for the i^{th} injector by:

$$K_{def\_i} = \frac{Q_{runner\_i}}{Q_{injector\_i}} \tag{5.49}$$

An "equivalent" nozzle stroke $y_{def}(t)$ corresponding to the discharge of the deflector times this deflector coefficient is determined from the nozzle characteristic $y(Q_{11})$. Finally the torque of the turbine is determined not from the nozzle position but from the equivalent nozzle position y_{def}. In this modelling the deflector function K_{def} has to be known. The algorithm for the consideration of the deflector is illustrated in figure 5.20.

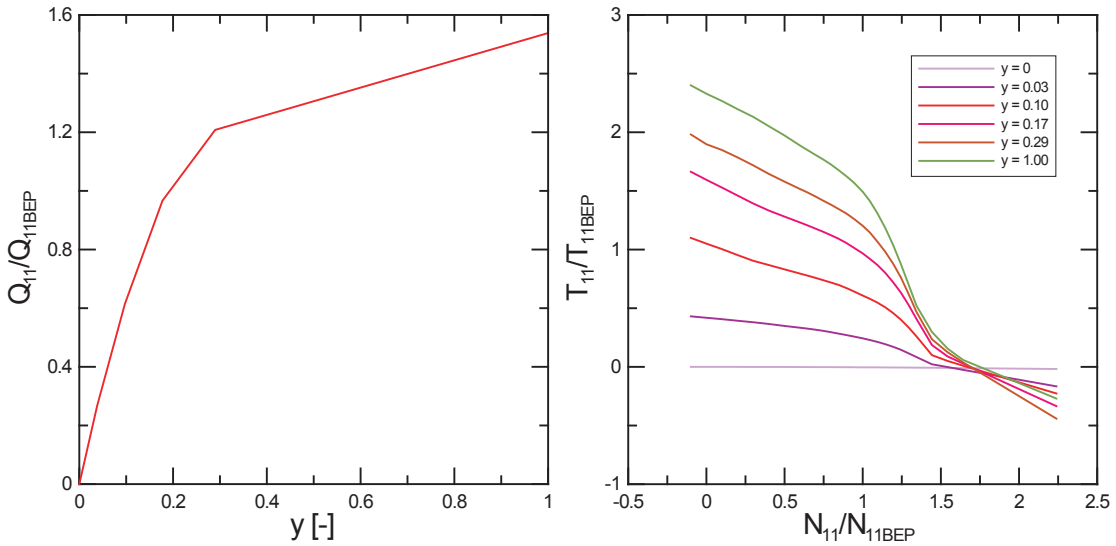

Figure 5.18: Single injector Pelton turbine characteristic.

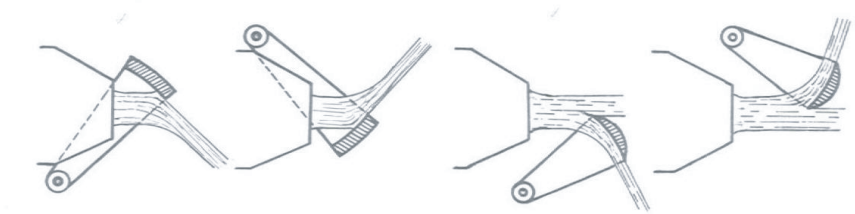

Figure 5.19: Different types of deflectors, deviating jet (left) and cutting jet (right) [81].

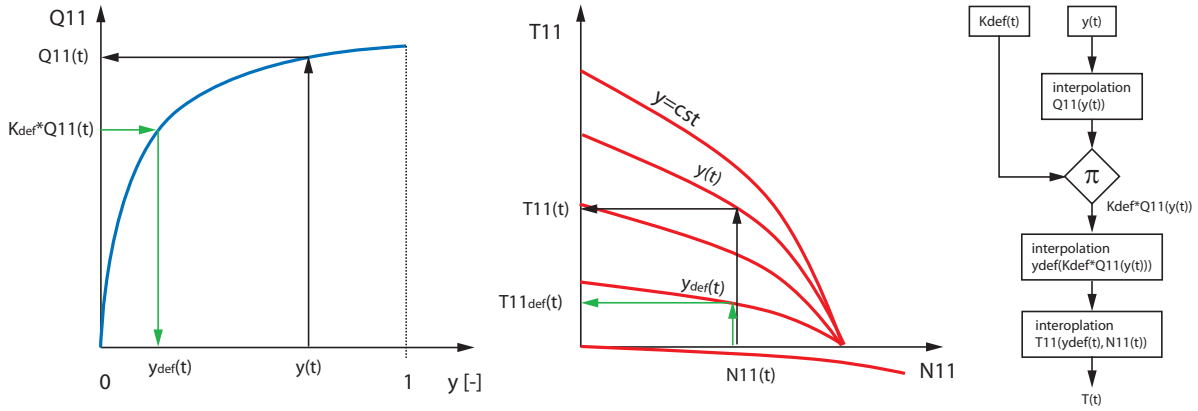

Figure 5.20: Consideration of the deflector in the torque calculation.

5.2.4 Kaplan Turbine

Kaplan turbines are reaction turbines, converting both kinetic and potential energy into mechanical work. Because Kaplan turbines are subject to high relative variations of the available energy $\Delta E/E$, they feature a double control system comprising the distributor and mobile blades in order to ensure high efficiency on the whole operating range, see figure 5.21. As a consequence, the characteristics of the Kaplan turbine has an extra parameter, compared to Francis turbines, *i.e.* the blade pitch angle β. Thus, the turbine characteristics is made of a family of characteristics defined for different blade angles. Figure 5.23 presents 2 characteristics for 2 different blade angles.

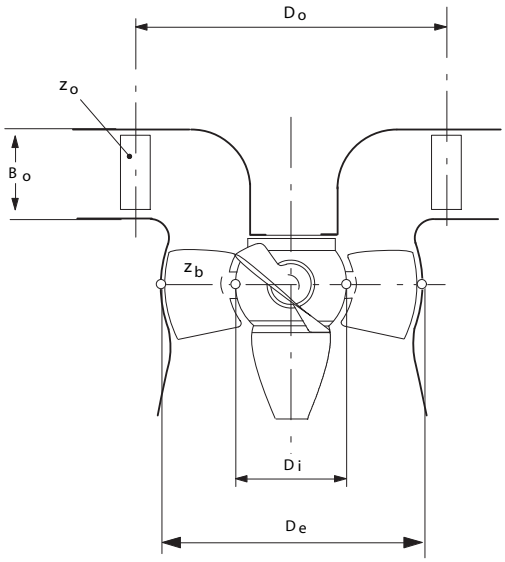

Figure 5.21: Kaplan turbine.

The model of the Kaplan turbine is also based on the polar representation of Suter, as for the Francis turbine model, but the $W_H(\theta, \beta)$ and $W_B(\theta, \beta)$ values are interpolated linearly between 2 blades angles as illustrated in figure 5.23 [44]. The linear interpolation is given by:

$$W_{H,B}(\theta, \beta) = \frac{W_{H,B}(\theta, \beta_2) - W_{H,B}(\theta, \beta_1)}{\beta_2 - \beta_1} \cdot (\beta - \beta_1) \tag{5.50}$$

Linear interpolation is preferred to higher order interpolation as it requires only 2 values for the calculations of the interpolated value, and therefore overlapping of only 2 characteristics is necessary. Indeed, experimental data are not always available on the same range for all tested blade angles, especially in the polar reference frame.

The equivalent scheme of the Kaplan turbine is identical to the Francis turbine model except the fact that the head of the turbine is also function of the blade angle β. Figure 5.24 presents the equivalent model of the Kaplan turbine made of an inductance, a resistance, and a source.

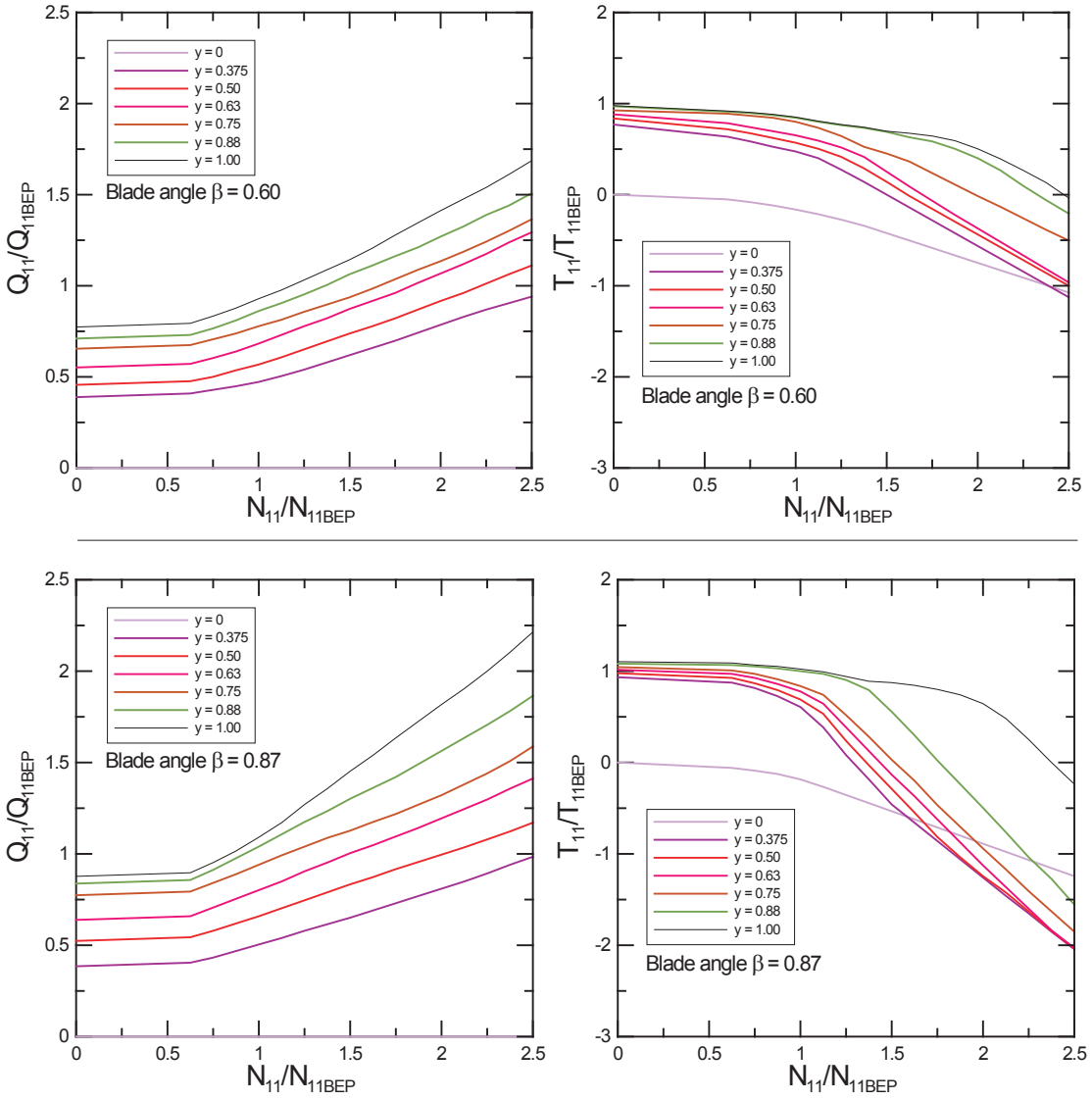

Figure 5.22: Kaplan turbine characteristic for 2 blades angles; $\beta = 0.60$ (top) and $\beta = 0.87$ (bottom).

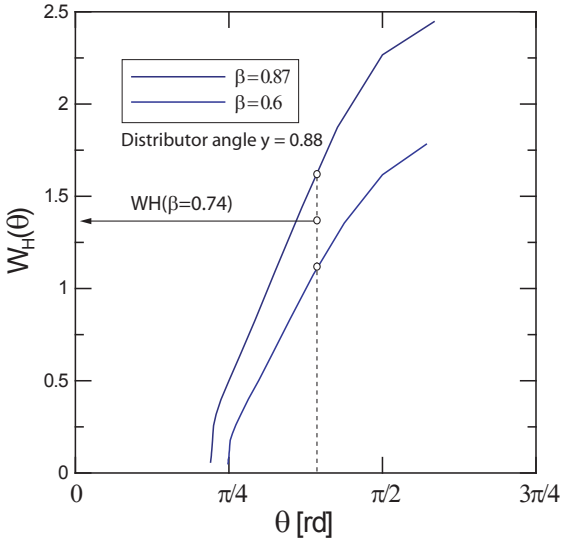

Figure 5.23: Linear interpolation of W_H between 2 different blade angles β for given guide vane opening y.

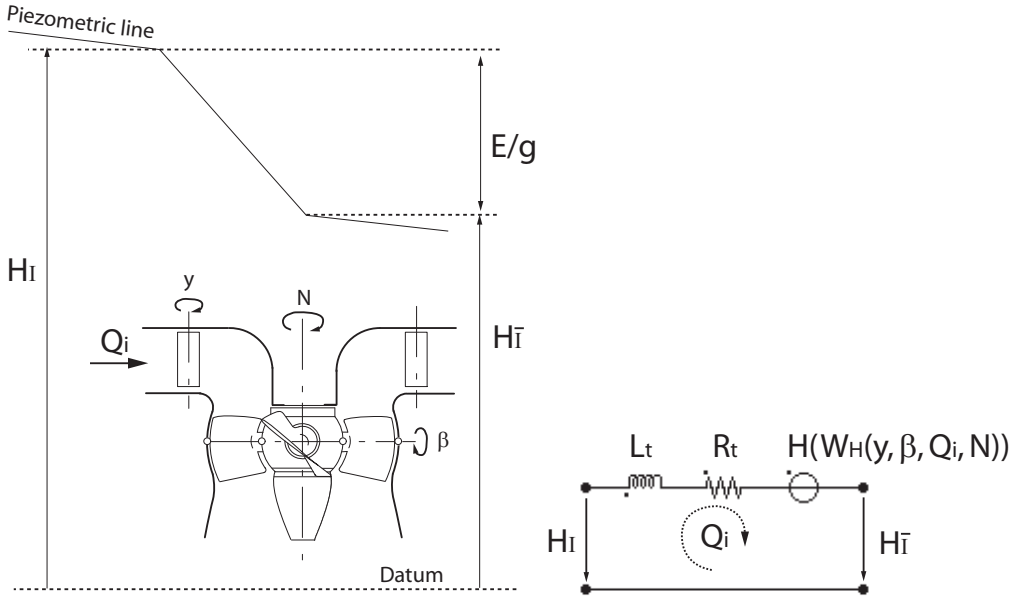

Figure 5.24: Kaplan turbine equivalent scheme.

5.3 Hydraulic Models Implementation in SIMSEN

5.3.1 General

Once the models of the main hydraulic components constituting the hydroelectric power plants are established, it is important to implement them in a software enabling a fast modelling of the system, robust and efficient time domain integration and results analysis in order to perform systematic analysis and optimization of the system. The Laboratory of Electrical Machines -LME- of the EPFL has developed a simulation software for the analysis of electrical power networks and adjustable speed drives called SIMSEN [83]. This software enables the time domain simulation of the dynamic behavior of an electrical installation featuring an arbitrary topology including the electrical machines, the mechanical inertias and the control devices.

The modelling of the hydraulic components with electrical equivalents offers the possibility to implement them in SIMSEN in an easy way as it is based on the same syntax and conventions. Thus, all the hydraulic components models described above have been implemented in SIMSEN with the following advantages:

- treating systems with arbitrary topology;
- modelling hydroelectric systems comprising hydraulic circuit, electrical installations, mechanical inertias and control devices;
- ensuring considering properly the interaction between all components of the installation as there is only one set of differential equations to be solved within the same integration time step.

However, there is a drawback resulting from the last point. Electrical systems feature time constants of about $\tau_{elec} = 0.001s$ while hydraulic system features time constants of about $\tau = 0.1s$, *i.e.* 100 times larger.

5.3.2 The Simulation Software SIMSEN

Structure of SIMSEN

The SIMSEN software enables to set up the simulation model of a system according to its own topology using electrical, mechanical and control modules through a Graphical User Interface (GUI). Once all the parameters of each components are setup, the software builds up a global system matrix using Kirchhoff's laws of the following form:

$$[A] \cdot \frac{d\overrightarrow{x}}{dt} + [B] \cdot \overrightarrow{x} = \overrightarrow{C} \tag{5.51}$$

With:

- $[A]$, $[B]$: system global matrix;
- $\overrightarrow{x}$: state vector;
- $\overrightarrow{C}$: boundary conditions vector.

Equation system 5.51 is solved in SIMSEN with the procedure of Runge-Kutta 4^{th} order taking into account all the non-linearities of the system as every parameter of each components can be parameterized using external functions. Finally, all the simulation results are stored in text files with vectors structure.

Electrotechnic Modules

SIMSEN offers a wide range of electrotechnic modules comprising:

- **electrical machines:** synchronous machine, induction, permanent magnet and DC motors; rotor,
- **mechanical inertias:** rotor, stator, shaft stiffness and damping, clutch, gear-box;
- **three-phase elements:** voltage supply, transmission lines, circuit breaker, transformers, loads;
- **semi-conductors:** diode, thyristor, thyristor GTO, IGTB;
- **single-phase elements:** voltage supply, resistance, inductance, capacitance, circuit breaker, linked inductor, transformer;
- **analog functions:** program, s-transfer function, regulators, points/grid functions, external DLL;
- **digital functions:** limiter, pulse, generator, z-transfer function, hysteresis, sample.

The above list is non-exhaustive. These modules have been successfully validated by comparison with experimental data [84] as illustrated by the example presented in figure 5.25. This example is the simulation of a load acceptance of an asynchronous machine with a frequency converter of the Three-level Voltage Source Inverter (VSI) type. Figure 5.26 presents the comparison of the simulated and experimental results witnessing the good agreement.

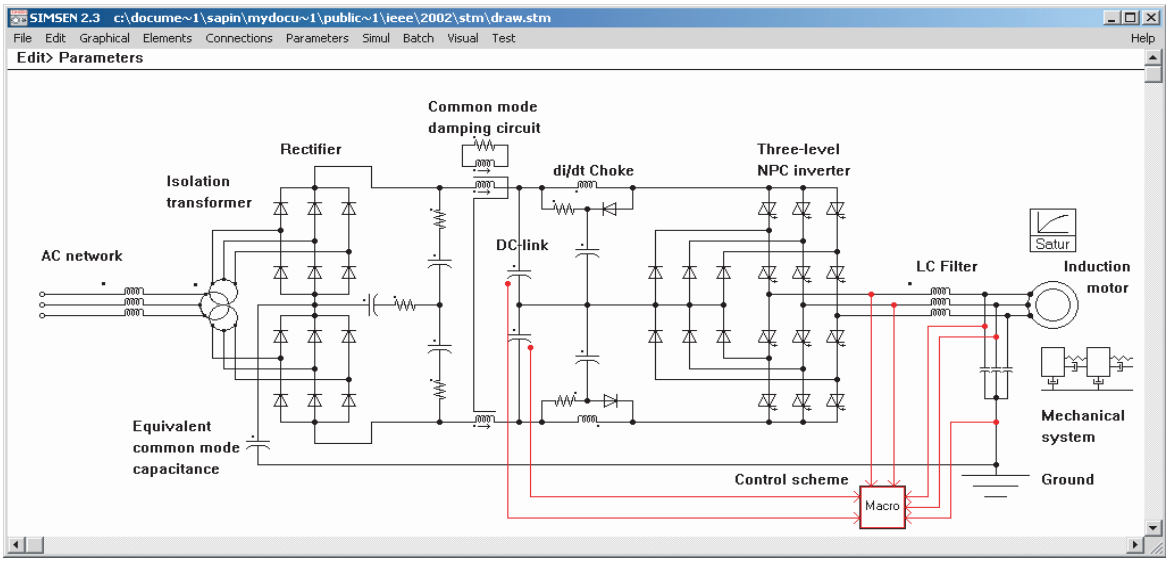

Figure 5.25: Three-level Voltage Source Inverter (VSI) simulation example.

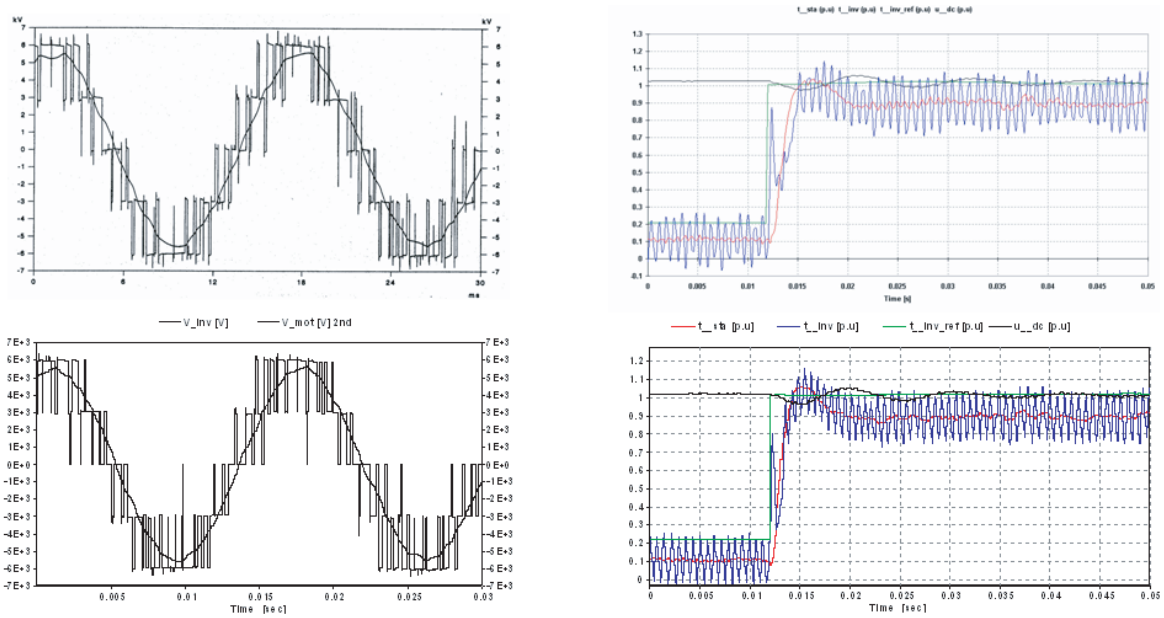

Figure 5.26: Comparison between simulation (bottom) and measurements (top) of voltages (left) and torques (right) resulting from load acceptance of the system of figure 5.25 [84].

Synchronous Machine Modelling

Synchronous machines are playing an important role in hydropower plants. Hydrogenerators features salient poles with laminated rotor (see figure 5.27 (a),) with strong geometric anisotropy and therefore their modelling is decomposed in 2 axis, the direct axis d and the quadrature axis q; as illustrated in figure 5.27 (b). Using Park's transformation, it is possible to represent the synchronous machine as 2 equivalent schemes in the direct and quadrature axis [17], see 5.27 (c). The equivalent scheme of the synchronous machine leads to a set of 5 first order differential equations with 5 currents as state variables and 5 voltages as boundary conditions and the rotor position as parameter. Introducing the momentum equation applied to the rotating inertias including the electromagnetic torque obtained from the current and flux, gives a system of 7 equations and 7 unknowns. The equivalent scheme parameters, state variables and boundary conditions of this set of equations are given in table 5.2 defined according to the scheme of figure 5.27 (c).

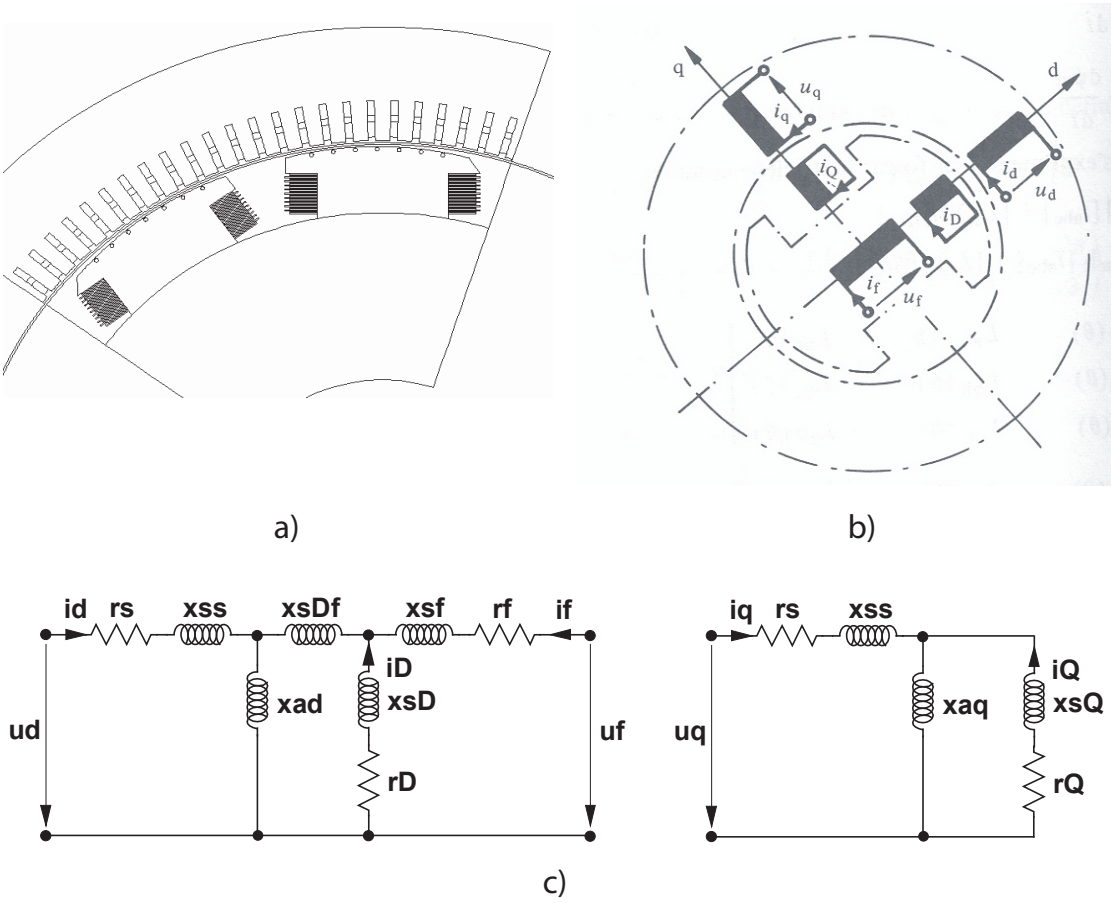

Figure 5.27: Modelling of a synchronous machine with decomposition in the direct and quadrature axis; a) geometry of salient pole [78], b) direct and quadrature axis [19], c) equivalent schemes [17].

Table 5.2: Synchronous machine equivalent scheme parameters, state variables and boundary conditions.

Parameters	**Units**	**Description**
r_s, X_{xs}	[p.u.]	statoric resistance and leakage inductance
X_{ad}	[p.u.]	inductance of principal field in axis d
X_{sDf}	[p.u.]	exclusive mutual inductance between dampers of d axis and excitation
r_f, X_{sf}	[p.u.]	excitation resistance and leakage inductance
r_D, X_{sD}	[p.u.]	damper circuit resistance and leakage inductance in axis d
X_{aq}	[p.u.]	principal field inductance in axis q
r_{Q1}, X_{sQ1}	[p.u.]	resistance and leakage inductance of the damper circuit in axis q
p	[-]	number of pair poles
State variables	**Units**	**Description**
i_d,i_q	[p.u.]	statoric phase in axis d and q
i_D	[p.u.]	damper circuit current in axis d
i_f	[p.u.]	excitation current
i_{Q1}	[p.u.]	damper circuit current in axis q
θ_m	[rd]	angular position of the rotor
$\omega_m = d\theta_m/dt$	[rd]	angular pulsation of the rotor
Boundary conditions	**Units**	**Description**
u_d,u_q	[p.u.]	statoric voltages in axis d and q
$u_D \equiv 0$	[p.u.]	damper circuit voltage in axis d
u_f	[p.u.]	excitation voltage
$u_Q \equiv 0$	[p.u.]	damper circuit voltage in axis q

Initial Conditions Determinations

The determination of the initial conditions of an electrical simulation should be achieved according to the boundary conditions prior to a time domain simulation. This initial conditions problem is solved for electrical systems in SIMSEN by performing a load flow calculation where 2 situations can be treated:

- the loads parameters are specified and the excitation voltage of the synchronous machines are adapted to match the demand of active and reactive power, see figure 5.28 (top);

- the active and reactive power of the synchronous machines are specified and the loads parameters are adapted to match the production, see figure 5.28 (bottom).

In both cases, the load flow calculation is achieved in SIMSEN using Newton-Raphson's algorithm.

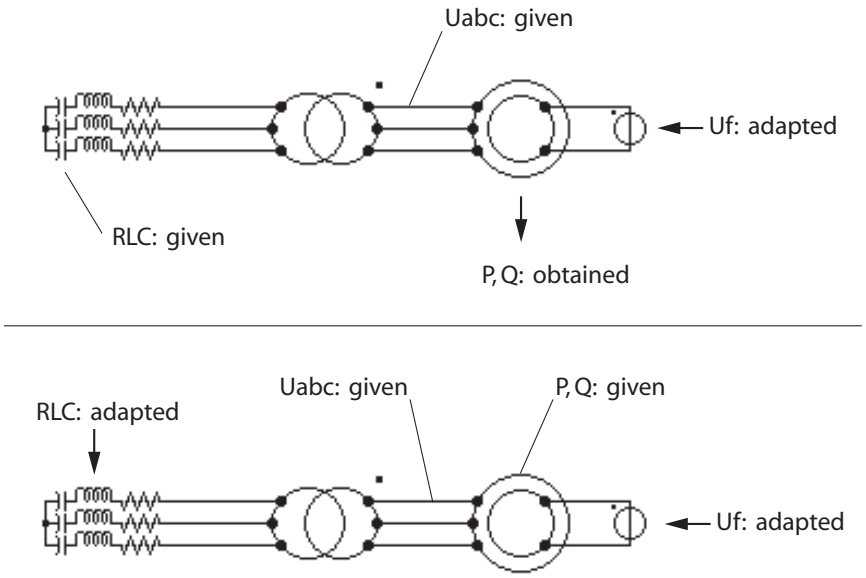

Figure 5.28: Load flow scenarios according to available data; excitation voltage adapted to the demand (top) or load parameters adapted to the production (bottom).

5.3.3 Extension to Hydraulic Systems: SIMSEN-Hydro

Hydraulic Modules

A hydraulic extension comprising all the hydraulic models presented above and called SIMSEN-Hydro, has been implemented in SIMSEN. These hydraulic models are summarized in figure 5.29 for the hydraulic circuit components and in figure 5.31 for the hydraulic turbines.

Turbine Characteristics Interpolation

The modelling of the turbines is based on their characteristics curves. Therefore it is necessary to perform interpolation of the $W_{H,B}$ values for the given abscissa y and θ. The interpolation method implemented in SIMSEN-Hydro is based on a Delaunay triangulation in the plane $y - \theta$. To each vertex of the triangle is associated the corresponding $W_{H,B}$ values. Then, a "planar" interpolation is performed from the equation of the plan in three dimensions. This method ensures the continuity of order 0 on the whole turbine characteristic. The representation of the $2D$ triangulation and the resulting 3D surface of the pump-turbine characteristic of figure 5.14 are presented in figure 5.31.

Initial Conditions Determination

Similarly to electrical systems, initial conditions of a hydraulic system simulation should be determined according to the system boundary conditions prior to perform time domain simulation. In SIMSEN-Hydro, the initial condition procedure is not achieved by Newton-Raphson algorithm but by performing a "fast" simulation of the transient behavior of the system leading to steady state conditions. However, to speed up the stabilization of the

Description	Scheme	Equivalent scheme
Elastic pipe	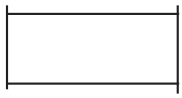	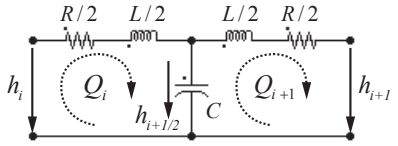
Viscoelastic pipe		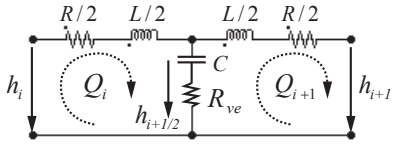
Valve	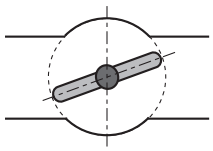	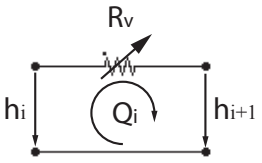
Surge tank	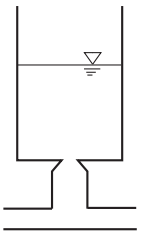	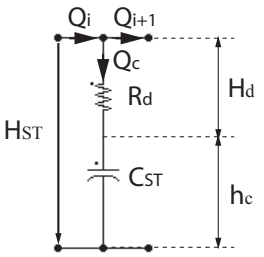
Surge shaft	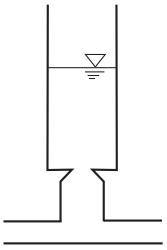	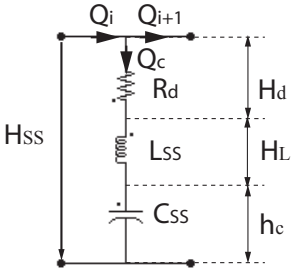
Air vessel	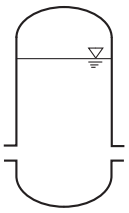	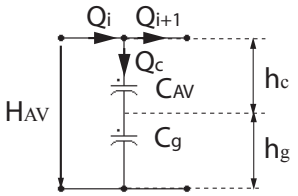
Cavitating flow	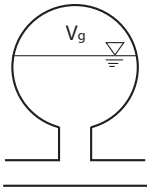	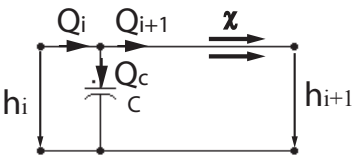

Figure 5.29: Summary of the models of the hydraulic circuit components.

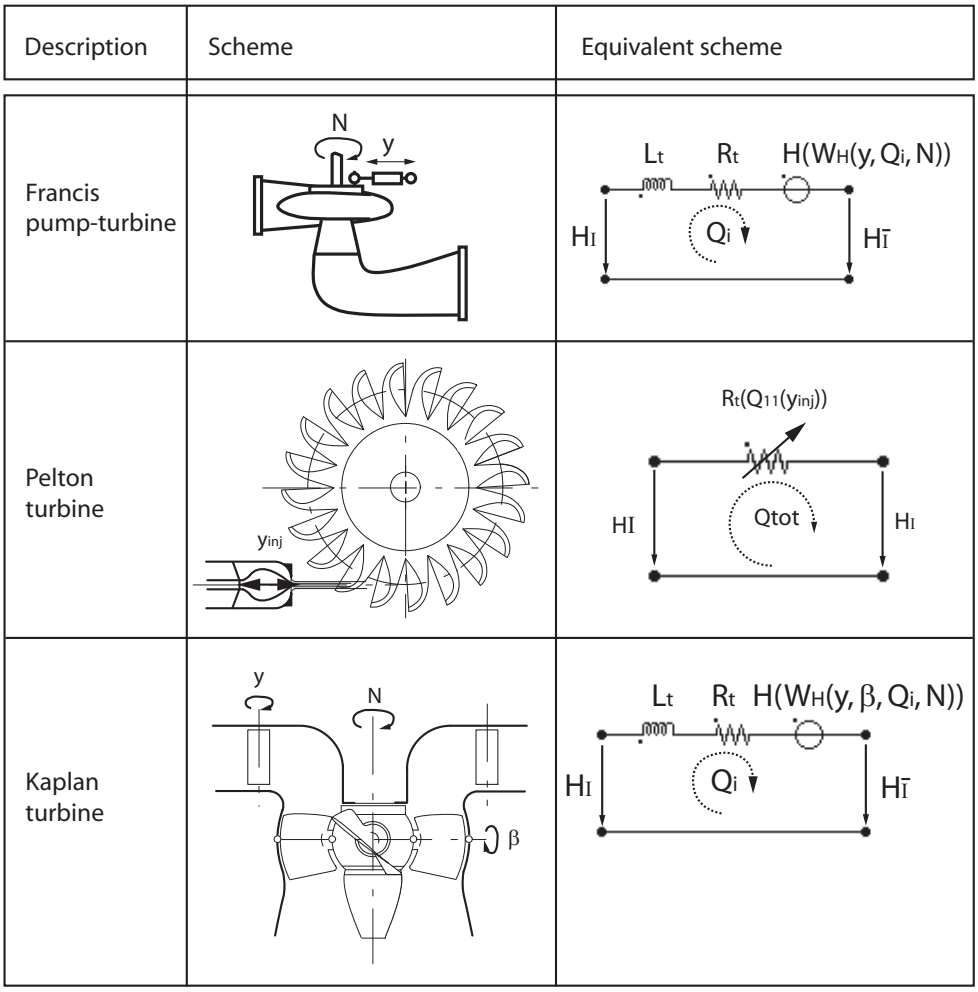

Figure 5.30: Summary of the models of the hydraulic turbines.

system, the system parameters are optimized. Basically, 3 optimizations are undertaken:

- an additional damping is introduced;
- large capacitance leading to high period oscillations are reduced;
- turbine characteristics are bounded in order to avoid errors due the search of a point outside the turbine characteristic.

The additional damping is introduced by setting the viscoelastic resistance of the pipes according to the system limit time constants. The time constant of the RC elements in series in the T-branch of the pipe model is given by:

$$\tau_{RC} = R_{ve} \cdot C \tag{5.52}$$

The value of the viscoelastic resistance can therefore be determined with respect to the integration time step to avoid numerical integration troubles by setting the integration

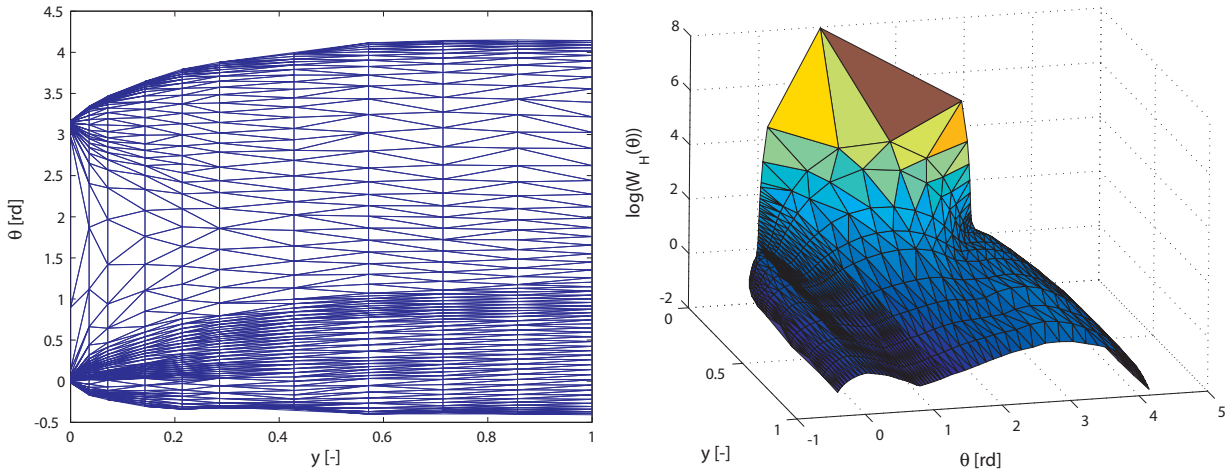

Figure 5.31: Delaunay triangulation of the pump-turbine characteristic of the figure 5.14; $2D$ (left) and $3D$ (right).

time step dt equal to the RC time constant divided by two leading to:

$$\tau_{RC} = R_{ve} \cdot C > 2 \cdot dt \tag{5.53}$$

Hence:

$$R_{ve} = \frac{2 \cdot dt}{C} \tag{5.54}$$

Regarding the initial condition determination, there is 2 possible scenarios:

- the pump-turbine is in generating mode: the water levels of the reservoirs, the mechanical torque and the rotational speed of the pump-turbine are specified and the corresponding guide vanes opening is determined;
- the pump-turbine is in pumping mode: the water levels of the reservoirs, the rotational speed and the guide vanes opening of the pump-turbine are specified and the resulting mechanical power is determined.

The 2 above scenarios are illustrated in figure 5.32.

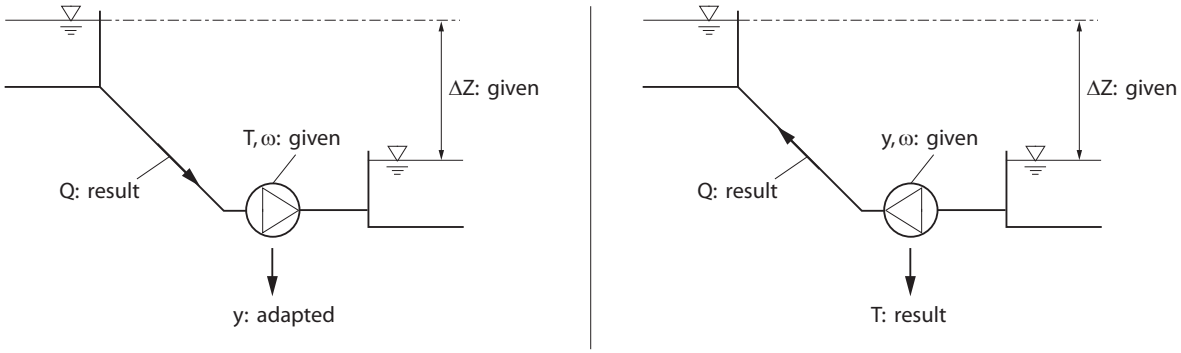

Figure 5.32: Hydraulic load flow scenarios for generating mode (left) and pumping mode (right).

Chapter 6

Analytical Analysis of Simplified Hydraulic Systems

6.1 General

The modelling by electrical equivalent enables to setup simplified models of hydraulic installation to study their global dynamic behavior. The simplified models are preferably of a low order to obtain the analytical solutions of the related differential equation set. Such solutions provide the main dynamic quantities of the system in terms of eigen frequencies and damping [1], [3], [18].

6.2 Mass Oscillations Problems

In the following sections, the eigen frequency related to mass oscillation problems is analyzed for various types of tanks, *i.e.* (i) a surge tank, (ii) a surge shaft and (iii) an air vessel.

6.2.1 System with Surge Tank

The dynamic behavior of the hydraulic circuit shown by figure 6.1 (left) comprising an upstream reservoir, a gallery, a surge tank and a penstock with a downstream valve is investigated. Focusing only on low frequencies, permits to neglect the compressibility of both pipes. Thus the equivalent circuit of this system is made of a pressure source H_o, the gallery inductance L_G and resistance R_G, the surge tank capacitance C_{ST} and the diaphragm resistance R_d, the penstock inductance L_P and resistance R_P and the valve resistance R_v as presented in figure 6.1 (right).

The consequence of a sudden closure of the valve is analyzed assuming an initial steady state condition with constant valve opening. Closing the valve yields to open the right hand loop of the equivalent scheme related to Q_2. The differential equations written using Kirchhoff's law applied to the left hand loop leads to:

$$\begin{cases} H_o = L_G \cdot \dfrac{dQ_1}{dt} + (R_d + R_G) \cdot Q_1 + h_{ST} \\ C_{ST} \cdot \dfrac{dh_{ST}}{dt} = Q_1 \end{cases} \tag{6.1}$$

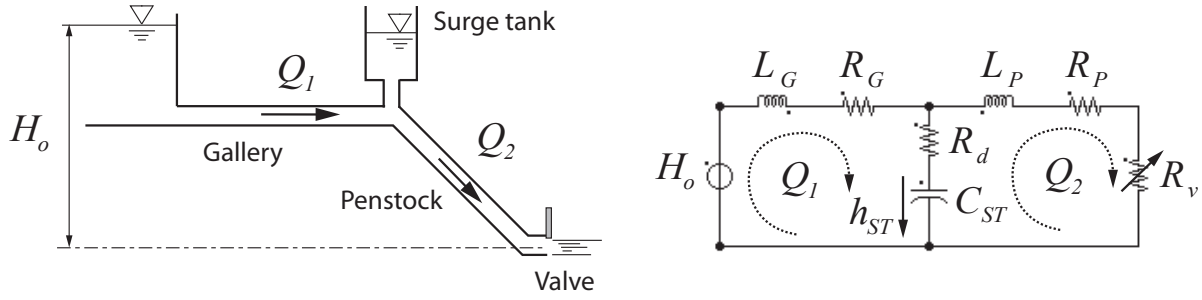

Figure 6.1: Hydraulic circuit with surge tank.

Combining the 2 above equations leads to the following characteristic equation:

$$\frac{d^2 h_{ST}}{dt^2} + \underbrace{\frac{R_d + R_G}{L_G}}_{2\cdot\mu} \cdot \frac{dh_{ST}}{dt} + \underbrace{\frac{1}{C_{ST} \cdot L_G}}_{\omega_o^2} \cdot h_{ST} = 0 \tag{6.2}$$

The general solution of the above equation is given by:

$$h_{ST}(t) = h_{STo} \cdot e^{-\mu \cdot t} \cdot sin(\omega_1 \cdot t) \tag{6.3}$$

With:

$$\omega_1 = \omega_o \cdot \sqrt{1 - \zeta^2} \quad ; \quad \zeta = \frac{\mu}{\omega_o} \tag{6.4}$$

The natural frequency of the frictionless system is given by:

$$\omega_o = \frac{1}{\sqrt{(C_{ST} \cdot L_G)}} \tag{6.5}$$

The related period is then given by:

$$T_o = 2 \cdot \pi \cdot \sqrt{\left(\frac{l_G \cdot A_{ST}}{g \cdot A_G}\right)} \tag{6.6}$$

Where:

- l_G: length of the gallery $[m]$
- A_{ST}: surge tank cross section $[m^2]$
- A_G: gallery cross section $[m^2]$

The period T_o is usually very low as the surge tank cross section and the gallery length are large and the gallery cross section is small. This period is called the mass oscillation period related the oscillation of the discharge in the gallery between the reservoir and the surge tank.

The amplitude of the water level oscillations in the surge tank, assuming a constant surge tank cross section and a frictionless system, is obtained considering a solution of the type $h_{ST}(t) = h_{STo} \cdot sin(\omega_o \cdot t + \phi)$ whose first derivative introduced in equation 6.1 gives the oscillation amplitude:

$$h_{STo} = \frac{Q_{1o}}{C_{ST}} \cdot \frac{1}{\omega_o} = C_{1o} \cdot \sqrt{\frac{l_G \cdot A_G}{g \cdot A_{ST}}} \tag{6.7}$$

Where $C_{1o} = \frac{Q_{1o}}{A_G}$ is the initial flow velocity in the gallery.

6.2.2 System with Surge Shaft

The dynamic behavior of the hydraulic circuit presented by figure 6.2 (top) comprising an upstream reservoir, a first part of gallery, an upstream valve, a surge shaft, a second part of gallery, a surge tank and a penstock with a downstream valve is investigated. Focusing again only on low frequencies, the compressibility of the pipes are neglected. The system is considered frictionless. Thus the equivalent circuit of this system is made of a pressure source H_o, the first gallery inductance L_{Go}, the valve resistance R_{v1}, the surge shaft capacitance C_{SS} and inductance L_{SS}, the second gallery inductance L_{G1}, the surge tank capacitance C_{ST}, the penstock inductance L_P and the downstream valve resistance R_v2 as presented in figure 6.2 (bottom).

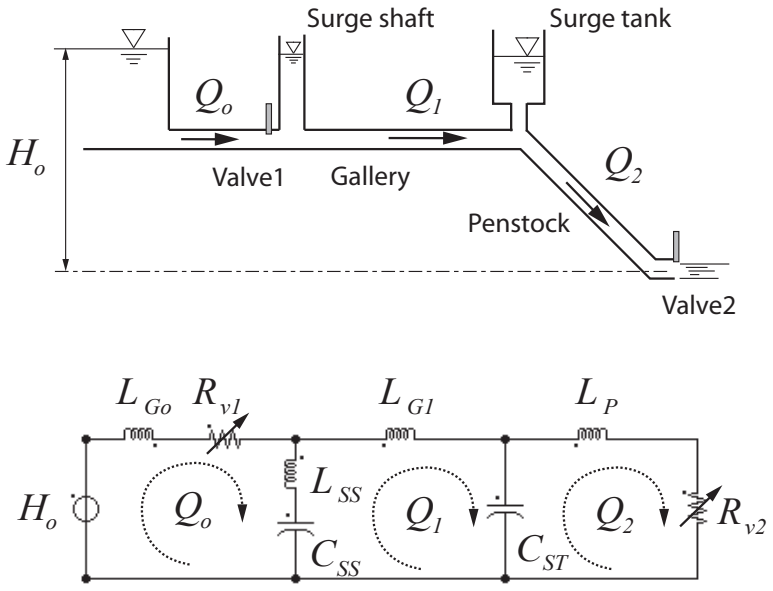

Figure 6.2: Hydraulic circuit with surge tank and surge shaft.

The consequence of a sudden closure of both valves is analyzed assuming an initial steady state condition with constant valves openings. Closing valves 1 and 2 yields to open loops related to Q_o and Q_2. The differential equations written using Kirchhoff's law

applied to the loop related to Q_1 leads to:

$$\begin{cases} (L_{G1} + L_{SS}) \cdot \dfrac{dQ_1}{dt} + h_{ST} - h_{SS} = 0 \\ C_{ST} \cdot \dfrac{dh_{ST}}{dt} = Q_1 \\ C_{SS} \cdot \dfrac{dh_{SS}}{dt} = -Q_1 \end{cases} \tag{6.8}$$

Combining the 3 above equations leads to the following characteristic equation:

$$\frac{d^2Q_1}{dt^2} + \underbrace{\left(\frac{1}{C_{ST}} + \frac{1}{C_{SS}}\right) \cdot \frac{1}{L_{SS} + L_{G1}}}_{\omega_o^2} Q_1 = 0 \tag{6.9}$$

The natural frequency of the frictionless system is given by:

$$\omega_o^2 = \frac{\frac{1}{C_{SS}} + \frac{1}{C_{ST}}}{L_{SS} + L_{ST}} \tag{6.10}$$

The corresponding mass oscillation period is given by:

$$T = 2 \cdot \pi \cdot \sqrt{\frac{\frac{l_{SS}}{g \cdot A_{SS}} + \frac{l_{G1}}{g \cdot A_{G1}}}{\frac{1}{A_{SS}} + \frac{1}{A_{ST}}}} \tag{6.11}$$

Once the 2 valves are closed the system constituted of the surge shaft, the gallery and the surge tank undergo mass oscillations. The mass of water oscillates between the surge shaft and the surge tank with amplitudes driven by the tanks cross sections. It can be seen that the inertia of the water in the surge shaft may strongly influence the oscillation period depending on the inductance ratio between the surge shaft and the gallery.

6.2.3 System with Air Vessel

The dynamic behavior of the hydraulic circuit presented by figure 6.3 (left) comprising an upstream reservoir, a gallery, an air vessel and a penstock with a downstream valve is investigated. Focusing only on low frequencies permits to neglect the compressibility of both pipes. The system is considered frictionless. Thus, the equivalent circuit of this system is made of a pressure source H_o, the gallery inductance L_G, the 2 air vessel capacitances C_{AV} and C_g, the penstock inductance L_P and the valve resistance R_v as presented in figure 6.3 (right).

The consequence of a sudden closure of the valve is analyzed assuming an initial steady state condition with constant valve openings. Closing the downstream valve yields to open loop related to Q_2. The differential equations written using Kirchhoff's law applied to the first loop leads to:

$$\begin{cases} L_G \cdot \dfrac{dQ_1}{dt} + h_{AV} + h_g = H_o \\ C_{AV} \cdot \dfrac{dh_{AV}}{dt} = Q_1 \\ C_g \cdot \dfrac{dh_g}{dt} = Q_1 \end{cases} \tag{6.12}$$

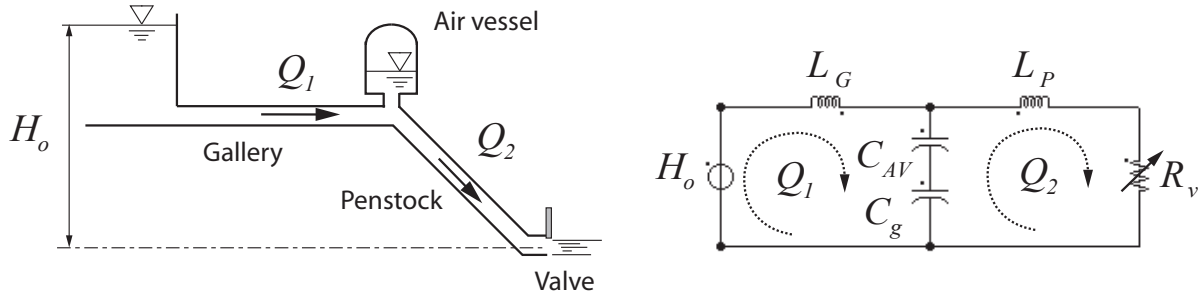

Figure 6.3: Hydraulic circuit with air vessel.

Combining the 3 above equations leads to the following characteristic equation:

$$\frac{d^2Q_1}{dt^2} + \underbrace{\left(\frac{1}{C_{AV}} + \frac{1}{C_g}\right) \cdot \frac{1}{L_G}}_{\omega_o^2} Q_1 = 0 \tag{6.13}$$

The natural frequency of the frictionless system is given by:

$$\omega_o^2 = \frac{\frac{1}{C_{AV}} + \frac{1}{C_g}}{L_G} \tag{6.14}$$

The corresponding mass oscillation period is given by:

$$T = 2 \cdot \pi \cdot \sqrt{\frac{\frac{l_G}{g \cdot A_G}}{\frac{1}{A_{AV}} + \frac{1}{\left(\frac{V_g}{H_g \cdot n}\right)}}} \tag{6.15}$$

Comparing the mass oscillation period obtained for a system with air vessel with the period obtained for a system with a surge tank, given by equation 6.5, it can be noticed that:

- if the gas volume tends to infinity, the period of the system with air vessel corresponds to the period of the system with a surge tank;
- if the volume of gas becomes small, the mass oscillation period decreases;
- for small gas volume and high oscillation amplitudes, the system becomes strongly non-linear as the air vessel capacitance is function of the gas volume and pressure.

To illustrate the influence of the gas volume on the mass oscillation period and time evolution, the simulation of the sudden closure of the downstream valve is performed for 3 different gas volumes. The dimensions of the hydraulic circuit are summarized in table 6.1. The time domain evolution of the gas piezometric head h_g, the water level in the air vessel h_{AV} and the total piezometric head $h = h_g + h_{AV}$ are represented in dimensionless values in figure 6.4. The 3 above statements are clearly confirmed by the simulations. Especially the non-linear behavior induced by the gas volume is clearly pointed out for the simulation results with $V_g = 50m^3$.

Table 6.1: Parameters of the hydraulic installation with air vessel of figure 6.3.

Gallery	Air vessel	Penstock	Nominal values
$l = 1100m$	$A = 38.48m^2$	$l = 1100m$	$H_o = 700m$
$a = 1100m/s$	$h_{go} = 100m$	$a = 1100m/s$	$Q_{1o} = 30.9m$
$D = 3.57m$	$h_{AVo} = 598m$	$D = 2.52m$	

6.3 Stability of Hydraulic Circuit

In the following sections, stability criteria are determined for the following installations: (i) power plant with regulated turbine and surge tank; (ii) piping with cavitation development; (iii) piping with valve leakage; (iv) pumping system; and (v) pump-turbine power plant.

6.3.1 Mass Oscillation Stability: Thoma Cross Section Criteria

A hydraulic circuit comprising an upstream reservoir, a gallery, a surge tank, a penstock connected to a turbine driven by a speed controller is subject to system instabilities. Therefore the stability limit of the system must be determined. The system and the corresponding equivalent scheme are presented in figure 6.5. For the purpose of the present investigation, the dynamic behavior of the penstock and the diaphragm losses are neglected and the perturbation are considered small so that the turbine efficiency assumed to be constant.

The differential equation related to the loop of discharge Q_1 is given by:

$$\begin{cases} L_G \cdot \dfrac{dQ_1}{dt} + R_G \cdot Q_1 + h_{ST} = H_o \\ C_{ST} \cdot \dfrac{dh_{ST}}{dt} = Q_{ST} \end{cases} \tag{6.16}$$

The continuity equation gives:

$$Q_{ST} = Q_1 - Q_2 \tag{6.17}$$

From the second loop, it can be stated that the piezometric head of the surge tank corresponds to the turbine head H_t which is equal to initial head H_{to} plus a perturbation z and is therefore given by:

$$h_{ST} = H_t = H_{to} + z \tag{6.18}$$

The similitude of the turbine efficiency gives:

$$Q_2 \cdot H_t = Q_{2o} \cdot H_{to} \tag{6.19}$$

Then the discharge of the turbine can be expressed with equation 6.18 and then expressed with the limited development $(1/(1+x) = 1 - x + x^2 - x^3...)$ leading to:

$$Q_2 = Q_{2o} \cdot \frac{H_{to}}{H_{to} + z} \simeq Q_{2o} \cdot \left(1 - \frac{z}{H_{to}}\right) \tag{6.20}$$

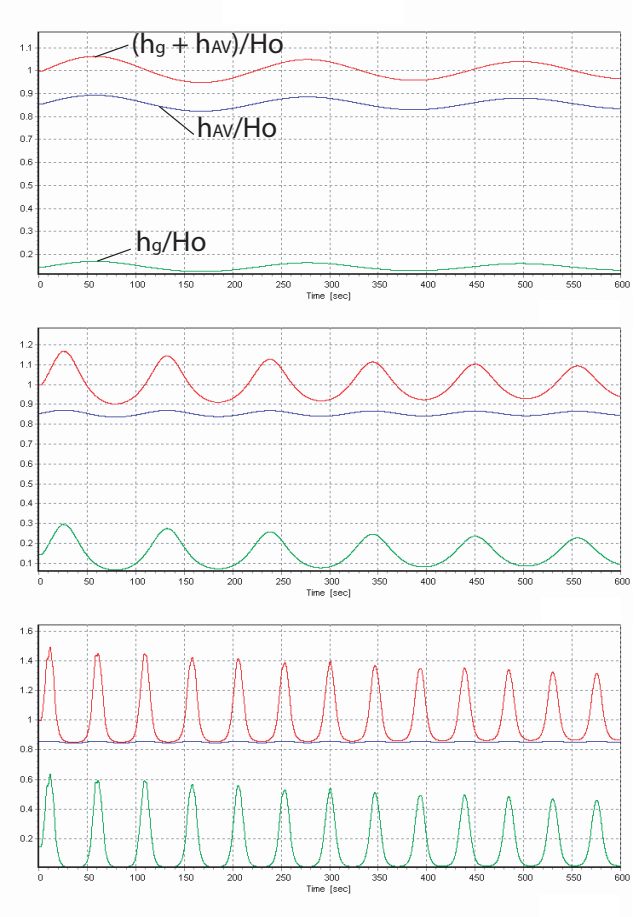

Figure 6.4: Mass oscillations with air vessel of volume: $V_g = 5000m^3$ (top), $V_g = 500m^3$ (middle), $V_g = 50m^3$ (bottom).

Combining equation 6.18 and 6.20 gives:

$$\frac{dQ_2}{dt} = -\frac{Q_{2o}}{H_{to}} \cdot \frac{dh_{ST}}{dt} \tag{6.21}$$

Introducing equations 6.17 and 6.21 in equations 6.16 leads to:

$$L_G \cdot \left[-\frac{Q_{2o}}{H_{to}} \cdot \frac{dh_{ST}}{dt} + C_{ST} \cdot \frac{d^2 h_{ST}}{dt^2} \right] + R_G \cdot Q_1 + h_{ST} = H_o \tag{6.22}$$

The head loss in the gallery is a non-linear term that requires to be developed, and therefore the head losses are expressed as follows:

$$R_G \cdot Q_1 = R'_G \cdot Q_1^2 \tag{6.23}$$

With equation 6.17 and 6.20, the discharge in the gallery gives:

$$Q_1^2 = (Q_{ST} + Q_2)^2 = \left(Q_{ST} + Q_{2o} \cdot \left(1 - \frac{h_{ST}}{H_{to}} \right) \right)^2 \tag{6.24}$$

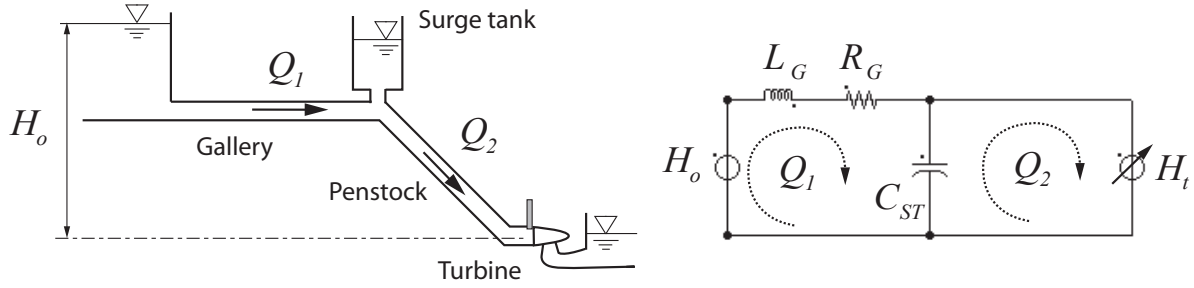

Figure 6.5: Hydraulic system with surge tank and regulated turbine.

Equation 6.24 above can be rearranged in the following form:

$$Q_1^2 = Q_{2o}^2 \cdot \left(1 + \left(\frac{Q_{ST}}{Q_{2o}} - \frac{h_{ST}}{H_{to}}\right)\right)^2 \simeq Q_o^2 \cdot \left(1 + 2 \cdot \left(\frac{Q_{ST}}{Q_{2o}} - \frac{h_{ST}}{H_{to}}\right)\right) \tag{6.25}$$

Introducing equation 6.16, 6.21 and 6.25 in equation 6.22 leads to the characteristic equation:

$$\frac{d^2 h_{ST}}{dt^2} + \underbrace{\left(2 \cdot \frac{R'_G \cdot Q_{2o}}{L_G} - \frac{Q_{2o}}{H_{to} \cdot C_{ST}}\right)}_{2 \cdot \mu} \cdot \frac{dh_{ST}}{dt} + \underbrace{\left(1 - 2 \cdot \frac{R'_G \cdot Q_{2o}^2}{H_{to}}\right) \cdot \frac{1}{L_G \cdot C_{ST}}}_{\omega_o^2} \cdot h_{ST} = \\ = \frac{H_{to} - R'_G \cdot Q_{2o}^2}{L_G \cdot C_{ST}} \tag{6.26}$$

The stability of the system is ensured while $2 \cdot \mu > 0$, leading to the following stability criteria:

$$C_{ST} > \frac{Q_{2o}}{H_{to}} \cdot \frac{L_G}{2 \cdot R_G} \tag{6.27}$$

After expressing the inductance, resistance and capacitances, the stability criteria gives the **Thoma cross section**:

$$A_{ST} > \frac{Q_{2o}^2}{2 \cdot g} \cdot \frac{l_G}{H_{to} \cdot H_{rGo} \cdot A_G} \tag{6.28}$$

Where H_{rGo} are the head losses in the gallery calculated with the initial discharge Q_{2o}, l_G and A_G are respectively the length and the cross section of the gallery, and H_{to} is the initial head of the turbine.

The Thoma cross section is the surge tank limit cross section below which the system becomes unstable after a perturbation induced by the turbine [89].

6.3.2 Cavitating Flow Stability

Cavitation development was early identified as a source of instabilities in pumping systems and is known as the POGO effect [82]. A theoretical model for the cavitation development was setup by Brennen and Acosta [15]. For simplicity, this model is applied to study the dynamic behavior of the piping system presented figure 6.6 (left) comprising an upstream reservoir, a first pipe, a cavitation development, a second pipe and a downstream reservoir. The 2 pipes of this system being identical, the equivalent model of this system is made of a resistance R and inductance L for the modelling of the pipes, the compressibility of the pipe being neglected, and a capacitance C related to the cavitation compliance. In addition, the model of the cavitation development includes the mass flow gain factor χ referring to the discharge of the second loop. The equivalent scheme of the hydraulic system is presented figure 6.6 (right).

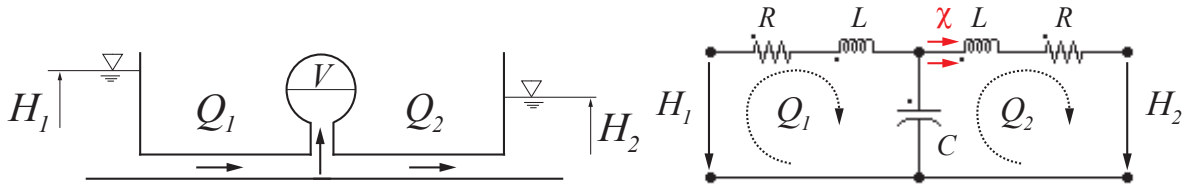

Figure 6.6: Hydraulic circuit with cavitation development in the middle.

The system of differential equations of the equivalent scheme of the hydraulic system is given by:

$$\begin{cases} H_1 = L \cdot \dfrac{dQ_1}{dt} + R \cdot Q_1 + H_c \\ \chi \cdot \dfrac{dQ_2}{dt} + C\dfrac{dH_c}{dt} = Q_1 - Q_2 \\ H_c = L \cdot \dfrac{dQ_2}{dt} + R \cdot Q_2 + H_2 \end{cases} \tag{6.29}$$

The determinant of this set of equations written in matrix form leads to the characteristic equation:

$$\left(\underbrace{\frac{R}{L}}_{1/\tau} + \delta \right) \left(\delta^2 + \underbrace{\left[\frac{R}{L} + \frac{\chi}{L \cdot C} \right]}_{2 \cdot \mu} \cdot \delta + \underbrace{\frac{2}{L \cdot C}}_{\omega_o^2} \right) = 0 \tag{6.30}$$

Where δ is the eigen value of the set of equation 6.29. The free motion time constant τ of the fluid in the pipe can be identified in the left hand term of equation 6.30. The frictionless eigen pulsation of the system ω_o and the stability criteria of the system given by $2 \cdot \mu > 0$ are determined from the right hand term. The stability criteria leads to the following criteria:

$$-R < \frac{\chi}{C} \tag{6.31}$$

The above criteria as illustrated in figure 6.7 indicates that the stability of the system depends on both values of the cavitation development, the cavitation compliance χ and the cavitation mass flow gain factor χ. The ratio χ/C can be viewed as a damping or amplification factor related to the cavitation development. The system starts to oscillate if this ratio is above the resistance of the system R. As R and C are always positive, it means that only negative values of the mass flow gain factor lead to system instabilities, *i.e.* for positive $\partial V/\partial Q$; when cavitation volume increases with the discharge.

Caution should be payed to the fact that the resistance of the system R is a function of the discharge and thus the criteria of equation 6.31 cannot be applied directly.

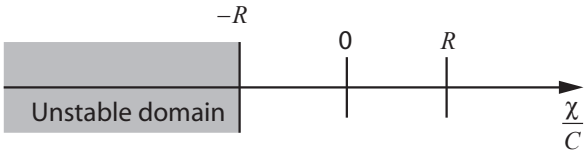

Figure 6.7: Stability domain related to cavitation development.

6.3.3 Valve Leakage Induced Instabilities

Hydraulic circuit comprising an upstream reservoir, a pipe and a downstream valve may present an unstable behavior after perturbations [54], [71]. Such a system can be modelled with a first order equivalent scheme of the pipe made of an inductance L_p and a capacitance C_p while the valve is modelled by a variable resistance R_v as presented in figure 6.8. The

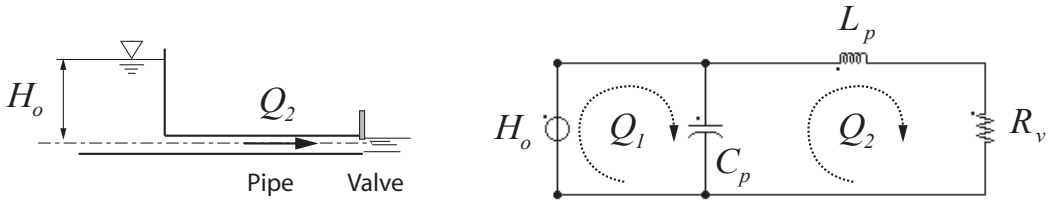

Figure 6.8: Hydraulic circuite with downstream valve.

corresponding set of differential equations is given by:

$$\begin{cases} L_p \cdot \dfrac{dQ_2}{dt} + R_v \cdot Q_2 + h_c = 0 \\ C_p \cdot \dfrac{dh_c}{dt} = Q_1 - Q_2 \end{cases} \tag{6.32}$$

Combining the 2 above equations leads to the following characteristic equation:

$$\frac{d^2Q_2}{dt^2} + \underbrace{\frac{R_v}{L_p}}_{2\cdot\mu} \cdot \frac{dQ_2}{dt} + \underbrace{\frac{1}{C_p \cdot L_p}}_{\omega_o^2} \cdot Q_2 = 0 \tag{6.33}$$

The system remains stable for $2 \cdot \mu > 0$, leading to the following stability criteria:

$$R_v > 0 \tag{6.34}$$

It means that negative slopes of a valve characteristic in the $Q - h$ diagram lead to system instabilities. Such phenomenon can occur for valves whose seals are located on the downstream side of the valve bearing axis. A pressure increase at the valve induces a valve deflection that reduces the leakage discharge because of the reduction of the seals gap. On the contrary, if the seals are located upstream the bearing axis, a pressure increase leads naturally to an increase of the leakage discharge. These 2 situations are illustrated in figure 6.9.

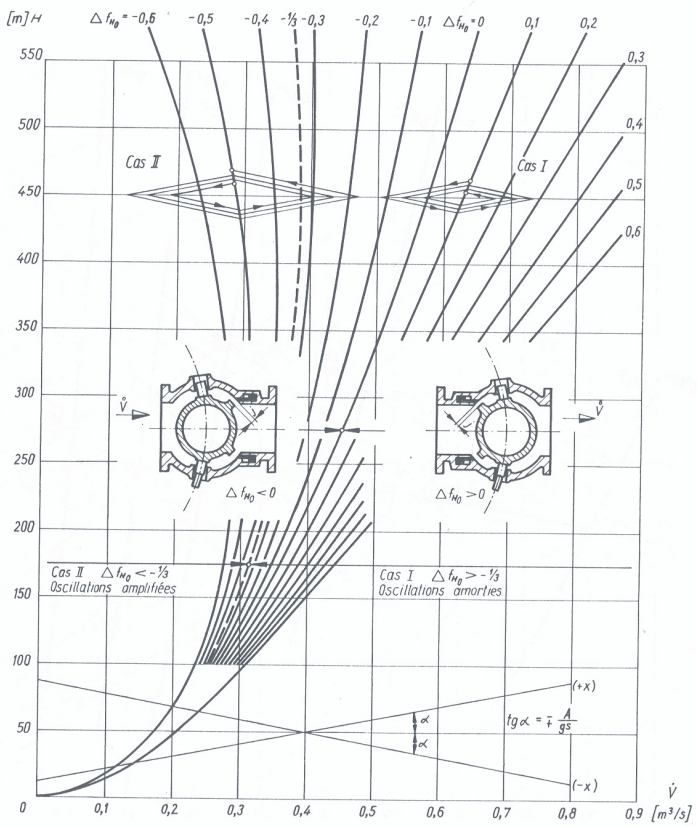

Figure 6.9: Diagram $Q - h$ for a valve with leakage [38].

6.3.4 Pumping System Stability

Pumping systems comprising air vessel may feature instabilities as reported by Greitzer [40]. Such a system can be simplified for investigation purposes to a system comprising a downstream reservoir, a pump with fixed rotational speed, a pipe, a valve, an air vessel and an upstream reservoir. The equivalent scheme of this system is made of the pump pressure source $H_p(Q)$, the pipe model with the pipe inductance L_p and resistance R_p, while the air vessel is modelled by its capacitance C_{AV} and the valve by its resistance R_v, see figure 6.10. The compliance of the pipe is neglected with respect to the air vessel compliance.

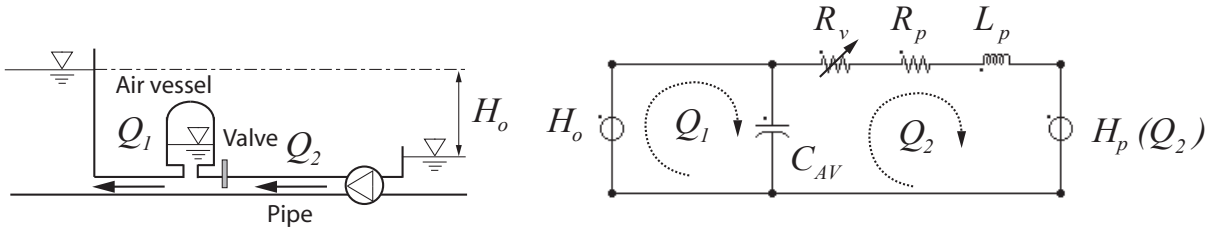

Figure 6.10: Hydraulic circuit with pump.

The corresponding set of differential equations is given by:

$$\begin{cases} L_p \cdot \dfrac{dQ_2}{dt} + R_p \cdot Q_2 + R_v \cdot Q_2 + H_p(Q_2) = h_{AV} \\ C_{AV} \cdot \dfrac{dh_{AV}}{dt} = Q_1 - Q_2 \end{cases} \tag{6.35}$$

The head of the pump can be linearized around the operating point Q_2* of interest as follows:

$$H_p(Q_2) = H_{p*} + \underbrace{\frac{dH}{dQ_2}|_{Q_2*}}_{R_{Q_2*}} \cdot (Q_2 - Q_2*) \tag{6.36}$$

Combining the 2 above equations and assuming that the upstream discharge fluctuations are negligible leads to the following characteristic equation:

$$\frac{d^2Q_2}{dt^2} + \underbrace{\frac{R_v + R_p + R_{Q_2*}}{L_p}}_{2\cdot\mu} \cdot \frac{dQ_2}{dt} - \underbrace{\frac{1}{C_{AV} \cdot L_p}}_{\omega_o^2} \cdot Q_2 = 0 \tag{6.37}$$

The system remains stable for $2 \cdot \mu > 0$, leading to the following stability criteria:

$$R_v + R_p > -\frac{dH}{dQ_2} \tag{6.38}$$

The above stability criteria shows that a negative slope of the characteristic curve of the pump $H_p = H_p(Q)$ considering a negative discharge in pump mode may lead to system

instabilities. Then, for system whose slope of energetic losses in the pipe and the valve are higher than the slope of the pump characteristic, the system is stable, as illustrated in figure 6.11 left. But, if the slope of the energetic losses are below the energetic losses, as illustrated in figure 6.11 right, the system is unstable.

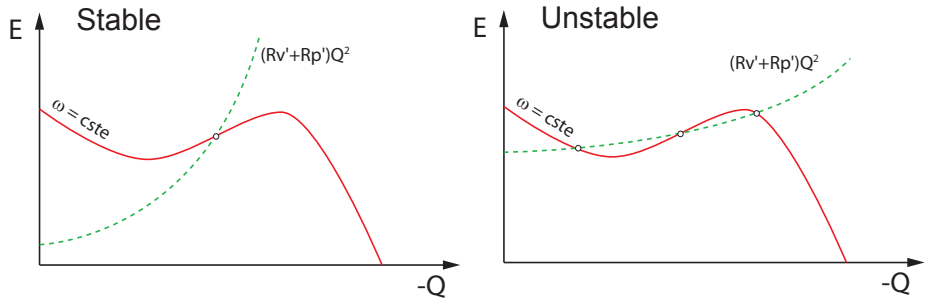

Figure 6.11: Condition of stability of a pumping system.

6.3.5 Pump-Turbine Installation Stability

Hydraulic circuit comprising an upstream reservoir, a pipe and a non-cavitating pump-turbine may exhibit an unstable behavior after perturbations (Greitzer [40], Martin [66], Jacob [50], Huvet [48]). For the stability analysis of such a system, the rotational speed changes of the pump-turbine has to be taken into account (Martin [66], Huvet [48]) and therefore the model should consider both hydraulic and mechanical properties. The hydraulic part of the system can be modelled with a first order equivalent scheme for the pipe made of a resistance R_p and an inductance L_p, compressibility effects being neglected, while the pump-turbine is modelled by a variable pressure source H_{pt} as presented in figure 6.12. For the mechanical model, the angular momentum law is applied to the inertia J accounting for both the rotor of the generator and the turbine inertia.

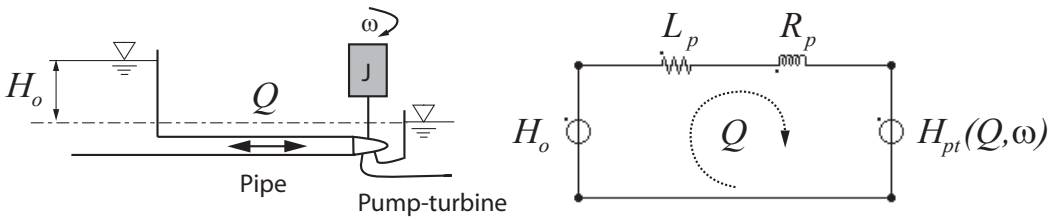

Figure 6.12: Hydraulic circuit with pump-turbine.

The corresponding set of differential equations is given by:

$$\begin{cases} H_o = L_p \cdot \dfrac{dQ}{dt} + R_p \cdot Q + H_{pt} \\ J \cdot \dfrac{d\omega}{dt} = T_{pt} + T_{el} \end{cases} \tag{6.39}$$

Where T_{el} is the electromagnetic torque and T_{pt} is the torque of the pump-turbine. The head and the torque of the pump can be linearized around the operating point $Q*, \omega*$ of interest as follows:

$$\begin{aligned} H_{pt}(Q,\omega) &= H_{pt*} + \underbrace{\frac{dH}{dQ}|_{Q*}}_{R_{Q*}} \cdot (Q - Q*) + \underbrace{\frac{dH}{d\omega}|_{\omega*}}_{R_{\omega*}} \cdot (\omega - \omega_*) \\ T_{pt}(Q,\omega) &= T_{pt*} + \underbrace{\frac{dT}{dQ}|_{Q*}}_{K_{Q*}} \cdot (Q - Q*) + \underbrace{\frac{dT}{d\omega}|_{\omega*}}_{K_{\omega*}} \cdot (\omega - \omega*) \end{aligned} \tag{6.40}$$

Combining equations 6.39 and 6.40 leads to the following matrix equation:

$$\frac{d}{dt} \cdot \begin{bmatrix} Q \\ \omega \end{bmatrix} = \underbrace{\begin{bmatrix} -\frac{R_{Q*}+R}{L_p} & -\frac{R_{\omega*}}{L_p} \\ \frac{k_{Q*}}{J} & \frac{k_{\omega*}}{J} \end{bmatrix}}_{[A]} \cdot \begin{bmatrix} Q \\ \omega \end{bmatrix} + \begin{bmatrix} H* - H_{pt*} + R_{\omega*} \cdot \omega_* + R_{Q*} \cdot Q* \\ T_{pt*} + T_{el} - k_{\omega*} \cdot \omega_* - k_{Q*} \cdot Q* \end{bmatrix} \tag{6.41}$$

The characteristic equation of the system 6.41 is obtained with the determinant $det([A] - [I] \cdot \delta)$, leading to:

$$\delta^2 + \underbrace{\left(\frac{R_{Q*} + R_p}{L_p} - \frac{k_{\omega*}}{J} \right)}_{2 \cdot \mu} \cdot \delta + \underbrace{\frac{k_{Q*} \cdot R_{\omega*}}{J \cdot L_p}}_{\omega_o^2} = 0 \tag{6.42}$$

The system remains stable for $2 \cdot \mu > 0$, leading to the following stability criteria:

$$\frac{R_{Q*} + R_p}{L_p} > \frac{k_{\omega*}}{J} \tag{6.43}$$

Expressing again the local derivative gives:

$$\underbrace{\frac{\frac{dH}{dQ}|_{Q*} + R_p}{L_p}}_{1/\tau_{fQ*}} > \underbrace{\frac{\frac{dT}{d\omega}|_{\omega*}}{J}}_{1/\tau_{m\omega*}} \tag{6.44}$$

In equation 6.44 above, the local fluid time constant τ_{fQ*} evaluated for a given Q_* and the local mechanical time constant $\tau_{m\omega*}$ evaluated for a given ω_* are introduced. The above stability criteria indicates that it is necessary that $\tau_{m\omega*} > \tau_{fQ*}$. The US Bureau of Reclamation even specifies that the stability of the power plant is ensured if $\tau_m > 2 \cdot \tau_f^2$ [63]. Where:

- $\tau_m = \frac{J \cdot \omega_{BEP}}{T_{BEP}}$: is the nominal mechanical time constant $[s]$;
- $\tau_f = \frac{l_p \cdot Q_{BEP}}{g \cdot H_{BEP} \cdot A_p}$: is the nominal fluid time constant $[s]$.

This criteria basically indicates that:

- a low penstock inductance L_p is suitable; *i.e.* a short penstock with large diameter;

- a high mechanical inertia J is suitable; *i.e.* a large diameter of generators rotors;
- the penstock and valves head losses have positive effect, as it was identified by Dörfler [27];
- negative slopes in the $H(Q)$ curves is not suitable; *i.e.* a positive slope in a $H-Q$ curve of a pump when the discharge is considered positive, or in the "S" part of the $Q_{11}(N_{11})$ curve in turbine mode;
- positive slopes of the $T(\omega)$ curves are not suitable.

From the above statements, it can be deduced that the stability criterion is intrinsically fulfilled for low head Francis turbines, but for high head francis turbines or pump-turbines with long penstock of small diameter, and low rotating inertia, the situation is more critical. Furthermore, high head pump-turbines are commonly of the low specific speed types and therefore presents "S"-shapes $Q_{11}(n_{11})$ and $T_{11}(n_{11})$ characteristic curves. But Martin [67], has demonstrated that overall, the relevant criteria is the sign of the slope of the $T_{11}(n_{11})$ for $T_{11}=0$, the runaway condition, which should be negative to ensure stability. Martin has also established the period of the undamped oscillations using linearization of the turbine characteristic curves in order to evaluate the values of the coefficient k_{Q*} and $R_{\omega*}$ of equation 6.42 yielding to ω_o [66]. This method was validated on full scale facilities by Dörfler[27]. The stability criterion of Martin is illustrated in figure 6.13.

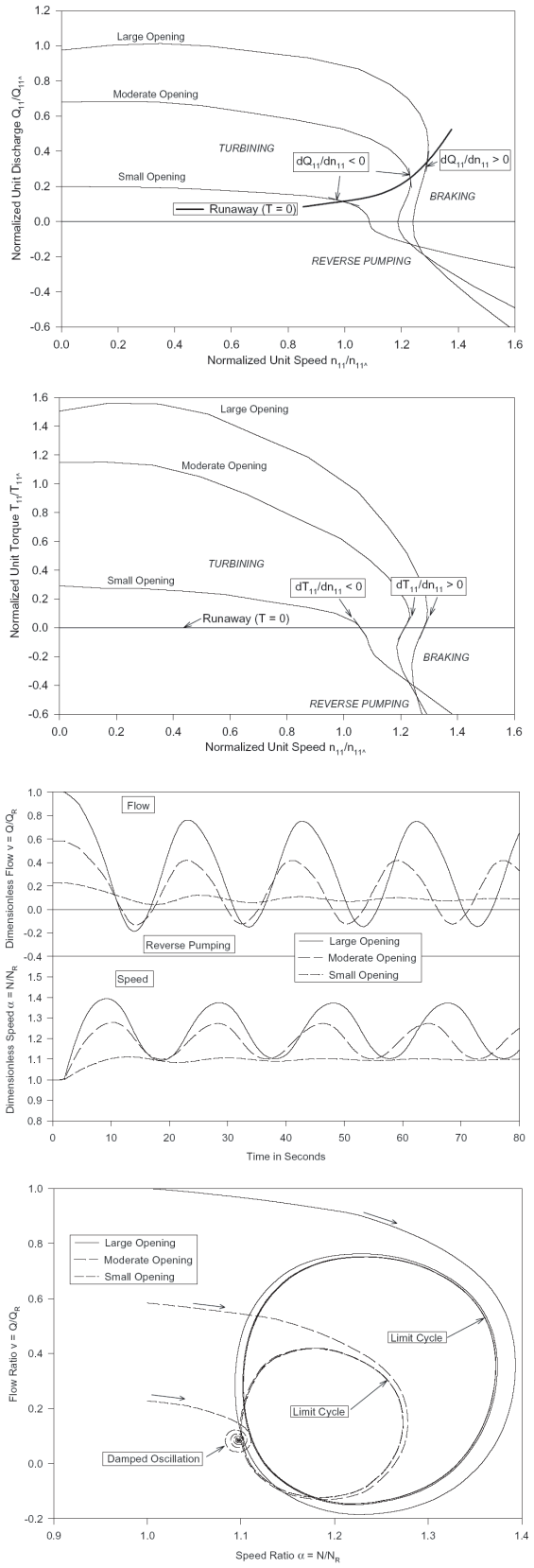

Figure 6.13: Stability analysis in the plane $Q_{11}(n_{11})$ and $T_{11}(n_{11})$ for a low specific speed Francis turbine [67].

Chapter 7

Transients Phenomena in Hydroelectric Power Plants

7.1 General

Once the models and the related equivalent scheme of the hydraulic components are established, transient simulation can be performed to highlight the possible hydroelectric interactions. The following aspects are treated in the following sections:

- validation of the hydraulic modules of SIMSEN-Hydro;
- investigation of the impact of classical hydraulic or electric disturbances on the dynamic behavior of a hydroelectric power plant;
- comparison of the stability of the turbine speed governor with strictly hydraulic model vs hydroelectric model in isolated production mode;
- investigation on the turbine speed governor stability in islanded production mode.

7.2 Validation of SIMSEN-Hydro

7.2.1 Case Study Definition

The validation of SIMSEN-Hydro is achieved by simulating the transient behavior of a 1260 MW pumped storage plant for generating and pumping load rejection and comparing the simulation results with the available data. The hydraulic layout of the pumped storage plant is presented in figure 7.1. A 590 meters long penstock is feeding 4 Francis pump-turbines, with 4 downstream surge chambers of variable sections that are all connected to a 304 meters long pressurized tailrace water tunnel. The exhaustive set of data related to the piping system is given in table 7.1 and the design values of the pump-turbines are given in table 7.2. The cross sections and elevations of the downstream surge chambers are given in figure 7.2. The loss coefficient of the surge chambers sudden cross section changes is calculated to be $K = 1.5$. The number of nodes used for the modelling of each pipe is calculated in order to fulfill the CFL criterion with the same frequency resolution.

The pump-turbine characteristic of the pumped storage plant are represented in figure 7.3. The modelling of the pump-turbines takes into account the servomotor stroke vs.

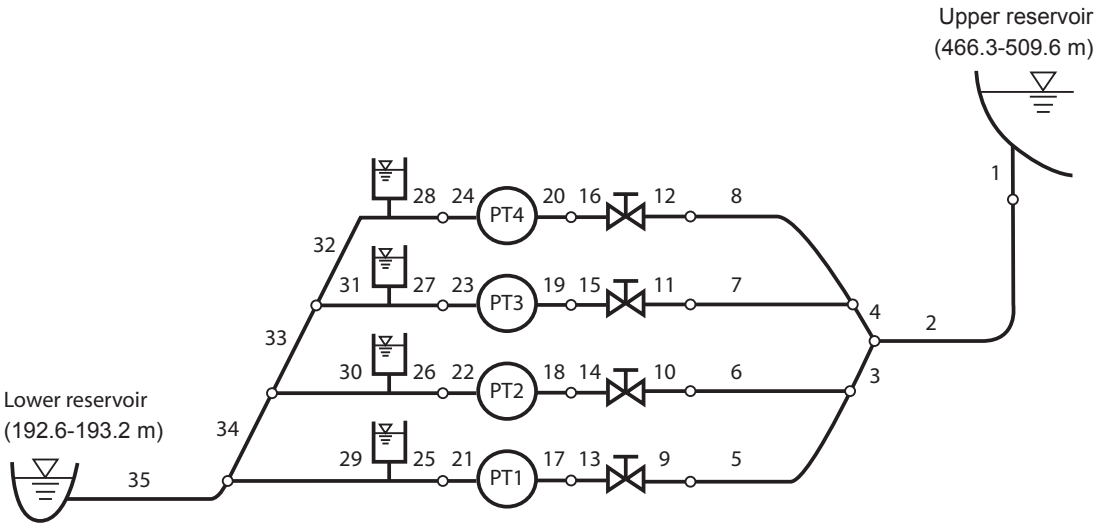

Figure 7.1: Layout and pipe numbering of the pumped storage plant test case.

Table 7.1: Rated values of the pump-turbines of the validation test case.

H_n $[m]$	Q_n $[m^3/s]$	P_n $[MW]$	N_n $[rpm]$	D_{ref} $[m]$	J_{tot} $[kg \cdot m^2]$	ν $[-]$
305	109	315	300	5.08	$2.77 \cdot 10^6$	0.272

guide vane opening cinematic relation. The spiral case and draft tube are modelled as pipes of equivalent length and diameters and correspond respectively to pipes N° $17-20$ and N° $21-24$. During the load rejection, the circuit breaker between the generator and the transformer is opened, and leading to an electromagnetic torque equal to zero. Consequently, the electrical installations are assumed to have no significant influence on the transient and are modelled as an external torque acting on the mechanical inertias.

Table 7.2: Pipes dimensions according to numbering of figure 7.1.

Pipe	**1**	**2**	**3**	**4**	**5**	**6**	**7**	**8**	**9-12**	**13-16**
$L[m]$	30.48	590.4	29.14	29.14	78.70	72.89	67.06	61.23	24.23	28.96
$D[m]$	13.02	10.67	7.47	7.47	5.33	5.33	5.33	5.33	4.18	3.05
$a[m/s]$	1219	1297	1166	1166	1311	1325	1341	1225	1212	1158
$\lambda[-]$	0.015	0.015	0.015	0.015	0.015	0.015	0.015	0.015	0.015	0.015
Pipe	**17-20**	**21-24**	**25-28**	**29**	**30**	**31**	**32**	**33**	**34**	**35**
$L[m]$	30.48	26.85	60.14	79.49	62.06	38.77	42.67	33.96	33.96	304.8
$D[m]$	2.20	5.015	5.33	5.33	5.33	5.33	5.33	7.47	9.30	10.67
$a[m/s]$	870	1342	1336	1324	1241	1292	1219	1358	1358	1287
$\lambda[-]$	0.015	0.015	0.015	0.015	0.015	0.015	0.015	0.015	0.015	0.015

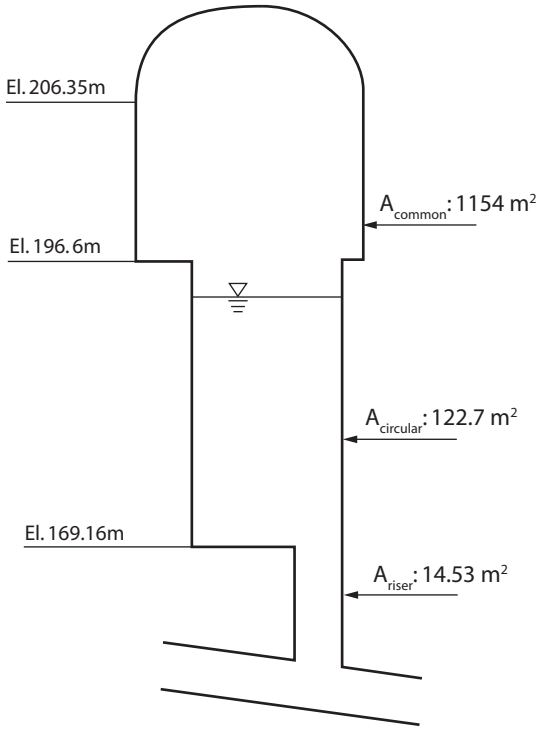

Figure 7.2: Surge chamber cross sections and elevations.

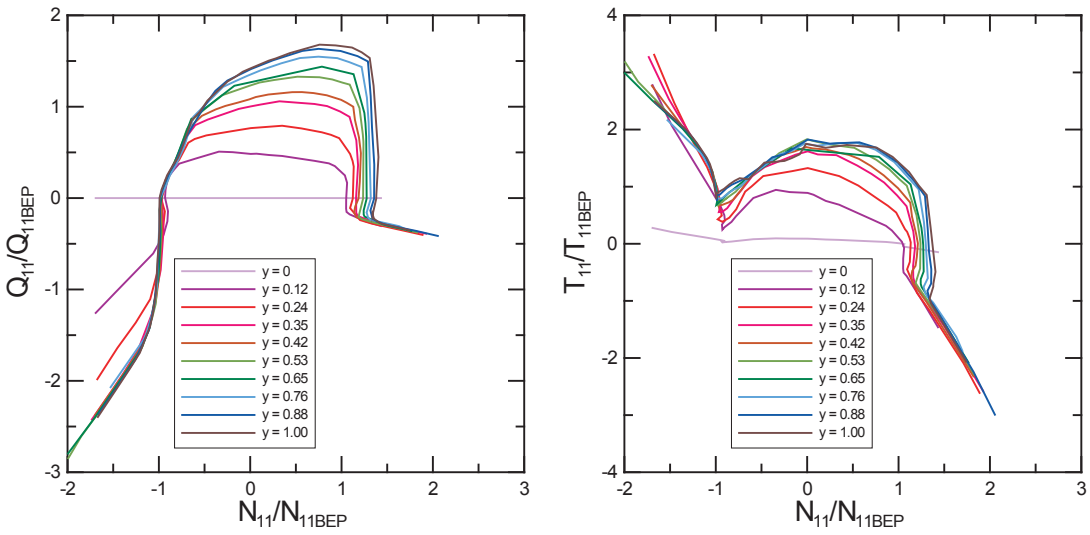

Figure 7.3: Pump-turbine characteristic of the pumped storage plant.

7.2.2 Simulation Results

Transients Simulation Scenarios

Transient tests carried out during commissioning have been performed for different situations of emergency shutdown and load acceptance/rejection. Two transients tests are selected for the validation of the simulation results and the corresponding sequences are the following:

- emergency generating shutdown test: Units 1, 3 and 4 are set to fully opened guide vanes, y=1, that corresponds to 390 MW under the test head defined by the upstream reservoir level of 489.2m (1605 ft), Unit 2 being kept in operating. The guide vanes of the pump-turbine 1, 3 and 4 are closed within 24 seconds with 2 slopes.

- emergency pumping shutdown test: Units 1,3 and 4 are set to 65% guide vane opening, best pump efficiency point, under an upstream reservoir water level of 481 m (1578 ft), Unit 2 being at rest with the guide vanes closed. The guide vanes of the pump-turbines 1, 3 and 4 are closed within 16.4 seconds, with two slopes.

The servomotor stroke closing law used for both simulations is based on a closure in 20 seconds from $y = 1$ to $y = 0.08$, and 4 seconds from $y = 0.08$ to $y = 0$.

Simulation Results for Emergency Shutdown in Generating Mode

The results of the simulation of the emergency shutdown of the units 1, 3 and 4 while Unit 2 is kept at the same operating point, are presented for the pump-turbine 1, for the surge tank of Unit 1, and for the level of the 4 surge tanks, in figure 7.4.

The pump-turbine of Unit 1 is operating at the full guide vane opening, $y = 1$, for $10s$, then the electromagnetic torque is set to zero. As a consequence the rotational speed of the Unit is increasing. To reduce the runaway rotational speed the guide vanes are closed linearly with 2 slopes thus reducing the discharge and therefore the mechanical torque of the pump-turbine. When the torque reaches the zero, the maximum overspeed is attained. Then the discharge becomes also negative and the pump-turbine is in the turbine dissipation quadrant. The closure of the guide vanes induces a waterhammer effect in the penstock leading to head fluctuations. The related head fluctuation is quickly damped as the discharge in Unit 2 remains almost constant. When the guide vanes are fully closed, after $24s$, the discharge value is zero, the rotational speed decreases because of the negative value of the torque. The operating points of the pump-turbine during the transient are represented in the $Q_{11}(N_{11})$ and $T_{11}(N_{11})$ plane in figure 7.5. Due to the shutdown of the pump-turbines of Unit 1,3 and 4, the water level of the surge chambers are first decreasing according to the downstream mass oscillation period between the tailrace tunnel and the surge chambers. The water level evolutions in the surge chambers are almost simultaneous for Units 1,3 and 4 while the water level decrease start later on Unit 2 because the pump-turbine is kept in operation. The influence of the different cross sections are visible on the time evolution of the water level in the surge tank. The mass oscillation period is about $100s$ and is dependant on the water level history as the cross section of the surge chambers are changing during the transient.

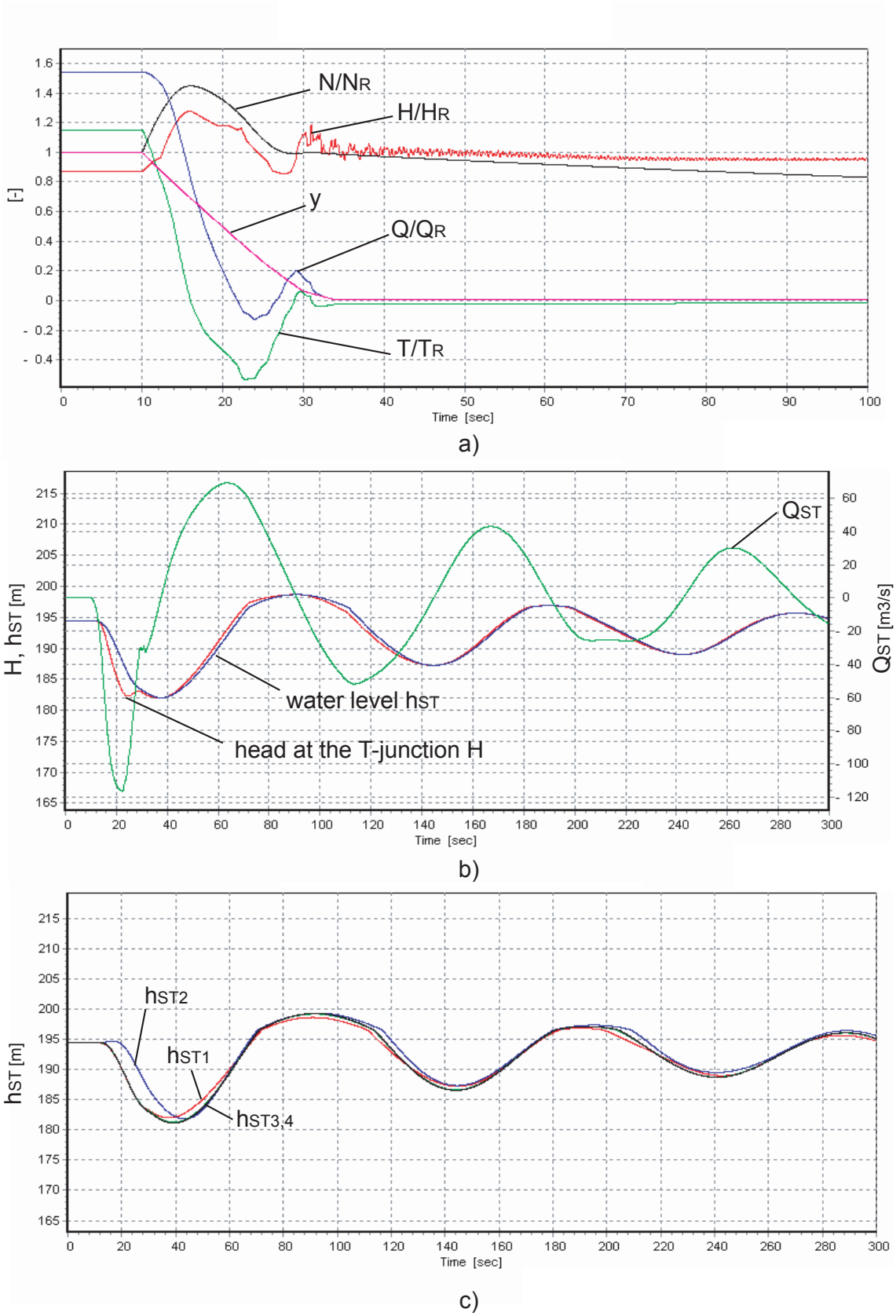

Figure 7.4: Transient behavior of the pumped storage plant resulting from an emergency shutdown in generating mode; transient of the pump-turbine Unit 1 in rated values a), transient of surge chamber of Unit 1 b), transient of the 4 surge tanks c).

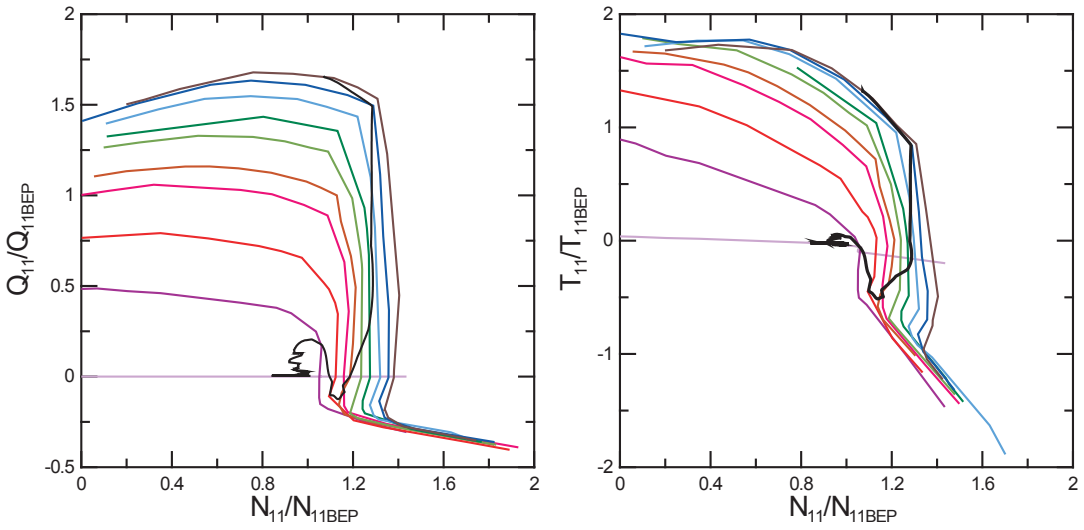

Figure 7.5: Operating point trajectory in the plan $Q_{11}(N_{11})$ and $T_{11}(N_{11})$ during the emergency shutdown in generating mode for Unit 1.

Simulation Results for Emergency Shutdown in Pumping Mode

The simulation results of emergency shutdown of Unit 1, 3 and 4 in pumping mode while Unit 2 is at rest are presented for pump-turbine 1, surge tank 1 and the 4 surge tanks water levels, in figure 7.6.

The pump-turbine of Unit 1 is operating at steady state pump operating point with $y = 0.65$, negative discharge and negative rotational speed for $10s$. Then the electromagnetic torque is set to zero, inducing the slow down of the rotational speed of the Unit 1, the decrease of the discharge, head and torque. Then the discharge becomes positive and the pump-turbine is operating in the pump dissipation quadrant. Once the guide vanes are fully closed the discharge value is zero and the rotational speed is positive but decreasing. Waterhammer is also induced in the penstock and leads to head fluctuations. Here the amplitudes require more time to be damped as there is no more discharge in the 4 pump-turbines. Here the mass oscillation starts by an increase of the water level in the surge chamber as the initial discharge is negative. The operating points of the pump-turbine during the transient are represented in the $Q_{11}(N_{11})$ and $T_{11}(N_{11})$ plane in figure 7.7.

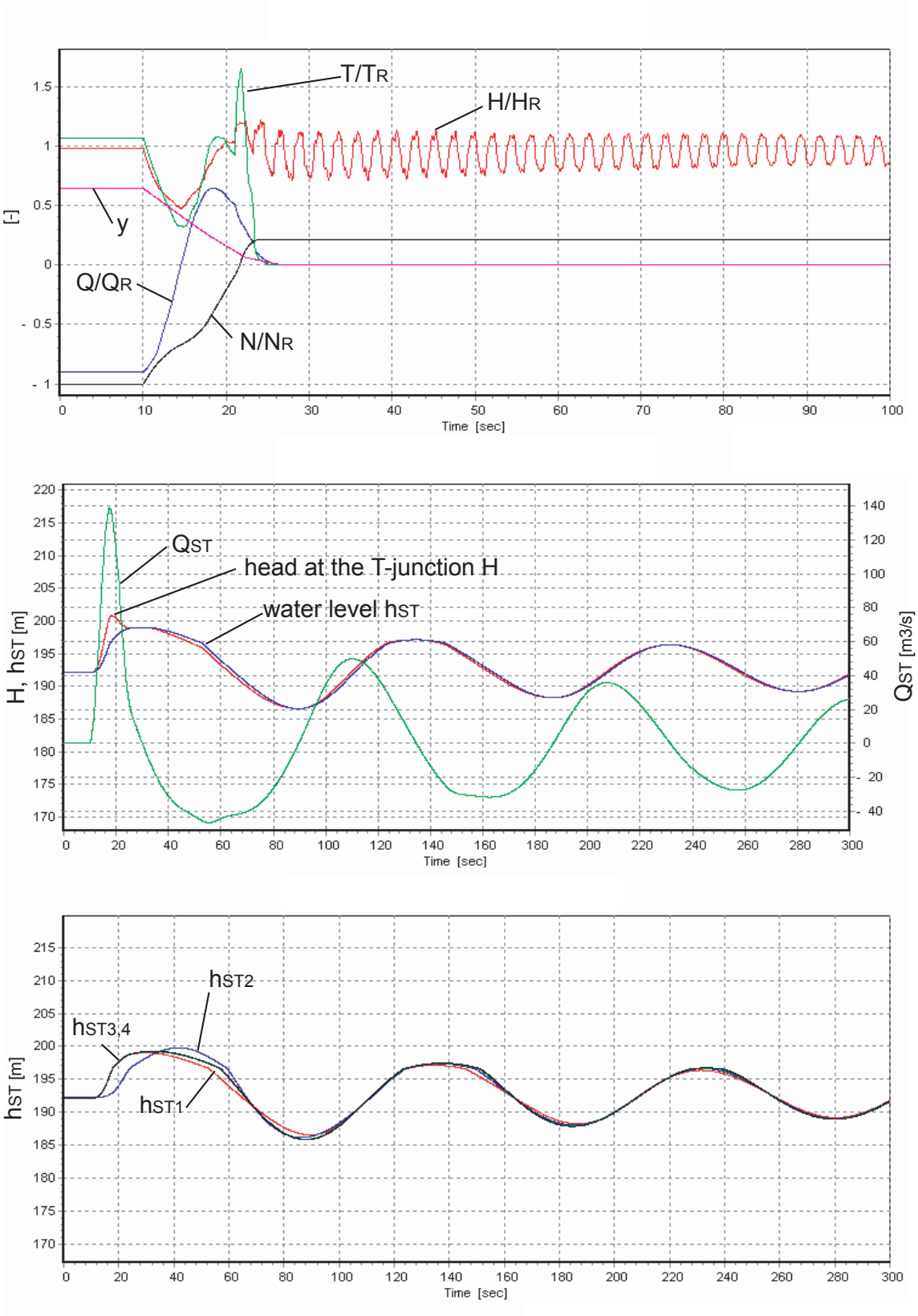

Figure 7.6: Transient behavior of the pumped storage plant resulting from an emergency shutdown in pumping mode; transient of the pump-turbine Unit 1 in rated values a), transient of surge chamber of Unit 1 b), transient of the 4 surge tanks c).

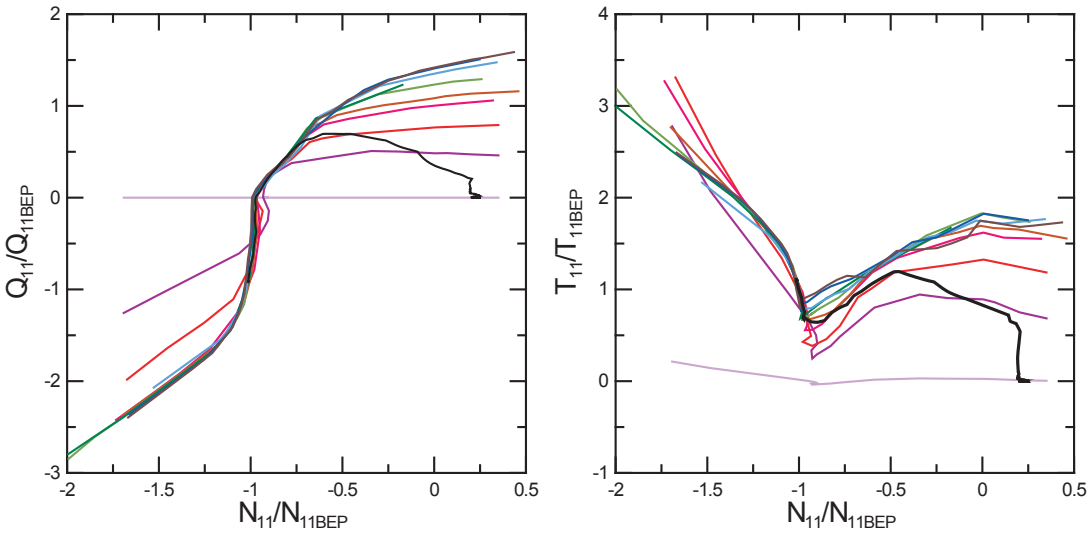

Figure 7.7: Operating point trajectory in the plan $Q_{11}(N_{11})$ and $T_{11}(N_{11})$ during the emergency shutdown in pumping mode for Unit 1.

7.2.3 Validation

During the transients tests carried out at the commissioning of the pumped storage plant, the piezometric head time history was recorded on the Unit 1 at the spiral case inlet, at the draft tube man-door, and the surge chamber. The simulation results in generating and pumping mode time evolution are compared for theses 3 values and represented in table 7.3.

Table 7.3: Comparison of simulation results with transients tests carried out on Unit 1 during an emergency shutdown in both generating and pumping mode; simulation in light red line and measurements in bold black line.

Generating Mode	Pumping Mode
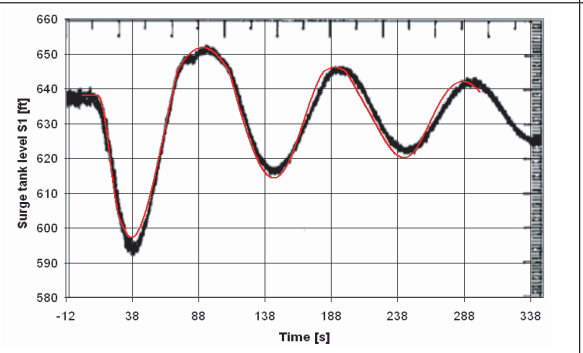	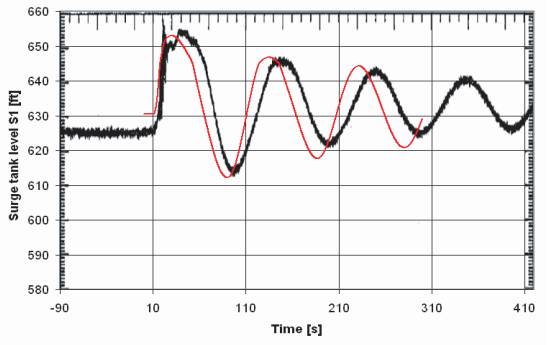
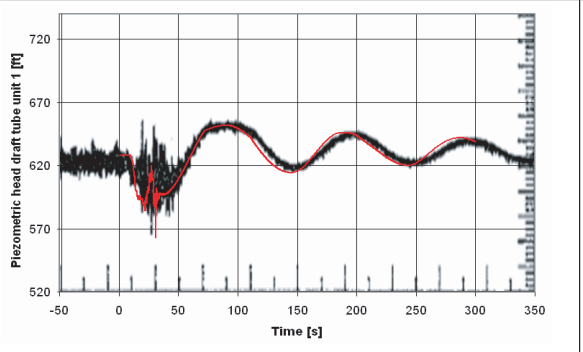	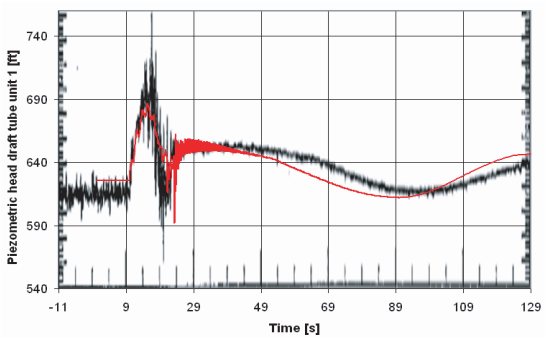
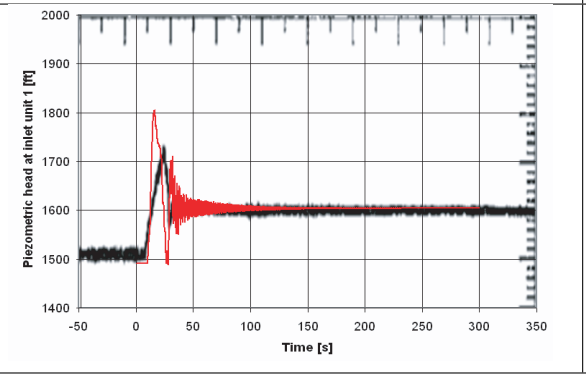	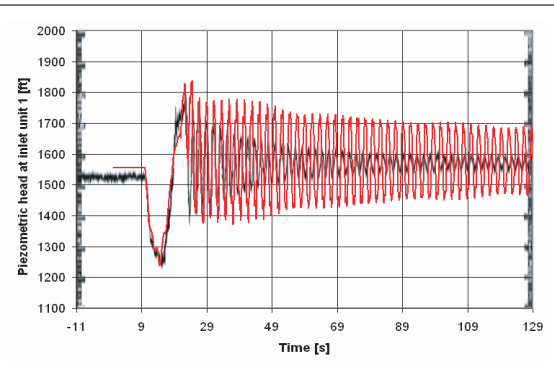

By comparing the simulation results with the measurements on site during an emergency shutdown in generating mode it can be noticed that:

- the steady state conditions before the transients presents a very good agreement;

- the amplitudes and time evolution of water level in surge tank 1 and piezometric head in draft tube of unit 1 present also a very good agreements;
- the overpressure amplitude of the piezometric head at the unit 1 inlet presents a discrepancy of 30%, however the time evolution of the piezometric head presents a good agreement.

By comparing the simulation results with the measurements on site during emergency shutdown in pumping mode it can be noticed that:

- the steady state conditions of the simulation presents small discrepancies that can be due to errors on the downstream water level, difference in the friction losses in pumping and generating mode or difference between scale model and prototype characteristics;
- the amplitudes of the piezometric head at pump-turbine 1 inlet presents a good agreement;
- the waterhammer at the pump-turbine 1 inlet is not as damped as in measurements;
- the time evolution of the water level in the surge tank 1 and piezometric head in the draft tube of unit 1 present discrepancies on the period of the mass oscillation but the amplitudes fit roughly.

In order to identify the origin of the discrepancies of the surge tank water level time evolution during the emergency shutdown in pumping mode, the steady state discharges obtained by simulation is compared to the discharge measured on site. The comparison of the steady state discharge for generating and pumping mode is presented in table 7.4. The measured values of the discharges are given with a confidence range of $\pm 8 m^3/s$ because of the poor resolution of the graphical representation of the time evolution of the discharge from which the value is deduced.

Table 7.4: Steady state initial conditions of discharge for Unit 1.

Test Case	**Simulation** $Q\ [m^3/s]$	**Measurements** $Q\ [m^3/s]$	**Error** $[-]$
Generating mode	166.8	155.7 ± 8	$+0.07$
Pumping mode	98.1	120 ± 8	-0.18

The comparison of the simulated and measured discharge points out an error on the discharge in the case of generating mode that is in the range of uncertainties of the measured value. However, a difference of about 18% is found on the initial conditions of the discharge in the pumping mode. If only small error arises in turbine mode the error in pumping mode is probably not due to errors on the friction parameters of the hydraulic circuit. Therefore, the error is probably due to differences of the pump-turbine characteristic between the scale model and the prototype.

Moreover, the mechanical power obtained in generating mode differs between the simulation and the measurements. The measurements report a power of 390 MW for

the chosen operating point while the simulation predicts only 362 MW. It corresponds to a difference of efficiency between the scale model and the prototype. It means that the prototype efficiency is higher than the scale model efficiency. This fact is commonly admitted.

As the initial discharge in pumping mode is smaller in the simulation than in the experiments, the amplitudes are also smaller, and thus it reduces the period of oscillation due to the non-linear cross section of the surge chambers. It also explains the difference on the initial conditions of the piezometric head whose value would be reduced in the case of higher discharge and thus presents a better fit with the experiments. Therefore, if the discharge was higher in the simulation, the waterhammer in the spiral case would show higher amplitudes in similar fashion as in generating mode.

The error on the amplitude of the waterhammer is also probably due to differences of the pump-turbine characteristics that influences strongly the overpressure of the emergency shutdown of the pump-turbine. Indeed, as the turbine goes through the "S" shape of the pump-turbine during such transient, see figures 7.5 and 7.7, the discharge becomes negative during the closure of the guide vanes and therefore induces higher overpressure than in the case of turbines without "S" shape characteristic.

In spite of the differences between the simulation and the experiments found in pumping mode, the models of hydraulic components developed and implemented in SIMSEN-Hydro are satisfactory.

7.2.4 Numerical Instabilities

The simulation of the emergency shutdown resulting from a full load rejection of a pump-turbine shows that the pump-turbine is going through the unstable part of the characteristic, *i.e.* the S-shape. The numerical integration of the differential equation set of the whole system using Runge-Kutta 4th order has proven its robustness, see Appendix A. However, when simulating the load rejection, numerical instabilities have been pointed out during the transit through the "S". To overcome this numerical problem, it has been identified that the CFL criteria, equation 3.60, must be fulfilled as follow:

$$\frac{dx}{a \cdot dt} = k \quad ; \quad k = 1, 2, 3... \tag{7.1}$$

Then, for each pipe, the wave speed has to be adapted in order to satisfy the above criteria. It is acceptable to adapt the wave speed as there are uncertainties on this value because its analytical value present dispersion compared to the experimental data due to errors on the wall material properties, dimensions, contact between the pipe and the support or concrete, or air content. A comparison of the simulation results of a load rejection of a pump-turbine with guide vane opening y kept constant is presented in figure 7.8 for both cases: wave speed adapted or not. It appears, that when the turbine is going through the unstable part of the characteristic, *i.e.* negative torque, the torque and the head start oscillating for the simulation without adaptation of the wave speed, while, the torque and head evolution show stable time evolution for the simulation with adaptation of the wave speed.

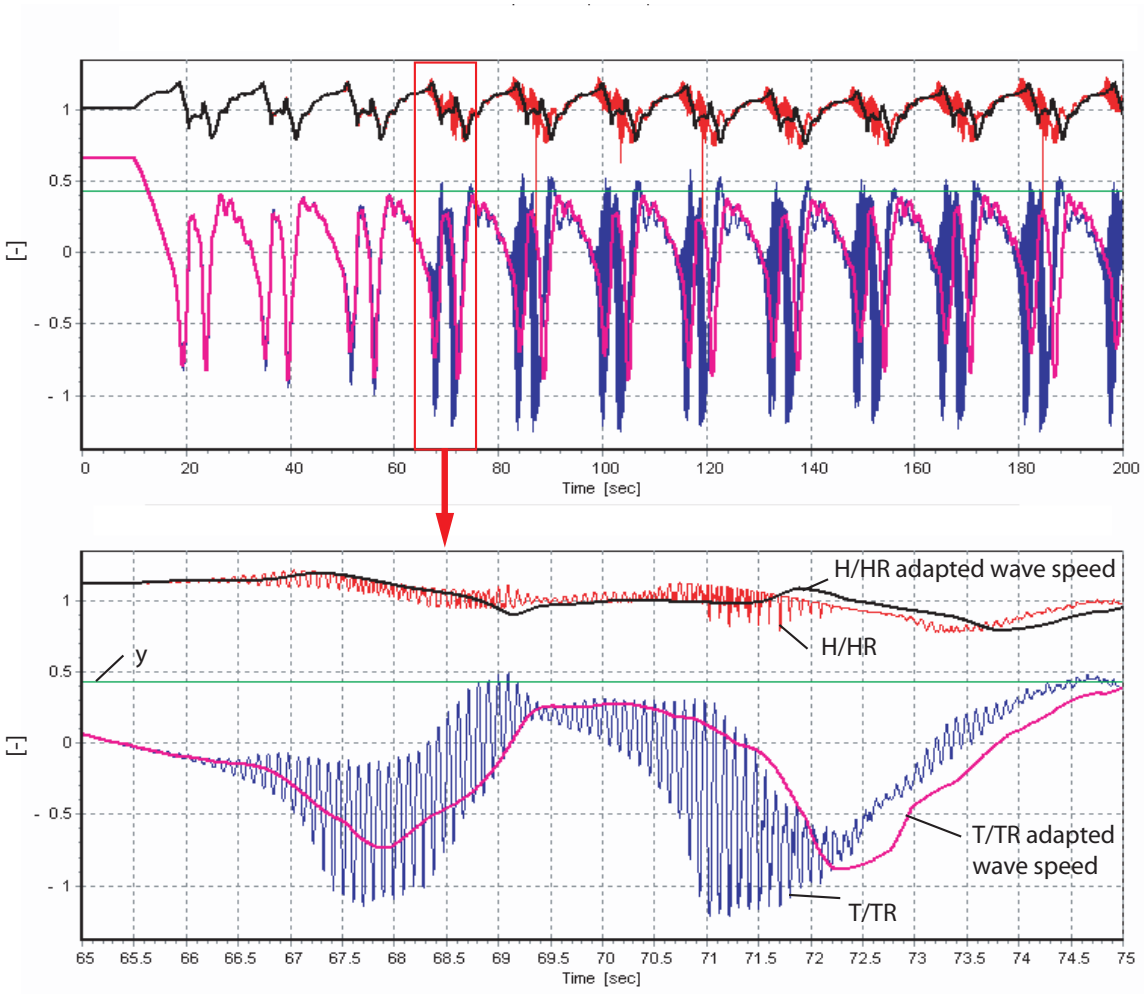

Figure 7.8: Simulation of a full load rejection with constant guide vane opening with and without adaptation of the wave speed.

7.3 Hydroelectric Transients

7.3.1 Case Study Definition

In order to highlight hydroelectric interactions, a hydroelectric power plant comprising both the hydraulic circuit and the electrical installation is modelled. The system investigated comprises an upstream reservoir, a gallery, a surge tank with variable cross section, 2 Francis turbines of 86 MW and 2 generators connected to a 205 kV network, see figure 7.9. The data related to this example are presented in table 7.5. The Francis turbine and the generator are regulated as follows:

- a turbine power or speed governor acting on the guide vane opening of the Francis turbine;
- a voltage regulator acting on the excitation field voltage of the generators.

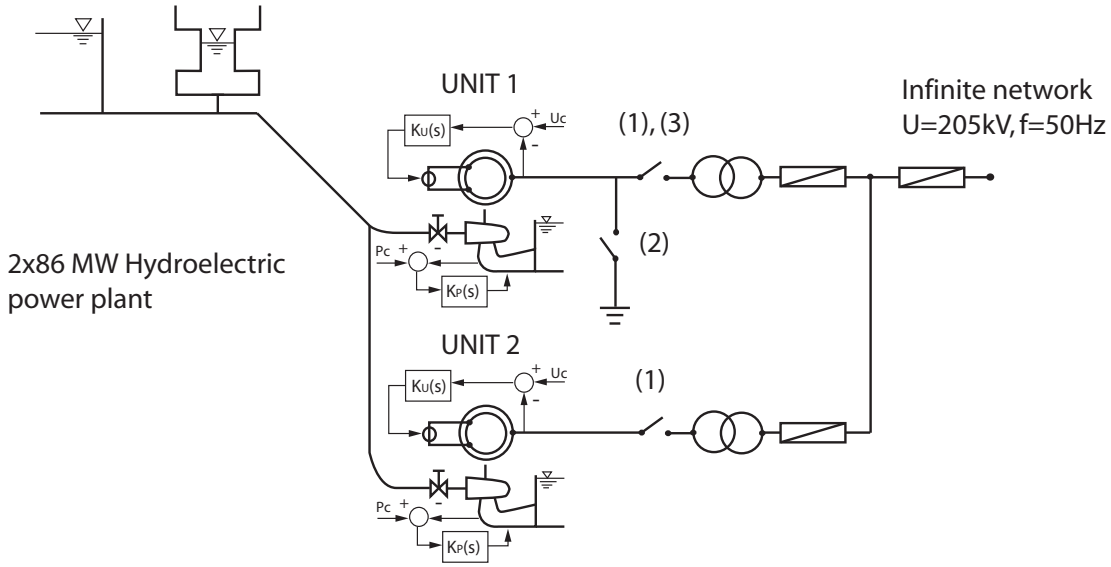

Figure 7.9: Layout of the hydroelectric power plant case study.

To investigate the dynamic behavior of the power plant 3 simulation models are used: (i) a hydraulic model, (ii) an electric model and (iii) a hydroelectric model. Then, the hydroelectric model simulation results are compared with either the hydraulic model or the electric model respectively for hydraulic disturbance and electric disturbances. Therefore, 3 standard disturbances are simulated:

- a total load rejection: the 2 circuit breakers between the transformers and the synchronous machines of both Units, see figure 7.9 (1), are opened at $t = 1\ s$, while the guide vanes of the 2 Francis turbines are closed linearly in 7 s; hydraulic and hydroelectric models are compared;

Table 7.5: Main dimensions of the power plant.

Reservoir	Gallery	Surge Tank
$H_o = 85\ m$	$L = 4000\ m$ $D = 10\ m$ $\lambda = 0.02$ $a = 1000\ m/s$	$A_{ST}(Z_{ST} < 77) = 700\ m^2$ $A_{ST}(77 < Z_{ST} < 87) = 400\ m^2$ $A_{ST}(Z_{ST} > 87) = 700\ m^2$
Penstock	**Turbine**	**Generator**
$L = 125\ m$ $D = 5.5\ m$ $\lambda = 0.02$ $a = 1250\ m/s$	$H_n = 82\ m$ $Q_n = 114\ m^3/s$ $N_n = 200\ rpm$ $T_n = 4.11 \cdot 10^6\ Nm$ $J_t = 8.415 \cdot 10^4\ kg \cdot m^2$	$S_n = 98\ MVA$ $U_n = 17.5\ kV$ $f = 50\ Hz$ pair pole = 15 $J_g = 1.683 \cdot 10^6\ kg \cdot m^2$ $K_{shaft} = 1.27 \cdot 10^{10}\ Nm$

- an earth fault: the 3 phases between the synchronous machine and the transformer of Unit 1 are connected to the ground by closing the circuit breaker (2) of figure 7.9, electric and hydroelectric models are compared;
- an out of phase synchronization: the circuit breaker between the transformers and the synchronous machines of Unit 1, see figure 7.9 (3), is closed with an error of synchronization with the infinite network, only the hydroelectric model is used.

7.3.2 Load Rejection

The first investigation deals with the case of a total load rejection where the circuit-breaker between the transformer and the generator is tripped. Simultaneously, the guide vanes of the two Francis turbines are closed in 7 seconds linearly. The evolution of the main variables during the total load rejection is presented in figure 7.10.

At the outset, the electromagnetic torque of the generators drops to zero instantaneously, as a result the rotational speed of the 2 Units increases. The closure of the guide vanes reduces the hydraulic torque quickly limiting the maximum rotational speed. The guide vanes closure induces a waterhammer effect in the adduction part of the power plant and a mass oscillation between the reservoir and the surge tank.

The comparison between the hydraulic and hydroelectric simulation results are shown in figure 7.11 for the rotational speed and the pressure at the turbine inlet. In the hydraulic model the electrical installation is modelled by a constant torque dropping to zero instantaneously at $t = 1s$. It can be seen that the 2 simulation results are identical and therefore a hydroelectric model is not required for simulating such transient phenomenon.

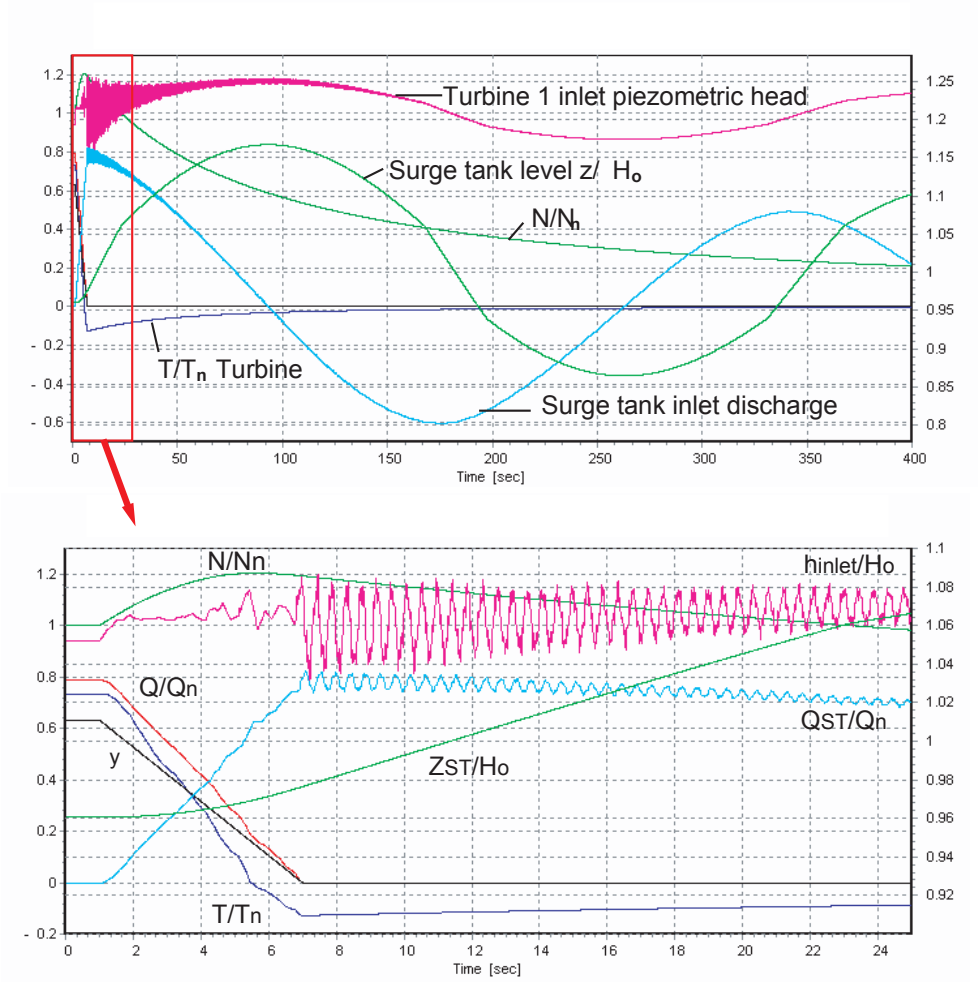

Figure 7.10: Evolution of the turbine 1 and surge tank variables during total load rejection.

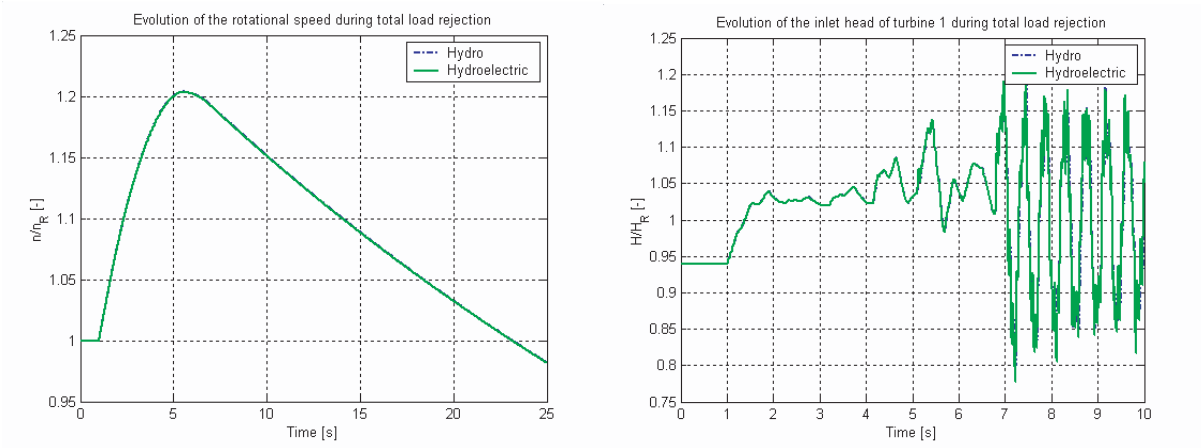

Figure 7.11: Comparison of the evolution of the turbine 1 rotational speed n (left) and inlet piezometric head H (right) obtained with two simulations: simulation with hydraulic model and simulation with the hydroelectric model.

7.3.3 Earth fault

The effect of an earth fault occurring between the generator and the transformer of Unit 1 is evaluated using both the electric and hydroelectric simulation models. Depending on the duration of the fault, the synchronization is maintained or lost after the fault is removed, leading to the critical time t_c. Figure 7.12 presents the comparison of the simulation results obtained using the two models, for a duration inferior and superior to the critical time t_c. It is pointed out that the critical time t_c is underestimated by 2% using the electric model in which the turbine torque is assumed constant. The difference between the 2 simulation results is due to the action of the turbine power regulator that is taken into account by the hydroelectric model. For the simulation, it can be seen that the maximum amplitudes are well predicted by the electric model but the time history is more realistic using the hydroelectric simulation as the influence of the turbine speed governor is properly taken into account. However, its influence on the critical time of the duration of the fault is negligible.

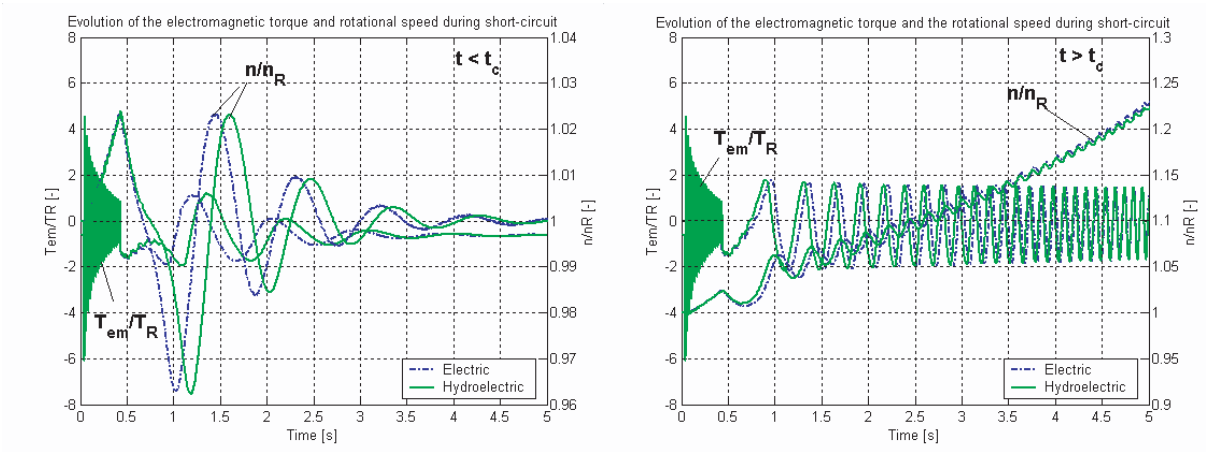

Figure 7.12: Comparison of the effect of an earth fault on Unit 1 with a duration under and over critical time t_c obtained with two simulation models: electric model and the hydroelectric model. On the left the synchronism is kept and on the right it is lost.

7.3.4 Out of Phase Synchronization

Three conditions are required for the success of the synchronization of the generator to the power network during the group start-up: the frequency, the phase and the magnitude have to match the corresponding network conditions before the closure of the circuit-breaker (3). The worst synchronization cases occur when the generator and the network are 120° and 180° out of phase. The simulation results obtained with the hydroelectric model are presented in figure 7.13 for Unit 1, and the impact on Unit 2 is presented in figure 7.14 for the out of phase synchronization of 120°. For these simulations a turbine speed governor is used in state of the turbine power governor.

In the case of a 120° out of phase synchronization, the closure of the circuit-breaker induces a strong transient electromagnetic torque up to 6 *pu* that produces rotational speed variations. This induces a reaction of the turbine speed governor acting on the

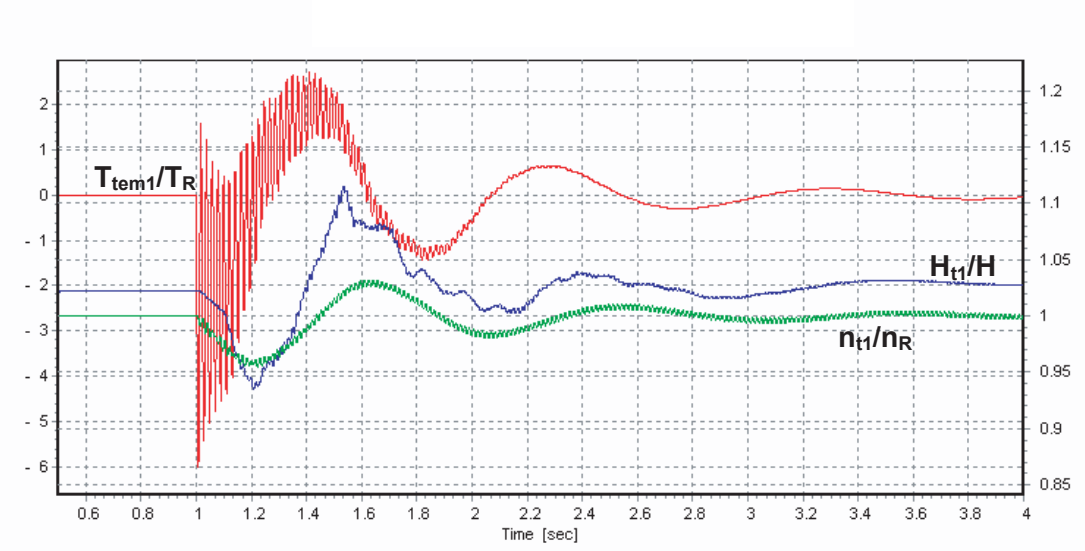

Figure 7.13: Evolution of the electromagnetic torque, the head of the turbine and rotational speed of the group number 1 during synchronization fault of 120° electrical degree.

guide vane opening in order to keep the rotational speed constant. Both effects contribute to the variation of the inlet pressure variations of the Unit 1 turbine. In addition, the first peak of the electromagnetic torque produces a free torsional vibrations at 63 Hz of the shaft line constituted of the turbine and the generator inertias linked through the connecting shaft. This dynamic response of the structure is observable on the pressure at the inlet of the turbine of Unit 1 that evidences the coupling between the hydraulic and mechanical parts. It is interesting to notice that Unit 2 is also affected by the fault on Unit 1 through both: the piping system and the electrical lines. Thus, the head of the turbine and the current of the stator of the generator of Unit 2 are disturbed by the out of phase synchronization of Unit 1.

The simulation results of the 180° out of phase synchronization are presented for Unit 1 in figure 7.15. It can be noticed that, as expected, this fault produces stronger current variations in the stator than for 120°. The statoric current reaches 8 pu while transient electromagnetic peak is reduced to 4 pu.

The simulation of the out of phase synchronization points out clearly the interaction between the hydraulic and electric parts of the installation due to the link between the 2 Units through the piping and the electrical lines. Such influence can be analyzed only with hydroelectric simulation model.

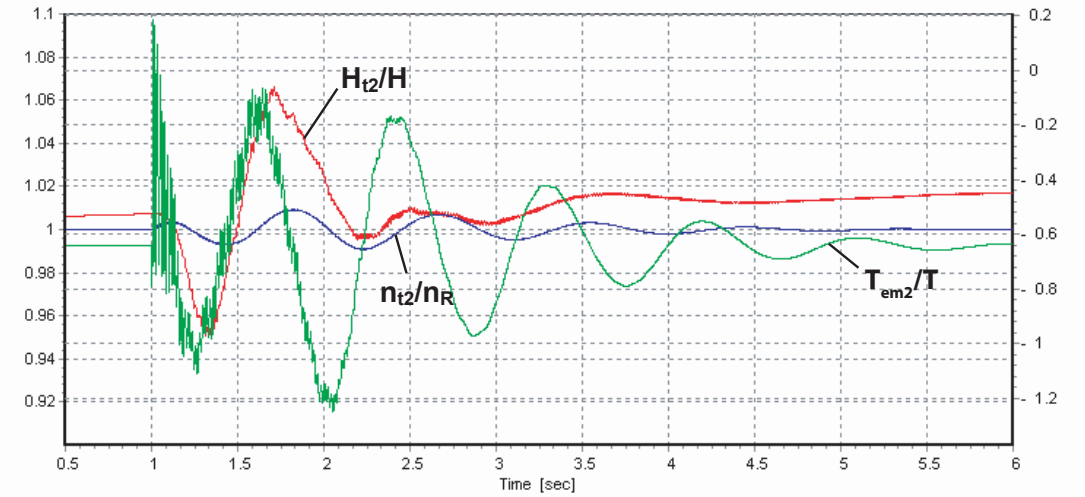

Figure 7.14: Effects of 120° out of phase fault of the Unit 1 on the Unit 2.

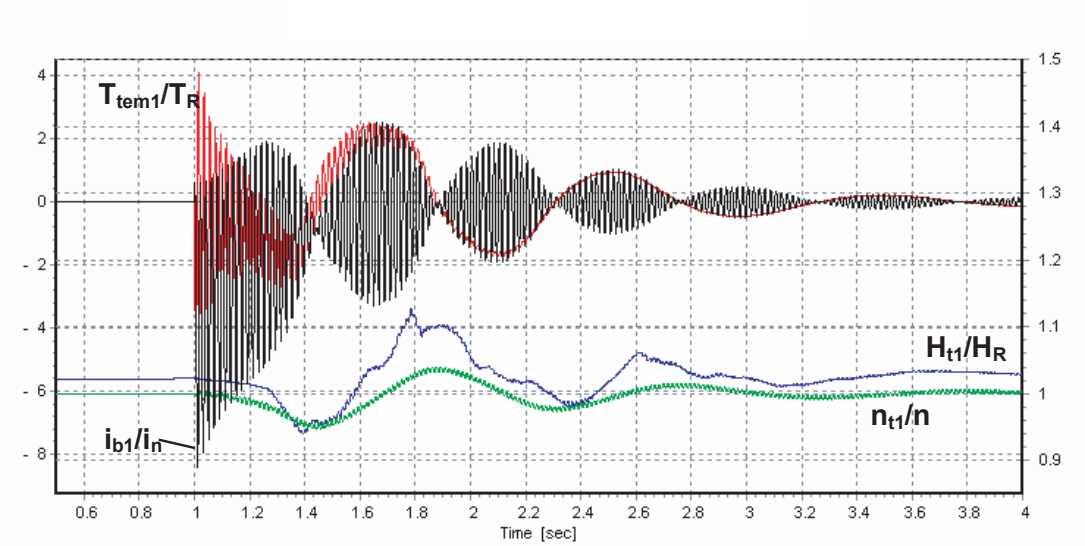

Figure 7.15: Time evolution of the electromagnetic torque, the head of the turbine and rotational speed of Unit 1 due to 180° out of phase synchronization.

7.4 Stability of Turbine Speed Governor

Hydroelectric interactions have been pointed out by simulating classical fault on a hydroelectric power plant such as total load rejection, earth fault and out of phase synchronization. The maximum amplitudes of dimensioning values such as current, pressure, and rotational speed, are properly predicted by either single electric or single hydraulic models as they depend mainly on short term transients. On the other hand differences on long terms transients are highlighted. As a consequence, the difference in the dynamic behavior of the single electric or hydraulic model compared with the hydroelectric model becomes more significant when the focus is put on the stability of the turbine speed governor.

This is the reason why the stability of turbine speed governor during load rejection is investigated using 2 different simulation models: (i) a hydraulic model and (ii) a hydroelectric model. In order to emphasize the possible interactions, the case of an islanded production mode resulting from the disconnection from the infinite electrical grid is simulated using the hydroelectric model.

7.4.1 Case Study Definition

The investigated hydroelectric power plant comprises an upstream reservoir, a 1100 meters long penstock, a 230 MW Francis turbine connected by mechanical inertias to a 250 MVA synchronous generator linked to a 205 kV infinite network through a 17.5/205 kV transformer. A passive RL load is also connected on the high voltage side. The layout of the hydroelectric power plant is presented by figure 7.16. The main dimensions of the power plant are summarized in table 7.6. The installation is driven by a turbine speed governor and a generator voltage regulator. Both are of the PID type.

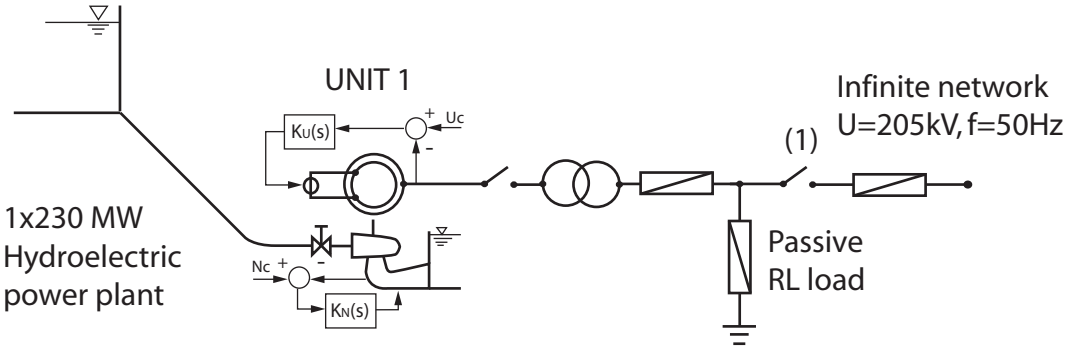

Figure 7.16: Layout of the hydroelectric power plant case study.

The transient behavior investigated is a 25% load rejection simulated as follows:

- (i) hydroelectric model: the infinite power network is disconnected at $t = 10\ s$ by tripping the circuit breaker (1), see figure 7.16. The synchronous generator faces an isolated production mode, *i.e.* connected with only the passive RL load 25% smaller than the original condition;

Table 7.6: Main dimensions of the power plant.

Reservoir	Penstock	Turbine	Generator
$H_o = 315\ m$	$L = 1100\ m$	$H_n = 309\ m$	$S_n = 250\ MVA$
	$D = 5\ m$	$Q_n = 85.3\ m^3/s$	$U_n = 17.5\ kV$
	$\lambda = 0.02$	$N_n = 375\ rpm$	$f = 50\ Hz$
	$a = 1100\ m/s$	$T_n = 5.85 \cdot 10^6\ Nm$	pair pole = 8
		$J_t = 5 \cdot 10^4\ kg \cdot m^2$	$J_g = 1 \cdot 10^6\ kg \cdot m^2$
			$K_{shaft} = 5 \cdot 10^8\ Nm$

- (ii) hydraulic model: the dynamic behavior of the synchronous generator is modelled by a constant torque dropping by 25% instantaneously at $t = 10s$.

The initial conditions in terms of power distribution are given in table 7.7.

Table 7.7: Initial conditions of power distribution.

Element	Active Power	Reactive Power
Generator	$P = -200$ MW	$Q = -100$ MVAR
Passive Load	$P = 150$ MW	$Q = 50$ MVAR
Network	$P = 50$ MW	$Q = 50$ MVAR

7.4.2 Simulation Results and Analysis

The simulation results of the 25% load rejection obtained with the hydraulic and the hydroelectric models are presented respectively in figure 7.17 top and bottom. The time evolution of the rated head H/H_n, discharge Q/Q_n, rotational speed N/N_n, torque T/T_n, guide vane opening y and electromagnetic torque T_{el}/T_n are represented. It can be seen that the simulation results obtained using the hydraulic model is fully stable and stable operating conditions are recovered $40s$ after the disturbance. However, using the same turbine speed governor settings with the hydroelectric model leads to a dynamic response at the limit of stability of the system, and after $90s$, the system still not recovers stable operating conditions. This difference is due to the strong influence of the dynamic behavior of the electrical installation in the isolated production mode. This difference is evidenced by the time evolution representation of the rated electromagnetic torque T_{el}/T_n obtained with that of the hydroelectric model compared with the hydraulic model. This means that **for isolated production modes, the set of parameters of a turbine speed governor cannot be determined with only a hydraulic simulation model.**

In order to deeply analyze the dynamic behavior of both models, the transfer function of the turbine $G(s)$ is identified by simulation considering the guide vane opening y as input variable and the turbine rotational speed N as output variable. The transfer function of the turbine is expressed in the Laplace domain as follows:

$$G(s) = \frac{N(s)}{Y(s)} \tag{7.2}$$

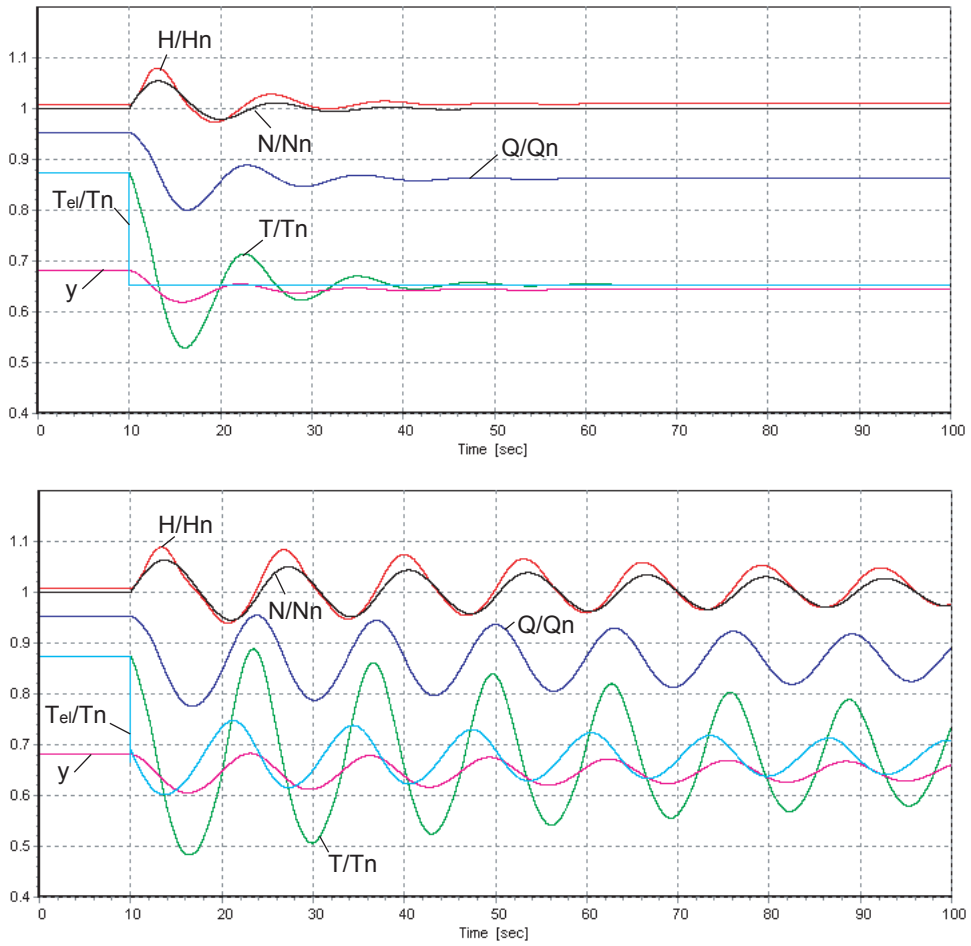

Figure 7.17: Simulation results of the transient of the Francis turbine resulting from a 25% load rejection with the hydraulic model (top) and the hydroelectric model (bottom).

A PRBS signal of 2% amplitude is superimposed on the mean value of the guide vane opening y for the identification of the transfer function of the turbine. From the time domain simulation the time history of the rated rotational speed and of the guide vane opening are used for the calculation of the transfer function using the hydraulic and hydroelectric models. The 2 resulting transfer functions are compared in figure 7.18. First, the natural frequencies of the mechanical inertias are visible at 3.5 Hz and 16.3 Hz. The lowest one is an anti-resonance of the generator inertia while the second one is the resonance of the turbine inertia. The odd eigen frequencies of the penstock are also visible for $f = 0.25, 0.75, 1.25,$ Hz and so on, corresponding respectively to $f = a/(4l), 3a/(4l), 5a/(4l)$, and so on, up to the 20^{th} eigen frequency as the penstock is modelled using 20 nodes.

However, the 2 transfer functions are almost identical except for very low frequencies where the amplitude of the hydroelectric transfer function exhibits much higher amplitudes than the hydraulic transfer function. These high amplitudes result from the dynamics of the electrical installation in the isolated production mode. Because this difference appears at very low frequency, it restrict the performances of the turbine speed governor.

As consequence, to be stable in the hydroelectric production mode, the integrator time constant T_i of the PID turbine speed governor is increased to reduce the amplification at low frequencies. The initial integration time constant was $T_i = 3.7\ s$ and is increased to $T_i = 14\ s$ to have an efficient governor; the gain and the derivative time constant remain unchanged ($K_p = 1, T_d = 1.21\ s$). The simulation results of the dynamic behavior of the installation resulting from a 25% load rejection using the hydroelectric model is presented in figure 7.19. It can be seen that, as expected, the system is again fully stable in the isolated production mode.

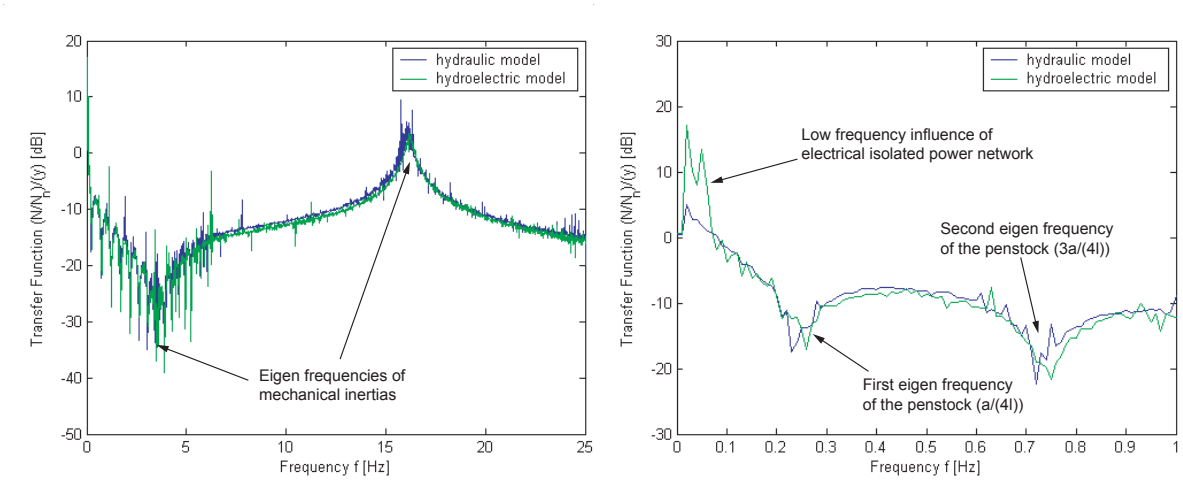

Figure 7.18: Transfer function of the turbine $G(s) = N(s)/Y(s)$ in the range $0 \rightarrow 25Hz$ on the left, and $0 \rightarrow 1Hz$ on the right.

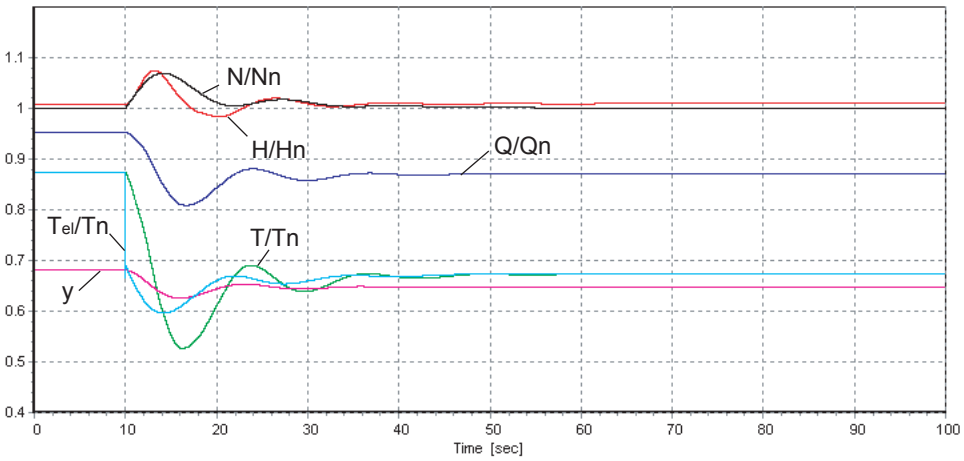

Figure 7.19: Simulation results of the transient of the Francis turbine resulting from a 25% load rejection with the hydroelectric model and the modified integration time constant of the turbine speed governor.

7.5 Hydroelectric Stability in Islanded Production Mode

Islanded power networks feature a small number of power plants and loads leading to high interactions between all the components. Therefore high performance governors must be used for each power unit. It is even more important for hydraulic power plants having a dynamic behavior strongly related to the hydraulic circuit layout. Since every hydraulic power plant is unique, no standard governor setting can be used. Hydraulic power plants featuring a long penstock and a surge tank need to be properly modelled in order to take into account waterhammer, surge tank water level oscillations and the effects of the turbine characteristics. All these phenomena present a non-linear behavior, thus restricting the performances of the turbine speed/power governor. To ensure the stability of the turbine governor, the governor parameters have to be validated by a time domain simulation. The order of the model of the hydraulic installation has to be adapted to the hydraulic layout and the investigated case, as advised by the "working group on prime mover and energy supply models for system dynamic performance studies" [92]. It appears that hydroelectric power plants featuring a surge tank and a long penstock connected to an islanded power network require a high order model. Such an installation is investigated in this section.

7.5.1 Case Study Definition

The investigated test case is an islanded power network comprising:

- a 1 GW hydroelectric power plant with 4×250 MW Francis turbine;
- 4×1.3 GW thermal power plants;
- 2 passive consumer loads: one 200 MW load that can be tripped and one 2.1 GW to 6 GW whose power is adapted to the network power level considered.

The 5 power plants and the 2 loads are connected through a 400 kV transmission line network as presented by figure 7.20. The case is investigated with a 3-step approach. (i) The modelling of a 1 GW hydroelectric power plant in an islanded power network considering the waterhammer effects, the surge tank water level oscillations and the dynamics due to turbine characteristics is performed. The determination of the governor parameters is based on the identification of the turbine transfer function using a time domain simulation with a PRBS excitation. (ii) A 1.3 GW thermal power plant is modelled using a simplified approach based on the steam flux. (iii) Combining both models, the whole 6.2 GW islanded power network comprising the 4 thermal and the hydraulic power plants is set up. The turbine governor performances are assessed for 5 different hydro to thermal power ratios.

7.5.2 Modelling of the Hydroelectric Power Plant

Hydraulic power plant model

The power plant is made of a $1'515$ meters long gallery, a surge tank with variable section, a $1'388$ meters long penstock and a manifold feeding 4×245 MW Francis turbines. The

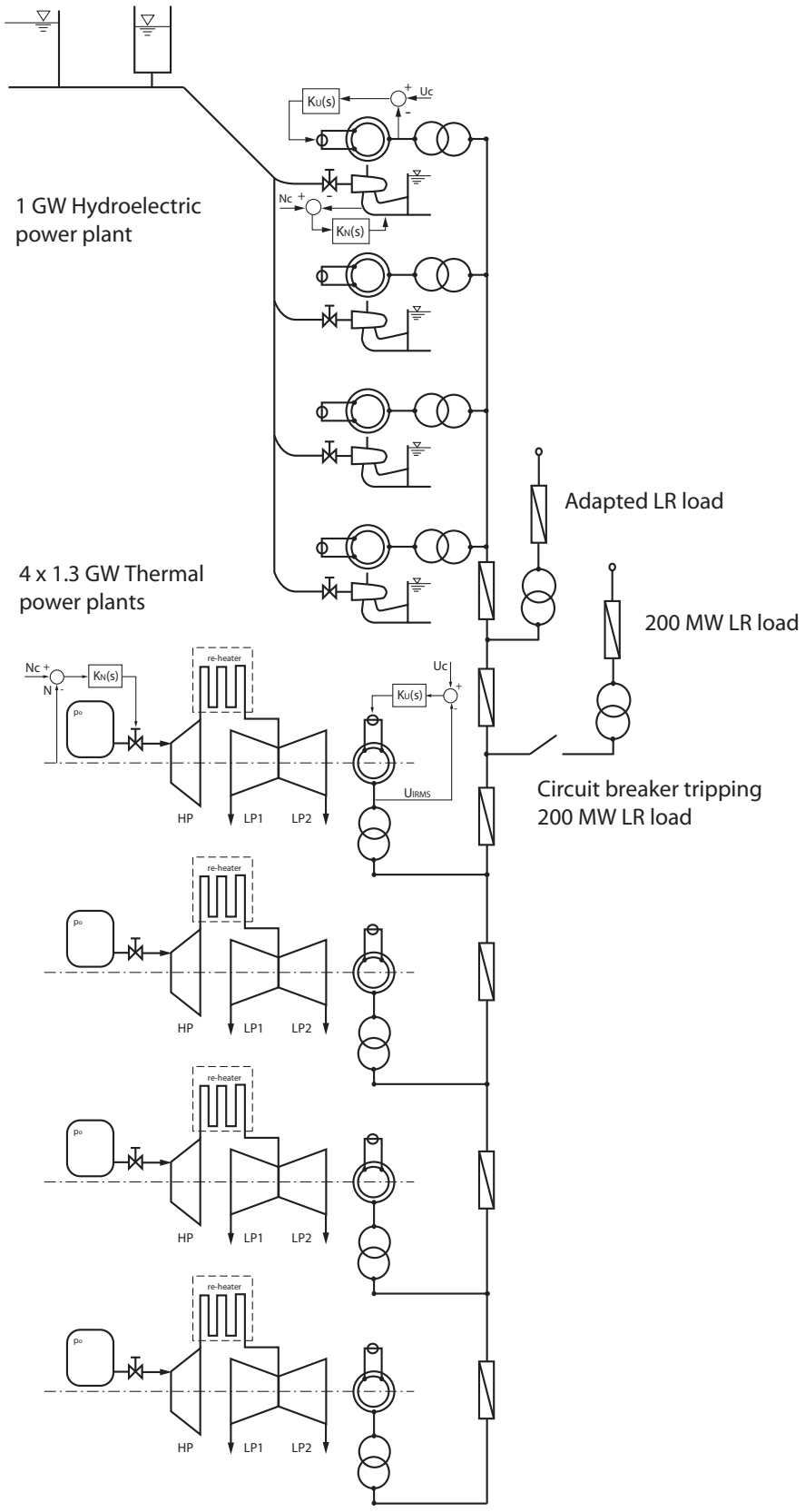

Figure 7.20: Islanded power network structure.

main parameters of the hydraulic circuit are summarized table 7.8.

Table 7.8: Main dimensions of the hydraulic installation.

Element	Dimensions
Reservoir	$H_o = 364\ m$
Gallery	$L = 1'515\ m$ $D = 8.8\ m$ $a = 1'000\ m/s$
Surge tank	Mid tank section: $A_{ST} = 133\ m^2$
Penstock	$L = 1'388\ m$ $D = 8.8/7.15\ m$ $a = 1'200\ m/s$
Francis turbine	$P_n = 250\ MW$ $N_n = 333.3\ rpm$ $Q_n = 75\ m^3/s$ $H_n = 350\ m$ $\nu = 0.23$ $D_{ref} = 2.82\ m$ $J_t = 1.7 \cdot 10^5\ kg \cdot m^2$
Generator	$S_n = 270\ MVA$ $U_n = 18\ kV$ $f = 50\ Hz$ Pole pairs: $p = 9$ Stator windings: Y $J_G = 1.54 \cdot 10^6\ kg \cdot m^2$
Coupling shaft	$K = 3.62 \cdot 10^8\ Nm/rad$ Viscous damping: $\mu = 6.7 \cdot 10^3\ Nms/rad$

The gallery and the penstock are respectively discretized into 22 and 31 elements. The turbine draft tube is also modelled by 2 pipe elements. The Francis turbine characteristics, discharge and torque factors versus the speed factor are presented for different guide vane opening values y, see figure 7.21.

The block diagram of the PID governor of the Francis turbine is presented in figure 7.22. The governor structure includes both speed and power feedbacks. The network frequency feedback is neglected in this study because only islanded and isolated production modes are considered. The servomotor of the guide vanes is modelled using a first order transfer function with a time constant of $\tau_{sv} = 0.1\ s$.

Turbine governor parameters determination

The transfer function of the system to be regulated, $G(s)$, should be determined for setting the parameters of the turbine governor. The system consists of a turbine with the guide vane opening y as input parameter and the rotational speed N as output parameter. The transfer function of the turbine is identified for 4 different power levels: $P/P_n = 0.4, 0.7, 1$

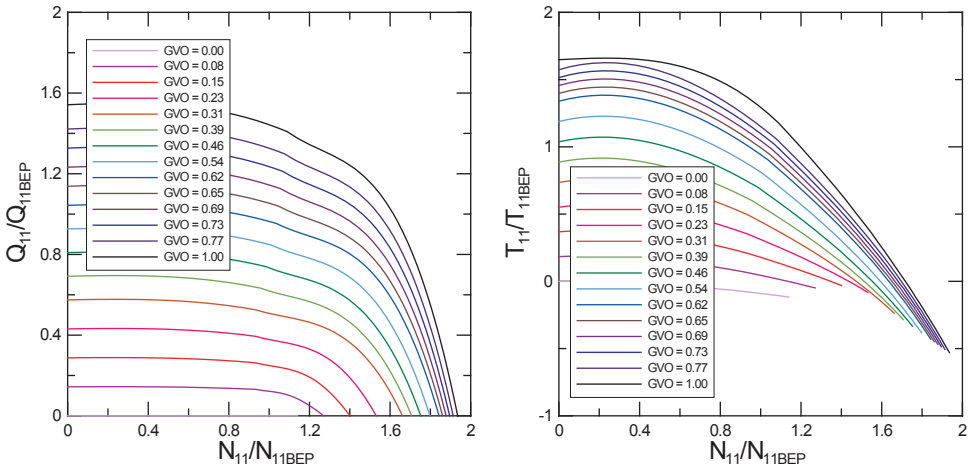

Figure 7.21: Turbine characteristics $Q_{11} = Q_{11}(N_{11})$, left, and $T_{11} = T_{11}(N_{11})$, right, for different GVO opening.

and 1.15 *p.u.*, in order to take into account the influence of the local gradient of the turbine characteristics.

The model of the hydraulic installation setup using SIMSEN-Hydro is of a high order (up to 150 ODE), however the transfer function of the system cannot be directly inferred from them. The transfer function of the turbine including the hydraulic circuit is identified through a time domain simulation considering a white noise excitation. A PRBS signal of 5% amplitude around a mean value of guide vane opening is used as excitation signal, see figure 7.23. The mean value is set in accordance with the turbine power for which the transfer function is identified. The PRBS excitation function [91] is preferred to an indicial response because of its higher frequency content that evidences all natural frequencies of the system. The PRBS signal is obtained using a shift register [36].

The amplitude and phase spectra of the turbine transfer function obtained from the PRBS identification, for $P/P_n = 0.4$ is presented in figure 7.24. The amplitude of the transfer function reveals that the hydraulic system natural frequencies are mainly related to the piping system, the mechanical masses and the surge tank. The first natural frequency of the piping system is $f_o = 0.2\ Hz$ and corresponds to the fourth wavelength free oscillation mode of the penstock given by $f = a/(4l)$. The natural frequencies above correspond to higher mode eigen frequencies of the piping system. The natural frequency of the mechanical masses presents a high amplitude at $f_m = 7.6\ Hz$ and is given by [75]:

$$\omega^2_{m1,2} = \frac{1}{2} \cdot \left(\Omega_1^2 + \Omega_2^2\right) \pm \sqrt{\left(\frac{\Omega_2^2 - \Omega_1^2}{2}\right)^2 + \Omega_{12}^4} \tag{7.3}$$

Where :

$$\Omega_1^2 = \frac{K_{shaft}}{J_G} \quad ; \quad \Omega_2^2 = \frac{K_{shaft}}{J_T} \quad ; \quad \Omega_{12}^4 = \frac{K_{shaft}^2}{J_G \cdot J_T} \tag{7.4}$$

The anti-resonance of the generator inertia corresponding to Ω_1 is also visible for $f_m = 2.44$ Hz. The eigen frequency of the mass oscillation between the upstream reservoir and

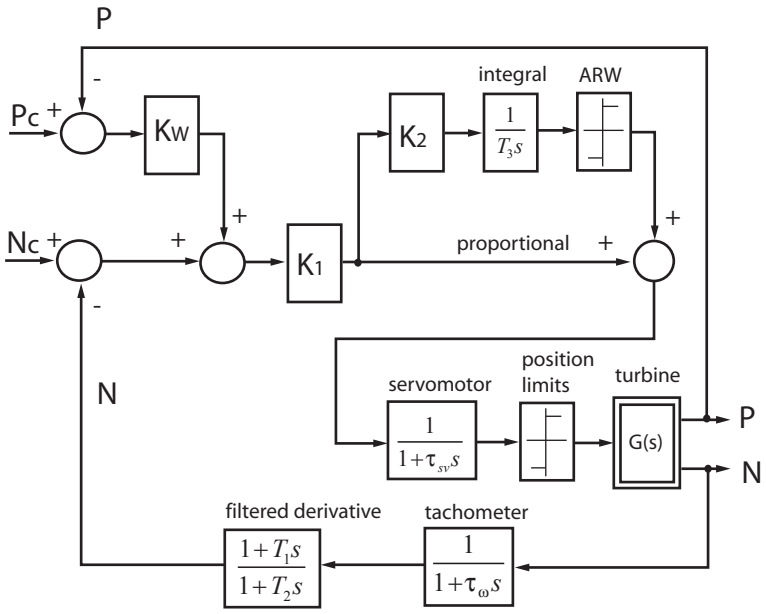

Figure 7.22: Block diagram of the turbine governor.

the surge tank is calculated with equation 6.6 and is equal to $f_{ST} = 0.00866\ Hz$, *i.e.* $T_{ST} = 115.5\ s$. This frequency is visible also as an anti-resonance on the spectrum. The anti-resonance behavior results from the fact that when more power is required, the guide vanes open, resulting in an increase of the discharge coming from the surge tank but reducing its water level, thus the available head at the turbine inlet. As a consequence, the hydraulic power may decrease depending on the governor action. Similarly, the gate opening induces a pressure drop at the turbine inlet resulting from a waterhammer effect leading to a non-minimum phase visible on the lin-lin phase plot. The non-minimum phase corresponds to half a period of the penstock, *i.e.* 2.5 seconds. This non-minimum phase is clearly pointed out in figure 7.25 where the guide vane step response are simulated for the

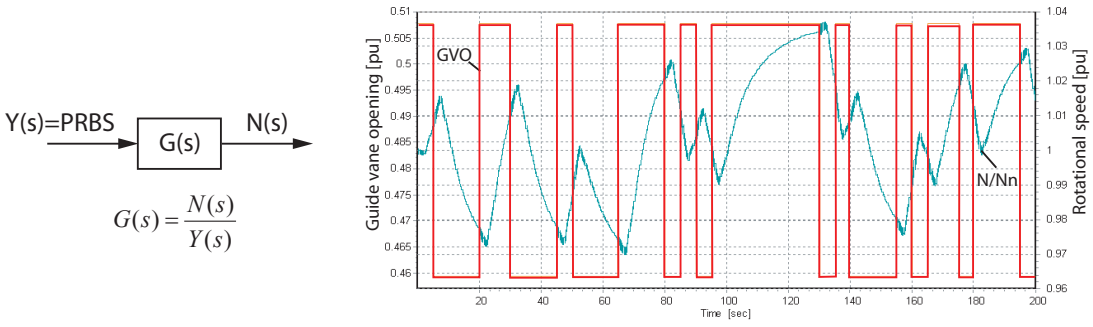

Figure 7.23: Open loop transfer function identification with a PRBS excitation for $P/P_n = 0.4$.

4 different power levels. It can be noticed that even if the guide vanes open, the rotational speed does not increase immediately due to the waterhammer under pressure. It can be also noticed that the higher the power level the higher the non-minimum phase influence. Therefore, this non-minimum phase is strongly restrictive for the governor performance. A large integrator time constant T_i is consequently required to ensure the system stability.

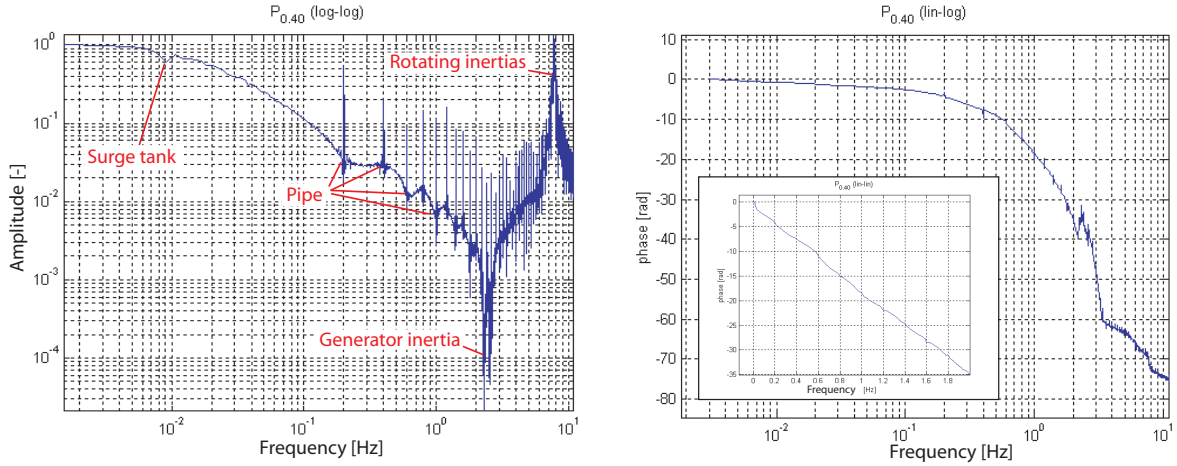

Figure 7.24: Amplitude (left) and phase (right) of the transfer function of the Francis turbine for $P/P_n = 0.4$ including the hydraulic circuit and mechanical inertia.

The transfer function of the turbine is identified for the 4 power levels considered $P/P_n = 0.4, 0.7, 1$ and 1.15 $p.u.$ and are represented in figure 7.26. As the 4 transfer functions are different because of the turbine characteristic, the determination of the PID parameters is based on the most restrictive one, *i.e.* on the most critical behavior of the system. The parameters of the governor are set in order to ensure a phase margin of $60 - 90^{\circ}$, a gain margin of $6 - 9$ dB, a cut-off frequency of 0.02 Hz to avoid resonance amplification and a slope of -20 dB/decade at the cut-off frequency.

Then, the assessment of the regulator performance is performed by simulating the dynamic behavior of the hydraulic power plant resulting from a successive 6% load rejection and acceptance for $P/P_n = 0.4, 0.7, 1$ and 1.15 $p.u.$. The electromagnetic torque is modelled by an external torque function which does not take into account the dynamic behavior of any electrical installation. The resulting time evolution of the rotational speed N/N_n and guide vane position y are presented in figure 7.27 for $P/P_n = 0.7$ and 1.15 $p.u.$. The speed deviations obtained from the simulation correspond to 1.5% and 4.5% of the nominal speed. For $P/P_n = 0.7$ $p.u.$ the speed is stabilized after 10 seconds while it takes 150 seconds to stabilize the speed for $P/P_n = 1.15$ $p.u.$ The full load appears to be more critical because of the influence of the surge tank. A surge phenomenon occurs between the PID governor and the surge tank. It is clearly visible from the time evolution of the guide vane opening that fluctuates at the mass oscillation period ($T_{ST} = 115$ s). The cross section of the surge tank is far from the Thoma section calculated to be $80m^2$ according to equation 6.28. It appears clearly that this criterion is not sufficient, especially at full load where the turbine efficiency gradient becomes negative ($d\eta/dQ < 0$). The governor parameter values have to be validated by a time dependent simulation to ensure

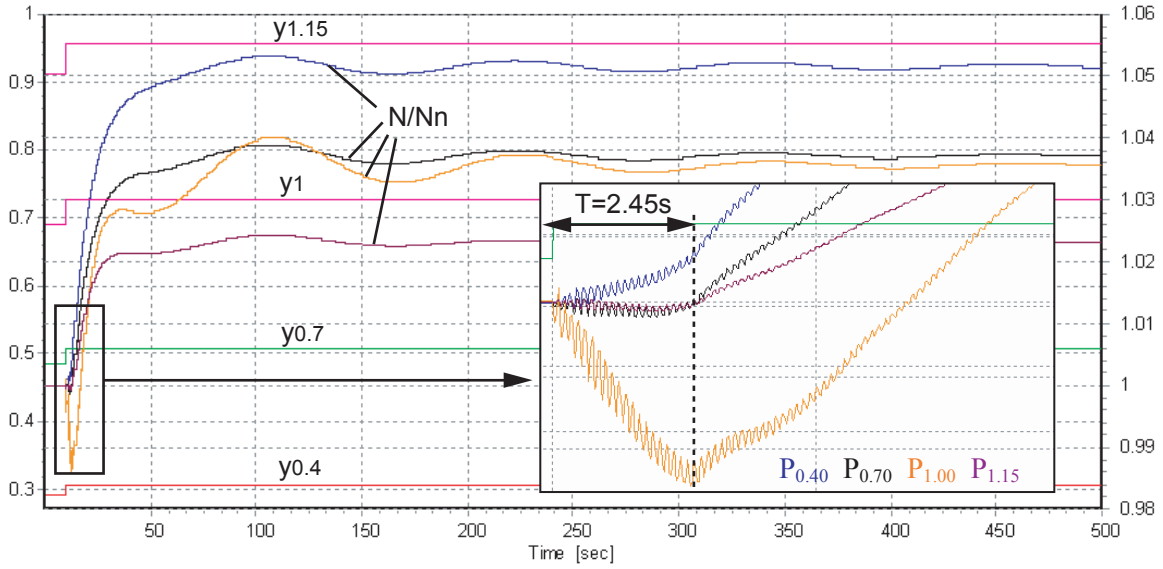

Figure 7.25: Non-minimum phase of the turbines evidenced by rated transient rotational speed N/N_n resulting from a guide vane opening step response for different power levels $P/P_n = 0.4, 0.7, 1, 1.15$.

the stability on the whole operating range, even for large stroke variation of the guide vanes.

7.5.3 Modelling of the Thermal Power Plant

The turbine governor parameter values are validated only with the hydraulic simulation model. To investigate the influence of the connection to an islanded power network, a model of a thermal power plant is set up. The thermal power plant is modelled with a constant pressure tank, the steam generator dynamic being neglected, feeding the High Pressure steam turbine (HP) through a regulating valve. Then the vapor flux transits through a re-heater before feeding 2 Low Pressure (LP) steam turbines as presented in figure 7.28. The model of this thermal power plant is made of a proportional governor with a frequency drop feedback and a speed feedback, a valve model, the model of the HP, LP1 and LP2 steam turbines and the mechanical masses as presented in figure 7.29. The parameter values of the model are given in table 7.9. The model of the steam turbines is made of 3 parallels branches, one for each steam turbine, driven by the valve opening. A time delay of $b = 4$ seconds is considered between the high pressure steam turbines and the low pressure steam turbines to take into account the transit time of the steam through the re-heaters. The 3 turbines are modelled by first order transfer functions with a short time constant for the high pressure and a long time constant for the low pressure steam turbines. The model includes also simplified steam turbines characteristics that are deduced from [9]. The inertia, stiffness and damping of the mechanical shaft are obtained from [37]. The synchronous machine excitation is controlled by a ABB Unitrol voltage

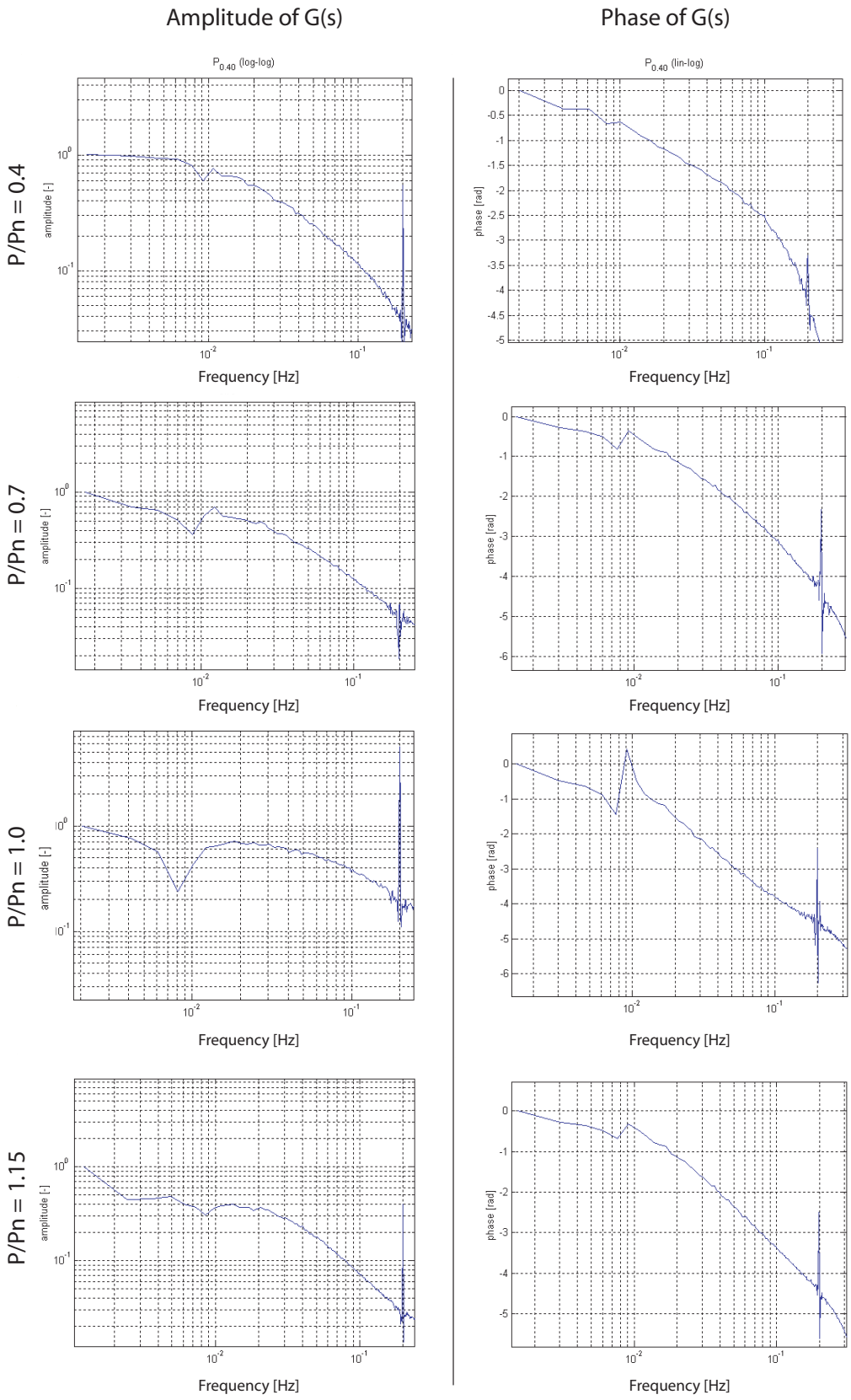

Figure 7.26: Amplitude (left) and phase (right) of the transfer function of the Francis turbine for $P/P_n = 0.4, 0.7, 1$ and 1.15 $p.u.$.

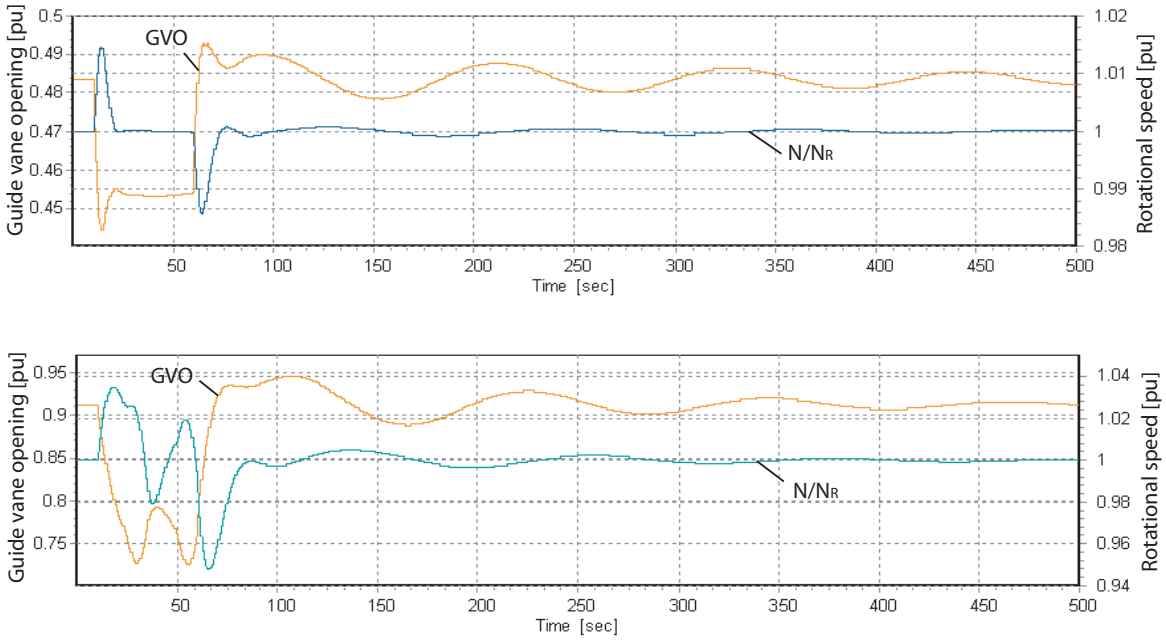

Figure 7.27: Time evolution of rotational speed N/N_n and guide vane opening GVO of the Francis turbine during a 6% load rejection at 0.7 $p.u.$ (top) and 1.15 $p.u.$ (bottom) power level.

regulator. The synchronous machine is connected to a 28.5/400 kV transformer with Yd5 connection. As the synchronous machine is of the solid iron rotor type, its modelling takes into account the damping of the windings, saturation and leakage effects.

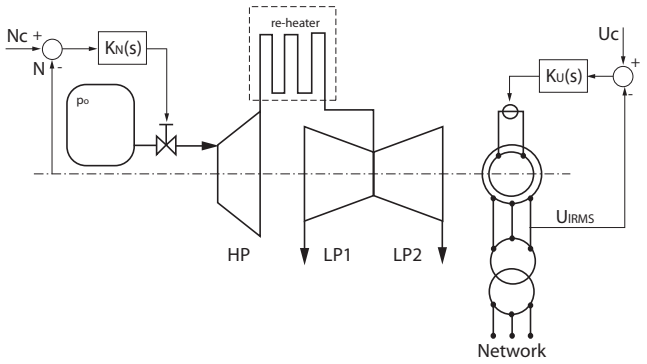

Figure 7.28: Layout of the thermal power plant.

The dynamic response of the thermal power plant is investigated for a 6% load rejection. The time evolution of the rotational speed N/N_R, the electromagnetic torque T_{em}/T_R and the valve opening y_{valve} are represented in $p.u.$ in figure 7.30. The rotational speed recovers stability after 10 seconds, demonstrating that the dynamic response of the thermal power plant is very efficient. However, due to the proportional nature of the gov-

ernor, a static error can be noticed after full stabilization of the system. The pressurized steam reservoir enables the thermal power plant to have short time constant. The static error is not compensated because steam generator dynamic is neglected. The transient response of this thermal power plant was validated by comparison with measurements on a power plant performed by EDF [24].

Table 7.9: Main dimensions of the thermal power plant.

Element	Dimensions
Steam turbines model	$\tau_{HP} = 0.5\ s$ $\tau_{LP} = 12\ s$ $b = 4\ s$ $K_p = 25$
Mechanical inertias	$J_{HP} = 1.867 \cdot 10^4\ kg \cdot m^2$ $J_{LP1} = 1.907 \cdot 10^5\ kg \cdot m^2$ $J_{LP2} = 2.136 \cdot 10^5\ kg \cdot m^2$ $J_{gen} = 5.223 \cdot 10^4\ kg \cdot m^2$
Mechanical shaft stiffness and damping	$K_1 = 3.614 \cdot 10^8\ Nm/rd$ $K_2 = 8.206 \cdot 10^8\ Nm/rd$ $K_3 = 4.116 \cdot 10^8\ Nm/rd$ $\mu_1 = 6.719 \cdot 10^3\ Nms/rd$ $\mu_2 = 7.06 \cdot 10^3\ Nms/rd$ $\mu_3 = 7.06 \cdot 10^3\ Nms/rd$
Generator	$S_n = 1400\ MVA$ $U_n = 28.5\ kV$ $f = 50\ Hz$ Polepaire: $p = 2$ Stator windings: Y

7.5.4 Simulation of a Load Rejection in Islanded Power Network

To investigate the influence of the power network, a simulation model of an islanded power network is build up. The islanded power network of concern, see figure 7.20, is composed of the hydraulic power plant, 4 thermal power plants and 2 passive consumer loads. The 5 power plants represent all together a 6.2 GW power network. Figure 7.31 presents the topology of this power network where the power plants are connected to 2 passive consumer loads through 400 kV transport lines. The LR parameters of the 2 consumer loads are set in order to absorb the production of all the power plant of the network. One is a 200 MW load and the other one represents the complement to the total power of the islanded power network. In order to investigate the transients due to a load rejection, the 200 MW consumer load is disconnected by tripping the circuit breaker considering the 5 different network power levels given in table 7.10.

For completness, the electrical installation of the hydroelectric installation is included in the simulation model. The 4 hydrogenerators are 270 MVA synchronous machines and are connected to the islanded network through 18.5/400 kV Yd5 transformers. The

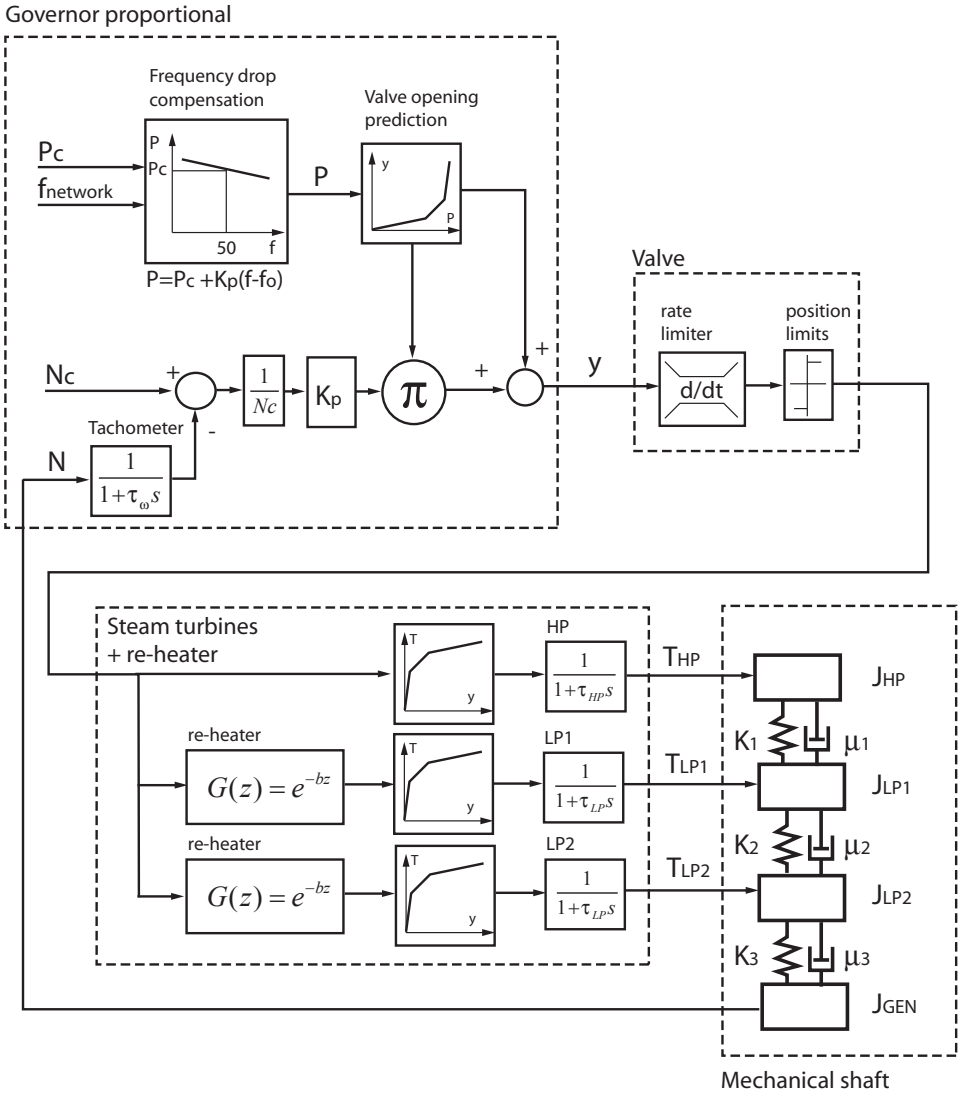

Figure 7.29: Block diagram of the model of the thermal power plant.

Table 7.10: Power distribution.

Hydraulic Power Production P_{hydro}	**Thermal Power Production** P_{TH}	**Power Ratio** P_{Hydro}/P_{tot}
1 GW	1.3 GW	0.43
1 GW	2.6 GW	0.28
1 GW	3.9 GW	0.20
1 GW	5.2 GW	0.16
1 GW	∞	0

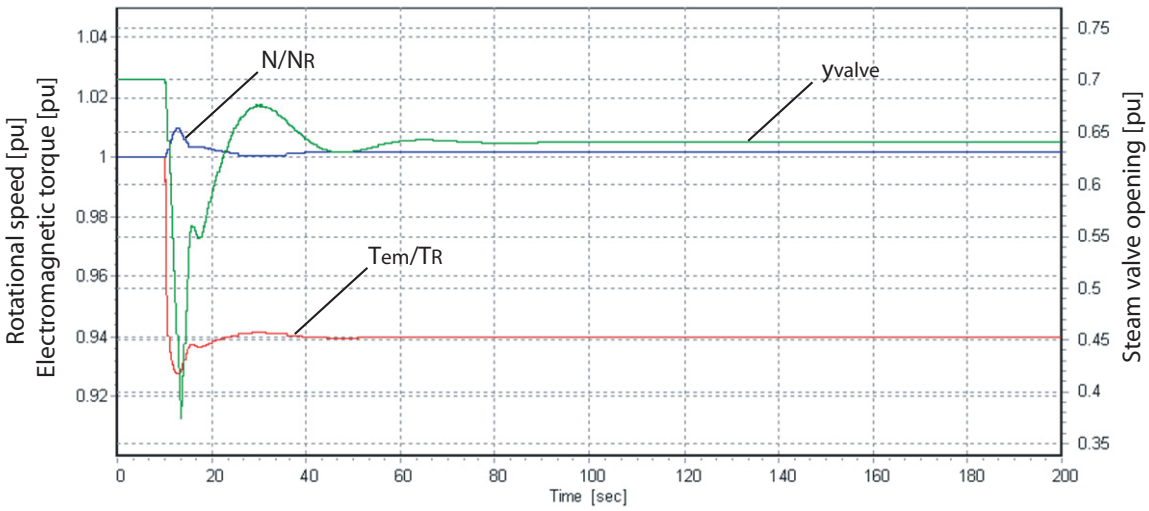

Figure 7.30: Transient response of the 1300 MW thermal power plant resulting from a 6% load rejection.

synchronous machine excitations are controlled by an ABB Unitrol voltage regulators. The synchronous machines are of the laminated rotor type. The model is considering saturation, leakage and damping effects of windings, allowing taking into account a sub-transient behavior.

The Power System Stabilizers -PSS- of the hydroelectric power plant is not considered in this investigation in order to focus on the performances and stability of the turbine speed governors. The use of PSS would help reducing the speed deviations as demonstrated by Kamwa *et al.* [56] but the influence of such device is out of the scope of the present work

Frequency analysis

The transfer function of the turbine connected to the power network is re-identified for 3 different network power levels: $P_{tot} = \infty$, 6.2 and 2.3 GW, the power of the hydraulic power plant being 1 GW. The amplitude spectra of the resulting transfer function are presented by figure 7.32. From the new transfer function an additional natural frequency with high amplitude is pointed out at $1.36Hz$. This corresponds to the synchronous machine natural frequency that depends on the operating point of the generator, voltage regulator and system configuration [59]. The source of this frequency was checked by introducing a sinusoidal excitation added to the wicket gate mean value in open loop conditions.

A high stabilization effect of the power network can be noticed on the amplitude spectrum of the turbine transfer function for the low frequencies. The attenuation and the frequency range affected by the network become smaller as the level of the power network decrease. The power network behaves like a high-pass filter. It means that the perturbations of the rotational speed at low frequencies are compensated by the power network "stiffness" and that the higher the power level of a network, the lower the performances of the governor required.

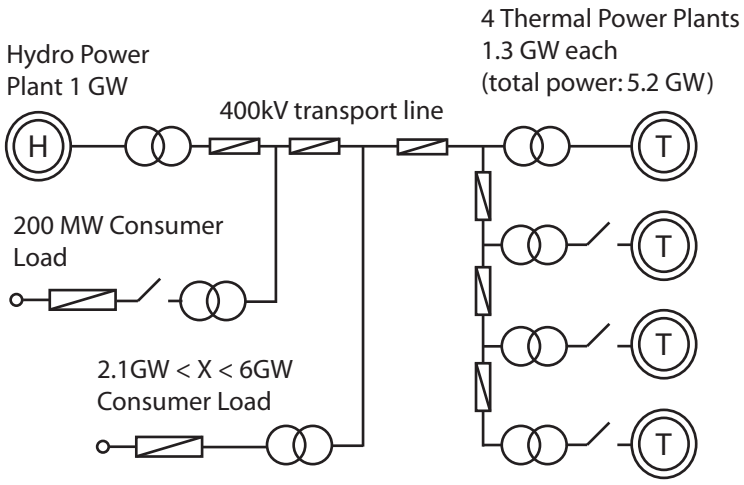

Figure 7.31: Islanded power network.

Transient analysis

A time domain simulation of the tripping of the 200 MW consumer load is performed without considering the synchronous machine natural frequency in the turbine speed governor design. The resulting turbine rotational speed evolutions are presented figure in 7.33. As expected, whatever the power level of the network, the turbines operation is unstable and the rotational speed exhibits a fluctuation at 1.36 Hz. To avoid a resonance between the turbine speed governor and the synchronous machine, the filter time constant of the turbine rotational speed is reduced to $\tau = 0.3\ s$. Consequently, the turbine rotational speed remains stable as presented in figure 7.34. As expected from the turbine transfer function analysis, the islanded network power level has a strong influence on the speed deviation. For infinite power level the tripping of the 200 MW load is almost not perceptible while for a ratio $P_{Hydro}/P_{tot} = 0.43$ the speed deviation reaches 3.5%. The amplitudes of the speed deviation are reported in figure 7.35 as a function of the ratio between the power of the hydraulic part (1 GW here) and the power of the whole network.

7.5.5 Concluding Remarks

This investigation demonstrates the importance of a high order modelling in the case of a hydroelectric power plant featuring a surge tank with small diameter and a long penstock in islanded power networks. A detailed set up and an analysis procedure necessary to ensure the hydraulic turbine governor stability are presented. The case of a 1 GW hydroelectric power plant connected to a 5.2 GW islanded power network is investigated. The transfer function of the hydraulic turbine is identified using a time domain simulation with a PRBS excitation. This method has the advantage to evidence all the natural frequencies of the hydraulic system. The governor performances are tied to the natural frequencies of the power plant. To overcome the restrictions on the stability criterion of the surge tank due to the turbine characteristics linearization, the turbine governor parameters are validated by time domain simulations. The analysis of the transfer function of the tur-

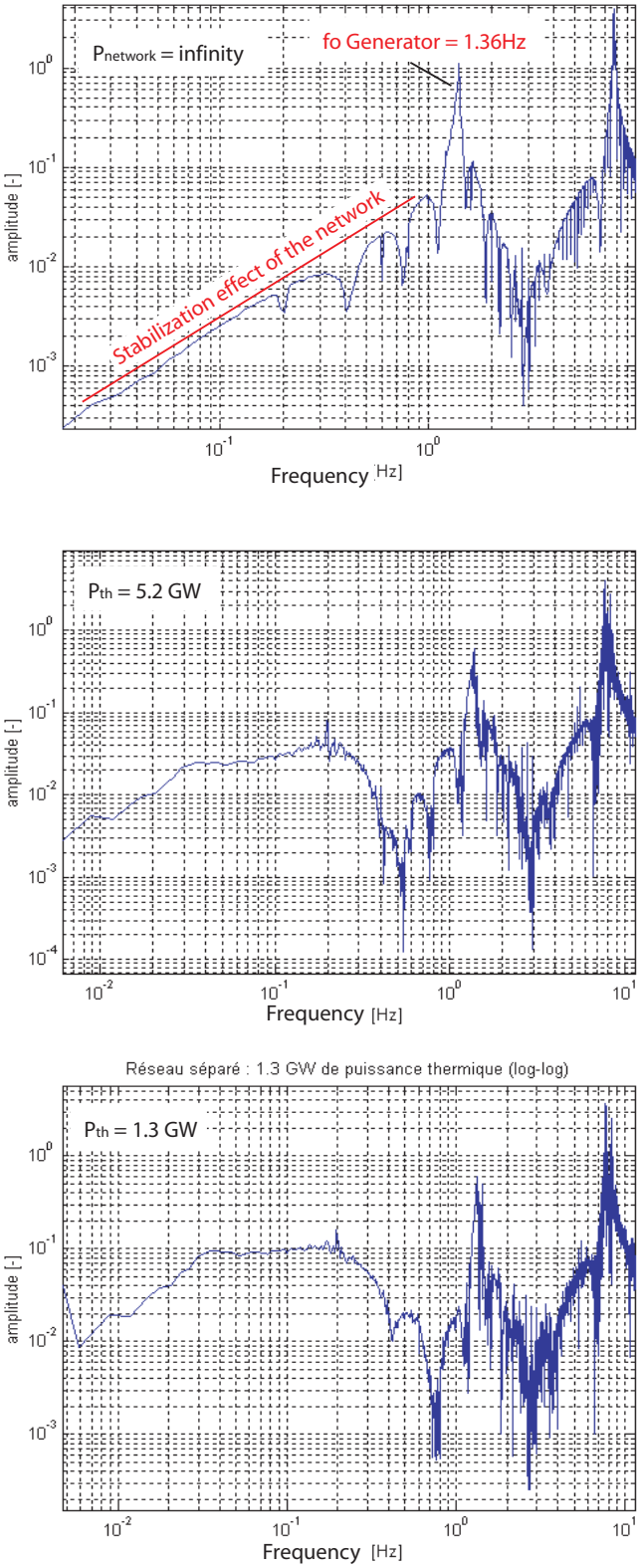

Figure 7.32: Francis turbine transfer function considering connection to an infinite power network (top), 5.2 GW power network (middle) and 1.3 GW power network (bottom).

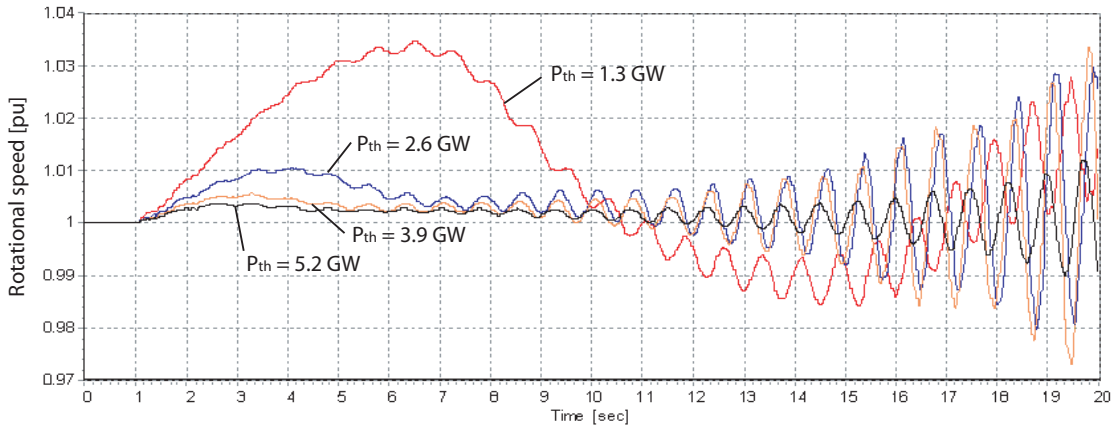

Figure 7.33: Francis turbine rotational speed evolution after 200 MW load tripping for $P_{Hydro}/P_{tot} = 0.43, 0.28, 0.2$ and 0.16 without filter modification.

bine in different islanded production levels, evidences a stabilization effect below 1 Hz in larger power networks. In the case of weak power networks, the stability of hydraulic installations with a long penstock featuring natural frequencies in this frequency range can be strongly affected. A study taking all these considerations into account eases the final tuning of governors and hence reduces the commissioning delay.

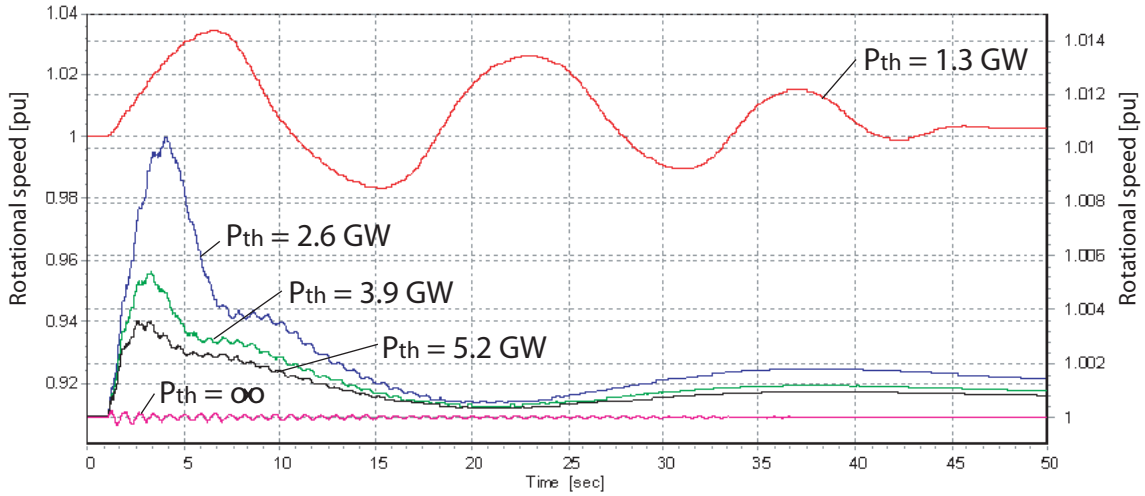

Figure 7.34: Time evolution of the turbine rotational speed resulting from the tripping of a 200 MW load for different thermal power plant level, with filter modification.

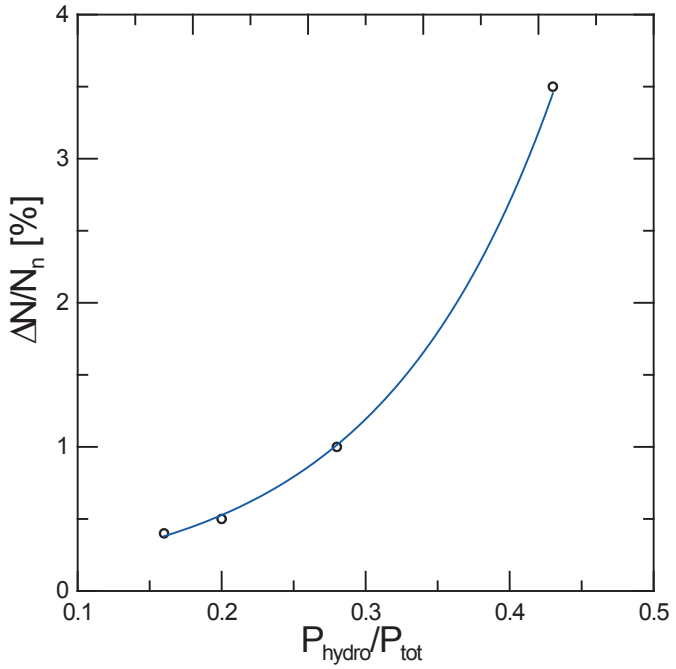

Figure 7.35: Speed deviation due to a 200 MW load tripping as a function of power ratio between the hydraulic power plant and the total power of the islanded power network.

APPENDICES

Appendix A

Numerical Integration Methods

The set of ordinary differential equations (ODE) to be solved in SIMSEN is the following:

$$[A] \cdot \frac{d\overline{x}}{dt} + [B(t,x)] \cdot \overline{x} = \overline{c} \tag{A.1}$$

The integration method used in SIMSEN to solve the system of equation A.1 is the explicit 4^{th} order Runge-Kutta method (RK). This method might presents some restrictions in terms of stability for solving stiff problems. Stiff problems are characterized by:

- high stiffness in the problem resulting in very high eigen frequencies of the system to be solved;
- or, system presenting large differences of order of magnitudes leading to large difference between the smallest and the highest eigen values.

Stiff systems might be encountered in multi-physics system such as hydroelectric power plants where electrical devices present time constants of $\tau = 0.001$ s and hydraulic mass oscillations period of $T = 500$ s. In addition, the explicit RK method presents a stability domain covering the main part of the left hand complex plan that excludes system physically unstable. Therefore, a more robust method for checking the validity of simulation results is necessary. Implicit integration methods are usually used to overcome integration stability problems. Three test cases are considered for comparing the explicit and the implicit methods: (i) waterhammer effect in pipe; (ii) surge effect due to physical instabilities; and (iii) van der Pol equation.

A.1 Integration Methods

The differential equation set of interest can be expressed in the following compact form:

$$\frac{dy}{dx} = f(x,y) \quad ; \quad y(x_o) = y_o \tag{A.2}$$

To solve this ordinary differential equation set, explicit an implicit RK methods are investigated.

A.1.1 Explicit Runge-Kutta Method

The explicit Runge-Kutta s^{th} order method applied to the system A.2 gives:

$$\begin{aligned}
&k_1 = f(x_o, y_o) \\
&k_2 = f(x_o + c_2 \cdot h, y_o + h \cdot a_{21} \cdot k_1) \\
&k_3 = f(x_o + c_3 \cdot h, y_o + h \cdot (a_{31} \cdot k_1 + a_{32} \cdot k_2)) \\
&... \\
&k_s = f(x_o + c_s \cdot h, y_o + h \cdot (a_{s1} \cdot k_1 + ... + a_{s,s-1} \cdot k_{s-1})) \\
&y_1 = y_o + h \cdot (b_1 \cdot k_1 + ... + b_s \cdot k_s)
\end{aligned} \tag{A.3}$$

Where $h = x_1 - x_o$ and the parameters a_{ij}, b_i, c_i are given in the table A.1.

Table A.1: Parameters of the explicit Runge-Kutta method.

0					
c_2	a_{21}				
c_3	a_{31}	a_{32}			
$\vdots$	$\vdots$	$\vdots$	$\ddots$		
c_s	a_{s1}	a_{s2}	$\cdots$	$a_{s,s-1}$	
	b_1	b_1	$\cdots$	b_{s-1}	b_s

Using the simplified approach described by Butcher for a 4^{th} order method, the parameters of table A.1 gives the parameters table A.2:

Table A.2: Parameters of the Runge-Kutta explicit method 4^{th} order.

0				
1/2	1/2			
1/2	0	1/2		
1	0	0	1	
	1/6	2/6	2/6	1/6

The table A.2 gives the following set of equations:

$$\begin{aligned}
&k_1 = f(x_o, y_o) \\
&k_2 = f(x_o + h/2, y_o + h/2 \cdot k_1) \\
&k_3 = f(x_o + h/2, y_o + h/2 \cdot k_2) \\
&k_4 = f(x_o + h, y_o + h \cdot k_3) \\
&y_1 = y_o + h/6 \cdot (k_1 + 2 \cdot k_2 + 2 \cdot k_3 + k_4)
\end{aligned} \tag{A.4}$$

The triangular structure of the table indicates that a k_n can be calculated directly from the previous $k_{i<n}$. No iteration are necessary for the computation of y_1. The method is named ERK.

A.1.2 Implicit Runge-Kutta Method

The implicit s-stage Runge-Kutta method [42] leads to the following expression:

$$\begin{aligned} k_i &= f(x_o + c_i \cdot h, y_o + h \cdot \sum_{j=1}^{s} a_{ij} \cdot k_j) \quad ; \quad i = 1, ..., s \\ y_1 &= y_o + h \cdot \sum_{i=1}^{s} b_i \cdot k_i \end{aligned} \tag{A.5}$$

The table used for the explicit method is extended to the a_{ij} above the diagonal. The method is named IRK method. Then a given k_n is computed by iteration considering $k_{i>n}$. The k_i values converge if the Lipschitz condition (with the L is a constant) is fulfilled:

$$h < \frac{1}{L \cdot \max_i \sum_j |ai_j|} \tag{A.6}$$

Several set of a_{ij}, b_i, c_i parameters can be used and present different stability patterns and have to be chosen by experience depending on the nature of the system to be solved. Here 3 methods are tested, the Euler and Radau IIA 3^{rd} and 5^{th} order method.

Implicit Euler Method

The Euler implicit method provides the parameters of table A.3:

Table A.3: Parameters of the Euler implicit method.

1	1
	1

Implicit Radau IIA 3^{rd} Order Method

The Radau IIA 3rd order method provides the parameters of table A.4.

Table A.4: Parameters of the Runge-Kutta Radau IIA 3^{rd} order method.

1/3	5/12	−1/12
1	3/4	1/4
	3/4	1/4

The table A.4 gives the following set of equations:

$$\begin{aligned} k_1 &= f(x_o + 1/3 \cdot h, y_o + h/12 \cdot (5 \cdot k_1 - k_2)) \\ k_2 &= f(x_o + h, y_o + h/4 \cdot (3 \cdot k_1 + k_2)) \\ y_1 &= y_o + h/4 \cdot (3 \cdot k_1 + k_2) \end{aligned} \tag{A.7}$$

Implicit Radau IIA 5^{th} Order Method

The Radau IIA 5^{th} order method provides the parameters of table A.5.

Table A.5: Parameters of the Runge-Kutta Radau IIA 5^{th} order method.

$\frac{4-\sqrt{6}}{10}$	$\frac{88-7\cdot\sqrt{6}}{360}$	$\frac{296-169\cdot\sqrt{6}}{1800}$	$\frac{-2+3\cdot\sqrt{6}}{225}$
$\frac{4+\sqrt{6}}{10}$	$\frac{296+169\cdot\sqrt{6}}{1800}$	$\frac{88+7\cdot\sqrt{6}}{360}$	$\frac{-2-3\cdot\sqrt{6}}{225}$
1	$\frac{16-\sqrt{6}}{36}$	$\frac{16+\sqrt{6}}{36}$	$\frac{1}{9}$
1	$\frac{16-\sqrt{6}}{36}$	$\frac{16+\sqrt{6}}{36}$	$\frac{1}{9}$

A.2 Comparison of the Methods

Three test cases have been selected to compare performances and stability of the 3 integrations methods described above. The test cases are the following: (i) the waterhammer effect in pipe due to valve closure; (ii) the surge effects due to physical instabilities related to mass flow gain factor; and (iii) the van der Pol equation.

For both hydraulic cases, the parameters of the piping system are the same. The test case piping layout is presented in figure A.1 and the related parameters are given in table A.6. The number of nodes used to model the pipe is 10. To solve the differential equation set with RK methods, the equation set A.1 is reordered as follows:

$$\frac{d\overline{x}}{dt} = \underbrace{[A]^{-1} \cdot \overline{c} - [A]^{-1} \cdot [B(x,t)] \cdot \overline{x}}_{f(t,x)} \tag{A.8}$$

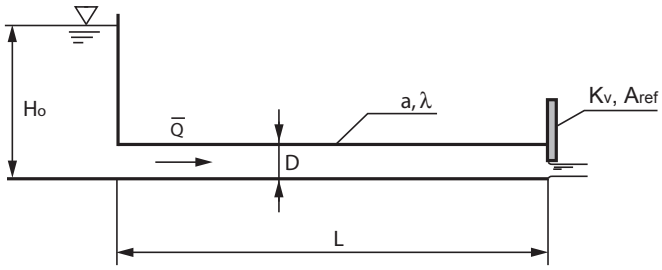

Figure A.1: Test case.

Table A.6: Test case parameters.

L $[m]$	D $[m]$	a $[m/s]$	λ $[-]$	Q_o $[m^3/s]$	fo = a/(4L) $[Hz]$
600	0.5	1200	0.02	0.5	0.5

A.2.1 Waterhammer Phenomenon

First, the waterhammer effect is simulated for 10 seconds for a partial closure law from fully opened valve to 10% valve opening within 2.1 seconds. The comparison of head and

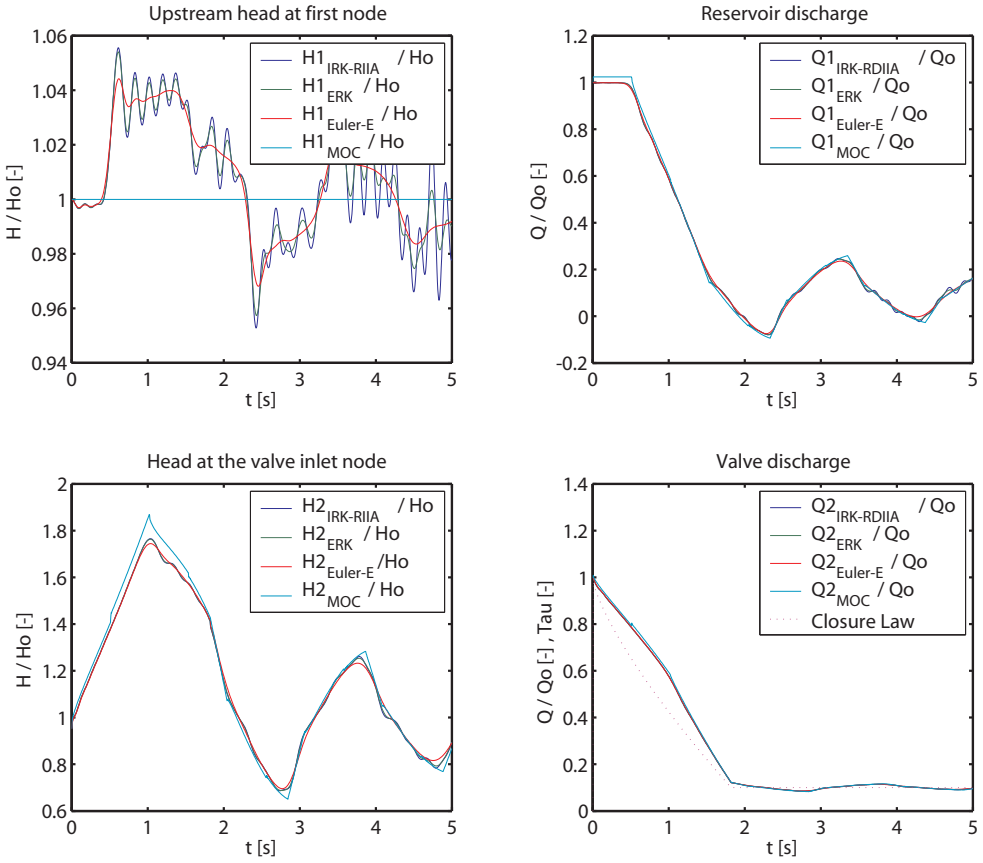

Figure A.2: Comparison of integration method for slow valve closure.

discharge at both end of the pipe are presented in figure A.2. The Method of Characteristic (MOC) is taken as reference.

Secondly a fast valve closure of 0.2 seconds is simulated. The comparison of the simulation results is presented in figure A.3 and in figure A.4.

The comparison of the different integration method shows that there is only a little difference between all the integration methods. The number of iteration of the method IRK-5^{th} required to reach an error of $\varepsilon = 10^{-5}$ for these simulations is 4.71 if 10 nodes are used to model the pipe. Increasing the number of nodes to 20 induces a number of iteration of 5.94 for the same error limit. Thus, the computational time required for a simulation is 5 times greater. In addition, when the number of nodes increases, the integration time step has to be reduced in the same proportion to fulfil CFL criteria. The IRK methods can provide more accurate solutions than ERK methods but to detrimentally to the computational time.

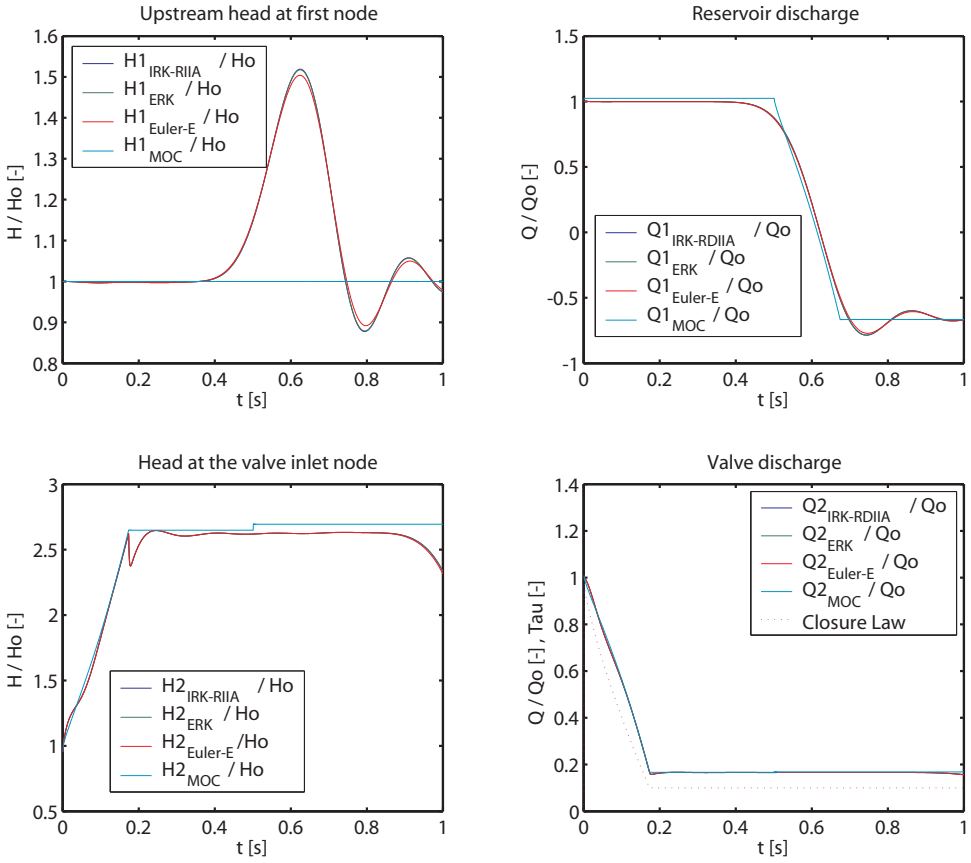

Figure A.3: Comparison of integration method for fast valve closure.

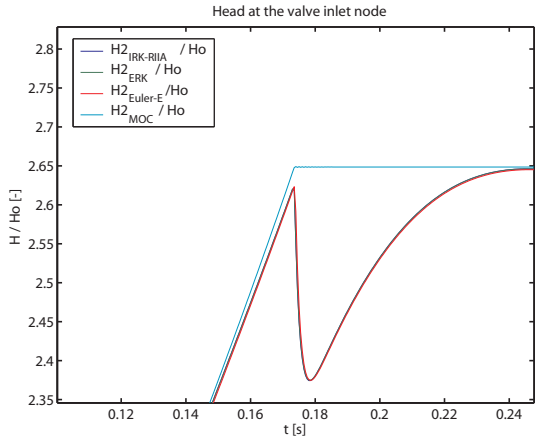

Figure A.4: Comparison of integration method for fast valve closure.

A.2.2 Surge Phenomenon

The surge phenomenon is simulated by considering a cavitation volume in the middle of the pipe. The cavitation volume is modelled as a compliant element featuring also a mass flow gain factor. Assuming that the cavitation volume is function of the head and the discharge yields to:

$$V(Q,H)_2 \Rightarrow dV = \frac{\partial V}{\partial H_2} \cdot dH_2 + \frac{\partial V}{\partial Q_2} \cdot dQ_2 \tag{A.9}$$

Time variation is given by:

$$\frac{dV}{dt} = \frac{\partial V}{\partial H_2} \cdot \frac{dH_2}{dt} + \frac{\partial V}{\partial Q_2} \cdot \frac{dQ_2}{dt} \tag{A.10}$$

Let's define:

- the cavity compliance $C = \frac{\partial V}{\partial H}$
- the mass flow gain factor $\chi = \frac{\partial V}{\partial Q}$

It yields to:

$$Q_2 - Q_1 = C \cdot \frac{dH_2}{dt} + \chi \cdot \frac{dQ_2}{dt} \tag{A.11}$$

When the mass flow gain factor is negative, the hydraulic system might become unstable. In this test case, the limit of the stability is reached for $\chi = -0.035$. The simulation of the unstable behavior of the pipe is initiated by a 50% valve closure is presented in figure A.5. This case features differences between the Euler method and the RK methods. However, again, no big differences between ERK and IRK are visible.

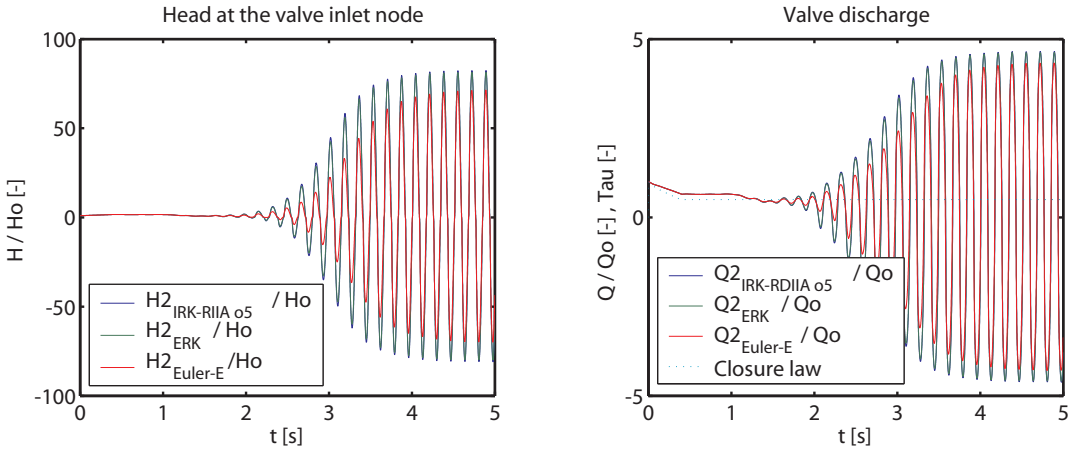

Figure A.5: Comparison of integration method for hydraulic surge.

A.2.3 Van der Pol Equation

The van der Pol equation is chosen as test function to evaluate performances of the different integration methods. The van der Pol's equation is given by:

$$\frac{d^2y}{dt^2} + \varepsilon \cdot (y^2 - 1) \cdot \frac{dy}{dt} + y = 0 \tag{A.12}$$

In order to have a first order ODE, equation A.12 can be rearranged as follows:

$$\frac{dy_1}{dt} = y_2 \quad ; \quad \frac{dy_2}{dt} + \varepsilon \cdot (y_1^2 - 1) \cdot y_2 + y_1 = 0 \tag{A.13}$$

The matricial expression gives:

$$\begin{bmatrix} 1 & 0 \\ 0 & 1 \end{bmatrix} \cdot \frac{d}{dt} \begin{bmatrix} y_1 \\ y_2 \end{bmatrix} + \begin{bmatrix} 0 & -1 \\ 1 & \varepsilon \cdot (y_1^2 - 1) \end{bmatrix} \cdot \begin{bmatrix} y_1 \\ y_2 \end{bmatrix} = \begin{bmatrix} 0 \\ 0 \end{bmatrix} \tag{A.14}$$

The system is solved considering the following initial conditions:

$$y_1(0) = 2 \quad ; \quad y_2(0) = 0 \quad \rightarrow \quad y_o = \begin{bmatrix} 2 \\ 0 \end{bmatrix} \tag{A.15}$$

The van der Pol equation represents a dynamic system whose damping is negative for small amplitudes ($y < 1$) and is positive for high amplitudes ($y > 1$). The parameter ε enables emphasizing the instability of the system; the higher the ε, the more unstable is the system. The simulation results obtained for $\varepsilon = 10$ using 5 different integration methods are presented in table A.7 for different integration time steps and tolerances.

For high integration time step, the Euler's methods, explicit or implicit, do not provide accurate solution. The frequency of the oscillation is underestimated by implicit method while it is overestimated by explicit method. However, all RK methods, implicit or explicit, provide reasonable solution. The solution of ERK is almost identical to the IRK RADAU IIA order 3. The tolerance of implicit method does not influence significantly the results but increases the number of loop by time step. Decreasing the integration time step improves strongly the simulation results of the Euler's methods. To reach the accuracy of RK method, the time step has to be divided by 100. So Euler's methods are not suitable for the simulation of unstable systems. Compared to the IRK methods, the ERK method provides good results in a reasonable computation time. Figure A.6 shows that all the methods provides the same results only for very small time step and tolerance. Between the IRK methods, the 3^{rd} order method is the most accurate method even for large tolerance and time step as the solution is only slightly influence by the reduction of the integration time step. The solution of the 5^{th} order converge to the solution of the 3^{rd} order when the time step is reduced.

The ERK method is found to be the most suitable integration for the integration of hydraulic systems. IRK RADAU IIA o3 might be useful for the verification of solution of the simulation of hydraulic system physically unstable.

Table A.7: Comparison of simulation results for the van der Pol equation.

	$Tolerance = 0.01$	$Tolerance = 0.0001$
$dt = 0.01s$	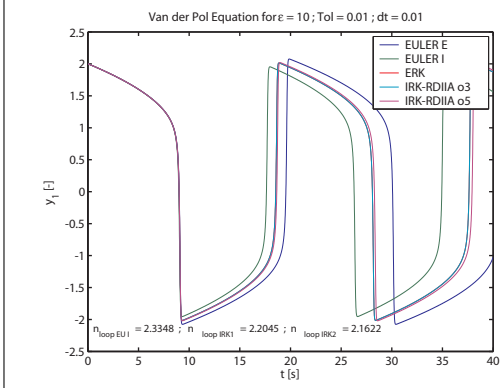	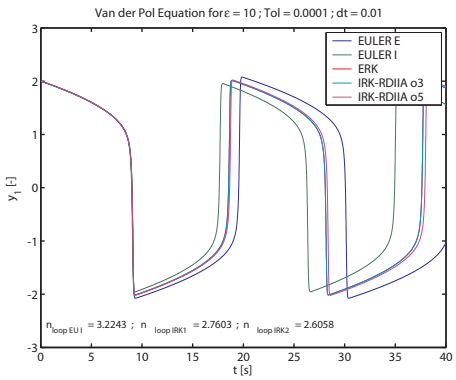
$dt = 0.001s$	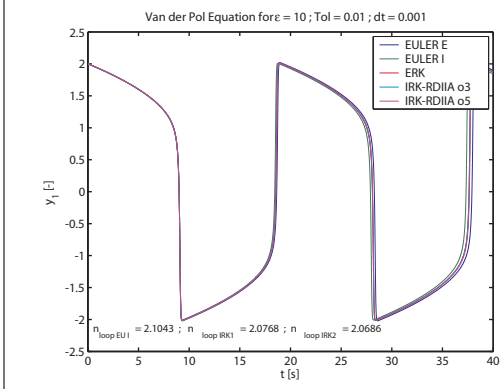	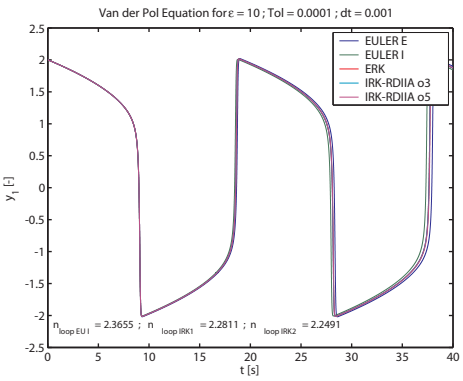

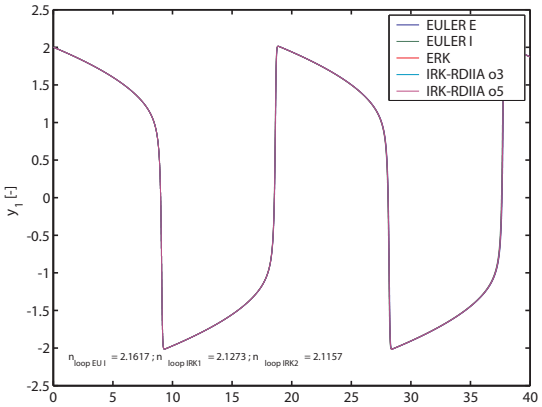

Figure A.6: Comparison of simulation results for the van der pol equation with small integration time step.

A.3 Stability Analysis of RK Methods

Let consider the smooth solution $\varphi(x)$ of equation A.1, $dy/dx = f(x, y)$. Linearizing $f(x, y)$ in its neighborhood as follows [43]:

$$\frac{dy(x)}{dx} = f(x, \varphi(x)) + \frac{\partial f}{\partial y}(x, \varphi(x)) \cdot (y(x) - \varphi(x)) + ... \tag{A.16}$$

Introducing $y(x) - \varphi(x) = \overline{y}(x)$ leads to:

$$\frac{d\overline{y}(x)}{dx} = \frac{\partial f}{\partial y}(x, \varphi(x)) \cdot \overline{y}(x) + ... = J(x) \cdot \overline{y}(x) + ... \tag{A.17}$$

As a first approximation, considering the Jacobian $J(x)$ constant and neglecting the errors terms yields to:

$$\frac{d\overline{y}(x)}{dx} = J \cdot \overline{y} \tag{A.18}$$

Using an explicit method to solve the equation above gives:

$$y_1 = R(h \cdot J) \cdot y_o \tag{A.19}$$

With the stability function $R(z)$:

$$R(z) = 1 + z + \frac{z^2}{2!} + ... + \frac{z^s}{s!} + O(z^{p+1}) \tag{A.20}$$

The stability function can be interpreted as the numerical solution of the Dalhquist test equation after one step for:

$$\frac{dy}{dx} = \delta \cdot y \quad ; \quad y_o = 1 \quad ; \quad z = h \cdot \delta \tag{A.21}$$

For an equations set of dimension k, y_m remains bounded for $m = 1 \rightarrow \infty$, if for all eigenvalues δ_k, the complex number $z = h \cdot \delta_k$ is contained in the domain S given by:

$$S = \{z \in C; |R(z) \leq 1\} \tag{A.22}$$

For implicit functions:

- Euler implicit:

$$R(z) = \frac{1}{1 - z} \tag{A.23}$$

- IRK RADAU IIA order 5:

$$R(z) = \frac{1 + z \cdot 2/5 + z^2/20}{1 - z \cdot 3/5 + z^2 \cdot 3/20 - z^3/60} \tag{A.24}$$

The stability domains related to ERK methods of order 1 to 4 are presented in figure A.7 while stability domain of implicit Euler and IRK RADAU IIA order 5 are respectively presented in figure A.8 left and right.

So these integration methods are stable if $R(h \cdot \delta_k) \leq 1$.

This inequality shows the influence of between the integration step h. The explicit methods feature more stable behavior for higher order method that encloses region close to the origin and higher frequencies. Highly damped systems might also present instabilities. However, implicit method do cover the whole part of the left hand side an extended part of the right hand part of the complex plan. The Euler implicit method appears to be a very stable method. More than the IRK RADAU IIA 5^{th} order method.

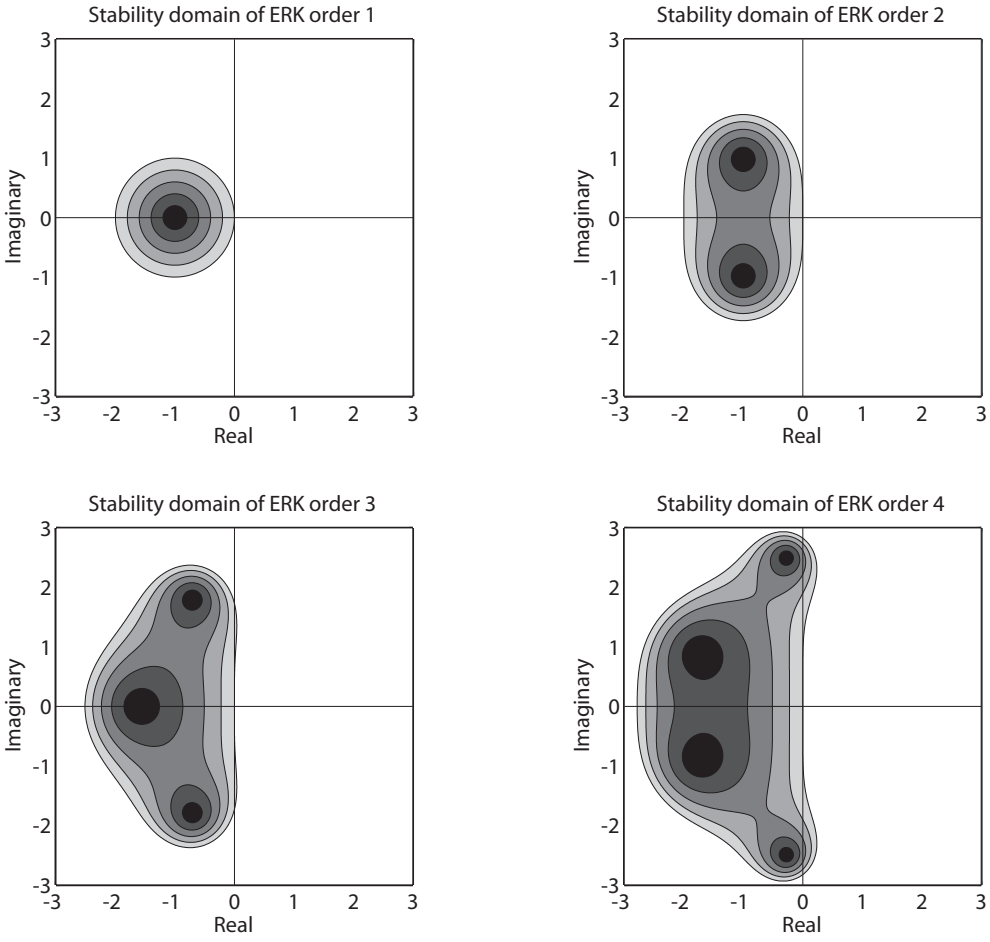

Figure A.7: Stability domain of ERK methods order 1 to 4.

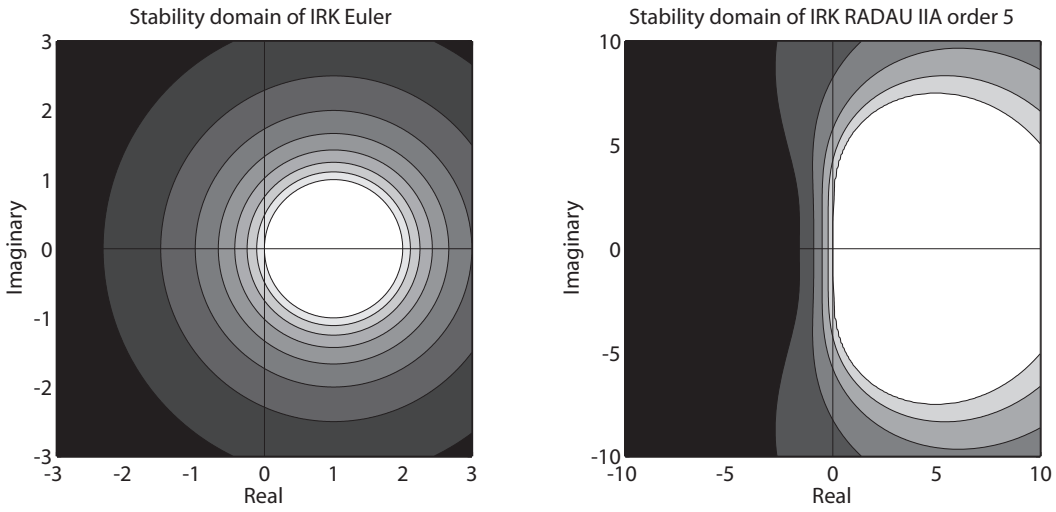

Figure A.8: Stability domain of the Euler implicit method (left), and stability domain of IRK RADAU method order 5 (right).

References

References

[1] Abbott, H. F., Gibson, W. L., and McCaig, I. W. Measurements of auto-oscillation in a hydroelectric supply tunnel and penstock system. *Trans. ASME, J. of basic Engineering 85* (December 1963), 625–630. Series D.

[2] Allievi, L. *Theory of Water Hammer*. Ricardo Garoni, Rome, 1925. Translated by E. E. Halmos.

[3] Anderson, A. Interaction of surge shafts and penstocks. In *Proceedings of the 4th Int- Conf. on Pressure Surges* (Bath, England, September 1983), pp. 297–312. paper G2.

[4] Angelico, F. M. G., Monaco, A. D., Fanelli, M., and Molinaro, P. A mechanical device for damping pressure oscillations in a hydroelectric power plant: a theoretical study through the transfer matrix method. In *Proceeding of the 17th IAHR Symposium on Hydraulic Machinery and System* (Beijing, September 1994), vol. 3, pp. 1221–1232.

[5] Arzola, F., Azuaje, C., Zambrano, P., and Gulbrandsen, G. Undesired power oscillations at high load in large francis turbines: experimental study and solution. In *Proceeding of the 23th IAHR Symposium on Hydraulic Machinery and System* (Yokohama, October 2006).

[6] Avellan, F. *Cours de machines hydrauliques*. EPFL, IMHEF, 2001, ch. I: Introduction.

[7] Bergeron, L. *Du coup de Bélier en hydraulique au coup de foudre en électricité*. Dunod, 1950.

[8] Biela, V., and Beltran, H. Draft tube fins. In *Proceeding of the 19th IAHR Symposium on Hydraulic Machinery and System* (Singapore, 1998), pp. 454–461.

[9] Bölcs, A. *Turbomachines thermiques*, vol. I. LTT/EPFL, 1993.

[10] Blommaert, G. *Etude du compretement dynamique des turbines Francis: contrôle actif de leur stabilité*. PhD thesis, EPFL, Lausanne, 2000. N°2222.

[11] Blommaert, G., Avellan, F., and Prénat, J.-E. Evaluation de la stabilité d'installations hydroélectriques à partir d'essais sur modèle réduit : étude expérimentale. In *Colloque SHF : machines hydrauliques, instationnarités et effets associés* (November 2000).

[12] Blommaert, G., Prénat, J.-E., Avellan, F., and Boyer, A. Active control of francis turbine operation stability. In *Proceedings of the 3rd ASME/JSME Joint Fluids Engineering Conference* (San Francisco, California, July 1999).

[13] Bolleter, U. Hydraulic and mechanical interactions of feedpump systems. Tech. Rep. TR-100990, EPRI, Sept. 1992. TR-100990.

[14] Bovet, T., and Henry, P. Le nouveau stand d'essai universel pour machines hydrauliques à réaction. Tech. Rep. 6, EPFL, Institut de Machines Hydrauliques, Lausanne, 1970. in french.

[15] Brennen, C., and Acosta, A. J. Theoretical, quasi-static analysis of cavitation compliance in turbopumps. *J. Space Craft 10*, 3 (March 1973), 175–180.

[16] Campmas, P. Stability of operating conditions for francis turbines. In *Proceeding of the 1st IAHR Symposium on Hydraulic Machinery and System.*

[17] Canay, I. M. Extended synchronous machine model for calculation of transient processes and stability. *Electric machines and Electromechanics 1* (1977), 137–150.

[18] Chapman, A. D. R., and Robbie, J. F. Eigenvalue stability analysis of surge systems involving double vented shafts - theory and practice. In *Proceedings of the 4th Int. Conf. on Pressure Surges* (Bath, England, September 1983), pp. 353–377. paper H3.

[19] Chatelain, J. *Traité d'électricité: machines électriques*, georgi ed., vol. X. Presse polytechniques romandes, Lausanne, 1983.

[20] Chaudhry, M. H., and Mays, L. W. *Computer modeling of free-surface and pressurized flows.* Kluwer Academic Publischer, Dordrecht, Boston, London, 1994.

[21] Chen, Y. N. Water-pressure oscillations in the volute casings of storage pumps. *Sulzer Technical Review* (1961), 21–34. Research Number.

[22] Council, W. E. Survey of energy resources 2004. Tech. rep., WEC, London, 2004. online publication: http://www.worldenergy.org.

[23] Courant, R., Friedrichs, K., and Lewy, H. Über die partiellen differenzengleichungen der mathematischen physik. *Mathematische Annalen Volume 100*, number 1 (December 1928), 32–74.

[24] Delbe, C. *Modélisation comportementale et commande découplée d'un groupe turbo-alternateur connecté à un réseau fini de distribution d'énergie Electrique.* PhD thesis, INSA, 1991. .91 ISAL (in french).

[25] Dörfler, P. K. System dynamics of the francis turbine half load surge. In *Proceeding of the 11th IAHR Symposium on Hydraulic Machinery and System* (Amsterdam, 1982). paper 39.

[26] Dörfler, P. K. On the role of phase resonance in vibrations caused by blade passage in radial hydraulic turbomachines. In *Proceeding of the 12th IAHR Symposium on Hydraulic Machinery and System* (Stirling, 1984), pp. 227–241. paper 3.3.

[27] Dörfler, P. K., Engineer, A. J., Pendse, R. N., Huvet, P., and Brahme, M. V. Stable operation achieved on single-stage reversible pump-turbine showing instability at no-load. In *Proceeding of the 19th IAHR Symposium on Hydraulic Machinery and System* (Singapore, 1998), pp. 430–440.

[28] Dériaz, P. A contribution to the understanding of flow in draft tubes of francis turbines. In *Proceeding of the 1st IAHR Symposium on Hydraulic Machinery and System*.

[29] Dube, B. *Optimisation des dispositifs de reglage primaire d'une installation hydro-electrique*. PhD thesis, EPFL, Lausanne, 1975. n°205.

[30] Energy Information Administration, O. E. S. f. t. U. G. International energy outlook 2006. Tech. rep., Official Energy Statistics from the U.S. Government, June 2006. Report N°:DOE/EIA-0484(2006).

[31] Fischer, R. K., Palde, U., and Ulith, P. Comparison of draft tube surging of homologous scale models and prototype francis turbines. In *Proceeding of the 10th IAHR Symposium on Hydraulic Machinery and System* (Tokyo, 1980), pp. 541–556.

[32] Fox, J. A. *Transient flow in pipes, open channels and sewers*. Ellis Horwood Limited, Chichester, 1989.

[33] Franc, J.-P., Avellan, F., Belhadji, B., Billard, J.-Y., Briançon-Marjolet, L., Fréchou, D., Fruman, D. H., Karimi, A., Kueny, J.-L., and Michel, J.-M. *La Cavitation: Mécanismes Physiques et Aspects Industriels*. Collection Grenoble Sciences. Presse Universitaires de Grenoble, Grenoble, 1995.

[34] Franke, G., Powell, C., Seidel, U., Koutnik, J., and Fischer, R. K. On pressure mode shapes arising from rotor/stator interactions. *Sound and Vibration* (March 2005), 14–18.

[35] Fritsch, A., and Maria, D. Comportement dynamique d'une turbine francis à charge partielle: comparaison modèle-prototype. *La Houille Blanche*, 3/4 (1988), 273–280. in french.

[36] Godfrey, K. Design and application of multifrequency signals. *Computing and Control Engineering Journal 2*, Issue 4 (July 1991), 187–195.

[37] Goosen, J., Simond, J.-J., Steigleder, K., Soenen, L., Steffens, J.-C., and Stubbe, J. Several aspects of the torsional fatigue damage of turbo-group shafts due to electrical disturbances. *A.I.M.* (1985). Liège, 63.1-10.

[38] Graeser, J.-E. *Régime transistoires en hydrauliques - Coup de Bélier*. EPFL-IMH, 1983.

[39] Grein, H. Vibration phenomena in francis turbines: their causes and prevention. In *Proceeding of the 10th IAHR Symposium on Hydraulic Machinery and System* (Tokyo, 1980), pp. 527–539.

[40] Greitzer, E. M. The stability of pumping systems. *Trans. of ASME, J. of Fluids Eng. 103* (june 1981), 193–242.

[41] Haban, V., Koutnik, J., and Pochyly, F. 1-d mathematical model of high-frequency pressure oscillations induced by rsi inculding an influence of fluid second viscosity. In *Proceeding of the 21st IAHR Symposium on Hydraulic Machinery and System* (Lausanne, 2002), pp. 735–740.

[42] Hairer, E., Nørsett, S. P., and Wanner, G. *Solving ordinary differential equations 1, nonstiff problems.* Springer, 2000.

[43] Hairer, E., and Wanner, G. *Solving ordinary differential equations 2, stiff and differential algebraic problems.* Springer, 2002.

[44] Harbort, T. *Eintwicklung eines echtzeifähigen Simulationsprogramms zur Untersuchung instationärer Vorgänge in Wasserkraftwerken.* PhD thesis, Universität Stuttgart, 1999. in german.

[45] Hartog, J. P. D. *Mechanical vibrations*, 4th edition ed. McGraw-Hill, New York, 1956. pp. 7-9.

[46] Henry, P., Graeser, J.-E., Prénat, J.-E., and Wegner, M. Scale effect concerning hydraulic quasi-stationary oscillations on a turbine model and test circuit. In *Proceeding of the 12th IAHR Symposium on Hydraulic Machinery and System* (Stirling, 1984), pp. 356–371.

[47] Henry, P., Lecoffre, Y., and Larroze, P. Y. Effets d'échelle en cavitation. In *Proceeding of the 10th IAHR Symposium on Hydraulic Machinery and System* (Tokyo, 1980), pp. 103–113.

[48] Huvet, P. Steady oscillatory conditions between pump-turbine operating at partial flow and surge shaft. In *Proceeding of the 16th IAHR Symposium on Hydraulic Machinery and System* (Sao Paolo, 1992), pp. 349–358.

[49] IEA. World energy outlook: 1999 insights. International Energy Agency.

[50] Jacob, T. *Evaluation sur modèle réduit et prediction de la stabilité de fonctionnement des turbines Francis.* PhD thesis, EPFL, Lausanne, 1993. N° 1146.

[51] Jacob, T., and Prenat, J.-E. Francis turbine surge : discussion and data base. In *Proceeding of the 18th IAHR Symposium on Hydraulic Machinery and System* (Valencia, Spain, 1996), vol. 2, pp. 855–864.

[52] Jacob, T., Prénat, J.-E., Buffet, G., and Winkler, S. Improving the stability of operation of a 90 mw francis turbine. In *Proceedings of the international Conference on Hydropower into the next Century* (Barcelona, Spain, June 1995).

[53] Jacob, T., Prénat, J.-E., Vullioud, G., and Araguas, B. L. Surging of 140 mw francis turbines at high load, analysis and solution. In *Proceeding of the 16th IAHR Symposium on Hydraulic Machinery and System* (Sao Paolo, 1992).

[54] Jaeger, C. The theory of resonance in hydropower systems. discussion of incidents and accidents occuring in pressure systems. *Trans. ASME, J. of Basic Engineering* (December 1963), 631–640.

[55] Jaeger, C. *Fluid transients in hydro-electric engineering practice*. Blackie, Glasgow, 1977.

[56] Kamwa, I., Grondin, R., and Trudel, G. Ieee pss2b versus pss4b:the limits of performance of modern power system stabilizers. *IEEE Transactions on Power Systems 20* (May 2005), 903 – 915. Issue 2.

[57] Karimi, A., and Avellan, F. Comparison of erosion mechanisms in different types of cavitation. *Wear 113* (1986), 305–322.

[58] Knapp, R. T. Complete characteristics of centrifugal pumps and their use in the prediction of transient behavior. *Transaction of the ASME* (1937), 683–689. 59(3).

[59] Konidaris, D. N., and Tegopoulos, J. A. Investigation of oscillatory problems of hydraulic generating units equipped with francis turbines. *IEEE Trans. on Energy Conversion 12* (1997). Issue 4.

[60] Kopf, E., Brausewetter, S., Giese, M., and Moser, F. Optimized control strategies for variable speed machines. In *Proceeding of the 22nd IAHR Symposium on Hydraulic Machinery and System* (Stockholm, June 2004), pp. 1–9. paper A 15-2.

[61] Koutnik, J. Analysis of pressure oscillations measured in the twin-penstock of pspp stechovice. In *Proceeding of the 20th IAHR Symposium on Hydraulic Machinery and System* (Charlotte, USA, 2000).

[62] Koutnik, J., and Pulpitel, L. Modeling of the francis turbine full-load surge. In *Modeling, Testing and Monitoring for Hydro Power plants - II* (June 1996).

[63] Krueger, R. E. Selecting hydraulic reaction turbines. *Engineering Monograph 20* (1980).

[64] Lowys, P. Y., Paquet, F., Couston, M., Farhat, M., Natal, S., and Avellan, F. Onboard measurments of pressure and strain fluctuations in a model of low head francis turbine - part 2: Measurments an dpreliminary analysis results. In *Proceeding of the 21st IAHR Symposium on Hydraulic Machinery and System* (Lausanne, September 2002), pp. 873–880.

[65] Marchal, M., Flesh, G., and Suter, P. The calculation of waterhammer problems by means of the digital computer. In *Proc. Int. Symp. Waterhammer Pumped Storage Projects* (Chicago, 1965), ASME.

[66] Martin, C. S. Stability of pump-turbines during transient operation. In *Proceedings of the 5th Int. Conf. on Pressure Surges* (Hannover, Germany, 1986), pp. 61–71. paper C3.

[67] Martin, C. S. Instability of pump-turbines with s-shaped characteristics. In *Proceeding of the 20th IAHR Symposium on Hydraulic Machinery and System* (Charlotte, USA, 2000).

[68] Miller, D. S. *Internal flow system*, 2nd ed. BHRA, Cranfield, 1990.

[69] Nishi, M. Study on swirl flow and surge in an elbow type draft tube. In *Proceeding of the 10th IAHR Symposium on Hydraulic Machinery and System* (Tokyo, 1980), pp. 557–565.

[70] Nishi, M. Surging characteristics of conical and elbow type draft tubes. In *Proceeding of the 12th IAHR Symposium on Hydraulic Machinery and System* (Stirling, 1984), pp. 272–283.

[71] Nishihara, T., Akimoto, T., and Yamamoto, K. Self-induced pressur epulsation in penstock caused by movable-seat seal using tapper water from penstock. In *Proceedings of Waterpower XIII* (Buffalo, USA, 2003), pp. 1–12.

[72] Ohura, Y., Fujii, M., Sugimoto, O., Tanaka, H., and Yamagata, I. Vibration of the powerhouse structure of pumped storage power plant. In *Proceeding of the 15th IAHR Symposium on Hydraulic Machinery and System* (Belgrade, 1990). section U2.

[73] on Hydropower & Dams, T. I. J. Hydropower & dams world atlas 2001.

[74] Paynter, H. M. Surge and water hammer problems. *Transaction of ASCE 146* (1953), 962–1009.

[75] Pedro, M. D., and Pahud, P. *Mécanique vibratoire - Système discret linéaires*. Presses Polytechniques et Universitaires Romandes, 1997.

[76] Pejovic, S. Troubleshooting of turbine vortex core resonance and air introduction into the draft tube. In *Proceeding of the 21st IAHR Symposium on Hydraulic Machinery and System* (Lausanne, 2002), pp. 511–516.

[77] Pejovic, S., Obradovic, D., and Gajic, A. Field tests and calculations of the effects of air introduction into the draft tube upon hydraulic oscillations in a hydropower plant. In *Proceeding of the 13th IAHR Symposium on Hydraulic Machinery and System* (Montréal, 1986). paper 9.

[78] Ramirez, C. *Plate-forme numérique d'essais pour machines électriques de puissance*. PhD thesis, EPFL, Lausanne, 2003. N°2821.

[79] Ratsaramody, J. *Programme de CAO-DAO d'installations hydroélectriques utilisable au stade d'un avant projet*. PhD thesis, EPFL, Lausanne, 1992. Thèse EES Polytechnique Antsiranana,.

[80] Rheingans, W. J. Power swing in hydroelectric power plants. *Transaction ASME 62* (1940), 171–184.

[81] Ribaux, A. *Hydraulique appliquée III, Turbo-machines*. Editions de la Moraine, Genève, 1953.

[82] Rubin, S. Longitudinal instability of liquid rockets due to propulsion feedback (pogo). *J. Space Craft 3*, 8 (august 1966), 1188–1195.

[83] Sapin, A. *Logiciel modulaire pour la simulation et l'étude des systèmes d'entraînement et des réseaux électriques*. PhD thesis, EPFL, 1995. n° 1346.

[84] Sapin, A., Steimer, P. K., and Simond, J.-J. Modeling, simulation and test of a three-level voltage source inverter with output lf filter and direct torque control. In *IEEE, Conference Record of the 38th Industry Applications Conference Annual Meeting* (12-16 Oct. 2003), vol. 1, pp. 492–498.

[85] Souza, O. H. J., Barbieri, N., and Santos, A. H. M. Study of hydraulic transients in hydropower plants through simulation of nonlinear model of penstock and hydraulic turbine model. *IEEE Transactions on Power Systems 14* (1999), 1269 – 1272. Issue 4.

[86] Streeter, V. L., and Wylie, E. B. *Fluid transients in systems*. Prentice Hall, Englewood Cliffs, N.J., 1993.

[87] Susan-Resiga, R., Vu, T. C., Muntean, S., Ciocan, G. D., and Nennemann, B. Jet control of the draft tube vortex rope in francis turbines at partial discharge. In *Proceeding of the 23rd IAHR Symposium on Hydraulic Machinery and System* (Yokohama, October 2006). paper 192.

[88] Swaffield, J. A., and Boldy, A. P. *Pressure surge in pipe and duct systems*. Avebury Technical, Aldershot, 1993.

[89] Thoma, D. *Zur Theorie des Wasserschlosses bei selbsttätig geregelten Turbinenanlagen*. Munich (Oldenbourg), 1910. in german.

[90] Vatcher, T. R., Hunter, M., Perreault, G., and Coulson, D. M. Hydraulic resonance in a 78mw francis turbine - field test results. In *Proceeding of the 12th IAHR Symposium on Hydraulic Machinery and System* (Stirling, 1984), pp. 371–391.

[91] Wang, D., and Johnson, C. D. A comparison study of some impulse-response identification methods. In *IEEE Proceedings. Twenty-First Southeastern Symposium* (March 1989), System Theory, pp. 52 – 56.

[92] WorkingGroup. Hydraulic turbine control models for system dynamic studies. *Trans. Power Systems 7*, 1 (February 1992). Working group on Prime Mover and Energy Supply Models for System Dynamic Performance Studies.

Index